Abstract

Rare Event Searches in Liquid Xenon with EXO-200, nEXO and Beyond

Ako Jamil

2022

Liquid xenon detectors operated as time projection chambers have emerged as a key technology over the past decades in the search for extremely rare events, such as the interaction of dark matter or neutrinoless double beta decay ($0\nu\beta\beta$) of ^{136}Xe. These experiments need to operate in an ultra-low background regime. The remaining backgrounds need not only to be reliably and accurately modeled but also rejected using sophisticated reconstruction techniques that distinguish signal from background. In this work, three generations of liquid xenon experiments are examined.

Data from the decommissioned $\sim$200 kg EXO-200 experiment was analyzed for a recently-proposed interaction mechanism of fermionic dark matter with ordinary matter via charged-current absorption.

A detailed understanding of the light and charge transport in liquid xenon for the upcoming tonne-scale nEXO experiment is described, including a robust estimate of the discovery and exclusion sensitivity for $0\nu\beta\beta$ of ^{136}Xe.

Lastly, a conceptual design for a possible kilotonne-scale liquid xenon detector is presented, which includes requirements on the photon detection system to enable novel Cherenkov and scintillation light separation for improved discrimination between β-like background and $\beta\beta$-like signal events.

Rare Event Searches in Liquid Xenon with EXO-200, nEXO and Beyond

A Dissertation
Presented to the Faculty of the Graduate School
of
Yale University
in Candidacy for the Degree of
Doctor of Philosophy

by
Ako Jamil

Dissertation Director: David C. Moore

December 2022

Acknowledgements

I was fortunate enough to have met many great individuals whose passion, life stories, and advice have allowed me to grow tremendously and have contributed to this work in many different ways. This thesis is a culmination of all their help, influence, and patience that finally got me here. I thank all of you and I am looking forward to learning so much more from you in the future.

First, I would like to thank my advisor, David Moore, who has been incredibly supportive and a role model. He taught me to never lose sight of the bigger scientific picture while always helping me to identify the most important aspect of the technical problem ahead. I am hoping that some of his ingenuity and creativity in finding and solving new problems have rubbed off on me.

I thank all the former and current members of the Moore group for making our daily group lunches and coffee breaks one of my favorite activities in graduate school. I hope to carry on with this tradition which will hopefully inspire similarly interesting conversations about physics and beyond. I have learned a great deal from Fernando Monteiro and Gadi Afek about scientific rigor, enjoying your every step along the way even if it is very frustrating at times, and not taking yourself and your work too seriously. You were great mentors.

My colleagues in the EXO-200 and nEXO collaborations have created a wonderful environment for young aspiring scientists like myself to learn the proper scientific methods and to contribute to the bigger project in meaningful ways. Thank you for

allowing me to be part of this exciting endeavor. A special thank you to Mike Jewell who has helped me patiently with the EXO-200 code as I was trying to modify it for the dark matter analysis.

Additionally, I would like to acknowledge all the people in the Physics Department at Yale and at Wright Lab for their support and for making working there so much more enjoyable: Sidney Cahn, David Johnson, Thomas Langford, Frank Lopez, Craig Miller, Victoria Misenti, and most importantly, Kimberly Tighe.

None of this would have been possible without the unconditional support of my family. My brother and sister are the anchors that keep me grounded and help me see the world outside of physics and academia. I am forever thankful to my parents for placing education above all else, even if that meant uprooting their own lives to secure a better future for us. From a very young age, you have allowed me to chase my dreams and interests and I can't thank you enough. Finally, I am incredibly grateful for my wife, Yasemin, who has been by my side since college, crossing the ocean from Europe with me for my Ph.D. and going back soon. You bring joy to my life and your love is what got me to the finish line. I am looking forward to what the next chapter in our lives together will bring.

This thesis is dedicated to my parents.

Contents

1 Rare Events as a Probe for New Physics **1**

1.1 Majorana Neutrinos . . . 2

1.1.1 Neutrino Oscillations . . . 3

1.1.2 Origin of Neutrino Masses . . . 6

1.1.3 Neutrinoless Double Beta Decay . . . 10

1.2 Dark Matter . . . 14

1.2.1 Evidence . . . 15

1.2.2 Properties . . . 19

1.2.3 Beyond the WIMP Paradigm . . . 21

2 Search for MeV Electron Recoils from Dark Matter in EXO-200 **23**

2.1 The EXO-200 Experiment . . . 24

2.2 Event Signature and Monte-Carlo . . . 26

2.3 Analysis . . . 29

2.4 Systematics . . . 32

2.5 Results . . . 36

3 nEXO: A Tonne-scale Experiment Searching for $0\nu\beta\beta$ **41**

3.1 Detector Design . . . 42

3.2 Charge Collection with Tiles . . . 44

3.3 Light Collection with Silicon Photomultipliers . . . 46

3.4 Comparison between EXO-200 and nEXO 53

4 Light and Charge Transport in nEXO 55

4.1 Photon Transport and Optical Simulations 56

4.1.1 Chroma and GPU-acceleration 57

4.1.2 Detector Geometry and Optical Properties 59

4.1.3 Systematic Error on Photon Transport 61

4.1.4 Photon Distribution 67

4.1.5 Lightmap 70

4.1.6 Alternative Designs 72

4.1.7 Channel Size and Dynamic Range 74

4.1.8 Conclusion and Outlook 76

4.2 Charge Transport and Liquid Xenon Purity 77

4.2.1 Modelling Outgassing of Impurities 78

4.2.2 Electronegative Impurity Control in nEXO 95

4.2.3 Vacuum Outgassing Setup 99

4.2.4 Liquid Xenon Purity Monitor 107

4.2.5 Conclusion and Outlook 120

4.3 Energy Resolution 121

5 Exclusion and Discovery Sensitivity of nEXO 130

5.1 Monte Carlo Simulation 131

5.2 Event Reconstruction and Background Rejection 133

5.2.1 Position Reconstruction 133

5.2.2 Energy Reconstruction 134

5.2.3 DNN-Based Background Rejection 139

5.3 Background Model 142

5.3.1 Intrinsic Radioactivity 144

5.3.2 Exposure-based Radioactivity . . . 147
5.3.3 Radon-based Radioactivity . . . 148
5.3.4 Background Budget . . . 150
5.4 Statistical Analysis . . . 151
5.4.1 Likelihood Function and Test Statistic . . . 152
5.4.2 Exclusion Sensitivity . . . 154
5.4.3 Discovery Sensitivity . . . 155
5.4.4 Fit Model . . . 158
5.5 Results . . . 163
5.5.1 Baseline Physics Reach . . . 164
5.5.2 Dependence on Energy Resolution . . . 167
5.5.3 Dependence on Background Mismodeling . . . 169
5.5.4 $2\nu\beta\beta$-only Case . . . 171
5.5.5 Counting Experiment and Background Index . . . 172
5.6 Effective Majorana Neutrino Mass Sensitivity . . . 180
5.7 Conclusion and Outlook . . . 185

6 Kilotonne Liquid Xenon Detectors for Rare Event Searches 188
6.1 Motivation . . . 189
6.2 Irreducible Backgrounds . . . 191
6.2.1 $2\nu\beta\beta$ . . . 192
6.2.2 Solar Neutrinos . . . 193
6.3 Detector Concept . . . 194
6.4 Optical Simulations and Light Collection . . . 196
6.5 Scintillation and Cherenkov Light Separation . . . 198
6.6 Sensitivity to $0\nu\beta\beta$ . . . 203

7 Conclusion 206

Bibliography **213**

Acronyms

^{enr}Xe enriched Xenon

^{nat}Xe natural Xenon

AmBe Americium Beryllium

AP Afterpulsing

ARC Anti-reflective Coating

CA Correlated Avalanches

CT Cross-talk

DCR Dark Count Rate

dCT delayed Cross-talk

EXO Enriched Xenon Observatory

LNGS Laboratori Nazionali del Gran Sasso

LXe Liquid Xenon

pCT prompt Cross-talk

PDE Photon Detection Efficiency

PFPE Perfluorinated Polyether

PTFE Polytetrafluoroethylene

RGA Residual Gas Analyzer

SiPM Silicon Photomultiplier

SM Standard Model

SURF Sanford Underground Research Facility

TPC Time Projection Chamber

VUV Vacuum Ultra Violet

YPM Yale Purity Monitor

List of Figures

1.1 Possible ordering of neutrino mass eigenstates ν_i. The ambiguity arises from the fact that neutrino oscillation experiments measuring the atmospheric mass splitting are not sensitive to the overall sign. Figure from [12]. 5

1.2 Feynman diagram for the $2\nu\beta\beta$ (left) and $0\nu\beta\beta$ (right), assuming that the dominant decay mechanism is the virtual exchange of a light Majorana neutrino, denoted as ν_{M}. 11

1.3 Available parameter space of $\langle m_{\beta\beta}\rangle$ as a function of light neutrino mass (left) and the sum of all neutrino masses (right). The value for $\langle m_{\beta\beta}\rangle$ and therefore the rate of $0\nu\beta\beta$ depends on the neutrino mass ordering, where the realization for the NH and OH are shown in blue and orange, respectively. The spread of the bands arises from the unconstrained Majorana phases (dashed lines) and the uncertainties in the neutrino mixing parameters of the PMNS matrix (solid lines) [28]. 12

1.4 Rotation curves of stars in the galaxy NGC 6503. The rotational velocity of gravitationally bound objects is expected to fall off as $1/\sqrt{r}$ beyond the bulk matter of the galaxy using Newtonian dynamics. The measured flatness of the rotational velocity requires the existence of significant amounts of additional non-luminous matter in a spherical halo around the galaxy with a mass distribution of $M(r) \sim r$. Figure from [40]. 16

1.5 X-ray image of the merging Bullet cluster. The contours of gravitational potential, which are measured through gravitational lensing of the background objects, are shown in green. The significant offset between the gravitational centers of mass and the location of the luminous matter indicates the presence of significant amounts of dark matter, which unlike baryonic matter does not self-interact. Figure from [41]. 17

1.6 (left) The CMB anisotropy measured by the Wilkinson Microwave anisotropy Probe (WMAP) [46] (right) The power spectrum of the CMB anisotropy expanded in multiple moments of spherical harmonics. The red curve represents the best fit according to the ΛCDM model of cosmology. Figure from [47]. 18

2.1 Section view of the EXO-200 detector inside the cleanroom at WIPP. Figure from [72]. 25

2.2 Monte Carlo simulation of the EXO-200 detector response to electrons at energies of 2 MeV, 4.5 MeV and 7 MeV in Phase II. The simulated distribution of the maximum reconstructed ionization energy in an event is shown, where the non-Gaussian shape comes from the increased emission of bremsstrahlung for the higher energy βs. 27

2.3 (top) AmBe calibration source energy spectrum in Phase II, demonstrating linear energy response of the EXO-200 detector throughout the energy range of interest. (bottom) Residuals between the measured and known energies ΔE.Calibration errors at the photo-peaks are less than 20 keV, resulting in a systematic error on the energy scale of $<0.5\,\%$. 31

2.4 The energy dependence of the parameters a (solid) and b (dashed) in equation 2.3 for quantifying the systematic error from spectral shape disagreements is parameterized by $a(E) = a_1 \cdot E + a_2$ and $b(E) = b_1 \cdot e^{-b_2 \cdot E} + b_3$, respectively. 33

2.5 The top panel of the plot shows the upper limit (solid orange) on the number of dark matter events as a function of energy at 90 % CL. The median sensitivity (dashed blue) and the $\pm 1\,\sigma$ (dark blue) and $\pm 2\,\sigma$ (light blue) percentiles around the median are also shown. The bottom panel shows the local significance of our observation against the no-signal hypothesis. Taking into account the "look-elsewhere" effect we report no statistically significant evidence for dark matter. 37

2.6 Limit on the absorption cross-section of fermionic dark matter by ^{136}Xe nuclei at the 90 % CL. We show our main 2D fit result in addition to a de-excitation γ agnostic 1D fit result (see text for more details). The grey region is excluded by direct constraint from colliders searches at the LHC [81]. 38

2.7 Rotated energy spectrum of the low-background data and the best fit (blue) to the data with a background-only model in Phase I (a) and Phase II (c) is shown. The resulting residual number of counts between data and the best from Phase I and Phase II is shown in panels (b) and (d), respectively. No significant disagreement is seen between the data and the background-only model. The average electron-recoil background rate above 4 MeV is $4.0 \times 10^{-4}\,\mathrm{cts\,kg^{-1}\,yr^{-1}\,keV^{-1}}$ in Phase I and $6.8 \times 10^{-4}\,\mathrm{cts\,kg^{-1}\,yr^{-1}\,keV^{-1}}$ in Phase II with a total exposure of 117.4 kg yr and 116.7 kg yr, respectively. 39

3.1 (left) Artistic view of the nEXO experiment in the SNOLAB cryopit. (right) Section view of nEXO's carbon-fiber-based inner and outer cryostats and the copper Time Projection Chamber (TPC) vessel in the center, supported by titanium liners. 42

3.2 (left) Photograph of a prototype charge collection tile mounted into a test Liquid Xenon (LXe) setup. This iteration still used a provisional connection scheme to the external, discrete component electronics at room temperature. A future version will include integrated ASIC electronics on the backside, avoiding the need for discrete wiring and electronics. (right) Early prototype of a Silicon Photomultiplier (SiPM) array consisting of 24 $1\,\mathrm{cm^2}$ FBK devices from 2017. No particular attention was paid to radiopurity or maximal coverage since this prototype only intended to demonstrate the safe operation of a large number of Silicon Photomultiplier (SiPM)s in Liquid Xenon (LXe). Figures from [85]. 45

3.3 Distribution of photoelectron equivalents for parent and subsequent pulses as a function of the time since the pixel was triggered. See the text for a detailed explanation. Figure from [102]. 47

3.4 View of the photon detection system of nEXO, showing a view of the Silicon Photomultiplier (SiPM) staves (left) consisting of a 2x10 array of photon detection modules, each of which is made of 96 Silicon Photomultiplier (SiPM)s. A total of 24 staves will make up the photon detection system (right) covering the barrel of the Time Projection Chamber (TPC) vessel and will be situated behind the field shaping rings. 50

4.1 Rendering of the EXO-200 detector (left) including the fine cathode mesh and the nEXO detector (right) geometries in Chroma for performing light transport simulations. 58

4.2 A CAD model of the nEXO Time Projection Chamber (TPC) as it is imported into Chroma, where only detector components relevant for light propagation are shown. This includes the anode (top), cathode (bottom), field shaping rings, field cage support rods, Silicon Photomultiplier (SiPM) staves, the Silicon Photomultiplier (SiPM) modules, and the copper vessel (not shown). 60

4.3 Shown are the estimated average PTE inside the FV from light simulations with varying input optical parameters. These studies include changes to the Liquid Xenon (LXe) absorption length λ_{abs} (top), Liquid Xenon (LXe) Rayleigh scattering length λ_{scat} (middle) and the fraction of diffuse reflection (bottom). 62

4.4 Spatially averaged PTE inside the fiducial volume as a function of the specular reflectivity of the cathode and the FSRs. The different curves are for different angle-dependent reflectivities of candidate Silicon Photomultiplier (SiPM)s for nEXO. The reflectivities of VUV4 #1, VUV4 #2 and VUV-HD1 #1 were measured [108], [109] and [109], respectively. 65

4.5 Spatially averaged PTE inside the fiducial volume as a function of the specular reflectivity of the cathode and the FSRs. The results from our current light simulations with updated optical parameters (black circles) are compared against results from previous simulations (orange diamonds) [85]. The grey band indicates a systematic error due to the choice of Silicon Photomultiplier (SiPM)s and light simulators. Figure taken from [33]. 66

4.6 Shown is the percentage of photons absorbed by the components in the detector based on a Chroma simulation for three different sets of optical parameters: (1) Completely absorbing detector except for Silicon Photomultiplier (SiPM)s in green (2) Intrinsic specular reflectivity of components at $\lambda_{\text{scint}} = 175\,\text{nm}$ in orange (3) Baseline optical parameters in blue. The two largest contributions to absorbed (and not detected) photons come from the anode and the FSRs. The error bars here represent the spread across the FV. 67

4.7 Spatially averaged PTE inside the fiducial volume as a function of the specular reflectivity of the cathode and the FSRs. The different curves are for different reduction factors of the surface reflectivity of the Silicon Photomultiplier (SiPM) when applying an ARC. 68

4.8 Angular distribution of detected photons in Chroma as they impinge on the Silicon Photomultiplier (SiPM) surfaces. 69

4.9 Lightmap of the nEXO detector showing the probability of photons reaching the avalanche region of the Silicon Photomultiplier (SiPM)s, i.e., the PTE as a function of the radial, r, and longitudinal, z, positions in the detector. Time Projection Chamber (TPC) components such as the FSRs, the anode, and the cathode are visible due to their high opacity. 71

4.10 Boxplot of PTE as a function of z-position (left) and standoff distance (right). The box comprises data within the 25 % and 75 % quantile around the median which is shown as an orange line inside the box. The whiskers ("error bars") extend over the full range of data in that region. The median PTE is strongly z-dependent whereas the median PTE has no standoff dependence but has a significantly larger spread as indicated by the whiskers. 72
4.11 Angular distribution of detected photons in Chroma as they impinge on the Silicon Photomultiplier (SiPM) surfaces. 73
4.12 Fraction of Silicon Photomultiplier (SiPM) readout channels that detected a certain number of photons as a function of radius in the Time Projection Chamber (TPC) for a 3.3 MeV β-event distributed uniformly inside the fiducial volume, for 6 cm^2 Silicon Photomultiplier (SiPM) channels. The dip at $\sim$560 mm occurs for events in between the field shaping rings for which a large solid angle is blocked by FSRs themselves. 75
4.13 Pressure limiting processes while pumping on a vacuum system. The plotted dependence qualitatively captures processes relevant to Liquid Xenon (LXe) detectors, although the quantitative outgassing of a given system depends on materials, geometry, and other system parameters. The plot was remade after [139]. 78
4.14 Outgassing rate due to desorption of water from a stainless steel surface as a function of pumping time. Shown are curves for various surface finishes and treatments. Even though there is a big spread in the initial value all curves roughly follow a t^{-1} relationship. Plot remade after [141]. 84

4.15 Total outgassing rate from desorption of four different desorption sites with different activation energies. The rate of each desorption site follows an exponential, but the sum of all rates follows the empirically found t^{-1} relationship. Figure from [139]. 84
4.16 The average lifetime in the EXO-200 detector for each run in Phase I and Phase II. One can notice a systematic decrease in electron lifetime in Phase II (starting after run 6800). The detector did not only receive some electronics upgrades during the shutdown but the cartridges in the purifiers were renewed as well. 85
4.17 Calculated outgassing rate as a function of time for the PTFE in EXO-200. 87
4.18 Calculated outgassing rate as a function of time for the acrylic in EXO-200. 88
4.19 Outgassing rate of mono-layers of impurities on stainless steel walls as a function of pumping time in EXO-200. The light blue band shows the outgassing from warm plumbing with a surface area of 2000 cm^2 to 4000 cm^2 and the dark blue solid line is the steady state leak rate derived earlier. 89
4.20 Electron lifetime as a function of time and residuals, averaged over time blocks of three months, in EXO-200 Phase-II. The average electron lifetime is indicated by the dashed-magenta line; the vertical green and blue lines mark the dates where the return and recovery lines are evacuated, respectively. 90
4.21 Number of ^{85}Kr atoms in EXO-200 as a function of time. Data points in blue and orange are for Phase I and Phase II, respectively. The null (no leak) hypothesis is disfavored at $\sim 3.7\sigma$ when combining the p-values from both phases. However, the leak rate is still below what is needed to explain the electron lifetime in EXO-200. 93

4.22 Calculated outgassing rate as a function of time for thin Kapton cables in nEXO. 96
4.23 Calculated outgassing rate as a function of time of 1 cm^2 thick epoxy used for the feedthroughs in nEXO. 97
4.24 The diffusion coefficient as a function of temperature plotted for different activation energies. The dashed line shows the value from [121] and the dashed-dotted line shows the measurements done at Yale. The grey band shows the uncertainty in the measurement. Due to the exponential dependence, small changes in the activation energy for the diffusion process can lead to orders of magnitude variation in the predicted outgassing at low temperature. 98
4.25 Pictures of the outgassing setup used to measure the activation energy and diffusion constant of sample materials for nEXO. 101
4.26 Pictures of installing a PTFE sample into the outgassing setup. . . . 102
4.27 Measured partial pressure of various gases from a PTFE sample. The increase in partial pressure in ∼12 h intervals is due to an increase in the temperature according to the procedure described in the text. . . 104
4.28 Measured partial pressure of oxygen from a PTFE sample and an example fit to the data to obtain the diffusion parameters E_a and D_0 using Equation 4.16. 105
4.29 Plot of the diffusion constant D_0 vs E_a/R, where R is the ideal gas constant, for results obtained with the Yale Outgassing Setup together with a metastudy of various other polymers [164] and the best fit line. 106
4.30 Image of the Yale Purity Monitor setup, including the gas handling system (left), the cryostat and xenon cell (center), and the DAQ system (right). 108

4.31 Section view of the CAD model of the xenon cell including the field cage, xenon level meter, and feedthroughs. 110
4.32 Schematic drawing of gas handling system of the YPM. 112
4.33 Diagram of the purity monitor circuit diagram for a switching HV setup. Frisch grids are shown as dotted lines. A simplified version of the electron path is shown in blue, traveling from the photocathode on the bottom into the HV switching region and then to the collection anode at the top. 115
4.34 Measured drift velocity as a function of drift field in the YPM (blue). The data from EXO-200 is shown for comparison (orange) [184]. . . . 116
4.35 Measurement of the oxygen concentration in the xenon cell as a function of Liquid Xenon (LXe) level. The reduction in oxygen concentration is consistent with a Henry coefficient of ~ 60, indicating that the oxygen is dissolving into the liquid phase. 120
4.36 Evaluation of the predicted energy resolution as a function of all input parameters to the resolution model. The white cross in each panel indicated the value for the energy resolution for the current baseline parameters that are summarized in 4.3. The grey bands in the 1D plots show the possible range of the given parameter. 127

5.1 Rendering of the nEXO detector geometry in Geant4. The left side shows a section view of the large-scale components such as the water tank, inner and outer cryostat, and the TPC. The right side shows a close-up view of the TPC. Figures from [33]. 132

5.2 Reconstructed light and charge for simulated events from the ^{232}Th decay chain originating from the TPC vessel. These events lie within the fiducial volume. The projected of these events onto the rotated energy axis, which is shown as a black line at an angle of $-45°$, results in a significantly improved energy resolution than any individual channel would allow. The implemented cut on the charge-to-light ratio is shown as red dashed lines and rejects all events outside their boundaries. Figure from [33]. 137

5.3 Normalized energy spectra of simulated $0\nu\beta\beta$, ^{232}Th and ^{238}U events inside the fiducial volume using the rotated energy variable. Gaussian fits to the known peaks of $0\nu\beta\beta$, ^{214}Bi and ^{208}Tl, indicated via dashed lines, yields the expected energy resolution σ_E/E. Figure from [33]. . 138

5.4 (left) Plot of the distribution of DNN scores for simulated $0\nu\beta\beta$, for ^{232}Th and ^{238}U background events originating from the TPC vessel. (right) ROC curves show the signal efficiency as a function of background misidentification, quantifying the performance of the DNN. The top row is for events within the full fiducial volume, whereas the bottom row applied a tighter fiducial volume cut using only events within the innermost 2000 kg (i.e. a standoff distance of larger than 104 mm). . . 141

5.5 Breakdown of the percent contribution of various intrinsic backgrounds based on the component (left) or the material (right). Only events with a DNN score of > 0.85, energy within one FWHM around $Q_{\beta\beta}$, and a standoff distance larger than 104 mm are selected. Figures from [33] . 144

5.6 nEXO's background budget, divided into contributions from ^{222}Rn based, intrinsic and exposure-based radioactivity. The reduction of the intrinsic background contribution through the planned use of in-house EFC makes this now the second largest contribution after background from ^{222}Rn. Figure from [33]. 150

5.7 Profile likelihood ratio curve for an example toy dataset. The intersection of the profile likelihood ratio curve with the critical lambda curve (blue) is the upper limit of signal counts that can be excluded at the 90 % CL. The expected value for exclusion at 90 % CL for the test statistic in the limit where Wilks' theorem holds is given by 2.71 and is shown as a red vertical line. Figure from B. Lenardo. 155

5.8 Distribution of 90 % CL upper limits on the number of $0\nu\beta\beta$ counts for 5000 toy datasets. The median corresponds to a bound on the $0\nu\beta\beta$ decay half-life of $T^{0\nu}_{1/2} > 1.35\times10^{28}$ years. The 68 % and 95 % percentiles around the median are shown in green and yellow, respectively. Figure from [33]. 156

5.9 (left) Distribution of ΔNNL for the null hypothesis $f(\lambda(0)|0)$ in grey and for alternative hypotheses $f(\lambda(0)|\mu)$ in color. The p-value is gotten from counting the number toy data sets in $f(\lambda(0)|0)$ that are above the median of $f(\lambda(0)|\mu)$, shown as vertical colored lines. The grey vertical dashed lines represent the values of ΔNNL that corresponds to a significance of $1\sigma, 2\sigma, 3\sigma, 4\sigma$, respectively. (right) Shown is the significance as a function of the average number of signal events used for generating the toy data sets. The number of signal events that the median experiment in an ensemble of toy experiments would have to have to be able to exclude the background-only hypothesis and claim a discovery with a 3σ significance can be calculated via linear interpolation between the data points. This is shown via the dotted lines. This dataset corresponds to an exclusion sensitivity of $T^{0\nu}_{1/2} > 0.74 \times 10^{28}$ yr at 3σ significance. Left figure is from [33]. 157

5.10 Shown are contours of the distribution of $0\nu\beta\beta$ events (in blue) and background events (in red) from ^{232}Th (left) and ^{238}U (right) in the TPC vessel in standoff distance vs DNN space. Only events with energy in the ROI and that have passed our quality cuts are shown. 162

5.11 Selection efficiency, defined as the fraction of events below or above a DNN value of 0.85 for background or signal, respectively, as a function of an approximate event size metric. This demonstrates that the DNN, as expected, discriminates γ-like backgrounds against $0\nu\beta\beta$ events based on their topological differences encoded in the initial event size during the interaction with the Liquid Xenon (LXe). 164

5.12 Projected median exclusion and discovery sensitivity as a function of livetime at the 90 % CL and 3σ CL, respectively. nEXO will surpass a half-life sensitivity of $>10^{27}$ yr and $>10^{28}$ yr after just $\sim$0.5 yr and 6 yr, respectively. During the initial few months, the experiment will be effectively running background free, resulting in fewer counts needed to make 3σ significant observation than can be excluded at 90 % CL. After the full ten years of data taking, the final projected exclusion at at 90 % CL and discovery sensitivities at 3σ CL are $T^{0\nu}_{1/2} > 1.35 \times 10^{28}$ yr and $T^{0\nu}_{1/2} > 0.74 \times 10^{28}$ yr, respectively. Figure from [33]. 165

5.13 Projections of the median discovery significance for $0\nu\beta\beta$ with ten years of nEXO data. The grey band indicates the 68 % symmetric quantile around the median. As a comparison, the excluded half-lifes of other xenon-based $0\nu\beta\beta$ experiments at 90 % CL are shown as vertical dashed lines, including EXO-200 [32] and KamLAND-Zen [31]. The median significance of a discovery in nEXO exceeds 5σ for $0\nu\beta\beta$ half-lifes as long as 0.38×10^{28} yr and even for a half-life of 1×10^{28} yr a median 2.4σ significant observation can be made. 166

5.14 Projected median exclusion and discovery sensitivity as a function of fiducial mass at the 90 % CL and 3σ CL, respectively. Using the innermost 2000 kg of Liquid Xenon (LXe) already delivers $\sim$95 % of the full exclusion and discovery sensitivity compared to the full fiducial mass of 3281 kg relative to the full 5000 kg total Liquid Xenon (LXe) mass. 167

5.15 Projected half-life exclusion sensitivity as a function of the energy resolution at $Q_{\beta\beta}$ at the 90 % CL. A linear fit to the data point is also shown. The baseline value for the projected energy resolution in nEXO is $\sigma/Q_{\beta\beta} = 0.8\,\%$. Figure from [33]. 168

5.16 Dependence of the exclusion and discovery sensitivity on changing the background components related to ^{222}Rn, ^{137}Xe or all γ-backgrounds. This shows the impact of potential mismodeling of backgrounds or the potential gain in further reducing these backgrounds. Figure from [33]. 169

5.17 (left axis) Estimated rate of ^{137}Xe backgrounds and (right axis) projected half-life exclusion sensitivity at 90 % CL as a function of vertical depth in meters of water equivalent. The current conceptual design is assuming that nEXO will run at SNOLAB. The reduction in sensitivity at a shallower site, such as SURF or Gran Sasso, can be counteracted with a more sophisticated muon veto scheme than the current and simplistic scheme used for this analysis. 170

5.18 Exclusion (left) and discovery (right) sensitivity as a function of the background index for scaling the backgrounds from ^{222}Rn, ^{137}Xe and all γs. A power law fit to the projected sensitivities as a function of all γ backgrounds yields a power of -0.23 and -0.26 for the exclusion and discovery sensitivity, respectively, highlighting that nEXO's sensitivity is scaling more favorably than the typical power of -0.5 for a counting experiment. 172

5.19 Discovery significance of a counting experiment as a function of the mean number of signal events. Each plot is for a different fiducial mass and each curve within is for a different livetime. Data points are connected via a linear interpolation curve to determine the mean number of signal events necessary for a 3σ discovery. 176

5.20 Shown is the exclusion significance (left) and discovery significance (right) as a function of mean background counts b for different values of the mean number of signal counts s. Different versions of the Poisson likelihood method are compared together with the Asimov approximation of the likelihood ratio method. 178

5.21 Shown is the 90 % CL upper limit of signal counts as a function of the mean number of background events. Compared are the Asimov approximation of the Poisson likelihood method (here just called Asimov) and the likelihood ratio method (here called CCGV for the initials of the authors in [218]) together with the standard FC method (here FC) and the likelihood weighted FC method (here FC Sum). All methods, besides the FC method, have a smooth transition while only the Asimov curve follows the standard FC curve most closely without over or underestimating the exclusion sensitivity. 179

5.22 Plot of the exclusion sensitivity (left) and the discovery sensitivity (right) as a function of the fiducial mass. The background index as a function of fiducial mass is listed in Table 5.3. This indicates that if nEXO would run as a counting experiment the optimal fiducial mass for the search that maximizes the sensitivity would be between 1500 kg and 2000 kg. 180

5.23 Exclusion sensitivity (left) and discovery sensitivity (right) as a function of the background index. This plot can be used to convert our likelihood analysis sensitivity into an equivalent background index. 181

5.24 Plot of the allowed parameter space of effective Majorana neutrino mass as a function of the lightest neutrino mass eigenstate. The bands correspond to uncertainties arising from the completely unknown Majorana phases in the PMNS matrix and the experimental uncertainties in neutrino mixing parameters at the 90 % CL [238]. The dashed lines only include the former uncertainties, whereas the solid lines include the contribution from both sources of uncertainties. The exclusion sensitivity of nEXO to the effective Majorana neutrino mass at 90 % CL is shown as horizontal green bands where the width arises from the uncertainties in the NMEs. Figure from [33]. 183

5.25 Exclusion (top) and discovery (bottom) sensitivity to $\langle m_{\beta\beta} \rangle$ for nEXO vs LEGEND-1000 (left) or CUPID (right), respectively. The sensitivities for LEGEND-1000 and CUPID are taken from [239] and [240], respectively. 185

5.26 Phase space factor weighted half-life exclusion (circles) and discovery (diamonds) sensitivity versus various NMEs values for the upcoming tonne-scale $0\nu\beta\beta$ decay experiments. Compared to Figure 5.25 the exactly calculable contribution $T^{0\nu}_{1/2} \times G_{0\nu}$ are separated from the NME contribution, which is subject to large theoretical uncertainties. The hollow points are the position of the median NME for each of the three isotopes. The different values for $\langle m_{\beta\beta} \rangle$ in this plot are shown as diagonal dashed lines and values in the inverted are shown in grey. With nEXO's projected exclusion sensitivity the inverted neutrino mass ordering can be ruled out at 90 % CL except for the least favorable NME. 186

5.27 Median exclusion (left) and discovery (right) sensitivity to $\langle m_{\beta\beta} \rangle$ for nEXO (top), LEGEND (center), and CUPID (bottom), for different NMEs. The dashed vertical lines represent the median value of $\langle m_{\beta\beta} \rangle$ and the grey area represents values in the inverted neutrino mass ordering. Even though the NME calculations don't follow a statistical distribution it is illustrative to compare the number of NMEs that yield an $\langle m_{\beta\beta} \rangle$ smaller than a given benchmark value. 187

6.1 Available parameter space for the half-life (left axis) and effective Majorana mass (right axis) in the normal ordering, based on the neutrino oscillation parameters from [28, 241]. The unknown Majorana phases are assumed to be uniformly distributed. The color scale indicates the likelihood of a given $\langle m_{\beta\beta} \rangle$ and m_1 pair. The regions for which 50% (solid), 90% (dashed), 95% (dash-dotted), and 99% (dotted) of the available parameter space can be excluded for a given $\langle m_{\beta\beta} \rangle$ sensitivity are given by the white contour curves. The conversion between $T^{0\nu}_{1/2}$ and $\langle m_{\beta\beta} \rangle$ assumes $|\mathcal{M}^{0\nu}| = 2.7$, which corresponds to the median value among currently published models [33]. For reference, the estimated sensitivities of the upcoming tonne-scale nEXO experiment and a proposed concept for a kilotonne-scale Liquid Xenon (LXe) detector are marked with a dashed and dotted line, respectively. 189

6.2 Event rate of $2\nu\beta\beta$ events inside the energy ROI defined as $Q_{\beta\beta} \pm$ FWHM/2 as a function of the energy resolution of the detector. Plot is based on [92]. 192

6.3 Estimated energy resolution at the $Q_{\beta\beta}$-value (based on the semi-empirical equation in Section 4.3) as a function of the PTE inside the detector for various electron lifetimes. The assumed PDE is taken from [102] and the charge readout noise is assumed to be $\sigma_{q,\text{noise}} = 600e^-$. There is only marginal improvement in the energy resolution when increasing the electron lifetime beyond 15 ms. 194

6.4 Sectional view of a conceptual design for a kilotonne-scale Liquid Xenon (LXe) detector, where only a simplified vessel, cathode, FSRs, PTFE reflectors, and photo-detectors are shown. Two different designs were studied: (left) open field cage design with photo-detectors positioned behind the FSRs around the barrel of the vessel and (right) closed-field cage design with the photo-detectors on the flat sides of the detector and PTFE reflectors covering the barrel inside the FSRs. 196

6.5 Estimated PTE from a Chroma light propagation simulation of a kilotonne Liquid Xenon (LXe) detector using a geometry as defined in Table 6.1 and assigned optical properties defined in Table 6.2. The dashed and solid curves are for $\lambda_{\text{scat}} = 30$ cm and $\lambda_{\text{scat}} = 50$ cm, respectively. 199

6.6 (left) Distribution of number of produced Cherenkov photons in Liquid Xenon (LXe) for β and $\beta\beta$ events with an energy of 2458 keV which are based on [249]. (right) Simulated arrival time of Cherenkov photons at $\lambda = 300$ nm and scintillation photons at $\lambda = 178$ nm from the center of a kilotonne Liquid Xenon (LXe) detector. 200

6.7 Distribution of detected photons for different integration times of 1 ns, 10 ns and 20 ns. For short integration times, not enough photons are detected to distinguish β-like from $\beta\beta$-like events. Conversely, for longer integration times more of the scintillation will be collected smearing out the Cherenkov light signature. An integration time of 10 ns provides the optimal separation. 202

6.8 Signal efficiency as a function of background rejection when using a time-of-flight based discrimination of β-like and $\beta\beta$-like events. This study suggests that a 10 ns time resolution of the photo-detectors maximizes the rejection capabilities and results in an optimal rejection of $\sim$65 % of background events while keeping $\sim$65 % of the signal events. 203

6.9 Sensitivity of Liquid Xenon (LXe)-based $0\nu\beta\beta$ experiments as a function of their detector mass, including the results from EXO-200 [32] and projection from nEXO [33] and this kilotonne Liquid Xenon (LXe) detector concept [83]. The 90 % CL exclusion sensitivity is shown with solid markers whereas the 3σ discovery sensitivity is shown with open markers. The cases with solar ν background rejection using the Cherenkov-based single β discrimination are shown as dashed lines. The half-life sensitivity goal of 1×10^{30} yr can only be reached in the case of a $\gtrsim 0.3$ kt enriched Xenon ($^{\mathrm{enr}}$Xe) detector. The natural Xenon ($^{\mathrm{nat}}$Xe) detector with the same sensitive mass, i.e. $\gtrsim 3$ kt total mass, only reaches a 40 % lower sensitivity due to the roughly tenfold increase in the solar ν background. 205

List of Tables

2.1 Summary of estimated systematic errors for this analysis in the EXO-200 Phase I and II data sets. 36

3.1 Summary of requirements on the performance of Silicon Photomultiplier (SiPM)s in nEXO together with the measured performance of candidate Silicon Photomultiplier (SiPM)s such as the FBK VUV-HD1 [102] and the HPK VUV4 [105]. 49

3.2 Comparison between EXO-200 and nEXO in terms of key design and performance parameters. 54

4.1 Summary of optical properties of components used in the light simulations of the nEXO Time Projection Chamber (TPC) using Chroma. . 61

4.2 Summary of measurements of the activation energy E_a and diffusion constant D_0 for the outgassing of O_2 from various materials. 104

4.3 Summary of baseline parameters for evaluating nEXO's energy resolution using the semi-empirical resolution model. 128

5.1 Summary of the improvement in discovery sensitivity vs different sets of variables used in the likelihood fits. The 21-fold improvement over a simple 1D energy search highlights the strength of nEXO's multi-dimensional analysis approach. 161

5.2 Comparison of the improvement in exclusion and discovery sensitivity between EXO-200 and nEXO for using different variables in the likelihood fits. Due to its bigger size and monolithic design, we see a larger improvement by adding the standoff distance to the energy in nEXO compared to EXO-200. The relative improvement of adding the DNN variable as an additional variable is similar for both experiments. . . . 162

5.3 Summary of the mean number of background counts, that have energy with the FWHM around $Q_{\beta\beta}$ and a DNN score of >0.85, for different fiducial masses after 10 yr of livetime of nEXO. 173

5.4 Summary of NME value used for calculating nEXO's sensitivity to the effective Majorana neutrino mass. 182

5.5 Comparison of upcoming tonne-scale experiments in terms of their kinematic phase space factor, median discovery, and exclusion sensitivities. 184

6.1 Summary of the dimensions of detector components used for the light transport simulations of a kilotonne Liquid Xenon (LXe) detector. . . 197

6.2 Summary of optical parameters used to simulate the light response of a kilotonne Liquid Xenon (LXe) detector in Chroma. 201

Chapter 1

Rare Events as a Probe for New Physics

1.1 Majorana Neutrinos 2

1.1.1 Neutrino Oscillations 3

1.1.2 Origin of Neutrino Masses 6

1.1.3 Neutrinoless Double Beta Decay 10

1.2 Dark Matter 14

1.2.1 Evidence 15

1.2.2 Properties 19

1.2.3 Beyond the WIMP Paradigm 21

The Standard Model (SM) of Particle Physics encompasses our current understanding of the fundamental constituents of matter and their interactions with each other. While it is extraordinarily successful, evidence exists for its incompleteness. Many of the breakthroughs in fundamental particle physics over the last century were tied to the peculiarity of the weak nuclear force. This chapter provides a brief overview of

the role rare event searches in the weak sector play in understanding the nature of neutrinos and dark matter.

1.1 Majorana Neutrinos

This section introduces neutrinos, their elusive nature, and their importance as a doorway for new physics beyond the SM.

The neutrino was initially proposed by Wolfgang Pauli in 1930 as an electrically neutral and light (possibly massless) new particle to solve the seeming violation of energy conservation in ordinary β-decay [1]. It took until 1956 for Reines and Cowan to make the first conclusive discovery of neutrinos from a nuclear reactor by measuring the inverse β-decay of protons in a water target [2] that was sandwiched between tanks of liquid scintillator. Later that decade in 1959, Chien-Shiung Wu showed that parity symmetry was maximally violated in β-decay [3–5], which suggests that only left-handed (spin and momentum directions are anti-aligned) neutrinos and right-handed anti-neutrinos partake in the weak interaction, which is responsible for radioactive decays. Since the standard Higgs-mechanism through which all other elementary particles obtain their rest mass, requires the mixing between their left and right-handed components, the neutrino is assumed to be massless in the SM as no right (left) handed neutrino (anti-neutrino) has been observed to date. This series of experiments led to the commonly accepted description of the neutrinos in the SM until the late 1990s. Through measurements of the atmospheric, reactor, and solar neutrinos by Super-Kamiokande [6], KamLAND [7], and the Homestake experiment and SNO [8] neutrino oscillations were firmly established, proving that neutrinos must have a non-zero mass. This provided the first direct experimental evidence for physics beyond the SM and showed that neutrinos have a non-zero mass. The understanding of the origin of neutrino masses is among the most important questions in neutrino

physics, as will be described in the following sections.

1.1.1 Neutrino Oscillations

The observation of neutrino oscillations, which Bruno Pontecorvo originally proposed in 1957 [9], has definitively demonstrated that at least two of the three neutrino mass eigenstates have to be non-zero. Therefore, there is no direct correspondence between the flavor states ν_α, participating in the weak interaction, and the mass eigenstates ν_i, which are the eigenstates of the free particle Hamiltonian. Transformations between the flavor eigenstates and the mass eigenstates ν_i are described via

$$\begin{pmatrix} \nu_e \\ \nu_\mu \\ \nu_\tau \end{pmatrix} = \begin{pmatrix} U_{e1} & U_{e2} & U_{e3} \\ U_{\mu 1} & U_{\mu 2} & U_{\mu 3} \\ U_{\tau 1} & U_{\tau 2} & U_{\tau 3} \end{pmatrix} \begin{pmatrix} \nu_1 \\ \nu_2 \\ \nu_3 \end{pmatrix} \tag{1.1}$$

where $\alpha = e, \mu, \tau$ and $U_{\alpha i}$ are the elements of the unitary Pontecorvo-Maki-Nakagawa-Sakata (PMNS) mixing matrix. One can parameterize the PMNS matrix by using three different mixing angles θ_{12}, θ_{23}, θ_{13}, a possibly CP-violating phase δ and two additional CP-violating Majorana phases α_1 and α_2

$$U = \begin{pmatrix} 1 & 0 & 0 \\ 0 & c_{23} & s_{23} \\ 0 & -s_{23} & c_{23} \end{pmatrix} \begin{pmatrix} c_{13} & 0 & s_{23}e^{-i\delta} \\ 0 & 1 & 0 \\ -s_{23}e^{-i\delta} & 0 & c_{13} \end{pmatrix} \begin{pmatrix} c_{12} & s_{12} & 0 \\ -s_{12} & c_{12} & 0 \\ 0 & 0 & 1 \end{pmatrix} \begin{pmatrix} 1 & 0 & 0 \\ 0 & e^{i\alpha_1/2} & 0 \\ 0 & 0 & e^{-i\alpha_2/2} \end{pmatrix} \tag{1.2}$$

where $s_{ij} = \sin\theta_{ij}$ and $c_{ij} = \cos\theta_{ij}$. For simplicity, one can examine the case of mixing only two flavor states for which the probability of finding a neutrino, that was initially produced in flavor state α, in flavor state β at a later time is given by

$$P(\alpha \to \beta) \approx \sin^2 2\theta \sin^2\left(\frac{\Delta m^2_{ij} L}{4E}\right) \tag{1.3}$$

where θ is the mixing angle, $\Delta m^2_{ij} = m^2_i - m^2_j$ is the mass squared difference between neutrino mass eigenstates of mass m_i and m_j, L is the traveled distance between production and detection of the neutrino and E is its energy. Equation 1.3 can be trivially extended to oscillation probabilities including all three neutrino flavor eigenstates but is often sufficient to describe experimental data as the mixing angle θ_{13} is measured to be very small and the mass eigenstates m_1 and m_2 are closer together in mass compared to m_3. This results in a negligible corrections to $\nu_\mu \leftrightarrow \nu_\tau$ and $\nu_e \leftrightarrow \nu_\mu, \nu_\tau$ in atmospheric and solar neutrino oscillations, respectively.

Neutrino oscillations experiments are only sensitive to mass squared difference and can therefore not probe the absolute neutrino mass scale. In addition, current neutrino oscillation measurements haven't conclusively determined the ordering of the mass eigenstates since we currently only have values for Δm^2_{12} and the absolute value of Δm^2_{23}. The former is based on the measurement of oscillations from solar neutrinos which are sensitive to matter effects as they propagate through the interior of the Sun on their way to our terrestrial detectors [8]. For the latter, we only know the absolute value as it is derived from vacuum oscillations of atmospheric neutrinos which don't depend on the overall sign. This results in an ambiguity in the neutrino mass ordering, as shown in Figure 1.1, where ν_3 is either the heaviest or lightest mass eigenstate. The former case is called the normal ordering (NO) of neutrino masses whereas the latter is referred to as the inverted ordering (IO) of neutrino masses. The determination of the neutrino mass ordering is a primary goal of the future Hyper-K [10] and Deep Underground Neutrino Experiment (DUNE) [11].

Understanding the reason behind the smallness of the neutrino mass compared to that of all other fermions in the SM is of utmost importance for neutrino physics. Other experimental efforts can provide complementary insight into neutrino masses and more importantly the absolute mass scale. Current upper limits on the sum of all

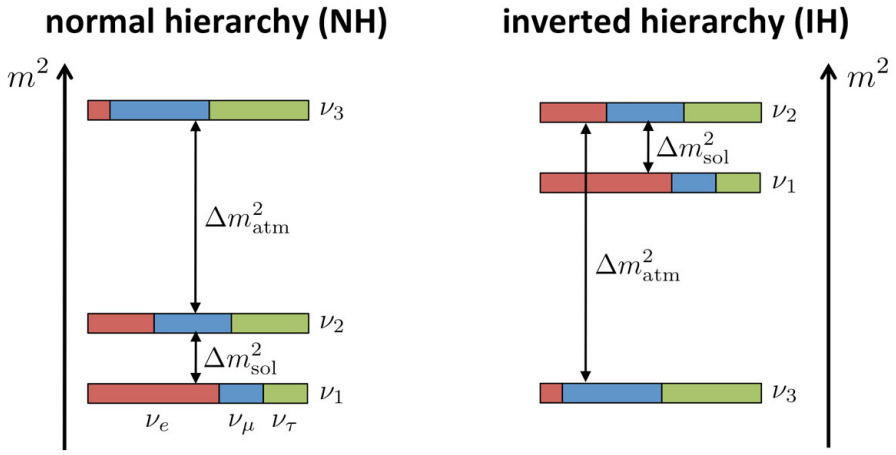

Figure 1.1: Possible ordering of neutrino mass eigenstates ν_i. The ambiguity arises from the fact that neutrino oscillation experiments measuring the atmospheric mass splitting are not sensitive to the overall sign. Figure from [12].

neutrino masses from measurements of the endpoint of tritium β-decay suggest that

$$m_{\nu_e} = \sum_i |U_{ei}|^2 m_i^2 < 0.8\,\text{eV} \tag{1.4}$$

at the 90 % CL [13], which is about six orders of magnitude smaller than the next lightest particle, the electron with $m_e = 511\,\text{keV}$. Additionally, cosmological constraints can be derived from measurements of the anisotropies in the cosmic microwave background. The temperature fluctuations in the CMB are the result of baryon acoustic oscillations in the primordial baryon-photon plasma and are sensitive not only to the total number of active neutrino flavors but also to the sum of the neutrino mass eigenstates. Current data suggests that

$$m_{\text{sum}} = \sum_i m_i < 0.16\,\text{eV} \tag{1.5}$$

at the 95 % CL [14]. The obtained limit strongly depends on the exact assumption about the potential foregrounds, inputs to the underlying cosmological model, and

the given dataset used [15].

The complementary information from neutrino oscillation experiments, β-decay kinematics, and cosmology all conclusively demonstrate small but non-zero neutrino masses. However, none of the above can provide any direct explanation of their mass generation mechanism. The next section will introduce the standard Higgs mechanism for acquiring mass in the SM and how a new mass generation mechanism, which is unique to neutrinos, can naturally explain not only its origin but its smallness too.

1.1.2 Origin of Neutrino Masses

The quarks and charged leptons in the SM are described by 4-component spinors and comprise both left and right-handed components of the particle and their anti-particle counterpart. They acquire their mass through interactions with the Higgs field, which couples the left-handed components of the spinor to the right-handed component of the same charge. This is called a Dirac mass term in the SM lagrangian and can be written as

$$\mathcal{L}_D = -m_e \overline{e_R} e_L + h.c. \tag{1.6}$$

where e_L is the left-handed electron field and $\overline{e_R}$ is the Dirac adjoint of the right-handed electron field. Since the weak interaction maximally violates parity symmetry and neutrinos only interact weakly (setting aside gravity due to the smallness of their mass) only the left-handed neutrino and right-handed anti-neutrino are needed to describe all their interactions. Therefore, a similar Dirac mass term for neutrinos does not exist in the original formulation of the SM, making it massless.

To account for the non-zero mass of neutrinos a minimal extension to the SM

would be the addition of a similar Dirac mass term for neutrinos

$$\mathcal{L}_D = -m_D \overline{\nu_R} \nu_L + h.c. \tag{1.7}$$

by introducing an additional right-handed neutrino and left-handed anti-neutrino component, which would be sterile under the weak interaction (i.e. they would be unobservable in weak interactions, but could mix with the other neutrino states through neutrino oscillations).

This would allow the neutrinos to gain their mass like all other particles in the SM through couplings to the Higgs boson. This, however, fails to explain the smallness of neutrino masses without the introduction of unmotivated adjustments of the coupling constant of the neutrino to the Higgs field, which is referred to as fine-tuning or unnaturalness. While the Higgs-fermion Yukawa coupling constant for none of the charged fermions can be derived from the SM framework and their masses need to be determined experimentally, one would expect their couplings and correspondingly their mass to be of similar magnitude.

An elegant way of circumventing this naturalness issue is the introduction of so-called Majorana mass terms for the neutrinos. Because neutrinos don't carry any electrical charge they could in principle be their own anti-particle and the 4-component spinor can be reduced to a 2-component spinor, fully describing the neutrino with just a left-handed ν_L and right-handed ν_R component. This idea of neutral fermions possibly being their own anti-particles was first suggested by Ettore Majorana in 1937 [16] and was further confirmed to possibly describe the nature of massive neutrinos by Giulio Racah in 1937 [17]. We know the left-handed neutrino component exists in nature and we can write down a Majorana mass term in the form of

$$\mathcal{L}_M^L = \frac{1}{2} m_L \overline{\nu_L^c} \nu_L + h.c. \tag{1.8}$$

This Majorana mass term couples a neutrino to an anti-neutrino with a Lepton number of $L = +1$ and $L = -1$, respectively. This implies that interactions in which Majorana neutrinos are involved also violate Lepton number conservation by $\Delta L = 2$. While Lepton number conservation happens to be a symmetry at the Lagrange level in the SM that is so far obeyed by all interactions measured to date, there is no underlying symmetry in the SM protecting it. However, if a right-handed component existed, which to date hasn't been observed through any measurement, the neutrino can also have a Dirac mass term as in Equation 1.7. This right-handed component could also have its own Majorana mass term

$$\mathcal{L}_M^R = \frac{1}{2} m_R \overline{\nu_R^c} \nu_R + h.c. \tag{1.9}$$

The neutrino is unique among all other particles in the SM as it is the only fermion that can have a combination of Dirac and Majorana mass terms

$$\begin{aligned} \mathcal{L} &= \mathcal{L}_M^L + \mathcal{L}_M^R + \mathcal{L}_D \\ &= \frac{1}{2} m_L \overline{\nu_L^c} \nu_L + \frac{1}{2} m_R \overline{\nu_R^c} \nu_R - m_D \overline{\nu_R} \nu_L + h.c. \end{aligned} \tag{1.10}$$

Since ν_L is charged under the weak force, i.e. it carries weak isospin of $I_3 = 1/2$ and participates in the weak interaction, the coupling of matter and anti-matter through the above Dirac mass term violates charge conservation and the gauge invariance of the SM. However, ν_R is sterile under the weak interaction and all other interactions of the SM and therefore carries no charge and a similar Dirac mass terms would be gauge invariant. Equation 1.10 can be refactored and written in matrix form as

$$\mathcal{L} = -\frac{1}{2} \overline{N_L^c} \mathcal{M} N_L \tag{1.11}$$

with

$$N_L = \begin{pmatrix} \nu_L \\ \nu_R^c \end{pmatrix} \quad \text{and} \quad \mathcal{M} = \begin{pmatrix} m_L & m_D \\ m_D & m_R \end{pmatrix} \tag{1.12}$$

This implies that the ν_L and ν_R are not the true states with definitive mass due to the off-diagonal Dirac mass terms. By diagonalizing the $\mathcal{M}$ we can find the eigenstates of the massive neutrinos with eigenvalues

$$m_{2,1} = \frac{1}{2}\left(m_L + m_R \pm \sqrt{(m_L - m_R)^2 + 4m_D^2}\right) \tag{1.13}$$

In the limit where the mass of this new and yet unobserved right-handed neutrino is at an energy scale far beyond anything that can be probed, i.e. $m_R \gg m_D \gg m_L$, one obtains

$$m_1 = \frac{m_D^2}{m_R} \tag{1.14}$$

$$m_2 = m_R \tag{1.15}$$

The Dirac mass is typically proportional to the Higgs vacuum expectation value of around $10^2\,\text{GeV}$ such as for all other fermions that received their mass through the Higgs mechanism. In order to explain the smallness of the measured neutrinos of around $m_1 \sim 1\,\text{eV}$ the mass of this new neutrino must be on the order of $m_2 \sim 10^{14}\,\text{GeV}$–$10^{16}\,\text{GeV}$. This formalism is known as the "see-saw" mechanism that naturally explains the neutrino mass by adding a new extremely heavy sterile neutrino. Coincidently, this mass is roughly as large as the energy scales where one would expect a grand unified theory to unite all forces of the SM into one [18–20].

In addition to possibly solving the mystery about the origin of neutrinos masses, a Majorana neutrino mass in the SM lagrangian also naturally provides the possibility for leptogenesis which could be linked to baryogenesis in the early universe via the

heavy right-handed neutrino. This could be a key ingredient in understanding the dominance of matter over anti-matter in our universe. The necessary conditions that are required for baryogenesis to occur were described by Andrei Sakharov in 1967 [21]. One required ingredient is baryon number violation, which in some theories of baryogenesis can be linked to lepton number violation through a sphaleron [22].

The experimentally most promising option to test the Majorana nature of neutrinos and conservation of lepton number is by looking for neutrinoless double-beta decay.

1.1.3 Neutrinoless Double Beta Decay

In 1939 Wendell Furry [23] applied the idea of a Majorana neutrino to the process of two-neutrino double beta decay ($2\nu\beta\beta$) initially introduced by Maria Goeppert-Meyer in 1935 [24]. In the $2\nu\beta\beta$ decay, which is a second-order weak decay that is allowed in the SM, two neutrons within the same nucleus simultaneously undergo β-decay, leaving two protons, two electrons, and two electron-anti-neutrinos in the final state:

$$(A, Z) \rightarrow (A, Z+2) + 2e^- + 2\bar{\nu}_e \tag{1.16}$$

This process is the dominant decay mechanism for nuclei with an even-even number of protons and neutrons for which regular β-decay is energetically disfavored. In the case of a Majorana neutrino, for which $\nu_e \equiv \bar{\nu}_e$ is true, the same process can happen under the virtual exchange of a neutrino, leaving no neutrinos in the final state of the decay:

$$(A, Z) \rightarrow (A, Z+2) + 2e^- \tag{1.17}$$

The Feynman diagrams for both processes are shown in Figure 1.2. This process is not allowed by the SM, since the emitted anti-neutrino at the upper vertex needs to be absorbed in the lower vertex as a neutrino in combination with flipping the right-handed component into a left-handed component. Both conditions can only

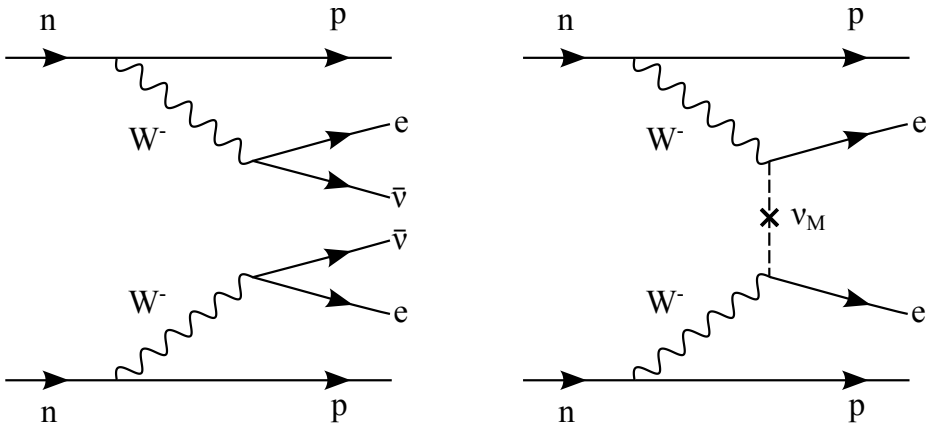

Figure 1.2: Feynman diagram for the $2\nu\beta\beta$ (left) and $0\nu\beta\beta$ (right), assuming that the dominant decay mechanism is the virtual exchange of a light Majorana neutrino, denoted as ν_{M}.

be satisfied simultaneously if the neutrino is a massive Majorana neutrino, that is emitted in a superposition of left and right-handed components, where the strength of the left-handed component is proportional to m_{ν_e}/E_{ν_e}. Therefore, the decay rate for $0\nu\beta\beta$ will be proportional to some effective Majorana neutrino mass, which accounts for the mixing of neutrinos and their propagation from the upper to the lower vertex and can be written as

$$\langle m_{\beta\beta} \rangle = \left| \sum_i U_{ei}^2 m_i \right| . \tag{1.18}$$

Under the assumption that this light Majorana neutrino exchange mediates this decay, the rate is given by

$$\left[T_{1/2}^{0\nu} \right]^{-1} = G_{0\nu}(Q_{\beta\beta}, Z) \left| \mathcal{M}_{0\nu} \right|^2 \langle m_{\beta\beta} \rangle^2 \tag{1.19}$$

where $G_{0\nu}(Q_{\beta\beta}, Z)$ is the phase space factor, $\mathcal{M}_{0\nu}$ is the nuclear matrix element (NME) and $\langle m_{\beta\beta} \rangle$ is taken to be in units of m_e. The former can be calculated with negligible precision [25], but the latter is subject to large theoretical uncertainties [26]. In 1982 Joseph Schechter and Jose Valle showed that the observation of $0\nu\beta\beta$, regardless of

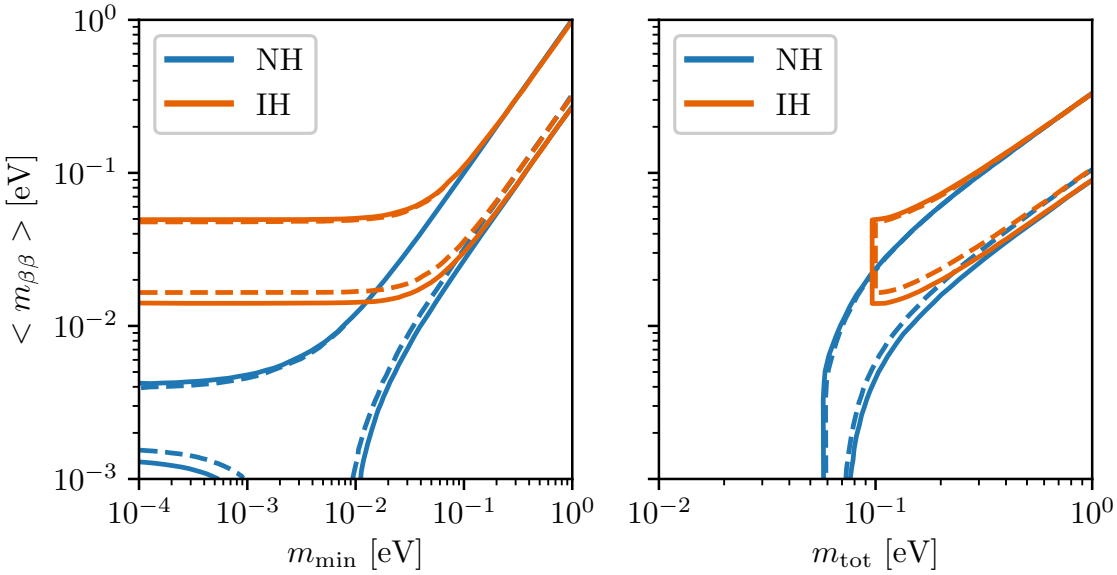

Figure 1.3: Available parameter space of $\langle m_{\beta\beta} \rangle$ as a function of light neutrino mass (left) and the sum of all neutrino masses (right). The value for $\langle m_{\beta\beta} \rangle$ and therefore the rate of $0\nu\beta\beta$ depends on the neutrino mass ordering, where the realization for the NH and OH are shown in blue and orange, respectively. The spread of the bands arises from the unconstrained Majorana phases (dashed lines) and the uncertainties in the neutrino mixing parameters of the PMNS matrix (solid lines) [28].

the details of the mediating process, would always imply that neutrinos are Majorana particles [27].

From Equations 1.18 and 1.19 it is clear that the decay rate is sensitive to the absolute mass scale of the neutrino mass eigenstates and the neutrino mass ordering. Figure 1.3 shows the available parameter space of $\langle m_{\beta\beta} \rangle$ as a function of either the lightest neutrino mass eigenstate or the sum of all mass eigenstates. Interestingly, in the limit where the lightest neutrino mass eigenstate is much larger than the mass splitting between the mass eigenstates, there will be no observable difference in $\langle m_{\beta\beta} \rangle$ and correspondingly the $0\nu\beta\beta$ decay rate. If the NH was realized in nature, the values for the two Majorana phases in the PMNS matrix could take on values for which $\langle m_{\beta\beta} \rangle$ could at least in principle vanish. In this scenario, the neutrino could still be a Majorana particle but the decay rate could be arbitrarily small and therefore unobservable. The Majorana phases are completely unconstrained and assuming

a uniform probability distribution for their values, the likelihood for cancellation becomes vanishingly small [29].

While the $2\nu\beta\beta$ has been observed in about a dozen isotopes using a variety of different techniques [30], so far only lower limits have been obtained for the half-life of $0\nu\beta\beta$. The current most stringent limit comes from the KamLAND-Zen experiment excluding $T^{0\nu}_{1/2} < 2.3 \times 10^{26}$ yr at 90 % confidence level (CL) using ^{136}Xe as the decaying isotope [31].

The search for $0\nu\beta\beta$ involves measuring the kinetic energy of the two outgoing electrons of the decay, which will produce a monoenergetic peak at the endpoint of the $2\nu\beta\beta$ energy spectrum since no neutrinos are present to carry away some of the energy. A typical figure of merit to assess the reach of an experiment is the obtainable sensitivity, which quantifies what size signal (converted into a half-life) would remain buried under the measured background B and is expressed as

$$T^{0\nu}_{1/2} = \ln 2 \, \epsilon \, \frac{N_A}{M} \sqrt{\frac{m\Delta T}{B\sigma}} \tag{1.20}$$

in the case of a flat background. Therefore, the challenge lies in maximizing the experimental sensitivity to larger half-lifes

- The rarity of this decay requires unprecedented background rates, which require the use of ultra radio-pure materials, running the experiment underground to shield against cosmic radiation, and developing powerful background rejection techniques.

- The expected number of $0\nu\beta\beta$ events N, that enter the above sensitivity estimate can be written as

$$N = \ln 2 \cdot \epsilon \cdot \frac{N_A}{M} \cdot \frac{m\Delta t}{T^{0\nu}_{1/2}} \tag{1.21}$$

The likelihood of observing $0\nu\beta\beta$ for a fixed half-life increases with the number of potentially decaying nuclei and livetime of the experiment. In order to observe a single event in one year, assuming a $T^{0\nu}_{1/2} = 1 \times 10^{28}\,\mathrm{yr}$, requires $10^{28}/N_A * M \sim 1000\,\mathrm{kg}$ of the isotope of interest, where N_A is Avogadro's number and M is the molar mass of a candidate isotope ($\sim$100 $\mathrm{mol\,g^{-1}}$).

- Since $2\nu\beta\beta$ events are an irreducible background, which can only be rejected based on their energy, the main handle to avoid a significant overlap between the two distributions is a good energy resolution.

Chapters 2 and 3 will introduce two ^{136}Xe-based experiments searching for $0\nu\beta\beta$ with half-life sensitivities of $\sim 10^{25}\,\mathrm{yr}$ [32] and $\sim 10^{28}\,\mathrm{yr}$ [33], respectively.

1.2 Dark Matter

The description of nature and its dynamics on a microscopic and macroscopic scale are governed by the laws of the SM of particle physics and the General Theory of Relativity (GR), respectively. Both are believed to be effective theories that describe our low-energy universe remarkably well but are expected to reveal new symmetries of nature upon unification at energy scales that were only present in the early universe. Modern measurements indicate that our most successful theories, the SM and GR, only provide a full description of about $\sim$20 % of the matter content or just $\sim$5 % of the entire energy density content of the universe. This conclusion is drawn from a century of observations of numerous astrophysical and cosmological systems whose dynamics and properties cannot be reconciled within either theory. This discrepancy between theoretical prediction and experimental observation is probably the most pressing problem in fundamental physics. This additional "stuff" whose properties we know nothing about so far is generally referred to as dark matter (DM).

1.2.1 Evidence

The evidence for the existence of additional gravitational pull on large scales is typically divided into astrophysical and cosmological. While various attempts at modifying the underlying theory of gravity are successful in accounting for some astrophysical behavior of matter on the galactic scale, they typically fail at scale reaching from galaxy clusters to the universe as a whole. Recently, proponents of modified gravity have been able to reproduce the intricate details imprinted onto the cosmic microwave background (CMB) [34], which are related to the dynamics in the early universe and have been measured with high precision [35].

To date, the proposition for the existence of additional matter in the form of cold dark matter is the only solution that matches all experimental observations, which will be described below.

Astrophysical Evidence The first astrophysical evidence for DM was collected by Jan Oort in 1932 [36] and Fritz Zwicky in 1933 [37], respectively, pointing out that the velocity dispersion among the stars of the Coma galaxy cluster was too large to be explained by their mutual visible mass. This implied that additional non-luminous matter had to be present, hence coining the term "dark matter".

Some of the most striking pieces of evidence for the existence of non-luminous matter are the rotational curves of stars in spiral galaxies, which are expected to fall as $1/\sqrt{r}$ past the edge of the galactic disk according to Kepler's law. However, studies initially performed by Vera Rubin [38] showed that the rotational velocities instead stayed constant, which would be consistent with the additional non-luminous matter being distributed in a spherical halo that extends far beyond the baryonic galactic matter [39].

When examining the gravitational interaction of some of the largest structures in the universe, galaxy clusters, we find that the visible matter confined within them

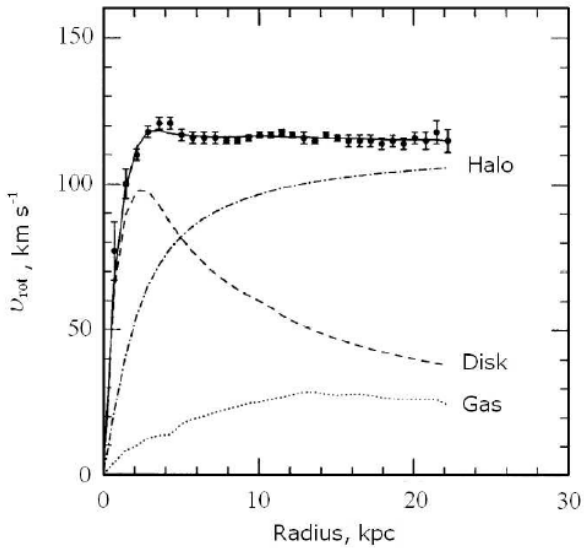

Figure 1.4: Rotation curves of stars in the galaxy NGC 6503. The rotational velocity of gravitationally bound objects is expected to fall off as $1/\sqrt{r}$ beyond the bulk matter of the galaxy using Newtonian dynamics. The measured flatness of the rotational velocity requires the existence of significant amounts of additional non-luminous matter in a spherical halo around the galaxy with a mass distribution of $M(r) \sim r$. Figure from [40].

is not sufficient to produce the measured gravitational lensing effects of background objects. Moreover, colliding galaxy clusters such as the Bullet cluster [41], provide additional strong evidence since the self-interacting ordinary matter, which is measured through its X-ray emission, is spatially separated from the gravitational center that is dominated by practically collisionless non-luminous matter [42].

All of the above point towards a mass density ratio between baryonic matter and dark matter of $\sim 1/5$.

Cosmological Evidence The Λ Cold Dark Matter (ΛCDM) model is referred to as the standard model of cosmology and in its simplest form only contains 6 free parameters to describe the evolution of the entire universe with remarkable accuracy. Fitting this model to cosmological data obtained from experiments such as the Planck satellite enable constraining the various contributions to the total energy density of

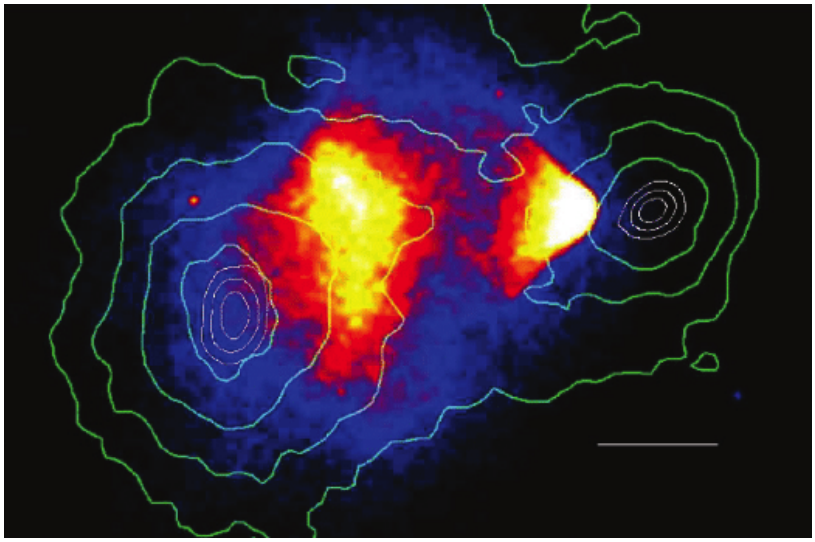

Figure 1.5: X-ray image of the merging Bullet cluster. The contours of gravitational potential, which are measured through gravitational lensing of the background objects, are shown in green. The significant offset between the gravitational centers of mass and the location of the luminous matter indicates the presence of significant amounts of dark matter, which unlike baryonic matter does not self-interact. Figure from [41].

the universe, which can be written as

$$\Omega = \Omega_r + \Omega_m + \Omega_\Lambda \tag{1.22}$$

where $\Omega_i = \rho_i/\rho_c$ with $\rho_c = 3H^2/8\pi G$ being the critical density for a flat universe [43] and H the Hubble constant. Ω_r is the energy density contained in radiation, Ω_m is the total matter density including baryonic matter and dark matter and Ω_Λ is the energy density attributed to dark energy. The current constraints show that the cold dark matter density is $\Omega_c = 0.267 \pm 0.025 \approx 5 \cdot \Omega_b$ [44]. The agreement with observations becomes considerably worse without the inclusion of dark matter and dark energy.

The earliest time that is accessible to photon-based telescopes is $\sim$380 000 yr after the big bang when the universe had cooled down enough for electrons and protons to form neutral hydrogen. After this recombination epoch, the universe became transparent to photons which are detected as the CMB photons today. Its spectrum follows that of black body radiation with a temperature of $2.72548 \pm 0.000\,57$ K [45]

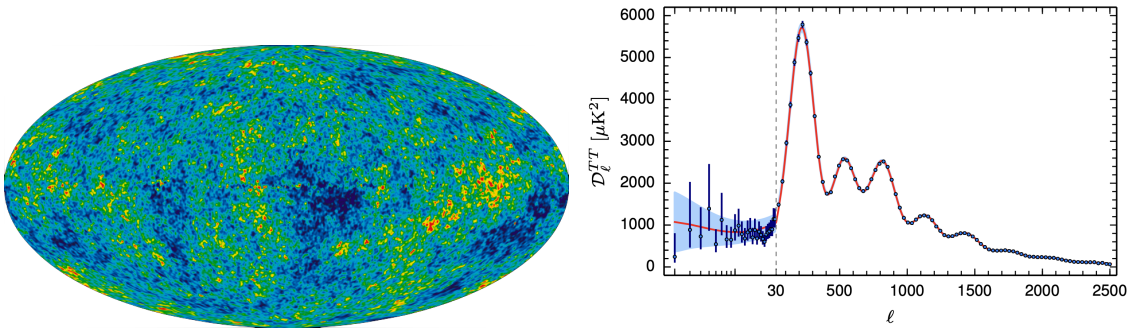

Figure 1.6: (left) The CMB anisotropy measured by the Wilkinson Microwave anisotropy Probe (WMAP) [46] (right) The power spectrum of the CMB anisotropy expanded in multiple moments of spherical harmonics. The red curve represents the best fit according to the ΛCDM model of cosmology. Figure from [47].

and appears to be remarkably uniform across the entire sky to within one part in 10^5. This is shown in the left plot in Figure 1.6. These small fluctuations are linked to density fluctuations in the matter distribution during the last scattering of the CMB photons, which have grown to the large-scale structures that can be observed in the universe today. Modeling the anisotropies in the CMB temperature can be used to tightly constrain the density of baryonic matter and dark matter during the era of recombination. If just baryonic matter had existed during the formation of overdensities in the primordial baryon-photon plasma, the increasing photon pressure would have acted as a restoring force against gravitational collapse. However, dark matter doesn't interact electromagnetically and could have fallen freely into the gravitational potential, laying seeds for the formation of large-scale structures after the decoupling of the CMB photons. This oscillatory behavior of pressure waves in this primordial matter-photon soup, which is enabled by the gravitational pull of dark matter, is called baryon acoustic oscillations (BAOs). The relative heights of various acoustic peaks in the BAO spectrum, as shown in Figure 1.6, are a sensitive probe of the amount of dark matter and can't be matched without including a significant amount of dark matter.

Furthermore, the local overdensities at the time of recombination at the level

measured from the CMB are not sufficient to explain the formation of large-scale structures if one assumes that only baryonic matter existed. Simulations of the evolution of the universe starting from the time of recombination to today are only able to match the observed complex distribution of large-scale structure if and only if dark matter was already present and formed deep gravitational potential wells into which ordinary could have fallen after decoupling from photons.

All of the above evidence points toward a reality in which the ordinary matter that we are familiar with only makes up a small fraction of the total energy density of the universe. About 95 % of the energy density content of the universe cannot be explained with any of our theories.

1.2.2 Properties

Regardless of the true nature of dark matter, it needs to have the following general properties to coherently describe all the astrophysical and cosmological evidence.

- Dark matter needs to be abundant since its relic density needs to account for ∼85 % of the total matter density in the universe.

- Due to tight constraints from models of large-scale structure formation and agreement with the CMB anisotropy data, DM had to be non-relativistic after the epoch of recombination. This precludes sub-keV mass neutrinos, which are similarly elusive as dark matter since they only interact with ordinary matter via the weak force (and only negligibly through gravity) as they are traveling effectively at the speed of light and are therefore referred to as "hot" dark matter.

- Additionally, dark matter can't have any strong self-interaction due to constraints from the dynamics of merging galaxy clusters and the required spatial distribution around galaxies to account for the rotation curves of stars.

- Since its effect on the baryonic matter can still be measured today its decay half-life (if it decays at all) must be long compared to the age of the universe.
- Finally, all the observational evidence for the existence of dark matter is based on gravitational attraction, indicating that dark matter otherwise has no or very weak interactions with ordinary matter.

Many theories have been proposed to explain the particle nature of dark matter, of which the weakly interacting massive particle (WIMP) hypothesis has received the most attention. New particles with a mass of GeV to TeV naturally emerge in many extensions of the SM, such as super-symmetry. Some of these theories' primary goal is to address the "hierarchy problem", which states that the mass of the Higgs particle should be quadratically diverging due to quantum loop corrections [48]. Yet the Higgs mass is measured to be at the weak scale around $\sim$100 GeV, which either requires fine-tuning of the coupling constants or the existence of a new particle at the weak scale that naturally cancels these corrections. If such a particle existed it would be thermally produced in the early universe similar to all the other SM particles and could provide the correct relic abundance via the freeze-out mechanism. While the temperature of the universe is larger than the mass of the WIMP its creation and annihilation are in thermal equilibrium. Upon expansion, the universe cooled enough to render the creation process energetically inaccessible. At this point, the WIMP-WIMP annihilation takes over until the annihilation rate is outpaced by the accelerated expansion rate of our universe. Since neither creation nor annihilation takes place anymore due to the scarcity of interactions between WIMPs their number density stays constant ("freeze-out"). To match the relic abundance of dark matter today it would require an annihilation cross-section that is expected for a new particle at the weak scale. This apparent coincidence of a proposed new particle, which was meant to solve the hierarchy problem, to also have the correct properties to be the dark matter is referred to as the "WIMP miracle".

Other well-motivated candidates include the axion [49], which is based on the solution to the strong CP problem by Roberto Peccei and Helen Quinn in 1977 [50,51] by introducing a new global symmetry. The CP problem states that the formulation of the quantum theory of the strong force, in principle, allows for a violation of CP-symmetry. However, all interactions measured to date involving the strong force have preserved CP-symmetry to high accuracy. Introducing a new global symmetry into the theory of the strong force would naturally preserve CP-symmetry. In 1978 it was realized by Frank Wilczek [52] and Steven Weinberg [53] that the spontaneous breaking of this new symmetry would lead to the generation of a new particle, the axion, which could be an excellent dark matter candidate.

There are a plethora of other models for the particle nature of dark matter and discussing them would be beyond the scope of this work. More details can be found in [54,55].

1.2.3 Beyond the WIMP Paradigm

Due to the lack of any confirmed detection to date of well-motivated candidates such as WIMPs or axions, alternative dark matter models have received recent theoretical and experimental interest [56,57]. A new generation of experiments is aiming to explore lower mass WIMP dark matter between 1 MeV and 10 GeV [58]. The primary detection method of these terrestrial experiments is through an elastic scattering of WIMPs off the target material. The transferred energy is proportional to the WIMP mass and its kinetic energy and typically lies in the $\mathcal{O}$(keV) range. The need to detect smaller energy deposits becomes an experimental challenge for interactions of dark matter through elastic scattering with nuclei or electrons. Other interaction mechanisms of dark matter with the SM have been studied, which could produce higher energy deposits, e.g., in the MeV energy range [59–61]. Detectors searching for neutrinoless double-beta decay ($0\nu\beta\beta$) are well optimized for this energy range and

have demonstrated some of the lowest background rates for any detector technology, along with well-understood background models [62–64]. This makes such detectors well suited to perform searches for dark matter interactions depositing energy in the MeV range, in addition to their primary focus of searching for $0\nu\beta\beta$. One such search will be presented in Chapter 2 using data from the EXO-200 experiment.

Chapter 2

Search for MeV Electron Recoils from Dark Matter in EXO-200

2.1 The EXO-200 Experiment 24

2.2 Event Signature and Monte-Carlo 26

2.3 Analysis 29

2.4 Systematics 32

2.5 Results 36

The EXO-200 experiment is a Liquid Xenon (LXe)-based detector that primarily searched for the $0\nu\beta\beta$ of ^{136}Xe. The demonstrated ultra-low background dataset was used to search for the charged-current absorption of fermionic dark matter by ^{136}Xe. This chapter gives an overview of the interaction signature, the estimated systematic errors, and the final exclusion limits. The following text closely follows [65] of which the author of this thesis is the main author.

2.1 The EXO-200 Experiment

From 2011 to 2018 the Enriched Xenon Observatory (EXO) Collaboration searched for the $0\nu\beta\beta$ of ^{136}Xe with the EXO-200 experiment using around 175 kg of LXe enriched to about 80.6 % in ^{136}Xe. The experiment was hosted at the Waste Isolation Pilot Plant (WIPP) in Carlsbad, New Mexico. EXO-200 was the first 100 kg class experiment and discovered the $2\nu\beta\beta$ of ^{136}Xe after just one month of data taking [66]. In addition, EXO-200 provided some of the most stringent limits on the half-life of $0\nu\beta\beta$ [32, 67–69] and served as a test bed for a future tonne-scale LXe experiment. This section will give a short overview of the detector design.

The EXO-200 detector consists of a square cylindrical vessel made of ultra low-background Aurubis copper [70], which a length and diameter of ∼44 cm and ∼40 cm, respectively, and a thickness of 1.37 mm to minimize the amount of introduced radioactive backgrounds. The core of the detector is two identical back-to-back time projection chambers (TPCs) that share a common cathode in the center. The detector is filled with 200 kg of liquid xenon that is kept at an average temperature of (166.6 ± 0.2) K via HFE-700 cryofluid [71] surrounding the vessel, providing an additional 50 cm of shielding against external backgrounds. The outermost layer is a vacuum-insulation cryostat that was covered by 25 cm of passive lead shielding. The entire experiment is covered with a total of 29 scintillator panels that allow 96 % (90 %) efficient tagging of cosmogenic muons and a consecutive vetoing of correlated events in the TPC. Figure 2.1 shows a section view diagram of the EXO-200 detector inside the cleanroom.

Due to an incident at the host facility operations had to be paused between February 2014 and January 2016. During this time significant upgrades to the detector were done to improve its performance including

- The front-end electronics for the light channel were upgraded resulting in a

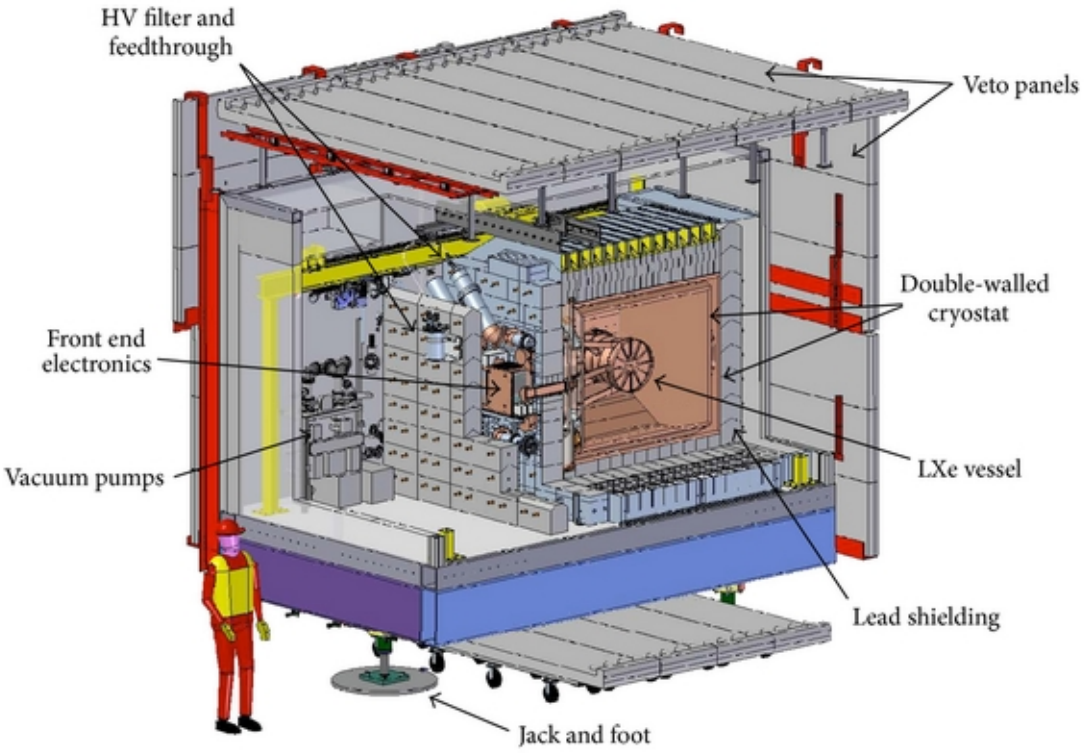

Figure 2.1: Section view of the EXO-200 detector inside the cleanroom at WIPP. Figure from [72].

significantly lower electronics noise and reducing the need for a soft-ware based denoising algorithm to achieve the designed energy resolution

- The cathode high voltage was increased from 8 kV to 12 kV providing in an increase of the electric drift field between the cathode and the V-wire plane from $(380 \pm 20)\,\mathrm{V\,cm^{-1}}$ to $(567 \pm 30)\,\mathrm{V\,cm^{-1}}$. The increased electric field resulted in a larger number of ionization charges being drifted towards the collection plane for which the collection was much more efficient compared to the light channel which helped boost the energy resolution from an average of 1.5 % to 1.15 %.

- A radon removal system was added to reduce the ^{222}Rn content in the air gap between the external lead shield and the cryostat.

Because of these significant changes, the EXO-200 data is split into two roughly equal

exposure datasets, ranging from September 2011 to February 2014 for Phase I and from January 2016 to December 2018 for Phase II.

A more detailed description of various parts of the EXO-200 experiment, including the detector design and performance [72,73], the analysis and reconstruction [32,66–69] can be found elsewhere.

2.2 Event Signature and Monte-Carlo

The absorption of a fermionic dark matter particle χ by a xenon nucleus will induce a β^--decay if the dark matter mass can bridge the gap between the masses of the initial and final nuclei and the mass of the outgoing electron (kinematic threshold). In addition, the daughter nucleus will essentially always be produced in an excited state for the isotopes of interest here due to angular momentum selection rules. The event rate for this process is given by [59]

$$R = \frac{\rho_\chi}{2m_\chi} \sum_j N_{T,j} \cdot n_j \cdot \mathcal{F}(Z+1, E_e) \times \frac{|\vec{p_e}|_j}{16\pi m_\chi M^2_{A_j,Z_j}} \overline{|\mathcal{M}|^2} \tag{2.1}$$

where m_χ is the dark matter mass, ρ_χ is the local dark matter density, $N_{T,j}$ is the number of targets of a given isotope j, n_j is the number of neutrons per target, $\mathcal{F}$ is the Fermi function, $\vec{p_e}$ is the momentum of the outgoing β, $M^2_{A_j,Z_j}$ the mass of nucleus ${}^A_Z\mathrm{X}$, and $\overline{|\mathcal{M}|^2}$ is the spin averaged nucleon level matrix element. Because of the higher kinematic thresholds and smaller isotopic fraction, absorption of fermionic dark matter by ^{134}Xe is negligible relative to absorption on ^{136}Xe, in EXO-200. The main channel considered is therefore $\chi + {}^{136}_{54}\mathrm{Xe} \rightarrow {}^{136}_{55}\mathrm{Cs}^* + e^-$, in which the cesium nucleus is produced in an $J^P = 1^+$ excited state, where J is the total angular momentum and P is the parity of the state. In the absence of a detection, such data can constrain the interaction cross-section of this charged-current absorption process, or equivalently, the effective energy scale, Λ, for a beyond the SM operator that could mediate the

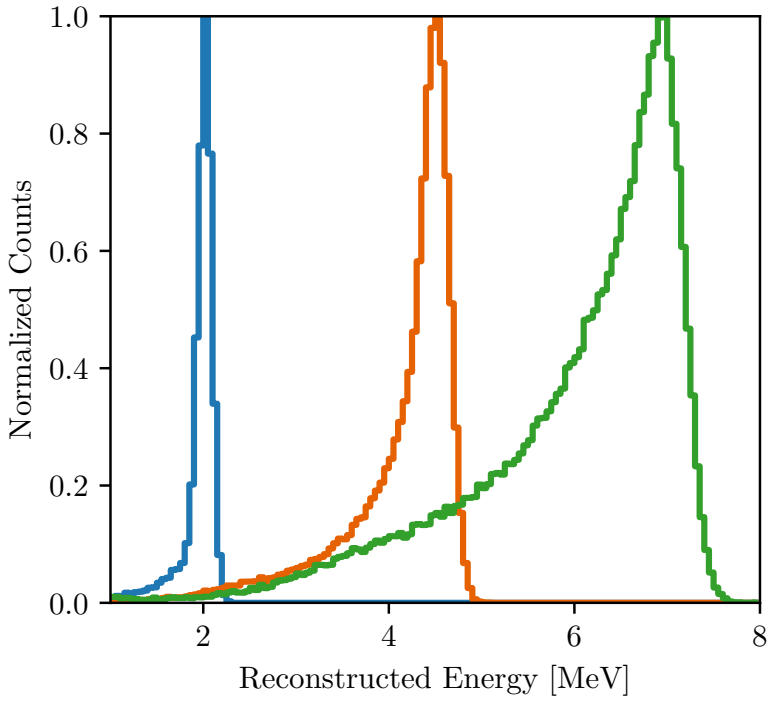

Figure 2.2: Monte Carlo simulation of the EXO-200 detector response to electrons at energies of 2 MeV, 4.5 MeV and 7 MeV in Phase II. The simulated distribution of the maximum reconstructed ionization energy in an event is shown, where the non-Gaussian shape comes from the increased emission of bremsstrahlung for the higher energy βs.

dark matter interaction

$$\frac{1}{\Lambda^2} \equiv \frac{g_R^2}{4M_{W_R}^2} \tag{2.2}$$

where g_R is the $SU(2)_R$ coupling constant of the theory, $M_{W_R} = \frac{1}{2} g_R u$ is the mass of the mediator (similar to the W-boson as the mediator of charged-current interactions via the weak nuclear force), with u being the vacuum expectation value of the scalar field ϕ through which the dark matter particle χ interacts with the SM via a Yukawa type coupling.

A major challenge in modeling these signals in EXO-200 comes from the fact that little data exists on the nuclear level structure of ^{136}Cs, with no sufficiently fast decaying states currently measured between the lowest-lying 1^+ excited states at 590 keV and its 5^+ ground state [74]. Assuming the dark matter absorption preferentially populates

the lowest-lying 1^+ state at 590 keV, there are only four known states to which the nucleus can decay: three excited states ($J^P = 9^-, 8^-, 4^+$), and the ground state ($J^P = 5^+$) [74]. In all cases, the decays are highly forbidden and order-of-magnitude Weisskopf estimates for the 590 keV state give a predicted half-life of $\gg 1$ s. In this case, the relaxation would appear as a secondary, uncorrelated event in the EXO-200 data, with similar signatures for excitations to higher energy nuclear levels of ^{136}Cs. However, if unknown intermediate levels of appropriate angular momentum and parity exist, then this half-life could be much shorter, allowing a DM absorption event to have a characteristic signature including both the primary beta as well as one or more coincident gammas. Since neither the decay times nor energies of the γs are currently known, we perform the analysis assuming that the only event signature is the outgoing β. However, as described in Sec., we also consider the case that one or more coincident γs of unknown energy are emitted, and present results that are insensitive to the presence of such γs. We note that the level structure of ^{136}Cs is under active investigation, with data suggesting the existence of new intermediate levels that may be relevant for such dark matter interactions [75]. In addition, recent shell model calculations predict a decay scheme in which the lowest-lying 1^+ state relaxes through levels that include an isomeric state with a lifetime of $\mathcal{O}(100\,\mu\text{s})$ [76], which could enable a time-coincidence analysis to separate charged-current absorption events from backgrounds. However, since the existence of these intermediate states has not been conclusively confirmed, we proceed as described above and leave their inclusion in dark matter analyses to future work.

The detector response to ionizing radiation is modeled by a detailed Monte Carlo (MC) simulation based on Geant4 [77]. The details of the MC simulation and reconstruction can be found in [32, 78]. The absorption event signature of a fermionic dark matter particle is modeled via a single β with a kinetic energy equal to the dark matter mass m_χ minus the kinematic threshold energy [59]. The transferred kinetic

energy of the dark matter particle results in a nuclear recoil of the ^{136}Xe atom which falls below the energy threshold and is therefore ignored. The maximum reconstructed ionization energy spectrum of βs at various energies in Phase II is shown in Figure 2.2. The more energetic the emitted β, the more bremsstrahlung it emits, leading to a non-Gaussian low energy tail.

2.3 Analysis

The energy region considered here can be divided into two regions based on the relevant backgrounds. In the low energy portion below 3 MeV, the dominant background sources are $2\nu\beta\beta$ events and γs from the ^{238}U and ^{232}Th decay chains. Above 3 MeV the main backgrounds arise from de-excitation γs from cosmogenically produced isotopes. To separate the β arising from dark matter interactions from backgrounds, one can exploit the fact that single MeV-scale βs typically deposit most of their energy at a single location (i.e., in the most energetic reconstructed charge cluster), in contrast to γ-backgrounds that predominantly Compton-scatter and therefore, on average, have less fractional energy contained in the most energetic cluster. An additional energy variable, defined as the energy of the most energetic charge deposit in an event, captures this topology difference. Therefore, in combination with the total event energy, the energy of the maximum reconstructed charge cluster is used as a second dimension in the likelihood fits discussed in Sec. 2.5.

Events within the fiducial volume are required to lie within a hexagon in the x-y plane with an apothem of 162 mm. They are further required to be more than 10 mm away from the cylindrical polytetrafluoroethylene (PTFE) scintillation light reflector, as well as the cathode and the V-wire planes. This fiducial volume contains 3.31×10^{26} atoms of ^{136}Xe, with an equivalent mass of 74.7 kg. The uncertainty in the fiducial mass is discussed in Section 2.4. The ^{136}Xe exposure of the entire dataset after data

quality cuts and accounting for live time loss due to vetoing events coincident with the muon veto is 234.1 kg yr with 117.4 kg yr (116.7 kg yr) in Phase I (II).

Compared to previous $0\nu\beta\beta$ analyses from EXO-200 [32, 72] this analysis

- extends the energy range up to 8 MeV
- combines all events into a single dataset irrespective of the number of interaction sites
- adds a second analysis variable capturing the energy of the most energetic charge deposit in an event.

The energy response of the detector is typically calibrated with external γ-sources placed on the outside of the detector near the cathode, using the full absorption peaks resulting from the decays of ^{60}Co and daughters of ^{226}Ra and ^{228}Th. At the end of the EXO-200 livetime, a composite Americium Beryllium (AmBe) neutron source was used to produce radiogenically activated ^{137}Xe, whose β-decay spectral shape was previously studied [79]. In addition, the AmBe source calibration provided a high statistics dataset of various other neutron and α activated by-products whose de-excitation gammas can be used for an energy calibration up to ∼8 MeV in Phase II only. This includes full absorption peaks at 1346 keV (^{64}Cu$(e,\gamma)^{64}$Ni), 2223 keV (^{1}H$(n,\gamma)^{2}$H), 4025 keV (^{136}Xe$(n,\gamma)^{137}$Xe), 4430 keV (^{9}Be$(\alpha,n\gamma)^{12}$C), and 7916 keV (^{63}Cu$(n,\gamma)^{64}$Cu). The energy spectrum resulting from the AmBe source and the corresponding energy calibration results are shown in Figure 2.3. The lower bound of the energy range considered for this analysis follows previous EXO-200 $0\nu\beta\beta$ analyses [32], whereas the upper bound is limited by the highest available energy calibration peak at 7916 keV.

While the analysis is limited to below 8 MeV to ensure the energy calibration is well-understood, the EXO-200 detector is sensitive to higher energy deposits. The low background data contains 18 (41) events above 8 MeV in Phase I (II) passing all

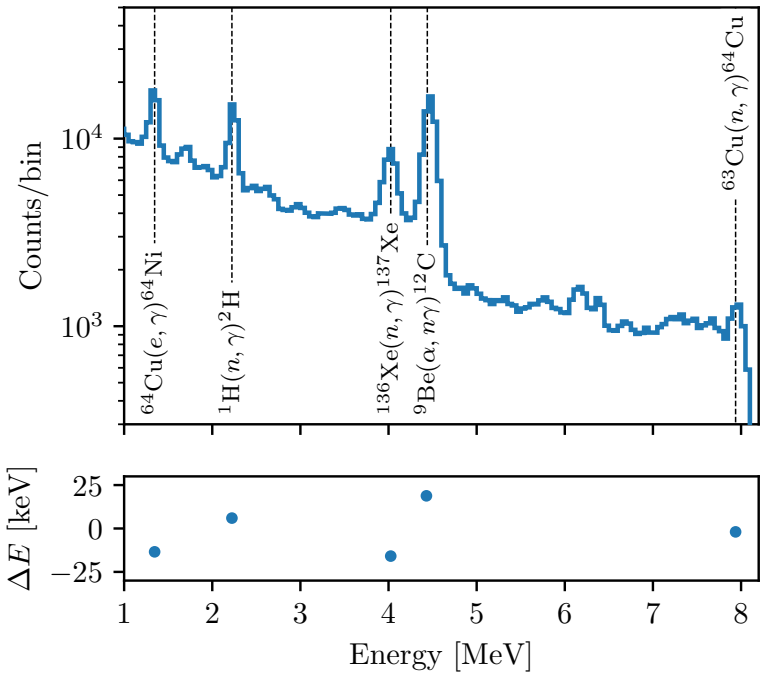

Figure 2.3: (top) AmBe calibration source energy spectrum in Phase II, demonstrating linear energy response of the EXO-200 detector throughout the energy range of interest. (bottom) Residuals between the measured and known energies ΔE.Calibration errors at the photo-peaks are less than 20 keV, resulting in a systematic error on the energy scale of $<0.5\,\%$.

event selection cuts, but which are not accounted for by any of the components in the EXO-200 background model [63, 64]. No events above 8 MeV are present in the veto-tagged data containing only events that were collected between 10 µs and 5 ms after any of the 29 muon veto panel triggers. This suggests that these events in the low-background data could arise, e.g., from long-lived cosmogenic activation products, or unaccounted for radiogenic processes not present in the veto-coincident data. The possible effect of such a small, unknown background on the results of this analysis will be discussed in Sec. 2.4.

To maximize the signal efficiency for β events in this energy range, this analysis does not require all ionization signals in an event to be fully reconstructed. Relative to the selection cuts used in $0\nu\beta\beta$ searches, this recovers events with multiple bremsstrahlung photons, for which there is a substantial probability that at least one low-energy

cluster is detected for which the x and y position can't be fully reconstructed. With all selection criteria included, the Monte Carlo simulation is used to estimate a signal reconstruction efficiency of $\epsilon > 99.7\,\%$ for both data-taking phases. Possible systematic errors in this efficiency will be discussed in Sec. 2.4.

MC events from all background and signal components, passing all quality cuts, are used to construct individual two-dimensional probability density functions (PDFs) that depend on the total rotated energy and the maximum charge cluster energy of an event. The components entering the background model are the same as in [32], whereas the $0\nu\beta\beta$ signal is replaced by a β-like PDF (see Figure 2.2) for a given m_χ (one for every 50 keV step within the analysis energy window). The search was performed by minimizing a binned negative log-likelihood (NLL) function when fitting the combined signal and background model PDFs to the data. Systematic errors are added to the fit as nuisance parameters that follow a normal distribution, with a width corresponding to the size of the systematic error estimated in stand-alone studies (see Sec. 2.4).

Toy datasets are generated from a background-only fit to the low-background data. These toy datasets were fit against the full background plus signal model, and the upper limit on the number of signal counts at the 90 % CL for each dark matter mass is determined from a profile likelihood. The sensitivity is obtained by calculating the median of an ensemble of 1000 upper limits.

2.4 Systematics

The assessment of systematic errors follows the same general approach as in [32] and includes an

1. uncertainty in the signal-specific detection efficiency caused by discrepancies in the shape of data and MC PDFs

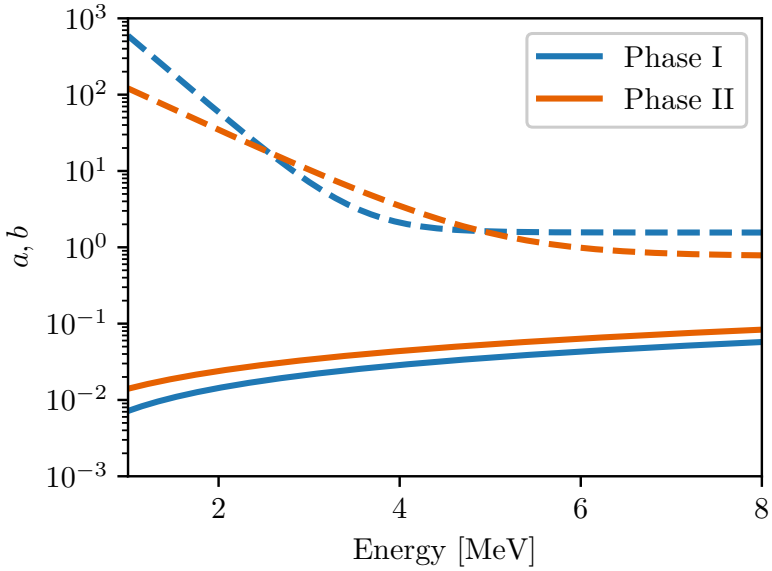

Figure 2.4: The energy dependence of the parameters a (solid) and b (dashed) in equation 2.3 for quantifying the systematic error from spectral shape disagreements is parameterized by $a(E) = a_1 \cdot E + a_2$ and $b(E) = b_1 \cdot e^{-b_2 \cdot E} + b_3$, respectively.

2. uncertainty in the activity of radon in the LXe as determined in stand-alone studies via measurement of time-correlated decays

3. uncertainty in the overall event detection efficiency due to possible errors in the estimated event reconstruction and selection efficiencies

The first systematic error arises from shape disagreements between data and MC PDFs and is propagated to the fit as a Gaussian constraint on the normalization of the signal PDF [32]. We performed a fit to the veto-tagged datasets in Phase I and II and treated the bin-by-bin ratio between the data and the best-fit model in each fit dimension as a possible error, reweighting the shape when building the PDFs for the likelihood fit to the low-background data to correct for the spectral distortions. Toy datasets were generated from these modified background model PDFs with the signal PDF present and were fit against the original unweighted PDFs. The bias in the number of fitted signal counts as a function of the injected number of signal counts is used to construct a conditional Gaussian constraint for the signal-only PDF

normalization that has the following functional form

$$\sigma/N = \sqrt{(a \cdot N)^2 + b^2}/N \tag{2.3}$$

It consists of a component proportional to the number of signal counts N with a proportionality factor a and a signal-independent component b. The signal-independent component quantifies shape errors in the background model that lead to a fixed bias in the number of signal counts, while the signal-dependent term quantifies a relative error that would be expected to scale with the signal size. The energy dependence of the parameters a and b were found to be approximately described by linear and exponential functions, respectively, and is shown in Figure 2.4. For Phase II an average between the bias from the spectral shape error in the muon veto-coincident data and the AmBe calibration data was used. The second uncertainty, quantifying possible error on the Rn activity in the LXe, was estimated in [64] to be 10 %. For the last item, this analysis assumes the same systematic error for the overall signal efficiency of 3.0 % (2.9 %) for Phase I (II) as was used in [32]. This systematic error may provide a slightly conservative estimate for the reconstruction efficiencies since β-like events above 3 MeV are easier to identify with smaller reconstruction errors due to their higher signal-to-noise.

As mentioned, the observed events above 8 MeV suggest that a small background component not included in the existing EXO-200 background model could be present. If such backgrounds arise from e.g., Compton scattering of high energy γs, this background component may also extend into the energy region below 8 MeV that is considered in this analysis. We estimated the effect that such an unknown background might have on our results by including an additional freely floating flat background PDF into the fit model and reevaluating the sensitivity. The relative difference in the sensitivity with and without this additional background is taken as a systematic error

due to the possible incompleteness of the background model and was calculated to be $\sim$0.1 %.

The signature of charged-current absorption events is similar to a solar neutrino interaction with the detector, where in the case of the charged-current interaction ($\nu + {}^{136}\mathrm{Xe} \rightarrow {}^{136}\mathrm{Cs}^{*} + e^{-}$) ^{136}Cs might also be produced in an excited state. In contrast, an elastic scattering process will only result in a single β in the final state. The solar neutrino background from both processes is estimated to produce a $\ll 1$ event throughout the livetime of the experiment within the entire energy region for this analysis [76] and can therefore be safely ignored.

Lastly, the systematic error on the energy scale is evaluated by taking the maximum spread in the calibrated energy for various possible calibration functions that interpolate between the measured photo-peaks of known energy (e.g. interpolating functions consisting of 1st or 2nd order polynomials, with or without a constant offset). The uncertainty in our energy calibration was estimated to be $\sim$2 % ($\sim$0.5 %) in Phase I (II). The larger error in Phase I arises from the lack of AmBe calibration data, which provides known energy peaks constraining the calibration functions to the 8 MeV upper energy threshold. This systematic is propagated as a Gaussian constraint on the γ-scale, which is a freely floating parameter in the likelihood fit that scales the energy of all PDFs representing interactions of γ events via a common multiplicative factor. This floating γ-scale can compensate for possible differences between calibrations and low-background data, but the best fit value was found to be consistent with unity within less than 0.2 %. An additional β-scale is introduced into the fit that allows the energy scale of PDFs arising from β-like events to float independently from γ-like PDFs, which allows the fit to correct possible differences in the energy response between βs and γs in the detector. However, this parameter was similarly found to be consistent with unity to within less than 1 %, in good agreement with previous studies [80]. Table 2.1 shows a summary of the systematic errors considered for this

Constraint	Phase I	Phase II
Energy scale	2%	$< 0.5\%$
Normalization	3.0%	2.9%
Background model	0.1%	0.1%
^{222}Rn	10%	10%

Table 2.1: Summary of estimated systematic errors for this analysis in the EXO-200 Phase I and II data sets.

analysis.

2.5 Results

Following [32], the likelihood fits are initially performed independently in each data-taking phase, minimizing a binned NLL function and then profiling over the signal PDF at a given m_χ. Hence, the combined NLL at a given m_χ is simply the sum of both NLLs where the efficiency and livetime corrected profile likelihood curves can be added to obtain the combined upper limit at 90 % CL.

The combined median 90 % CL sensitivity is similarly determined by combining the profile likelihoods of 1000 toy datasets from each phase. The combined 90 % upper limit and sensitivity are shown in Fig. 2.5, together with the 68 % and 95 % percentiles around the median sensitivity. We calculate the local p-value as the fraction of toy datasets under the no-signal hypothesis whose ΔNLL is at least as large as the one obtained from the data fit. We estimate the "look-elsewhere" effect [82] by noting that we perform approximately 30 independent searches for a signal within the energy range (assuming signal PDFs as independent if their peaks are separated by at least 2σ in rotated energy). The global p-value for each such search is then given by $p_{\text{global}} \approx 30 \times p_{\text{local}}$. We, therefore, find no statistically significant evidence for dark matter in our data.

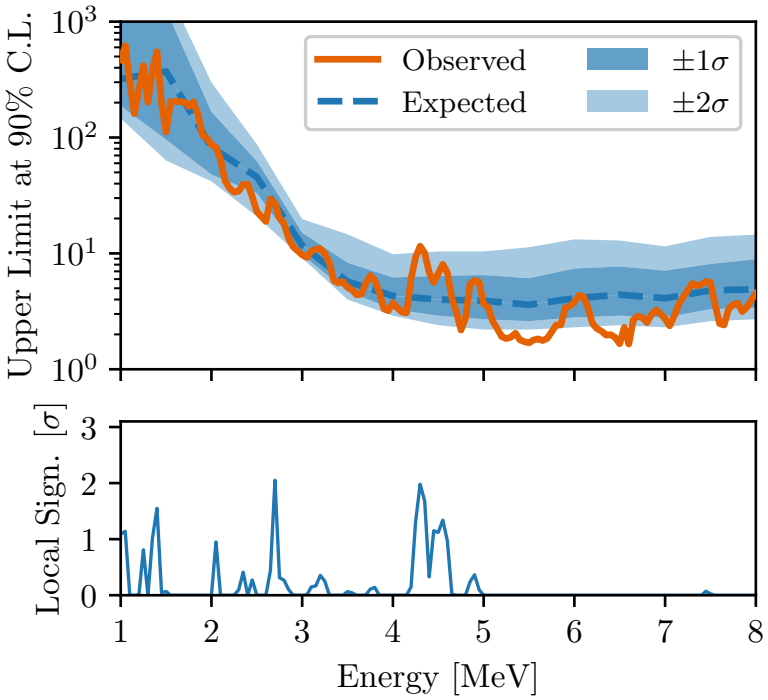

Figure 2.5: The top panel of the plot shows the upper limit (solid orange) on the number of dark matter events as a function of energy at 90 % CL. The median sensitivity (dashed blue) and the $\pm1\,\sigma$ (dark blue) and $\pm2\,\sigma$ (light blue) percentiles around the median are also shown. The bottom panel shows the local significance of our observation against the no-signal hypothesis. Taking into account the "look-elsewhere" effect we report no statistically significant evidence for dark matter.

Overall, the observed limit lies within the $\pm2\sigma$ distribution around the median sensitivity over most of the mass range. In the region between 5 MeV and 7 MeV, the limit is slightly stronger than the expected $\pm2\sigma$ region. This could arise from either a statistical under-fluctuation in the backgrounds at these energies or, possibly, a small overestimate of the background in this region relative to that assumed in the toy Monte Carlo studies.

Figure 2.6 shows the 90 % CL exclusion limit on the interaction cross-section as a function dark matter mass m_χ. In addition to the primary result using a two-dimensional likelihood fit consisting of the rotated energy and the maximum charge energy in an event, we also performed the fits using only the latter variable. These 1D fits have reduced sensitivity to a signal but provide an analysis that does not

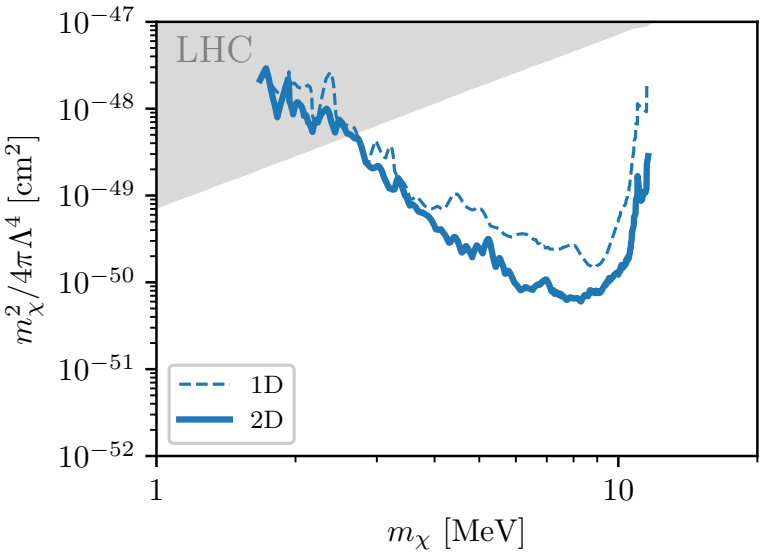

Figure 2.6: Limit on the absorption cross-section of fermionic dark matter by ^{136}Xe nuclei at the 90 % CL. We show our main 2D fit result in addition to a de-excitation γ agnostic 1D fit result (see text for more details). The grey region is excluded by direct constraint from colliders searches at the LHC [81].

strongly depend on the presence of additional de-excitation γs since the primary β cluster will contain the largest energy for nearly all events over the mass range considered, resulting in only marginal differences in the signal PDF shape. We also include limits from constraints on these models from collider experiments at the Large Hadron Collider (LHC) at CERN [81], demonstrating that relative to collider searches low-background detectors can perform competitive searches for certain dark models.

In Fig. 2.7 we provide the rotated energy spectrum of the low-background data from 1 MeV to 8 MeV, along with the best fit to the data with a background-only model, and the bin-wise residual counts for Phase I and Phase II. The excellent spectral shape agreement and linear detector response to both β-like and γ-like events are a result of more than ten years of work to build, run, and understand the EXO-200 detector and its response. These spectra, published here for the first time, may also constrain other physics beyond the SM which is outside the scope of the present work.

This analysis represents the first search for the absorption of MeV fermionic dark

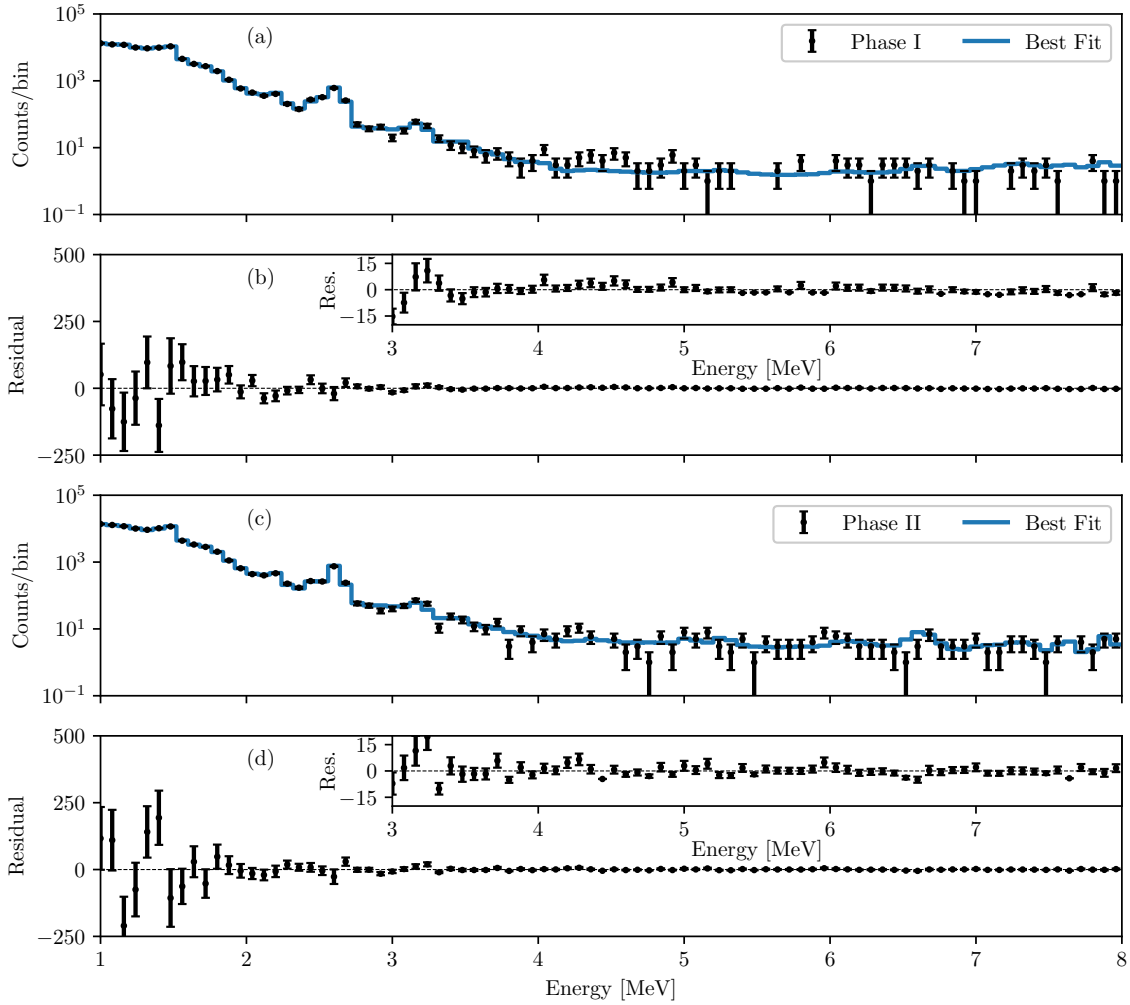

Figure 2.7: Rotated energy spectrum of the low-background data and the best fit (blue) to the data with a background-only model in Phase I (a) and Phase II (c) is shown. The resulting residual number of counts between data and the best from Phase I and Phase II is shown in panels (b) and (d), respectively. No significant disagreement is seen between the data and the background-only model. The average electron-recoil background rate above 4 MeV is $4.0 \times 10^{-4}\,\mathrm{cts\,kg^{-1}\,yr^{-1}\,keV^{-1}}$ in Phase I and $6.8 \times 10^{-4}\,\mathrm{cts\,kg^{-1}\,yr^{-1}\,keV^{-1}}$ in Phase II with a total exposure of 117.4 kg yr and 116.7 kg yr, respectively.

matter in a liquid xenon detector via a charged-current interaction, with a total ^{136}Xe exposure of 234.1 kg yr. As no statistically significant evidence was observed, we exclude new parameter space for these models at the 90 % CL for dark matter masses between 1.7 MeV and 11.6 MeV. Furthermore, this is the first analysis of the low-background data above 3 MeV in EXO-200, and a detailed understanding of the detector response is demonstrated. The low backgrounds achievable with the liquid xenon technology can enable future rare event searches such as $0\nu\beta\beta$, direct detection of WIMP dark matter or other dark matter interaction mechanisms [33, 83, 84].

Chapter 3

nEXO: A Tonne-scale Experiment Searching for $0\nu\beta\beta$

3.1 Detector Design 42

3.2 Charge Collection with Tiles 44

3.3 Light Collection with Silicon Photomultipliers 46

3.4 Comparison between EXO-200 and nEXO 53

This chapter describes the pre-conceptual design of nEXO [85], which is an upcoming tonne-scale experiment planning to search for the $0\nu\beta\beta$ in ^{136}Xe with a projected half-life sensitivity of $T^{0\nu}_{1/2} = 1.35 \times 10^{28}$ yr [33]. An overview of its detector design and novel light and charge readout systems is provided.

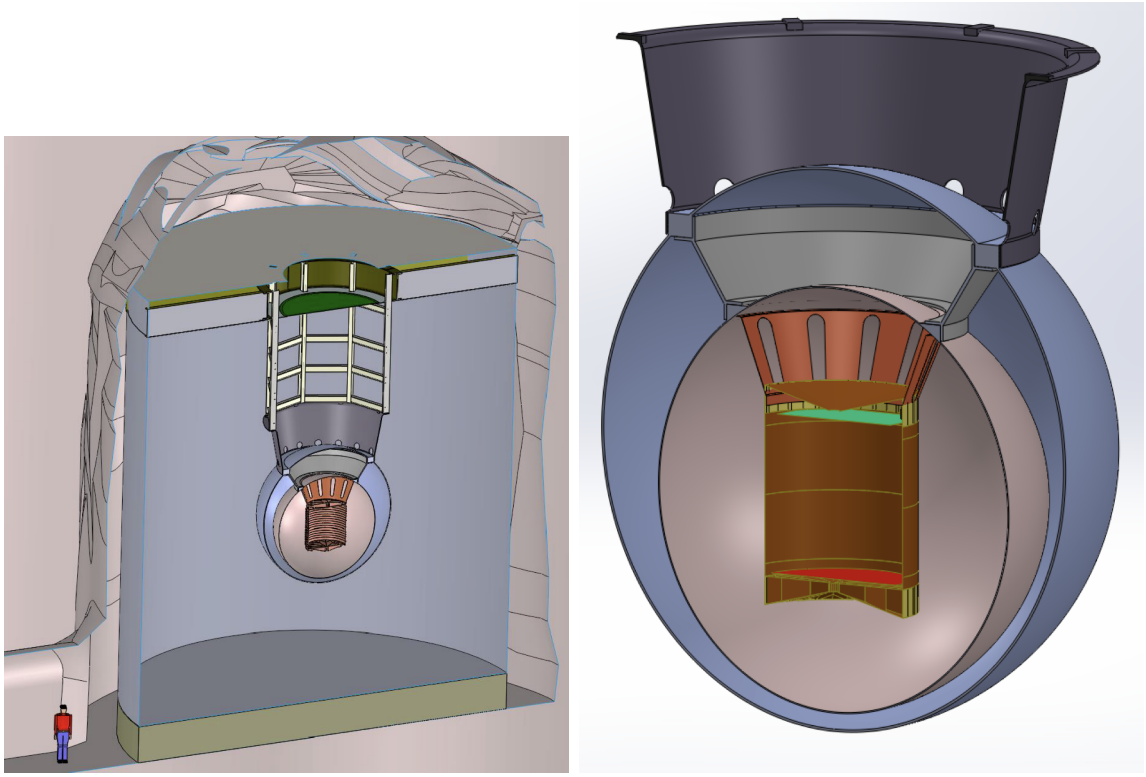

Figure 3.1: (left) Artistic view of the nEXO experiment in the SNOLAB cryopit. (right) Section view of nEXO's carbon-fiber-based inner and outer cryostats and the copper Time Projection Chamber (TPC) vessel in the center, supported by titanium liners.

3.1 Detector Design

The nEXO detector design is guided by the successful implementation of the EXO-200 experiment using a single-phase LXe-based time projection chamber. Figure 3.1 shows an artistic view of the entire nEXO experiment as it would be built in the cryopit at SNOLAB, while Figure 3.1 shows a more close-up view.

nEXO will utilize 5000 kg of LXe enriched to 90 % in the $0\nu\beta\beta$-decaying isotope ^{136}Xe. A single drift volume with a drift length of 1183 mm and diameter of 1250 mm realizes the largest possible monolithic xenon volume with this total mass. The volume can be instrumented with sensitive light and charge sensors and maximizes the suppression, identification, and discrimination of external backgrounds. The Time Projection Chamber (TPC) is vertically oriented with a thin copper cathode at the

bottom, designed for a high voltage of up to 50 kV to provide an electric field between the cathode and anode of 400 V cm^{-1} for drifting ionization charge. A total of 58 copper field shaping rings with a height of 1 cm and separated by 1 cm define the inner xenon volume and ensure a uniform electric field. The LXe will be filled inside an ultra-low radioactivity copper vessel and will be submerged in 32 t of heat transfer cryofluid (HFE-7000 [71]). The inner spherical cryostat holding the HFE will be surrounded by an additional vacuum-insulating spherical outer cryostat, both of which are made from a radio-pure carbon-fiber composite.

The entire detector will be housed inside a water tank which will serve as an active water Cherenkov detector for vetoing cosmogenic muons. The nEXO experiment is currently planned to be installed in the cryopit at SNOLAB, providing around 6300 m water equivalent of overburden which reduces the cosmogenic backgrounds significantly. Other sites, including Laboratori Nazionali del Gran Sasso (LNGS) in Italy and the Sanford Underground Research Facility (SURF) in the United States, have also been considered, but because of the higher rate of cosmogenic backgrounds, a more sophisticated veto system than currently implemented would be required to avoid significant livetime losses of the experiment. A more detailed overview of the current veto system, its efficiency, and the impact of the site selection on the sensitivity to $0\nu\beta\beta$ will be given in Section 5.5.3.

The ionization charge and scintillation light from events in the TPC are collected by modular charge readout tiles and Silicon Photomultiplier (SiPM) tiles, respectively, and will be discussed in more detail in 3.2 and 3.3. The placement of the light detectors behind the FSRs differs from the design of other noble liquid experiments, including EXO-200. This is in part motivated by the need to reduce the source of electronegative impurities such as plastics to improve the electron lifetime over the longer drift length. One commonly used plastic is Polytetrafluoroethylene (PTFE) which has a high reflectivity for Vacuum Ultra Violet (VUV) light [86] and can help

improve light collection efficiency. The major benefit is that this design allows for the collection of more light, improving the energy resolution and preserving the topological information better that could be used for background rejection (see Section 4.1.6). This "open field cage" design for nEXO has been studied in [87].

3.2 Charge Collection with Tiles

nEXO doesn't plan to use crossed wire planes for the charge collection, unlike in EXO-200 or other single-phase noble liquid detectors. Instead, a modular and integrated design is pursued that provides all necessary components including the charge collection system and accompanied electronics in a single unit. The benefit of this approach is the independent testability of these small charge modules outside the nEXO detector in a small-scale test setup before assembling the entire anode plane.

nEXO will use 10 cm × 10 cm modular charge tiles that are made of fused-silica and are 300 µm thick [85, 88]. A total of 60 electrically isolated strips made of layers of gold and titanium are directly deposited onto the substrate. Each strip has a length of 10 cm and consists of 30 squared pads, with a diagonal length of 3 mm, connected in series at their corners. 30 of these strips are oriented orthogonally to the other 30 and isolated via a 1.5 µm thin silicon dioxide layer, resulting in a crossed strip design for x-y-position reconstruction in the plane of the tiles. New prototype tiles will have a more optimized pixel pitch of 6 mm instead of 3 mm, which was determined by standalone studies of the background rejection capabilities and energy resolution [89].

While this design avoids many mechanical drawbacks of crossed wire planes it also lacks a Frisch grid, a second plane between the anode and cathode that is maintained at a different electric potential and shields the anode from the slow-rising induction signals as the ionization charge from an event drifts towards it. This poses constraints on the tolerable charge readout noise but has already been demonstrated to be within

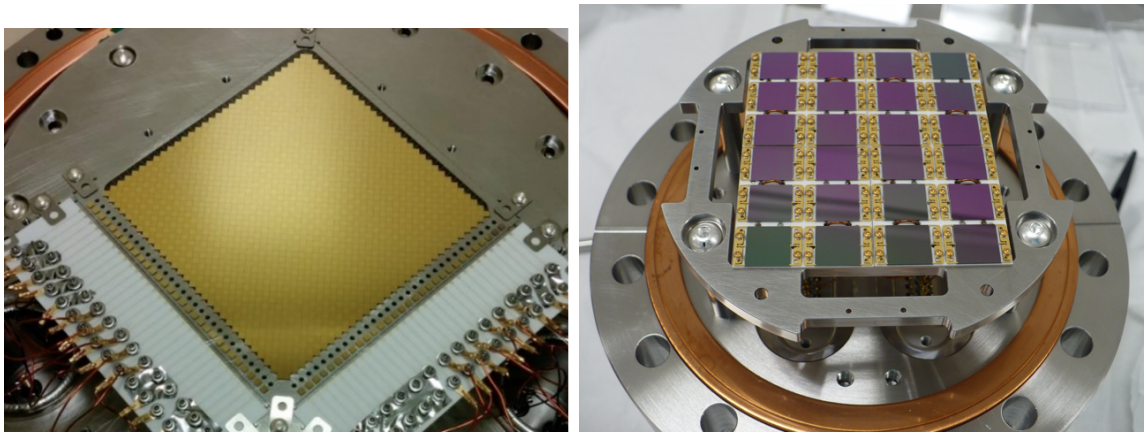

Figure 3.2: (left) Photograph of a prototype charge collection tile mounted into a test LXe setup. This iteration still used a provisional connection scheme to the external, discrete component electronics at room temperature. A future version will include integrated ASIC electronics on the backside, avoiding the need for discrete wiring and electronics. (right) Early prototype of a SiPM array consisting of 24 1 cm^2 FBK devices from 2017. No particular attention was paid to radiopurity or maximal coverage since this prototype only intended to demonstrate the safe operation of a large number of SiPMs in LXe. Figures from [85].

nEXO specifications [33]. Each charge tile module will have its ASIC readout attached to the back side, another departure from the EXO-200, where the electronics will be submerged in the LXe and are based on ASICs designed for large liquid argon TPCs. Initial prototypes have been successfully fabricated and tested in a LXe test stand [88]. While initial tests were carried out using discrete charge readout electronics, a new generation of charge tiles currently in production will be tested in combination with a prototype ASIC attached to the backside.

In addition, a dedicated simulation framework for the charge transport in nEXO has been developed [89] that includes realistic effects from longitudinal and transverse diffusion, with inputs from EXO-200 [90] and standalone test setups [91], and charge loss due to a finite electron lifetime τ_e. The induced current on the charge tiles is simulated and overlaid with realistic noise sampled from an example noise spectrum as measured in an early prototype charge readout ASICs.

3.3 Light Collection with Silicon Photomultipliers

While the stringent radiopurity requirements of nEXO [33, 85, 92] disfavor the use of traditional Photomultiplier Tubes (PMTs) the goal of $\leq$1 % energy resolution at $Q_{\beta\beta}$ prohibits the use of LAAPDs, previously deployed in EXO-200, due to their low gain and correspondingly large electronics readout noise. Even custom-developed low-background PMTs used in LZ and XENON1T [93] and the LAAPDs used in EXO-200 [94] are about a factor of 10000 and 100 (upper limit) too high in radioactivity, respectively, compared to the same surface coverage with SiPMs. Therefore, the scintillation light emitted by the LXe in nEXO will be detected by $\sim$4.5 m^2 of SiPMs covering the barrel of the TPC vessel, which are situated behind the field shaping rings. These silicon-based semi-conductor photo-detectors have emerged as a promising light detection technology and have substantially matured over the last decade [95, 96] to the point where several other large noble-liquid-based experiments plan to use them [97–99].

SiPMs [100, 101] consist of $\mathcal{O}$(10000) pixels, called single-photon avalanche photodiodes (SPADs), that are connected in parallel and typically have a pixel pitch of 10 µm–100 µm. Each pixel has a reverse bias beyond breakdown applied (Geiger mode) and triggers an avalanche of secondary electrons upon release of a primary photo-electron. The current from the avalanche is passively quenched via a pixel-by-pixel series resistor to protect the SPAD from long-term damage. The circuitry for providing the bias and the quenching resistor reduces the photo-sensitive area of the SPAD to 50 %–90 % and is called the geometric efficiency ϵ_{geo}. The response of the SiPM is the sum response of all SPADs and because of the high and stable gain between pixels, this results in a quantized response to individual photons. However, multiple photons releasing a photo-electron in a single SPAD at the same time cannot be resolved and result in the same binary response of the SPAD. In extension, this also means that a single SiPM can only detect as many photons as the number of

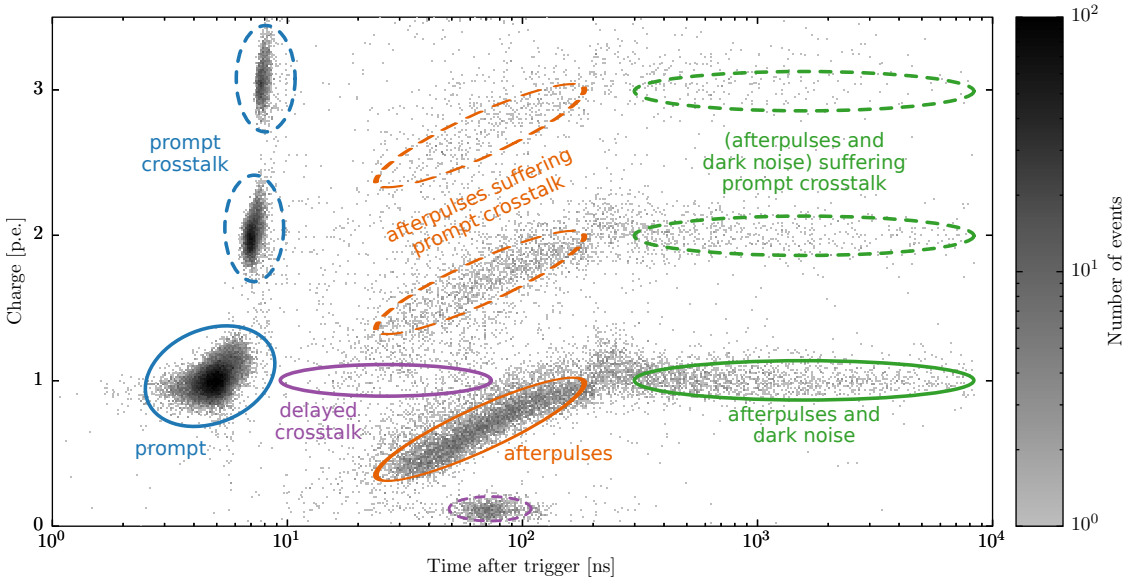

Figure 3.3: Distribution of photoelectron equivalents for parent and subsequent pulses as a function of the time since the pixel was triggered. See the text for a detailed explanation. Figure from [102].

SPADs it consists of at any given time. This could become an issue when working with high photon fluxes where saturation effects might affect the performance of the experiment. nEXO is far away from this regime since number of photons detected per SiPM readout channel for an event with ∼2.5 MeV is about 1 on average (see Section 4.1.7).

The characteristic parameters of a SiPM are typically evaluated as a function of overvoltage ΔU, which is the difference between the applied bias voltage U_{Bias} and the voltage U_{Break} at which the SiPM undergoes breakdown and operates in Geiger mode, and is defined as $\Delta U = |U_{\text{Bias}} - U_{\text{Break}}|$. Here is a list of key parameters [103] that need to be well characterized for nEXO:

- **The Photon Detection Efficiency (PDE)** is the probability of detecting a photon that impinged on the SiPM surface and is typically parametrized as

$$\text{PDE}(\Delta\text{U}, \lambda, \theta) = \epsilon_{\text{geo}} \cdot \text{QE}(\lambda, \theta) \cdot P_{\text{trigger}}(\Delta U, \theta) \tag{3.1}$$

where ϵ_{geo} is the ratio between the photosensitive area to total surface area and is called the geometric efficiency, QE(λ) is the wavelength and angle-dependent probability to absorb a photon in the avalanche region of the SiPM and to create an electron-hole pair and $P_{\text{trigger}}(\Delta U)$ is the successive overvoltage and angle-dependent probability of said photo-electron to trigger an avalanche resulting in a measurable signal.

- **The Dark Count Rate (DCR)** is the rate at which thermally produced electron-hole pairs are created that trigger an avalanche and are therefore indistinguishable from a photon-induced avalanche. This process is highly temperature dependent and its effect on the detector performance tends to become negligible for nEXO at LXe temperatures [102, 104, 105] because of the relatively large number of photons produced during a $0\nu\beta\beta$-event. For dark matter direct detection experiments these low DCRs still pose an issue due to the significantly smaller energy deposits and a correspondingly smaller number of emitted photons.

- **The amount of additional charge released from Correlated Avalanches (CA)** can originate from two parasitic processes, Afterpulsing (AP) and Cross-talk (CT), and will smear the measured number of detected photons. The former is a result of imperfections in the silicon lattice through which electrons in the avalanche process can get trapped and re-released at a later time. The trapping lifetime is device-dependent but can range from 10 ns–1000 ns. The latter CA source is a result of additional photons being emitted during the avalanche that can travel from its pixel of origin to a neighboring pixel and trigger a time-coincident secondary avalanche. This is referred to as prompt Cross-talk (pCT). The photon can also produce an electron somewhere in the SiPM outside the avalanche region which can slowly diffuse back into the avalanche region

Parameter	Requirement	VUV-HD1	VUV4
PDE	>15 %	∼21 %	∼15 %
CA within 1 µs	<40 %	<15 %	<20 %
Dark Noise Rate	<50 Hz mm^{-2}	<0.2 Hz mm^{-2}	<0.2 Hz mm^{-2}
Overvoltage	>3 V	2.2 V	3 V

Table 3.1: Summary of requirements on the performance of SiPMs in nEXO together with the measured performance of candidate SiPMs such as the FBK VUV-HD1 [102] and the HPK VUV4 [105].

to trigger a secondary pulse. Due to its time-separated nature, this is called delayed Cross-talk (dCT). In principle, another component of CT exists which is the additional illumination of SiPMs by CT photons that leave one SiPM and can be detected by another SiPM. However, significantly less is known about this process, including its probability and angular distribution. This needs to be carefully measured in a dedicated setup and could potentially make up a large fraction of the total number of CA.

Figure 3.3 summarizes the effects of DCR, AP, pCT and dCT in terms of their time and charge distribution in a candidate SiPM for nEXO [102]. nEXO has been running an extensive characterization campaign of SiPMs and is working together with two vendors, Fondazione Bruno Kessler (FBK) in Italy [106] and Hamamatsu Photonics K.K. (HPK) in Japan [107] to determine SiPM candidates that would meet the stringent requirements imposed on the photon-detection system. Table 3.1 summarizes the requirements together with the measured performance of candidate SiPMs from both companies, indicating that both would meet the requirements. The performance of these devices is expected to further improve with the next generation of devices.

Despite the successful development of single devices from both FBK and HPK meeting nEXO requirements additional R&D is still required to demonstrate large-scale integration, long-term stability, and uniformity for the ∼ 45000 SiPMs under

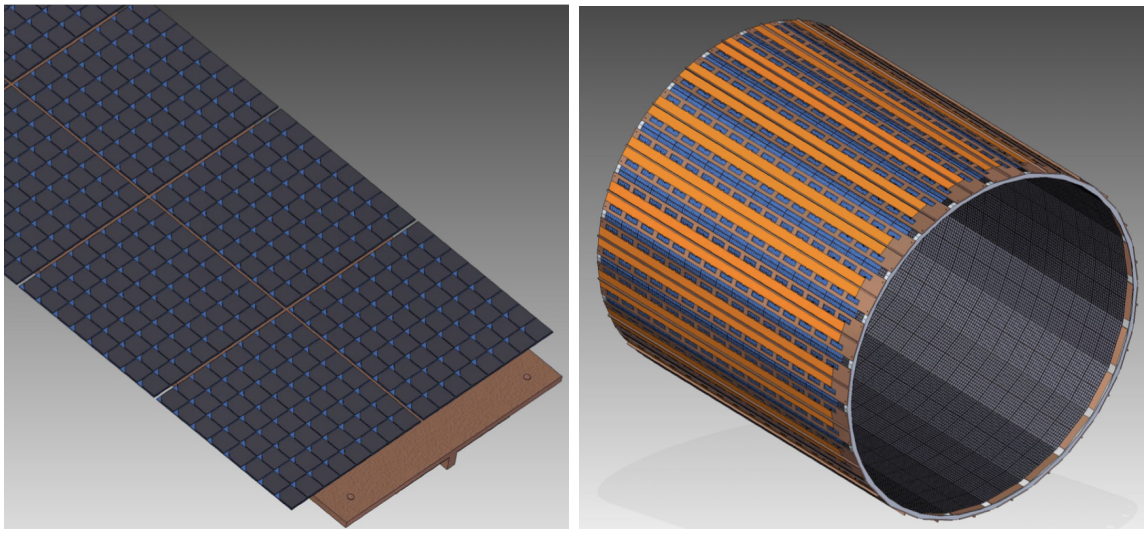

Figure 3.4: View of the photon detection system of nEXO, showing a view of the SiPM staves (left) consisting of a 2x10 array of photon detection modules, each of which is made of 96 SiPMs. A total of 24 staves will make up the photon detection system (right) covering the barrel of the TPC vessel and will be situated behind the field shaping rings.

LXe conditions. The current nEXO design envisions combining 6 SiPMs into a single readout channel, 16 of which will be mounted onto an interposer substrate that is either made of silicon or fused silica [85], that provides both mechanical support and electrical connections to the SiPMs. The channel size is a tradeoff between reduction in radioactivity due to fewer cables, increased parasitic capacitance coupled with larger electronics noise, and the dynamic range for measuring single photoelectrons while reliably measuring backgrounds close to the SiPMs (see Section 4.1.7 for more details). An additional silicon or silica daughterboard will be mounted on the backside of the interposer, which provides support for the light readout ASIC. This entire 96 cm^2 large package is a self-contained module and provides the smallest integrated unit for the photon detection system in nEXO. A total of 20 such units will make up a SiPM stave in a 2x10 array. To cover the entire barrel of the detector 24 staves are oriented to form a 24-sided polygon. A schematic of the modules, staves, and entire photon detection system is shown in Figure 3.4.

Early prototype arrays, such as the one in Figure 3.2, were built to demonstrate the

proof of principle of operating a large number of SiPMs in LXe. Here the SiPMs were mounted to an alumina ceramic substrate via dismountable spring-loaded tips. The primary focus of the design was the re-usability of the SiPMs due to the short supply and low outgassing of all components. No attention was paid to radiopurity at that stage and only little optimization was done for the geometric efficiency. The readout electronics were based on discrete components and placed in a cold nitrogen atmosphere outside the LXe. The final nEXO design will be substantially more optimized in terms of spatial efficiency, material selection, and radiopurity requirements.

Mounting the SiPMs to the interposer poses a significant challenge as it is heavily dependent on the geometry of the SiPM and the availability of the through-silicon-vias (TSV) technology to connect the front layer to the back layer for those devices, making the surface coverage with SiPMs more efficient and eliminating wire bonds in the high electric field region of the detector. While HPK has demonstrated the ability to incorporate TSVs into their devices the performance of their VUV4 generation SiPMs in terms of absolute PDE at the xenon scintillation light wavelength of 178 nm only marginally meets nEXO requirements [105]. The VUV-HD1 devices from FBK far exceed nEXO's requirements for the PDE [102] but no devices with TSVs are available as of now. Therefore, two options for mounting the SiPMs to the top surface of the interposer need to be considered:

- devices that have TSVs can be mounted to the interposer and packed efficiently without any substantial gaps and the electrical connection will be made only to the backside of the SiPMs. In principle, a suitable interposer prototype can be shipped to the SiPM vendor where they can mount the SiPMs to the interposer ensuring proper industry standard handling.

- devices without TSVs will be mounted to the interposer with some gap towards the edge leaving space for wire-bonding the top surface of the SiPM to metal pads on the interposer

In addition, a variety of options to bond the SiPMs to the interposer are investigated, including bonding to copper pillars, bump bonding, and conductive epoxy. While each one of the above-mentioned bonding techniques is well established, their success under nEXO conditions needs to be tested. This includes mechanical and electrical stability under repeated temperature cycles.

Assays within the nEXO collaboration indicate that some fused silica can be made very radiopure and previous radio-assay measurements within the collaboration indicate that not only the fused silica but the background contribution from all materials for such a tile module would meet nEXO requirements [33]. It remains unclear how clean the deposition processes are, which requires an iterative process with vendors that will assess the largest background contributions.

The final design and size of the tile module will also be driven (besides constraints due to radiopurity and xenon purity) by the front-end electronics. A 10-bit readout is currently envisioned for the light readout corresponding to a maximum of 1024 detected photons per channel before saturation. This dynamic range is necessary to maintain single-photon resolution for lower light yield events deep inside the detector and at the same time be able to tag high light yield alpha events close to the edge of the detector to discriminate ^{214}Bi induced backgrounds. The optimal size of the tiles and the number of channels per tile can be determined via optical simulation. Initial studies show that the photon density, i.e. the number of photons per channel, is well below saturation for all channels for events inside the fiducial volume of nEXO and for a channel size smaller than 40 cm $\times$ 20 cm. Furthermore, more dedicated studies of events in the LXe volume between the field shaping rings and the SiPMs where the photon density will be the largest are needed to determine the optimal channel size. Some more details are provided in Section 4.1.7.

3.4 Comparison between EXO-200 and nEXO

Table 3.2 provides a summary of the design differences between EXO-200 and nEXO. The design choices for nEXO are based on the successful implementations in EXO-200 and the experience gained from running the experiment and understanding its detector response for almost 10 years. The changes relative to EXO-200 are required to enable the goal of reaching a half-life sensitivity of $T^{0\nu}_{1/2} > 10^{28}\,\mathrm{yr}$.

Component	EXO-200	nEXO
Xenon Mass	175 kg	5000 kg
Enrichment	80.6 %	90 %
Location	WIPP	SNOLAB
Overburden (water equivalent)	1624 m	6300 m
Max. Drift Length	180 mm	1183 mm
Electron Lifetime	3 ms–5 ms	10 ms
Field Cage Design	Closed	Open [87]
Electric Drift Field	567 V cm^{-1}	400 V cm^{-1}
Light Readout	LAAPD	SiPM [102, 104, 105, 108–110]
Photo-detector Bias Voltage	∼1 kV	30 V–50 V
Photo-detector Gain	50-200	$\mathcal{O}(10^6)$
Total Photo-sensitive Area	0.094 m	4.6 m
Number of Photo-detectors	468	45600
Light Readout Channels	74	7600
Light Collection Efficiency	8.1 % [80]	6.1 %–9.5 % [33]
Charge Readout	Crossed Wire Planes	Charge Tile Modules
Charge Readout Channels	76	7200
Event Charge Electronics Noise	770 e^- [80]	1130 e^- [33]
Light Electronics Noise	148 p.e. [80]	0.1 p.e. [85]
Energy Resolution $\sigma/Q_{\beta\beta}$	1.15 % [111]	0.8 % [33]
Muon Veto	Scintillator Panels	Water Cherenkov
Copper (Cu)	Aurubis Cu	Electroformed Cu

Table 3.2: Comparison between EXO-200 and nEXO in terms of key design and performance parameters.

Chapter 4

Light and Charge Transport in nEXO

4.1 Photon Transport and Optical Simulations 56

4.1.1 Chroma and GPU-acceleration 57

4.1.2 Detector Geometry and Optical Properties 59

4.1.3 Systematic Error on Photon Transport 61

4.1.4 Photon Distribution 67

4.1.5 Lightmap 70

4.1.6 Alternative Designs 72

4.1.7 Channel Size and Dynamic Range 74

4.1.8 Conclusion and Outlook 76

4.2 Charge Transport and Liquid Xenon Purity 77

4.2.1 Modelling Outgassing of Impurities 78

4.2.2 Electronegative Impurity Control in nEXO 95

4.2.3 Vacuum Outgassing Setup 99

4.2.4 Liquid Xenon Purity Monitor 107
4.2.5 Conclusion and Outlook 120
4.3 Energy Resolution 121

The purpose of this chapter is to provide an overview of the modeling of light and charge transport in LXe for nEXO. It is important to perform detailed photon transport simulations in order to understand how light is collected throughout the entire detector volume. For the charge transport, the effects of the xenon purity need to be taken into account by accurately modeling charge loss through various sources of electronegative impurities. Combining our understanding of light and charge transport and collection, we can use a semi-empirical model to predict the achievable energy resolution in nEXO.

4.1 Photon Transport and Optical Simulations

Accurate modeling of the propagation of scintillation photons in a LXe detector is crucially important. However, the scintillation light information has traditionally been under-utilized due to limitations related to the photo coverage coupled with low channel granularity and statistical noise because of poor photon detection efficiency. Most of these shortcomings are overcome in nEXO by using SiPMs for light detection with a channel size of $6\,\mathrm{cm}^2$. The SiPMs will fully cover the barrel of the TPC and provide granular information about the light response of the detector with low noise.

However, to take advantage of this information, new simulation tools and reconstruction techniques are needed. The propagation of photons in traditional simulation tool kits such as Geant4 [77] is a notoriously slow and computationally intensive task. The complexity in light transport simulations arises from tracking the photons (on the order of ∼100k for a $0\nu\beta\beta$ event) through the geometry and testing whether it intersects with any object, which requires detailed ray-tracing simulations for 100k

photons for each event.

In addition to a Geant4-based light simulation for nEXO, a new simulation framework based on the `Chroma` software package [112–114] was developed with the primary focus on enhancements in speed performance and geometric realism.

The speed improvement is possible due to the intrinsic parallel architecture of graphical processing units (GPUs) handling the propagation of the photons in `Chroma`. An important advantage of this framework is the ability to import a 3D Computer-aided design (CAD) of the detector geometry which allows simulating the light response of the detector as a function of position with unprecedented geometric realism.

4.1.1 Chroma and GPU-acceleration

`Chroma` uses a surface-based approach via triangle meshes to define complex detector geometries. One of its key features is the ability to import Standard Tesselation Language (STL) files, which is a common file format for most CAD software and contains the geometry as a series of connected triangles that are defined by their surface normal and vertices in a 3D cartesian coordinate system. This allows for an exact remake of the detector geometry without substantial simplifications, which is crucial for detailed modeling of the light response to surface-based radioactive backgrounds. Figure 4.1 shows example renderings of the EXO-200 and nEXO detector geometries in `Chroma`. Each triangle can be assigned its unique properties defining the optical properties of the inside and outside bulk materials, which are anti-parallel and parallel to the surface normal, respectively, as well as additional surface-based optical properties for more complex optical models defined below. This granularity allows users to define complex, spatially varying optical properties for the same object.

Each photon is propagated in a separate CUDA core on the GPU allowing simulation of a vast number of photons per GPU at a time, thus significantly increasing the speed compared to Geant4 which uses central processing units (CPUs). While

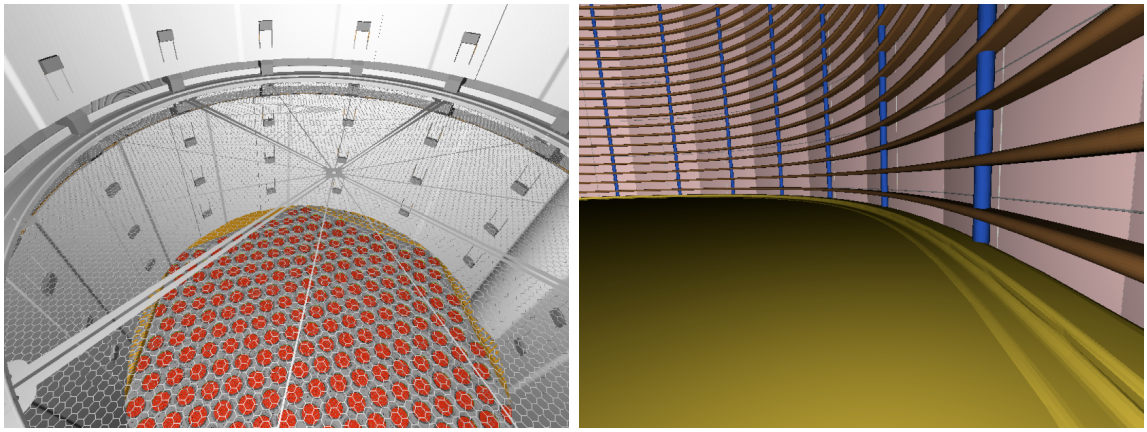

Figure 4.1: Rendering of the EXO-200 detector (left) including the fine cathode mesh and the nEXO detector (right) geometries in Chroma for performing light transport simulations.

standard ray-tracing libraries are not meant for accurate physics simulations because of the various simplifications used for speed improvements, `Chroma` includes a variety of physics models for dealing with the propagation of optical photons and includes processes such as

- Diffuse and specular reflection at surfaces
- Wavelength-dependent index of refraction to be used with Fresnel's equations for reflection and transmission at boundaries
- Rayleigh scattering
- Absorption in the bulk material
- Reemission from a wavelength shifter
- Angle and wavelength-dependent transmission and reflection at surfaces

Results obtained with `Chroma` and Geant4 are in agreement to within less than 2 % and therefore make `Chroma` an attractive alternative for simulating the light response of large scale neutrino detectors [33, 115–118].

A containerized version of the `Chroma` source code is made publicly available and can be downloaded via

```
singularity pull oras://ghcr.io/nexo-collaboration/chroma:c10-0_u18-04
```

4.1.2 Detector Geometry and Optical Properties

The LXe scintillation light emission spectrum can be described with good accuracy by a Gaussian with a mean at wavelength $\lambda_{\text{scint}} = 174.8\,\text{nm}$ and width of $\sigma_{\text{scint}} = 4.3\,\text{nm}$ [119]. For simplicity, the scintillation light emission in `Chroma` is modeled as monochromatic with $\lambda = 175\,\text{nm}$. Any temporal substructure due to delayed emission from different excited states [120] is ignored because of the comparatively long light readout integration time of 1 µs.

Measurements of the absorption length λ_{abs} and scattering length λ_{scat} of LXe are difficult to perform and depend on the purity of the xenon. Other large LXe experiments assume 30 m [121] and 50 m [122] for the absorption length based on their purification performance and extrapolation from [123]. The electron lifetime goal of $\tau = 10\,\text{ms}$ in nEXO sets an even tighter requirement on the purity of the LXe compared to the above experiments, hence our value of 20 m for the absorption length is conservative. Previously measured values for the scattering length range from 30 cm to 50 cm [124, 125], so we adopt a conservative value of $\lambda_{\text{scat}} = 30\,\text{cm}$. Section 4.1.3 will show the dependence of the photon transport efficiency (PTE) on λ_{abs} and λ_{scat}.

Many of the materials that are being considered for building the TPC components have a relatively low intrinsic reflectivity at 178 nm, including copper for the cathode and field rings, sapphire for the support rods and gold for the charge readout tiles. In order to increase the reflectivity of components and therefore boost the PTE, reflective coatings are being investigated, namely an Al and MgF_2 coating that has been shown in EXO-200 to have high reflectivity of larger than 80 % at 178 nm [72]. A 10 nm–100 nm thick coating of MgF_2 on top of the aluminum, which can be deposited

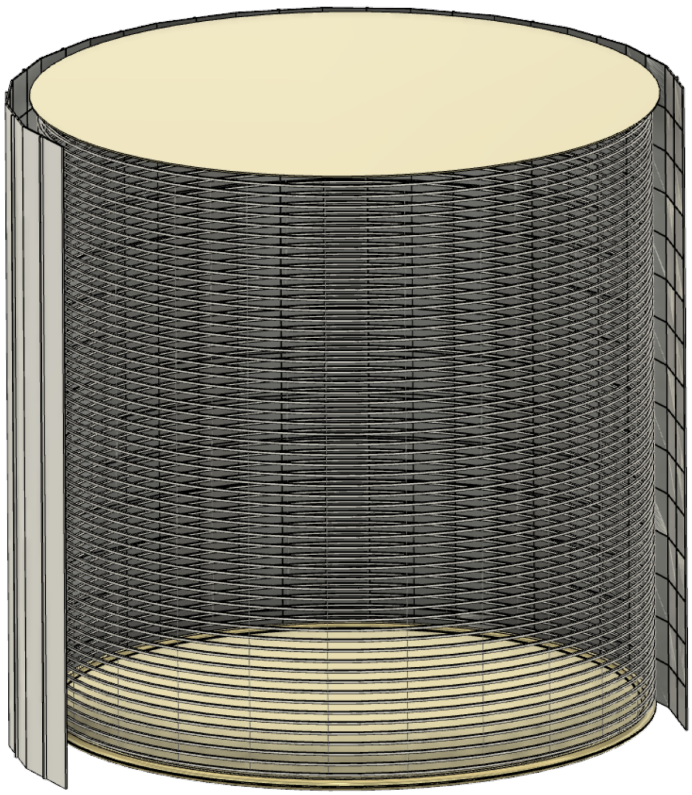

Figure 4.2: A CAD model of the nEXO TPC as it is imported into Chroma, where only detector components relevant for light propagation are shown. This includes the anode (top), cathode (bottom), field shaping rings, field cage support rods, SiPM staves, the SiPM modules, and the copper vessel (not shown).

directly onto the metal, is needed to prevent oxidation and a decrease in reflectivity. A summary of optical parameters used for the simulation is shown in Tab. 4.1.

In `Chroma`, two different surface models were used for different components inside the TPC. A simple surface model is used for all non-detecting surfaces in the TPC, including the field shaping rings, cathode, anode, sapphire support rods, SiPM staves, and the vessel. The photon interaction at the surface of those components is determined through coefficients for specular reflectivity R_S, diffuse reflectivity R_D, and absorption $A = 1 - R_S - R_D$. The coefficient R_D has been set to zero for all components based on results that will be discussed in Section 4.1.3. The SiPM surface was modelled by incorporating measurements performed within the collaboration of the angle-dependent

Parameter	Value	Component
Scintillation Wavelength; λ_{scint}	175 nm	LXe
LXe Absorption Length; λ_{abs}	20 m	LXe
LXe Rayleigh Scattering Length; λ_{scat}	30 cm	LXe
$\text{Al} + \text{MgF}_2$ Specular Reflectivity; $R_S(\text{Al} + \text{MgF}_2)$	80 %	FSRs and Cathode
Gold Specular Reflectivity; $R_S(\text{Au})$	20 %	Anode
Sapphire Specular Reflectivity; $R_S(\text{Al}_2\text{O}_3)$	5 %	Support Rods
Copper Specular Reflectivity; $R_S(\text{Cu})$	0 %	TPC Vessel
SiPM Reflectivity	[109, 126]	SiPM Modules

Table 4.1: Summary of optical properties of components used in the light simulations of the nEXO TPC using Chroma.

reflectance $R(\theta_i)$ and relative $\text{PDE}(\theta_i)$ as a function of angle in LXe [108,109]. Photons impinging on the SiPM surface at an angle θ_i will be reflected based on $R(\theta_i)$ and $(1-R(\theta_i))\cdot\text{PDE}(\theta_i)$ will be absorbed in the surface, accounting for the angle-dependent penetration depth and hence absorption of photons before reaching the avalanche region of the SiPM. The remainder of the photons will be detected.

4.1.3 Systematic Error on Photon Transport

The optical parameters that are used as an input for our light simulations are not precisely known and their uncertainty will propagate into a systematic error on our expected PTE. The speed improvements of `Chroma` relative to Geant4 allow us to perform an extensive list of simulations varying various parameters. Each parameter was varied independently while keeping all other parameters at their baseline value from Table 4.1.

- Because of nEXO's detector design with the SiPMs covering the barrel and being positioned behind the FSRs the use of highly reflective PTFE, commonly found in other LXe detector [72,121,122] to increase the PTE, is not possible. Therefore,

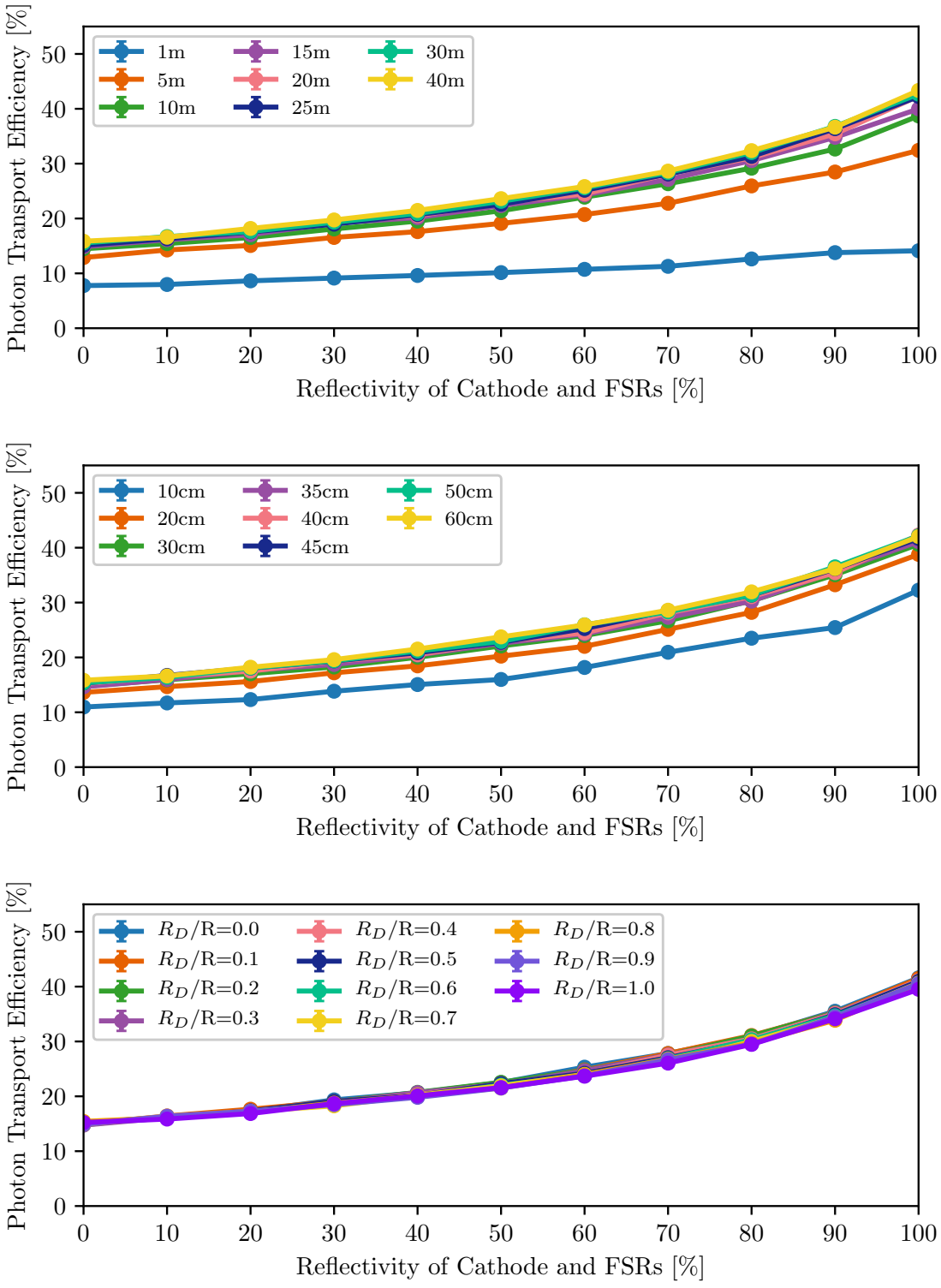

Figure 4.3: Shown are the estimated average PTE inside the FV from light simulations with varying input optical parameters. These studies include changes to the LXe absorption length λ_{abs} (top), LXe Rayleigh scattering length λ_{scat} (middle) and the fraction of diffuse reflection (bottom).

all optically passive components need to be made highly reflective since the intrinsic reflectivity at $\lambda_{\text{scint}} = 175\,\text{nm}$ of most metals and other special materials typically used in noble liquid detectors is very low. The specular reflectivity of the Al+MgF_2 coating that is currently envisioned to be applied to the FSRs and the cathode is expected to be at 80 % based on measurement of small-scale samples. In addition, optical simulations of the EXO-200 detector using `Chroma` and comparison with data also indicate a preference for a reflectivity of at least 80 % for Al+MgF_2. The panels in Figure 4.3 shows the average PTE inside the FV as a function of the specular reflectivity of the cathode and FSRs coated in Al+MgF_2, ranging from $0 - 100\,\%$. At our baseline value of 80 % we expect an average PTE of 33.3 %, exceeding the requirements for nEXO.

- The absorption length λ_{abs} starts playing a bigger role in an experiment as large as nEXO, compared to EXO-200, because photons can travel up to 1.3 m per reflection. Therefore, increasing the absorption length reduces the likelihood of a photon being absorbed by the LXe in a highly reflective detector geometry. λ_{abs} was varied from 10 m–40 m, as shown in the top panel in Figure 4.3, and was found to only significantly deteriorate the PTE for $\lambda_{\text{abs}} < 10\,\text{m}$ and resulted in only marginal improvement for absorption length larger than our current conservative expectation of $\lambda_{\text{abs}} = 20\,\text{m}$.

- Rayleigh scattering is the elastic scattering of the scintillation light off of the LXe. The scattered photons are emitted with an angular distribution of $I \propto 1 + \cos^2\theta$ which will randomize their direction and make their propagation more diffusive. The Rayleigh scattering length will impact the average travel distance of a photon with a longer distance for shorter λ_{scat}. Therefore, a short λ_{scat} in combination with a short λ_{abs} will significantly worsen the expected PTE. In the simulation λ_{scat} was varied from 10 cm–60 cm and the results shown in Figure 4.3 suggest

that only scattering lengths below $\lambda_{\text{scat}} < 20\,\text{cm}$ would have an impact on the PTE, which is outside its expected range of 30 cm–50 cm. Again, any increase beyond our estimated value of $\lambda_{\text{scat}} = 30\,\text{cm}$ appears to not significantly help improve the PTE.

- The reflections off of Al+MgF_2 coated surfaces are expected to be specular because of the smooth surface finish. However, given the size of the components on the order of meters that need to be coated compared to typical optical elements on the order $\mathcal{O}(\text{cm})$ surface non-uniformities and surface roughness might be unavoidable. A simple way to model this in the simulation is by increasing the diffuse component of the total reflectivity, which was changed from 0 %–100 %. As can be seen in the bottom panel in Figure 4.3, the diffusivity of the reflections on the cathode and FSRs have no significant impact on the PTE.

- As mentioned in Section 3.3 the nEXO requirements are currently met for two candidate SiPMs. The final decision on which SiPMs to use for nEXO will depend on a variety of factors, including their PDE, CA, radiopurity, availability of TSVs, and also their impact on the PTE through their surface reflectivity and absorption of photons. The angle-dependent reflectivity of both candidate SiPM, HPK VUV4 and FBK VUV-HD1, was measured in [108] and [109]. In addition, [108] also measured the angle-dependent relative PDE, i.e. the fraction of photons transmitted through the surface but absorbed in the layers above the avalanche region for HPK VUV4. In the case of the FBK VUV-HD1, one can estimate the relative PDE via

$$\begin{aligned} \text{PDE} &= (1 - R(\theta)) \cdot P_{\text{av}} \int_{d/\cos\theta}^{\infty} \frac{1}{\mu} e^{-l/\mu}\, \mathrm{d}l \\ &= (1 - R(\theta)) \cdot P_{\text{av}} e^{-\alpha/\cos\theta} \end{aligned} \tag{4.1}$$

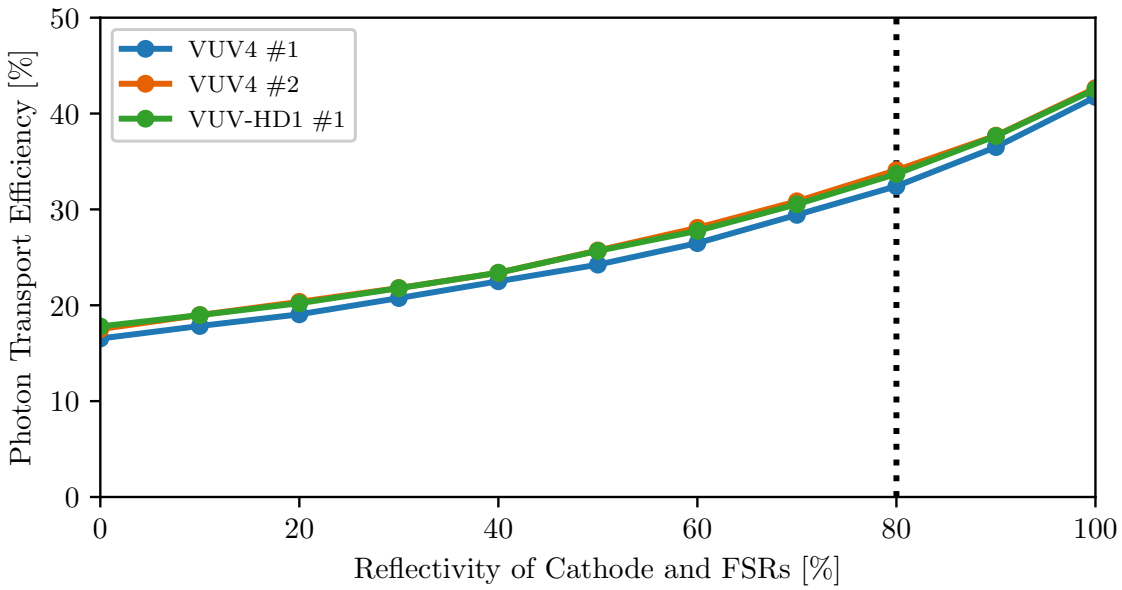

Figure 4.4: Spatially averaged PTE inside the fiducial volume as a function of the specular reflectivity of the cathode and the FSRs. The different curves are for different angle-dependent reflectivities of candidate SiPMs for nEXO. The reflectivities of VUV4 #1, VUV4 #2 and VUV-HD1 #1 were measured [108], [109] and [109], respectively.

with $\alpha = d/\mu$, d the thickness of the SiPM absorption layer, and μ the absorption length, which can be determined using PDE and reflectivity from vacuum measurements at $\theta = 0$ via

$$\alpha = -\ln\left(\frac{\mathrm{PDE}(\theta = 0)}{\epsilon_{\mathrm{geo}} - R(\theta = 0)}\right) \tag{4.2}$$

where one also needs to account for the geometric efficiency of the SiPM surface. The results for the PTE using different SiPMs and their corresponding angle-dependent reflectivities and relative PDE are shown in Figure 4.4 and suggest only marginal differences between the different devices. This is to be expected since their angle-averaged reflectivities, combining the data in [108, 109] and Figure 4.8, are very similar.

The above studies show that our prediction for the PTE of nEXO based on light simulations with `Chroma` is quite robust against small deviations from our optical

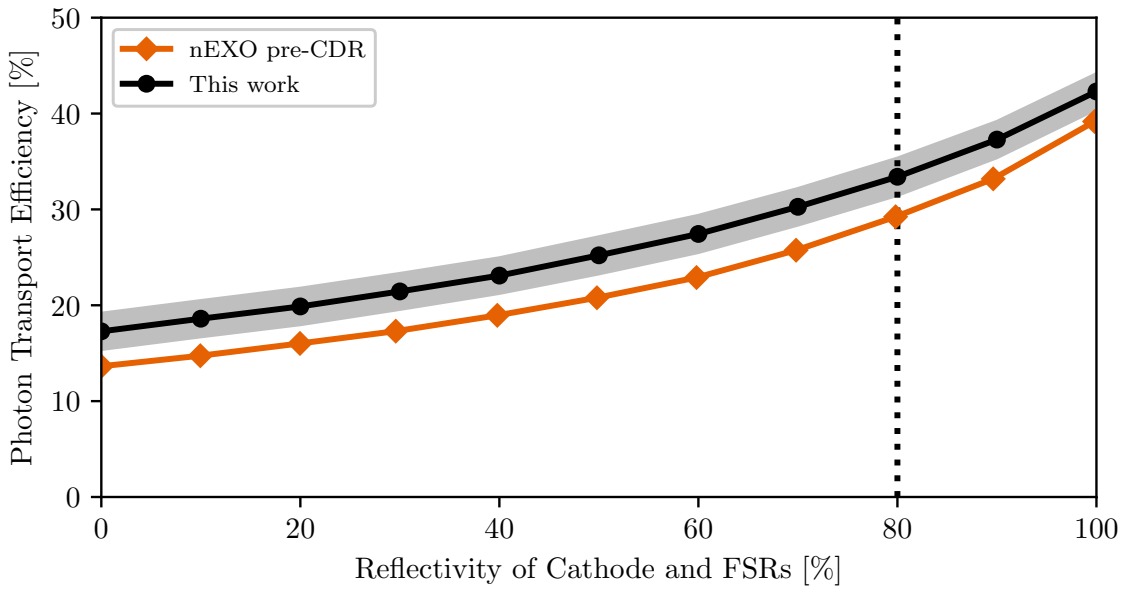

Figure 4.5: Spatially averaged PTE inside the fiducial volume as a function of the specular reflectivity of the cathode and the FSRs. The results from our current light simulations with updated optical parameters (black circles) are compared against results from previous simulations (orange diamonds) [85]. The grey band indicates a systematic error due to the choice of SiPMs and light simulators. Figure taken from [33].

parameters in Table 4.1 and show only significant differences for values outside the expected regions found in the literature. The current estimated average PTE is shown in Figure 4.5 where the grey systematic error band is comprised of the standard deviation across simulations in Figure 4.4 and the absolute difference in PTE between simulation results obtained with `Chroma` and Geant4, added in quadrature. For the current nEXO design reflectivity of 80 % for the cathode and FSRs, the expected average PTE is 33.3 %. The corresponding total light collection efficiency ϵ_p ranges from 6.1 %–9.5 % depending on the choice of SiPM and their respective difference in PDE [102, 105], which is at least a factor of two higher than the requirement of $\epsilon_p \geq 3\,\%$.

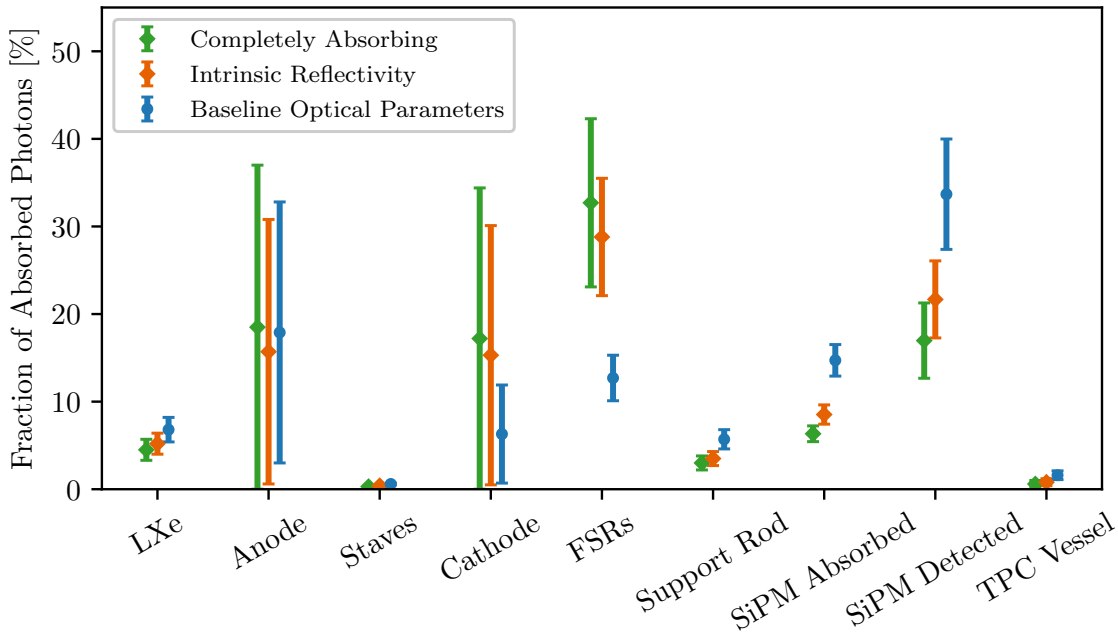

Figure 4.6: Shown is the percentage of photons absorbed by the components in the detector based on a Chroma simulation for three different sets of optical parameters: (1) Completely absorbing detector except for SiPMs in green (2) Intrinsic specular reflectivity of components at $\lambda_{\text{scint}} = 175\,\text{nm}$ in orange (3) Baseline optical parameters in blue. The two largest contributions to absorbed (and not detected) photons come from the anode and the FSRs. The error bars here represent the spread across the FV.

4.1.4 Photon Distribution

For ongoing R&D related to optimizing the light collection efficiency, it is useful to understand how often photons reflect off of surfaces and where they are being absorbed if not detected by the SiPMs. The former in combination with the absorption length λ_{abs} will determine the fraction of photons that are being absorbed in the LXe. The latter can help inform the detector design by either modifying the spacing of components or applying more reflective surface coatings.

Figure 4.6 shows the fraction of absorbed photons broken down by components in the TPC for three distinct cases. It is illustrative to consider the case in which all components except for the SiPMs are made perfectly absorbing at all wavelengths and angles, which is shown in green. As expected the FSRs situated directly in front of the

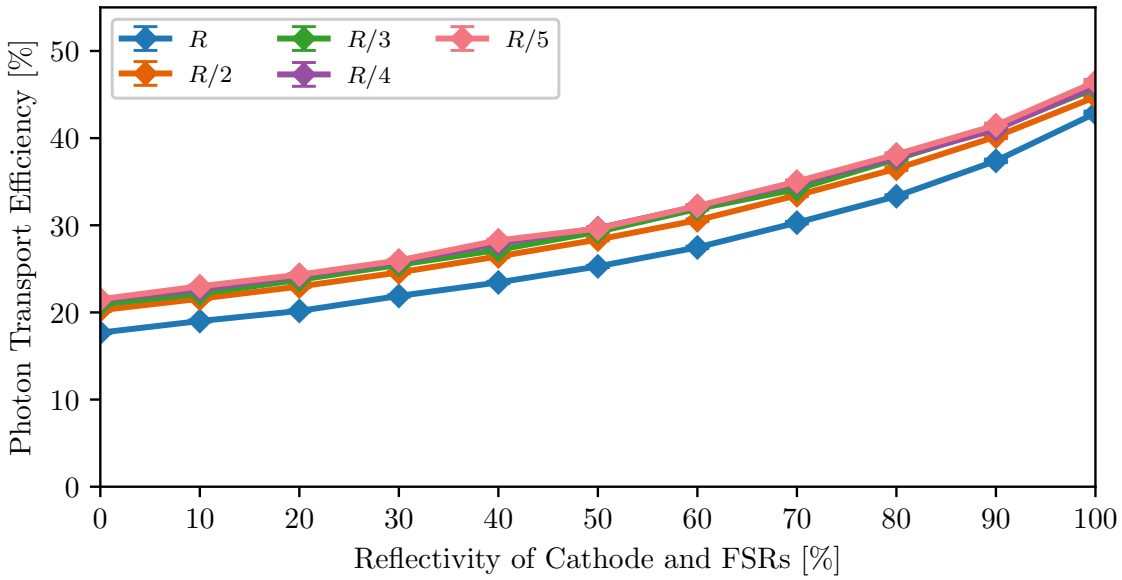

Figure 4.7: Spatially averaged PTE inside the fiducial volume as a function of the specular reflectivity of the cathode and the FSRs. The different curves are for different reduction factors of the surface reflectivity of the SiPM when applying an ARC.

SiPMs occupy a large solid angle and therefore absorb the largest fraction of photons that are not being detected (∼33 %). This worst-case and highly unphysical scenario would results in an average transport efficiency inside the FV of PTE = 17 % and therefore would not meet the nEXO specification of PTE > 20 %. Many materials, however, have non-zero intrinsic, albeit small, reflectivity at $\lambda_{\text{scint}} = 175\,\text{nm}$. This results in a reduced number of photons being absorbed by the passive components and increased the transport efficiency to PTE = 21.6 %. In this case, the FSRs are still absorbing most of the photons. Lastly, using the baseline optical parameters as defined in [33] and summarized in Table 4.1 the baseline transport efficiency is substantially improved to PTE = 33.3 %. This improvement stems from the increased reflectivity of the FSRs and cathode, which would be achieved through a highly reflective Al+MgF_2 coating. The high reflectivity of >80 % of this coating reduced the number of absorbed photons on FSRs by a factor of 2 making it only the 2nd most absorbing component after the anode.

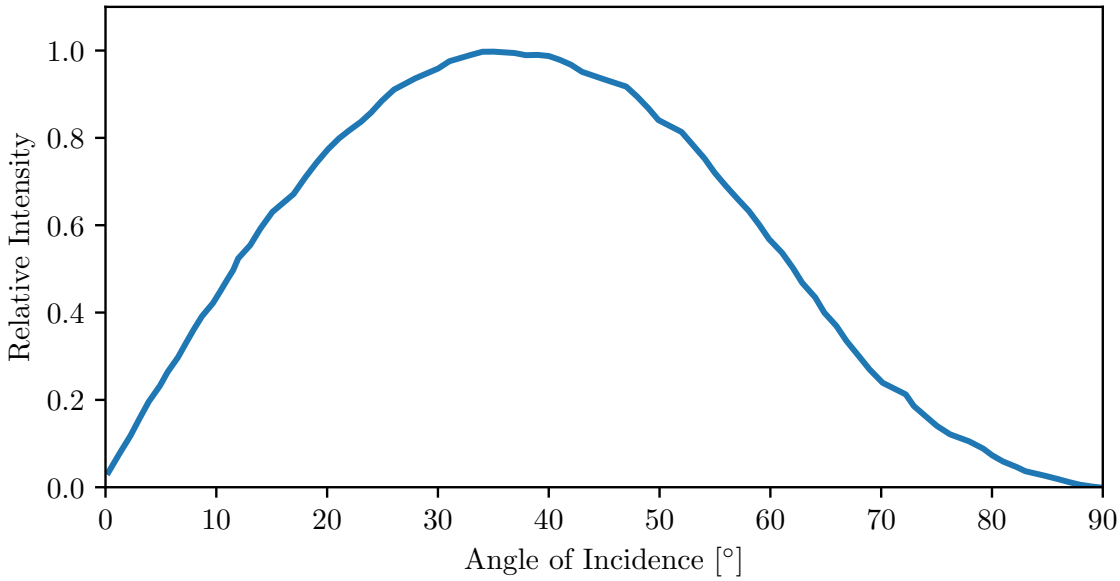

Figure 4.8: Angular distribution of detected photons in Chroma as they impinge on the SiPM surfaces.

As will be discussed in Section 4.1.5 the low specular reflectivity of the anode compared to the cathode and FSRs results in a non-uniform PTE inside the FV. The anode plane will be completely covered with the segmented charge readout tiles, that were discussed in Section 3.2, collecting the drifting ionization charge. It is currently not known how the deposition of a reflective coating would impact its charge collection capabilities. Due to the dielectric nature of the MgF_2 layer needed to passivate the Al-coating, an accumulation of charge on the surface is possible, deflecting the electric field lines and ultimately impacting the charge collection efficiency. The possibility of applying a VUV-reflective coating on the anode is still subject to ongoing R&D and a positive outcome would substantially improve the transport efficiency to PTE $\approx 41\,\%$.

While any photon that has been reflected off any SiPM surface still has a non-zero chance of being detected by another SiPM in the detector, reducing the reflectivity and hence increasing the direct photon detection might help improve the PTE. In [126] and [109] the angle-dependent specular reflectivity of HPK VUV4 and FBK VUV-HD1 SiPMs was measured and was found to have an angle-averaged reflectivity of

≈25 %. The results for the impact of a reduced SiPM surface reflectivity by scaling the measured angle-dependent reflectivity curves are shown in Figure 4.7 and indicate that an improvement by about 10 %–15 % can be expected. Reducing the reflectivity of the SiPM requires coating them with an Anti-reflective Coating (ARC) to reduce the mismatch in indices of refraction between LXe ($n = 1.57 - 1.72$ [125, 127] with $\langle n \rangle = 1.69$ [128]) and SiO_2 ($n = 1.55 - 1.69$ [129] with $\langle n \rangle = 1.6$ [129]). The expected angular distribution of photons on the SiPM surface is an important input parameter when designing such an ARC and it is shown in Figure 4.8.

4.1.5 Lightmap

In the process of reconstructing the energy of an event, the number of detected photons needs to be converted into an estimate of the number of initially produced photons. Instead of performing on-the-fly computationally expensive photon transport simulations to reconstruct the light energy, a pre-generated lightmap is used, which contains the information about the PTE as a function of position inside the detector. This lightmap for nEXO is shown in Figure 4.9 and was generated by simulating a total of 0.5×10^{12} photons, grouped into 5×10^7 events uniformly distributed throughout the entire xenon volume. The 10000 photons in each event were emitted isotropically and uniformly in all directions from a common event location. Due to the cylindrical symmetry of the nEXO detector geometry, the number of detected photons in each event was filled into a 2D histogram with 0.5 mm bin size in both the radial and z-position dimensions. The baseline optical parameters in Table 4.1 were used for generating this lightmap.

From the lightmap in Figure 4.9, it is apparent that the PTE is a smooth function of position in the FV but has an asymmetry with respect to the z-axis which comes from the significantly lower reflectivity of the anode at 20 % compared to the highly reflective cathode with 80 % reflectivity. This z-position dependence is quantified in

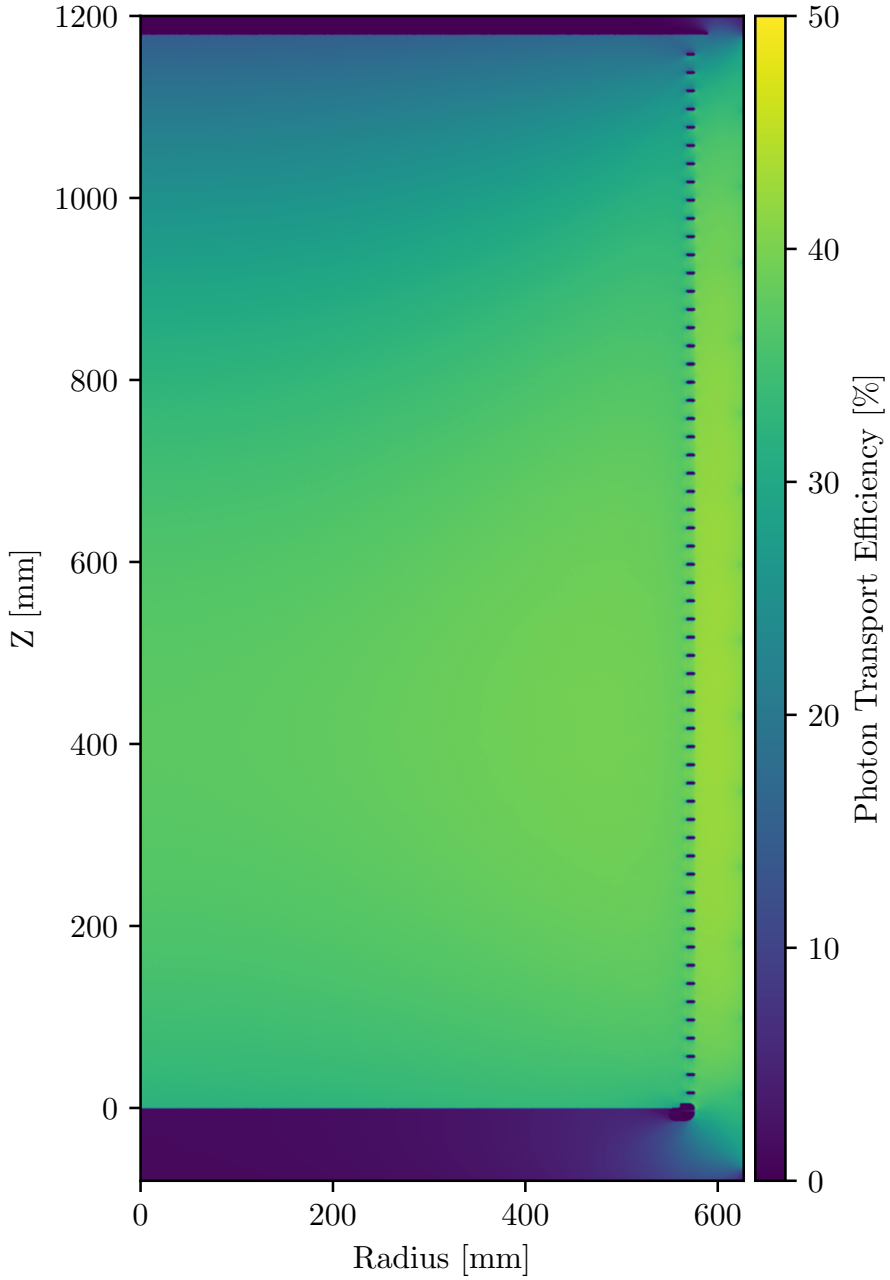

Figure 4.9: Lightmap of the nEXO detector showing the probability of photons reaching the avalanche region of the SiPMs, i.e., the PTE as a function of the radial, r, and longitudinal, z, positions in the detector. TPC components such as the FSRs, the anode, and the cathode are visible due to their high opacity.

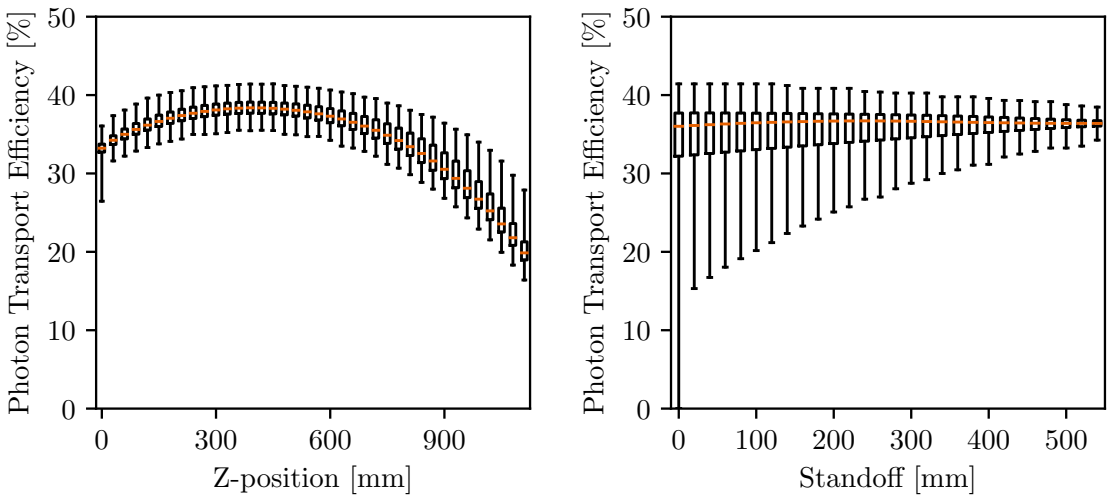

Figure 4.10: Boxplot of PTE as a function of z-position (left) and standoff distance (right). The box comprises data within the 25 % and 75 % quantile around the median which is shown as an orange line inside the box. The whiskers ("error bars") extend over the full range of data in that region. The median PTE is strongly z-dependent whereas the median PTE has no standoff dependence but has a significantly larger spread as indicated by the whiskers.

the left plot in Figure 4.10 with a boxplot, where the PTE ranges from 19 %–38 % from top to bottom. In contrast, there is no dependence of the median PTE as a function of standoff distance as shown in the right plot in Figure 4.10.

4.1.6 Alternative Designs

The nEXO baseline design aims to fully cover the 4.5 m^2 area around the cylindrical barrel of the TPC with SiPMs (see Section 3.3). This is a significant deviation from the design of EXO-200 [72] and other large LXe TPCs [121, 130], that placed the photo-detectors on the flat sides of the TPC and made use of PTFE reflectors around the barrel. Since nEXO plans to employ opaque charge tile modules at the anode (instead of crossed wires) no photo-detectors can be positioned behind.

Light transport simulations were performed to evaluate the tradeoff between the three different designs:

1. The SiPMs were placed only on one of the flat sides of the TPC behind a

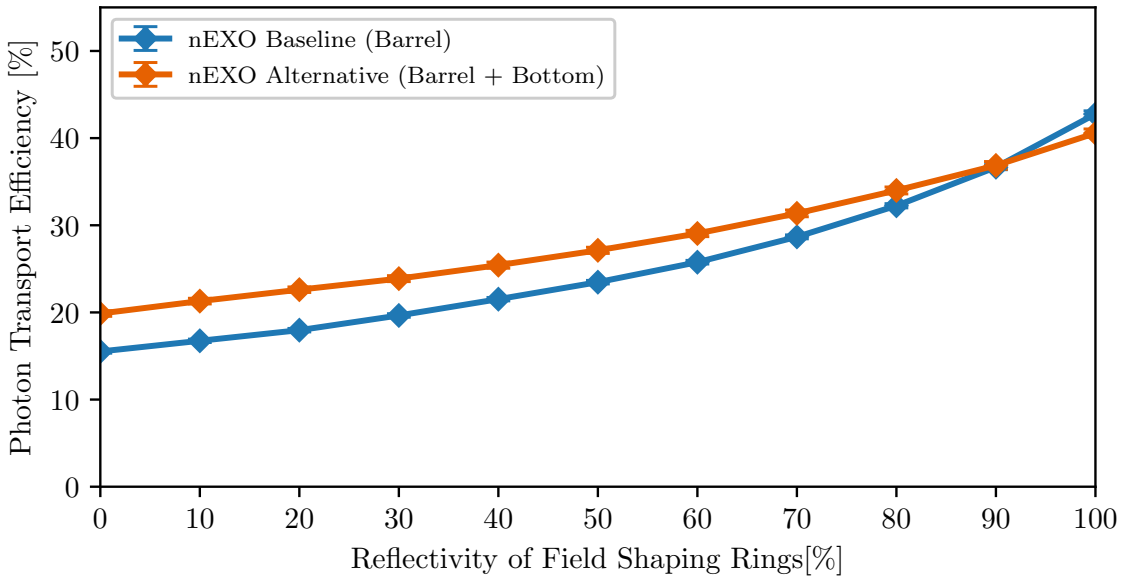

Figure 4.11: Angular distribution of detected photons in Chroma as they impinge on the SiPM surfaces.

transparent (or meshed) cathode and the inside of the FSRs was covered with cylindrical PTFE reflectors

2. The SiPMs are covering the barrel of the TPC behind the FSRs which is the nEXO baseline design

3. The SiPMs were placed only on one of the flat sides of the TPC behind a transparent (or meshed) cathode in addition to SiPM covering the barrel of the TPC behind the FSRs

A substantial improvement in PTE from ∼10 % to 33.3 % is achieved with design 2 over design 1 and only a small relative increase of 10 % is gained by going with design 3. Figure 4.11 shows the PTE of designs 2 and 3 as a function of FSR and cathode reflectivity.

These simulations favor design 2 due to the sufficiently larger expected PTE, exceeding the requirements for achieving nEXO's energy resolution goal. The marginally higher PTE with design 3 resulting in only a small improvement in the energy resolu-

tion and possible background rejection is likely to be outweighed by the additional engineering complexity and increased instrumented photodetector area.

4.1.7 Channel Size and Dynamic Range

The current baseline for the size of a SiPM readout channel is 6 cm^2, connecting 3 1 cm^2 SiPMs in series and 2 such groups in parallel. The optimal SiPM channel size depends on a variety of electronics and performance requirements. The electronics noise scales with the parasitic capacitance of the SiPM and grows as more SiPMs are connected in parallel. For both HPK and FBK the capacitance of the SiPMs is low enough to achieve the 0.1 SPE resolution goal [102, 105] for a channel size of 6 cm^2.

The performance requirements require enough dynamic range in the light readout ASIC to maintain single-photon resolution within the FV as well as staying below saturation for events close to the edge of the field cage during low-background data taking. A typical $0\nu\beta\beta$ event emits $\sim$ 90000 photons at an electric field of 400 $\mathrm{V\,cm^{-1}}$ [80], which after applying a PTE and PDE of 33.3 % and $\sim$20 %, respectively, results in $\sim$ 5500 detected photons across 7600 readout channels. This corresponds to an average number of detected photons of 1 per readout channel and requires good single photons resolution to not degrade the light energy measurement.

In addition, a sufficiently granular photon readout is needed to use the light information for position reconstruction of the events inside the TPC, which might be especially useful for tagging time-coincident surface backgrounds in regions with poor or compromised charge collection and reconstruction. The largest contribution to the background budget in nEXO currently is the 2448 keV γ-decay from ^{214}Bi [33], which comes from charged daughters of ^{222}Rn drifting towards the negatively biased cathode and FSRs and plating out on their surfaces. The rejection of this background relies on the time-coincident tagging of the α-decay of the ^{214}Po daughter with a half-life of 164 µs, which is $\sim$100 % efficient for events in the fiducial volume. Since on the

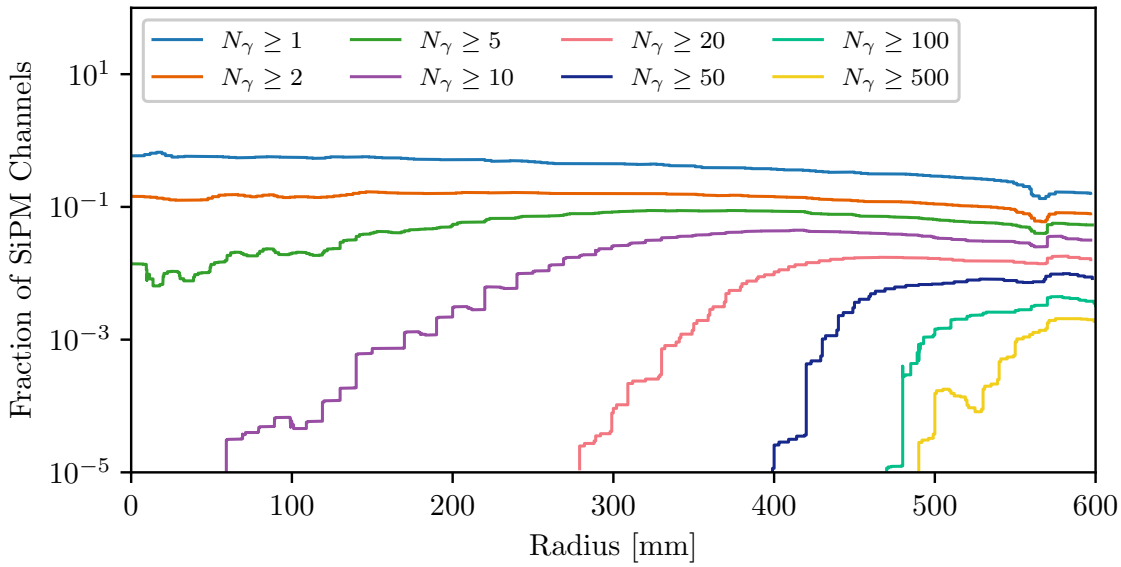

Figure 4.12: Fraction of SiPM readout channels that detected a certain number of photons as a function of radius in the TPC for a 3.3 MeV β-event distributed uniformly inside the fiducial volume, for 6 cm^2 SiPM channels. The dip at ~560 mm occurs for events in between the field shaping rings for which a large solid angle is blocked by FSRs themselves.

surface, the α-particle has 50 % chance of being emitted into the bulk of the cathode or FSRs the tagging efficiency correspondingly drops to ~50 % on these surfaces [33].

To determine the upper bound of the dynamic range light simulations were performed using the baseline optical parameters for a 3.3 MeV β-event, which corresponds to the Q-value of the β-decay of ^{214}Bi, uniformly distributed inside the field cage. The detected photons were grouped into channels of various sizes ranging from single devices with a surface area from 36 mm^2 up to 80 cm^2. The channel occupancy, i.e. the fraction SiPM readout channels that were triggered as a function of radial position in the detector and for the various channel sizes was determined and indicates that for any channel size larger than 6 cm^2 no saturation effects are expected with a dynamic range of 100 SPE for the SiPM readout ASIC. Figure 4.12 shows the result in the case of a 6 cm^2 where less than 0.1 % of channels registered 100 photons or more within the field cage. Therefore, this configuration provides enough segmentation to produce

sufficiently low occupancy such that the readout time doesn't prevent the measurement of the time-coincident ^{214}Po α-decay. This indicates that the upper limit on channel size from noise considerations is already sufficiently small to avoid additional dynamic range constraints. In addition, on average the spatial extent of the light pattern on the SiPMs for such events is $\gg 6\,\mathrm{cm}^2$. Therefore, a more granular segmentation of the SiPMs is not expected to improve a light-only position reconstruction of energy deposits.

4.1.8 Conclusion and Outlook

Light simulations are a crucial part of designing next-generation noble liquid experiments and the rise of advanced simulation techniques such as GPU-accelerated photon transport simulations allow for a significantly faster turnaround and for probing a significantly larger parameter space of optical properties to optimize the detector design. The light simulation framework that was built for nEXO and is based on the `Chroma` software package allowed studying a variety of aspects related to the light response of nEXO. In its current design, nEXO will exceed its photon transport and photon detection requirements and represents a significant improvement over EXO-200.

Nevertheless, the realism of the simulation can be further improved by adding the following details:

- Full emission spectrum of the xenon scintillation light
- Angle-dependent reflectivity of all detector components
- Inclusion of external cross-talk photons emitted by the SiPMs
- Adding surface sub-structures for SiPM modules

4.2 Charge Transport and Liquid Xenon Purity

LXe TPCs such as EXO-200 [72], XENON100 [131], XENON1T [132], XENONnT [122], LUX [133], LZ [121, 134], RED-100 [135], PandaX [136], PandaX-4T [137] and nEXO [33,85] require sufficient LXe purity to drift the ionization charge from the event location to the charge collection plane without significant losses to charge collection. For n_q initially produced electrons at $t = 0$ the number of collected electrons after some drift time $t > 0$ will be given by

$$n_q(t) = n_q(0) \cdot e^{-t/\tau_e} \tag{4.3}$$

where τ_e is the electron lifetime and can generally be expressed via [138]

$$\tau_e = \sum_I \frac{1}{N_I K_I} \tag{4.4}$$

with N_I and K_I being the concentration of electronegative impurities in the LXe and the electron attachment rate of type I, respectively.

The above detectors observed electron lifetimes from 0.5 ms–20 ms using various purification techniques. The source of the residual electronegative impurities that limit the lifetime in these detectors is an open question. One possible source of electronegative impurities could be the outgassing of atmospheric gases trapped inside plastics used in the detector. Other possibilities include small leaks to the atmosphere in the plumbing downstream of the purification system, desorption of mono-layers of impurities from the stainless steel surfaces in the plumbing, and possibly plastics dissolved by the LXe itself.

The work in this section aims to develop a model for the outgassing of electronegative impurities in nEXO and to model the effect on the electron lifetime, for which nEXO's goal is $\tau_e = 10$ ms [85]. Such a predictive model for outgassing and LXe purity

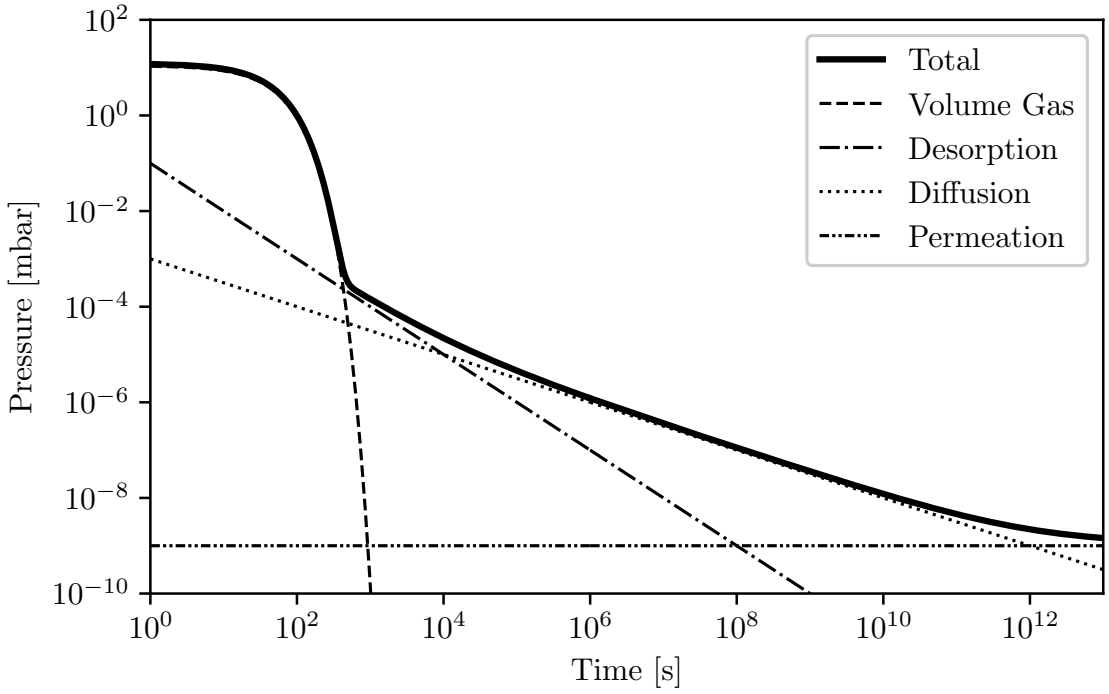

Figure 4.13: Pressure limiting processes while pumping on a vacuum system. The plotted dependence qualitatively captures processes relevant to LXe detectors, although the quantitative outgassing of a given system depends on materials, geometry, and other system parameters. The plot was remade after [139].

can be used to qualify candidate materials for the detector construction and assess their contribution to the overall impurity budget to achieve a certain target τ_e.

4.2.1 Modelling Outgassing of Impurities

The ultimate pressure achievable in a high vacuum system is dependent on the outgassing processes of all the materials inside and the pumping speed. In LXe detectors, these same processes are expected to lead to the continual introduction of impurities into the LXe. Sources of outgassing can be divided into these categories:

- Vaporization:

  Parts of the material itself is being released from the surface.

- Desorption:

Previously adsorbed molecules on surfaces are released.

- Diffusion:

  Molecules that are dissolved in the bulk of materials are released.

- Permeation:

  Molecules that diffuse from the outside through the bulk are released.

While the last process of permeation is typically only relevant for ultra-high vacuum systems below 1×10^{-10} mbar and can be neglected in our case, desorption and diffusion play an important role. Vaporization will be omitted in the discussion below since it is typically not important for metallic surfaces or the "low-outgassing" plastics and adhesives considered for use in nEXO. Chemical dissolution of the material surface due to the solvent properties of LXe will be considered in Section 4.2.1.4. Figure 4.13 shows the remaining pressure in a typical stainless steel vacuum system as a function of time while pumping on it and indicates qualitatively which outgassing processes dominate at each time scale.

4.2.1.1 Bulk Diffusion

At long timescales relevant for rare event search experiments based on LXe one of the most important processes for modeling the outgassing of plastics is the diffusion of impurities inside the material and the subsequent desorption of impurities at the boundary surface. The diffusion process is governed by the diffusion equation, also called Fick's 2nd law,

$$\frac{\partial c}{\partial t} = D\nabla^2 c \tag{4.5}$$

where c is the gas concentration and D is the diffusion constant specific to a particular gas species in a particular material and needs to be determined experimentally.

We can solve this differential equation for a finite slab of thickness d with the following initial and boundary conditions for the gas concentration

$$c = c_0 \quad \text{for} \quad 0 \leq x \leq d \quad \text{at} \quad t = 0 \tag{4.6}$$

$$c = 0 \quad \text{for} \quad x = 0 \quad \text{and} \quad x = d \quad \text{at} \quad t > 0 \tag{4.7}$$

A solution to this problem with the above conditions is given by [140]

$$c(x,t) = c_0 \frac{4}{\pi} \sum_0^\infty \frac{1}{2n+1} \sin\left(\frac{\pi(2n+1)x}{d}\right) \cdot \exp\left\{-\left(\frac{\pi(2n+1)}{d}\right)^2 \cdot Dt\right\} \tag{4.8}$$

whereas the solution for An infinitely long cylinder of radius $r = R$ with boundary conditions

$$c(r = R, t) = 0 \tag{4.9}$$

$$c(r, t = 0) = c_0 (r < R) \tag{4.10}$$

$$\frac{\partial c}{\partial r}|_{r=0} = 0 \tag{4.11}$$

can be written as

$$c(r,t) = 2c_0 \sum_{n=1}^\infty e^{-\alpha_n^2 Dt/R^2} \frac{J_0(\alpha_n r/R)}{\alpha_n J_1(\alpha_n)} \tag{4.12}$$

where J_n are Bessel functions of the first kind and α_n are the nth zero of J_0. To get the gas flow rate J of particles out of the bulk material one can plug this expression into Fick's 1st law to get

$$J = D\left(\frac{\partial c(x,t)}{\partial x}\right)_{x=0} \tag{4.13}$$

$$= \frac{4c_0 D}{d} \sum_0^\infty \exp\left\{-\left(\frac{\pi(2n+1)}{d}\right)^2 \cdot Dt\right\} \tag{4.14}$$

In the limit of short times, t this expression can be reduced to

$$J = c_0 \sqrt{\frac{D}{t}} \tag{4.15}$$

whereas in the limit of long times we get the following simplification

$$J = \frac{4c_0 D}{d} \exp\left\{ -\left(\frac{\pi}{d}\right)^2 \cdot Dt \right\} \tag{4.16}$$

where the first term in the infinite sum is used as an approximation. In the case of the cylinder with radius R, the outgassing flux is given by

$$J = \frac{2c_0 D}{R} \sum_{n=1}^{\infty} e^{-\alpha_n^2 Dt/R^2} \frac{J_1(\alpha_n r/R)}{J_1(\alpha_n)} \tag{4.17}$$

The outgassing process is expected to be highly temperature dependent since the diffusion coefficient is temperature-dependent and given by an Arrhenius-type relation

$$D(T) = D_0 \cdot \exp\left(-\frac{E_a}{k_B T} \right) \tag{4.18}$$

where D_0 is the diffusion constant at infinite temperature and E_a is the material-solute specific activation energy. Single activation energies are typically found to describe the diffusion process well over many orders of magnitude in temperature. Due to the temperature dependence of the diffusion process, pumping on a system at an elevated temperature is more efficient for removing gases trapped within the material. The temperature, however, should be chosen in compliance with the maximally allowed temperature for all components in the system.

The remaining concentration of impurities inside the bulk and the gas flow rate out of the bulk has a strong exponential dependence on the thickness or radius of the

sample

$$c(t) \sim \exp\left(-\frac{D \cdot t}{d^2}\right) \tag{4.19}$$

$$\sim \exp\left(-\frac{D \cdot t}{R^2}\right) \tag{4.20}$$

which results in a significantly faster depletion of impurities that are trapped in the bulk material if the material is thinner. This exponential dependence on thickness will be important in the model for impurities developed in later sections as thin plastics ($\lesssim 1$ mm) are quickly degassed, while thicker plastics can dominate the outgassing rate at longer times.

Typically, gas quantities are given in units of pressure times volume. However, through the ideal gas law

$$pV = Nk_{\mathrm{B}}T \tag{4.21}$$

this can be converted to the number of individual gas molecules or atoms, N.

4.2.1.2 Desorption from Stainless Steel Surfaces

The outgassing of impurities via desorption from metallic surfaces is not an intrinsic property of the material but depends on various factors, including surface finish, whether it was baked and for how long, previous pump-out time, chemical treatment, etc. Hence, there is a big spread in the literature on the desorption rate of water from stainless steel as can be seen in figure 4.14. Nevertheless, most gases adsorbed on metals follow a simple outgassing relationship

$$q(t) = \frac{q_0}{t^{\alpha}} \tag{4.22}$$

where $\alpha \in [0.7, 2]$ and $\sim$1 being the most frequent value observed [141]. It should be stressed that Equation 4.22 is only an empirically found relationship that depends on the gas-material-combination. The publications from which this plot was generated usually only contain data points at a few specific times and the definition of $t = 0$ might not be identical among all authors. A detailed microscopic model for this behavior is still lacking. However, there are attempts to justify this functional form by assuming that the metal surface has different adsorption sites where each has slightly different occupation energies. The outgassing rate from each site is generally given by [142, 143]

$$J = \frac{q(t)}{\tau} = \frac{q_0}{\tau} \exp\left(-\frac{t}{\tau}\right) \tag{4.23}$$

$$\tau = \tau_0 \exp\left(\frac{E}{k_B T}\right) \tag{4.24}$$

where q_0 is the number of initially adsorbed impurities per unit area, τ the residence time of an impurity at an absorption site and typically $\tau_0 = 10^{-13}\,\mathrm{s}$ [139]. The total outgassing from desorption from all possible sites on a surface then follows $J \sim t^{-1}$ as shown in figure 4.15.

4.2.1.3 Lessons from EXO-200

The EXO-200 detector has constantly seen electron lifetimes on the order of a few ms, which until a few years ago was the best among all other large LXe detectors. For instance, the average electron lifetime in Phase II of EXO-200 was about 3 ms as can be seen in figure 4.16. It is not well understood though what limited the purity of the LXe in EXO-200.

Assumptions According to [138] the electron attachment rate k_I to an impurity I at a drift field of $567\,\mathrm{V\,m^{-1}}$ is $k_S = 9.2 \times 10^{10}\,\mathrm{L\,mol^{-1}\,s^{-1}}$. For a steady-state electron

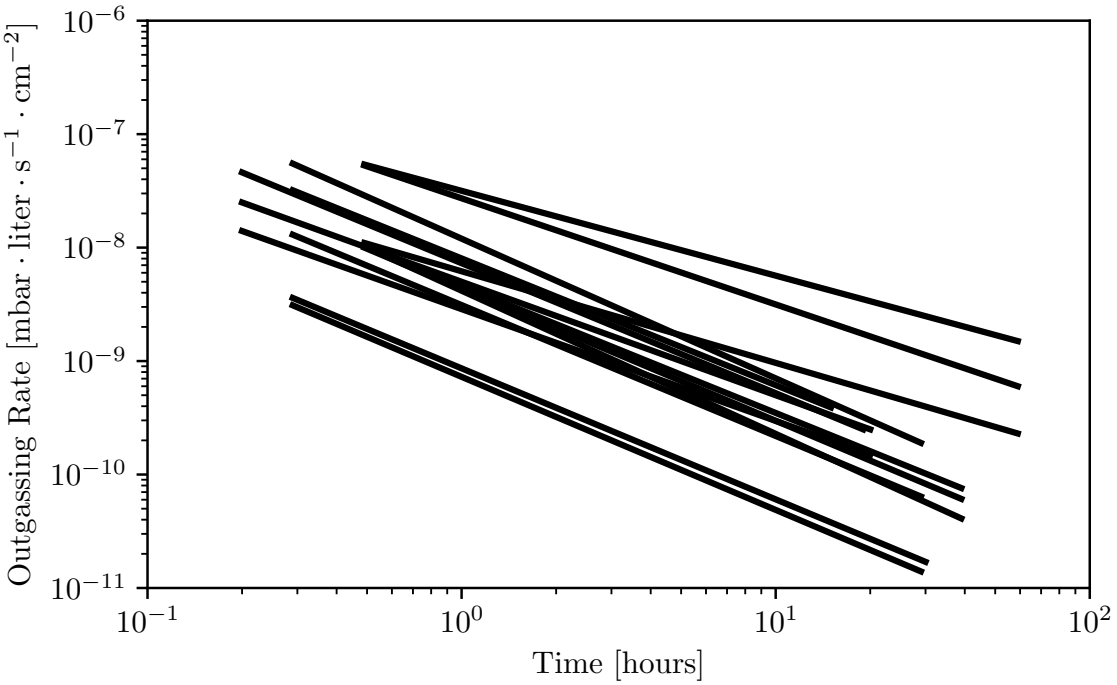

Figure 4.14: Outgassing rate due to desorption of water from a stainless steel surface as a function of pumping time. Shown are curves for various surface finishes and treatments. Even though there is a big spread in the initial value all curves roughly follow a t^{-1} relationship. Plot remade after [141].

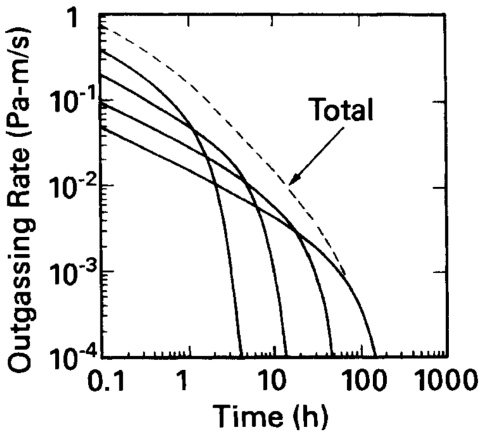

Figure 4.15: Total outgassing rate from desorption of four different desorption sites with different activation energies. The rate of each desorption site follows an exponential, but the sum of all rates follows the empirically found t^{-1} relationship. Figure from [139].

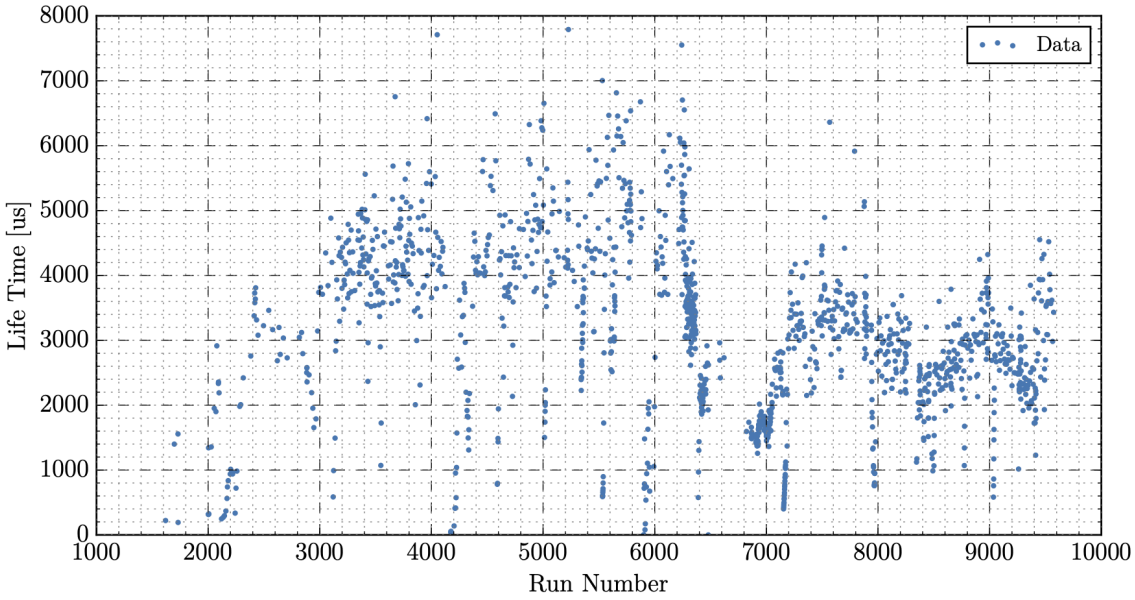

Figure 4.16: The average lifetime in the EXO-200 detector for each run in Phase I and Phase II. One can notice a systematic decrease in electron lifetime in Phase II (starting after run 6800). The detector did not only receive some electronics upgrades during the shutdown but the cartridges in the purifiers were renewed as well.

lifetime of

$$\tau = \frac{1}{k_I \cdot [I]} = 3\,\mathrm{ms} \tag{4.25}$$

we need to have a constant concentration of impurities at the level of

$$[I] = \frac{1}{\tau \cdot k_I} = \frac{1}{3 \times 10^{-3}\,\mathrm{s} \cdot 9.2 \times 10^{10}\,\mathrm{L\,mol^{-1}\,s^{-1}}} = 3.6 \times 10^{-9}\,\mathrm{mol\,L^{-1}} \tag{4.26}$$

converting this into ppb we get

$$[I] \quad = \quad \frac{3.6 \times 10^{-9}\,\mathrm{mol\,L^{-1}} \cdot 136\,\mathrm{g\,mol^{-1}}}{3000\,\mathrm{g\,L^{-1}}} = 0.16\,\mathrm{ppb} \tag{4.27}$$

For the whole detector, this corresponds at equilibrium to a constant leak rate into the detector of

$$\begin{aligned} J &= \frac{200\,\mathrm{kg}}{136\,\mathrm{g\,mol^{-1}}} \cdot 6.023 \times 10^{23}\,\mathrm{mol^{-1}} \cdot \frac{0.16\,\mathrm{ppb}}{3600 \cdot 24}\mathrm{s^{-1}} \cdot k_B \cdot 300\,\mathrm{K} \cdot H_{\mathrm{O_2,LXe}} \\ &\approx 4 \times 10^{-6}\,\mathrm{mbar\,L\,s^{-1}} \end{aligned} \tag{4.28}$$

This calculation is based on the assumption that the number of impurities added to the detector is the same as the number of impurities taken out by the purifier. The recirculation rate in EXO-200 was 15 SLPM, which results in a complete recirculation of all the xenon in about 1 d. We assume that the impurities are in equilibrium during the recirculation, so that the ratio of concentrations in the gas and liquid phase is given by the Henry's coefficient for O_2 in LXe ($H_{\mathrm{O_2,LXe}} = \frac{c_{\mathrm{O_2,gas}}}{c_{\mathrm{O_2,liquid}}} = 59 \pm 14$, see Section 4.2.4.4 for details). It should be noted that there is some uncertainty in this assumption of equilibrium, i.e. if the impurities in the liquid phase cannot diffuse into the gas phase quickly enough to support this concentration ratio, then a smaller leak rate would be consistent with the measured lifetime.

Outgassing from PTFE and Acrylic The EXO-200 experiment used thin PTFE sheets covering the barrel of the detector to increase the light collection efficiency. The PTFE reflector was 1.5 mm thick and had an inner radius of 18.3 cm, making the whole structure weigh about 693 g [72]. Before filling the EXO-200 detector with LXe, the TPC was first pumped on for 1–2 days and afterward filled with room temperature gaseous xenon. The xenon gas was recirculated for about one week. For these calculations, a pumping time of 1 day at a temperature of 20 °C and xenon re-circulation time of 1 day at 20 °C are used. Using these numbers together with values for the solubility of O_2 reported in [121] the outgassing rate as a function of time can be calculated. This is shown in Figure 4.17 together with the steady-state outgassing rate required to maintain a constant 3 ms as shown in Equation 4.28.

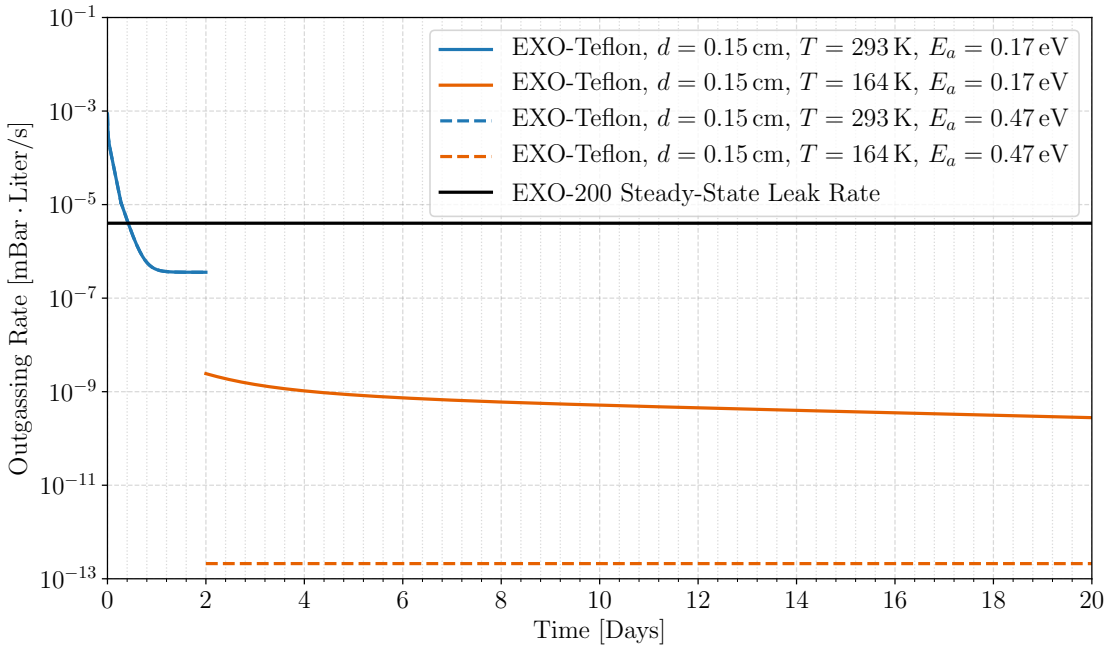

Figure 4.17: Calculated outgassing rate as a function of time for the PTFE in EXO-200.

The calculations show that the 1.5 mm thin PTFE reflectors would have outgassed sufficiently fast such that after just a couple of days its outgassing rate would be negligible. The conclusion, based on the numbers and model assumed above, is that the source of impurities that is required to explain the measured electron lifetime in EXO-200 is likely to be something other than atmospheric gases absorbed into the thin PTFE.

However, thicker plastics are more problematic and are not expected to be fully outgassed during the initial pumping stages. We currently assume that the effective surface area of all acrylic pieces in EXO-200 is the same as PTFE and that the average thickness is 2 cm, which is an overestimate but simplifies the calculations. Therefore, the real outgassing rate would have been smaller compared to what is shown in Figure 4.18.

The above calculations represent conservative assumptions for the outgassing of cold plastics in the LXe. In reality, all components wetted by the LXe in EXO-200

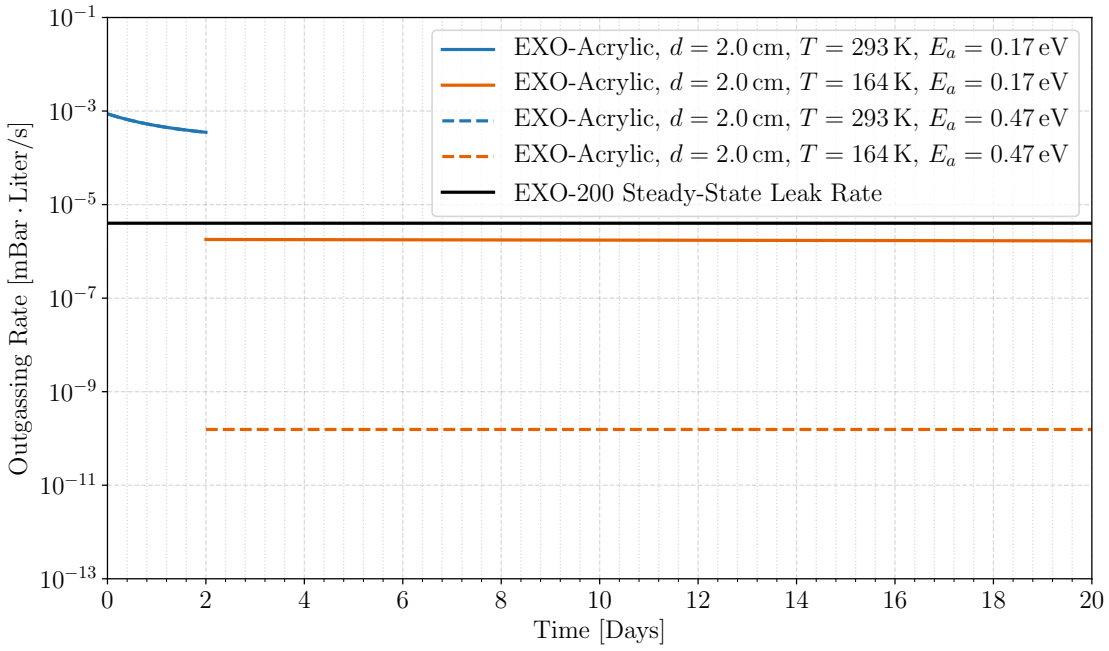

Figure 4.18: Calculated outgassing rate as a function of time for the acrylic in EXO-200.

were stored under a "dry-nitrogen" purge for 6 months before installation [72]. This purge would be expected to degas the majority of atmospheric oxygen from the plastics before installation in the detector. However, even ignoring such purging and assuming the worst possible case for the diffusion of impurities out of the bulk of EXO-200 plastics, the PTFE cannot explain the inferred leak rate and the thicker acrylic pieces also appear to be insufficient (for the expected temperature dependence of the diffusion process).

Outgassing from Stainless Steel Plumbing Most of the plumbing in EXO-200 is made of stainless steel and only about a third of it is downstream of the purifier. A typical value in the literature for the outgassing rate of H_2O from an unbaked stainless steel surface that has been pumped on for 1 h is about $J = 1 \times 10^{-8}\,\mathrm{mbar\,L\,s^{-1}\,cm^{-2}}$ [144]. Since O_2 outgassing from stainless steel is typically lower than H_2O, we assume that this value is the same for oxygen as an upper limit and a

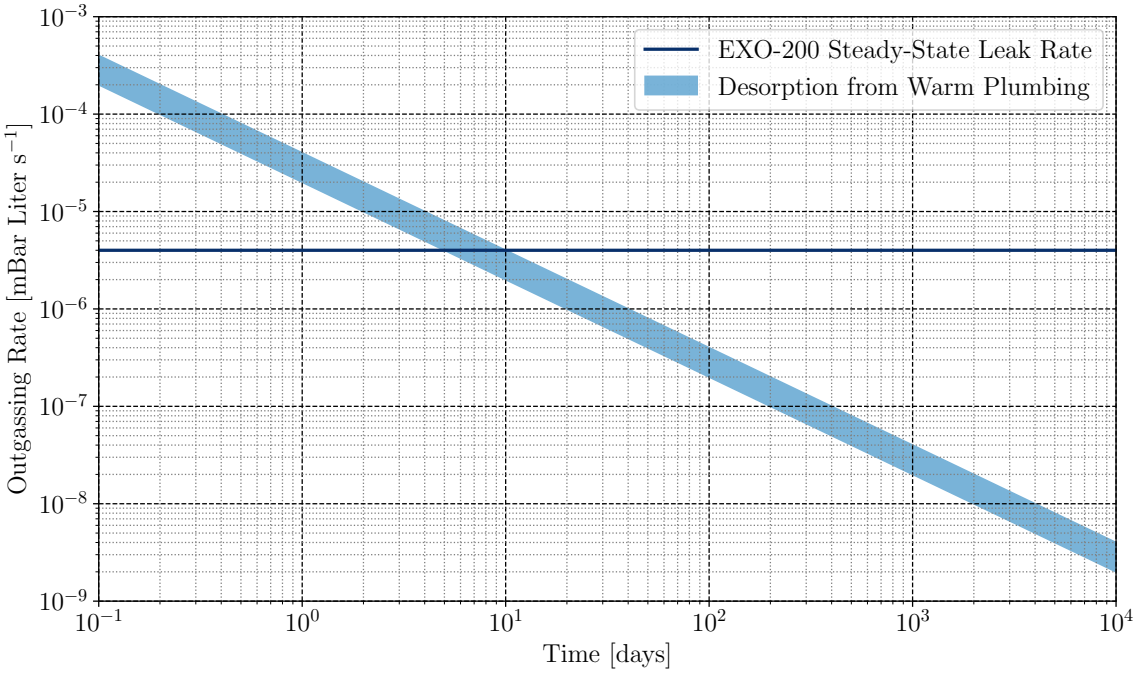

Figure 4.19: Outgassing rate of mono-layers of impurities on stainless steel walls as a function of pumping time in EXO-200. The light blue band shows the outgassing from warm plumbing with a surface area of 2000 cm^2 to 4000 cm^2 and the dark blue solid line is the steady state leak rate derived earlier.

conservative estimate. As discussed in section 4.2.1.2 the total outgassing rate was empirically found to be best described by

$$J_{\text{tot}} \quad = \quad J \cdot A_{\text{tot}} \cdot \frac{t_0}{t} \tag{4.29}$$

with $t_0 = 1\,\text{h}$. Figure 4.19 shows the outgassing rate as a function of pumping time. An order of magnitude estimate of the total surface area of warm plumbing downstream the purifier gives $A_{\text{tot}} = 2000\,\text{cm}^2 - 4000\,\text{cm}^2$ which requires a pumping time of about 10 d to achieve an outgassing rate of below $6.8 \times 10^{-8}\,\text{mbar}\,\text{L}\,\text{s}^{-1}$. Depending on the stainless steel the outgassing rate may vary as shown in Figure 4.14.

Figure 4.20 shows a correlation between anomalously low electron lifetimes and the pumping of vacuum spaces, i.e. the xenon return and recovering lines, which might change the pressure in the system and could cause the liquid levels to change. This

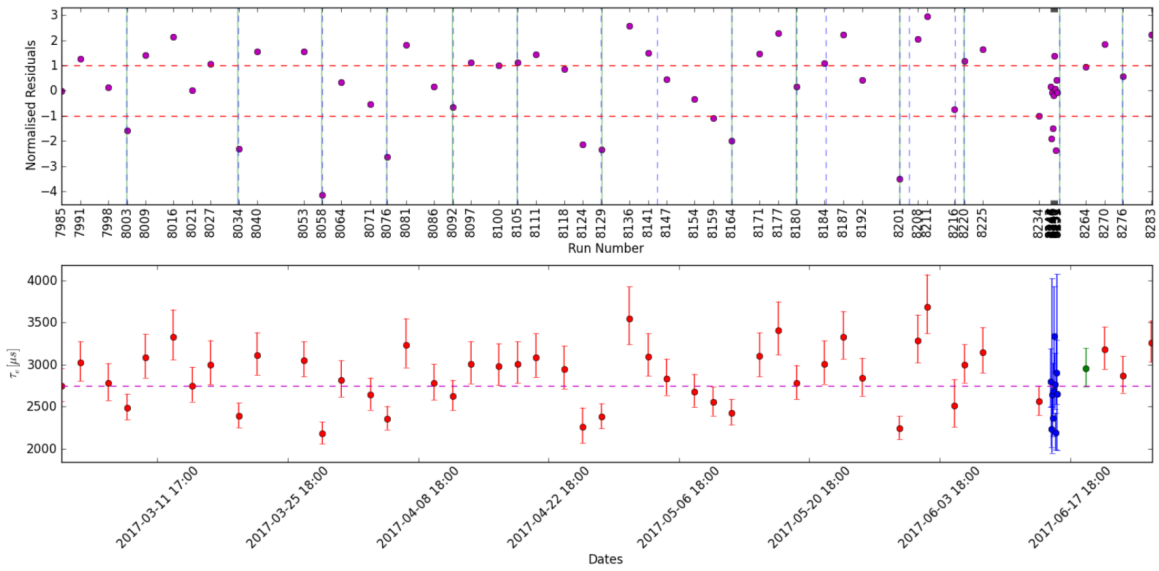

Figure 4.20: Electron lifetime as a function of time and residuals, averaged over time blocks of three months, in EXO-200 Phase-II. The average electron lifetime is indicated by the dashed-magenta line; the vertical green and blue lines mark the dates where the return and recovery lines are evacuated, respectively.

could result in previously in LXe submerged surfaces being exposed. Those surfaces could warm up and outgas impurities that were previously stuck to the surfaces due to freezing out and later being evaporated. While the mechanism here may be different from the continual desorption of impurities from warm plumbing over the lifetime of the experiment, a clear effect on lifetime is observed.

It is very difficult to fully model desorption from the plumbing due to the dependence on many factors related to handling, cleaning, surface finish, etc. It is difficult to rule out that this is a major source of impurities in EXO-200 and could have substantially limited the electron lifetime observed there. Desorption of impurities before filling could be enhanced by selectively baking portions of the plumbing or by circulation and purification of warm Xe gas.

Leaks to Atmosphere Due to the small leak rates required to account for the overall electron lifetime observed in EXO-200, it is important to ensure no leaks to the atmosphere were present that could account for the needed outgassing rate.

Standard VCR fittings are specified by Swagelok to have a maximum leak rate of about $4 \times 10^{-9}\,\mathrm{mbar\,L\,s^{-1}}$ and as low as $4.11 \times 10^{-11}\,\mathrm{mbar\,L\,s^{-1}}$ when using unplated gaskets [145]. In order to explain the impurity effect solely with leaks into the detector from the VCR fittings, the system should have about 16 VCR fittings downstream of the purifier, all leaking at this worst-case specification. Such a scenario seems unlikely (indeed the VCR fittings are expected to have leak rates substantially below the upper specification when properly installed). However, a single bad fitting that was undetected (due to low sensitivity leak checks) or opened up during the operation is difficult to rule out as the source of the impurities seen by EXO-200. In fact, for a continual leak rate to atmosphere of $4 \times 10^{-6}\,\mathrm{mbar\,L\,s^{-1}}$ then only 7 g of xenon would have been lost in 10 yr.

One possibility to prevent the constant leak of impurities into the detector is to encapsulate any fittings (or likely leak locations) with a nitrogen purge. Nitrogen is expected not to have any deteriorating effects on the electron lifetime due to its negative electron affinity ($-0.07\,\mathrm{eV}$ [146] compared to $1.46\,\mathrm{eV}$ [147] for oxygen). The electron affinity is defined to be the energy that is released when an electron is added to a neutral atom.

Kr Analysis to Test Leak Hypothesis The decay rate of ^{85}Kr in EXO-200 as a function of time can be used to set a limit on the leak rate of atmospheric gases into the EXO-200 detector. This makes use of the known concentration of ^{85}Kr atoms in the atmosphere that primarily decay via β-decay and have a Q-value of 687 keV. The decay has a half-life of $t_{1/2} = \ln(2)\tau = 10.756\,\mathrm{yr}$.

On average, ^{85}Kr has a isotopic abundance of $\sim 2 \times 10^{-11}$ [148] (disregarding spatial variations and differences between the hemispheres), while atmospheric Krypton (including all isotopes) has a concentration of $\sim 1.1 \times 10^{-6}$ [149]. The concentration of ^{85}Kr in the atmosphere is time-varying since it decays away but is also constantly

being produced through nuclear fuel processing. It is known to be the most abundant man-made radioactive isotope in the atmosphere [150]. It primarily decays via β-decay into ^{85}Rb:

$$^{85}\mathrm{Kr} \longrightarrow {}^{85}\mathrm{Rb}^{(*)} + e^{-} + \bar{\nu}_e \tag{4.30}$$

where it decays to the ground state with a branching ratio of 99.563 % by releasing a 514 keV de-excitation gamma. The released energy of the decay is $Q = 687.1\,\mathrm{keV} \pm 0.19\,\mathrm{keV}$ [151]. Due to the parity mismatch between the ground states of the mother and daughter nuclei and the total angular momentum of one unit carried away by the leptons, the decay into the ground state of ^{85}Rb is a unique first-forbidden decay and therefore suppressed which results in a long half-life of $T_{1/2} = 10.739\,\mathrm{yrs}$. Moreover, the spectral shape of the beta energy spectrum will be distorted.

Due to significant performance differences of the EXO-200 detector between Phase I and Phase II the limit on the leak rate is set within each phase separately. The null hypothesis is a no-leak hypothesis where the number of ^{85}Kr atoms in the detector should decay away according to the half-life. A small modification to this model would add a constant leak that introduced a fixed number of atoms per unit time α to the system. This is described by

$$N(t) = N_0 \cdot e^{-\frac{t}{\tau}} + \alpha\tau \cdot (1 - e^{-\frac{t}{\tau}}) \tag{4.31}$$

The fits to the data, the corresponding χ^2-values and p-values are shown in Figure 4.21. The upper limits on the leak rate for Phase I and Phase II are

$$J_{\mathrm{Phase\,1}} \approx 3.1 \times 10^{-7}\,\mathrm{mbar\,L\,s^{-1}} \tag{4.32}$$

$$J_{\mathrm{Phase\,2}} \approx 1.9 \times 10^{-7}\,\mathrm{mbar\,L\,s^{-1}} \tag{4.33}$$

respectively. By performing a $\Delta\chi^2$ analysis with $N_{\mathrm{DOF}} = 1$ between the null hypothesis

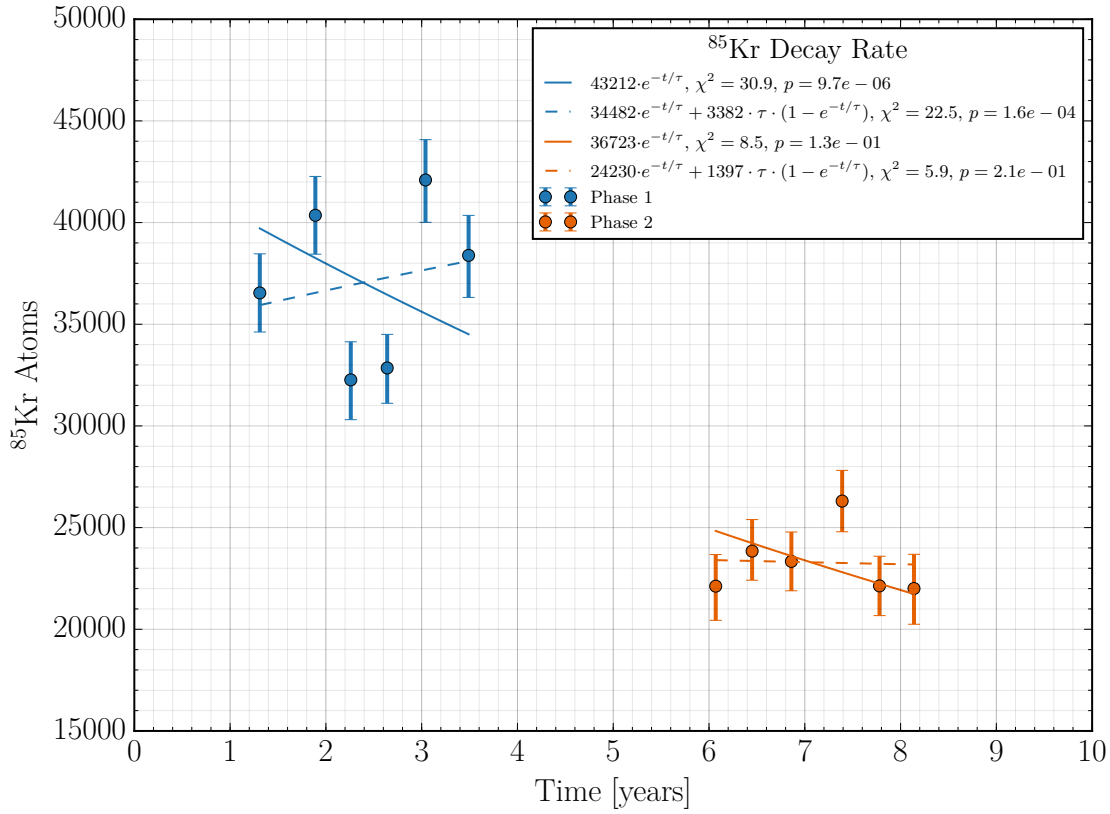

Figure 4.21: Number of ^{85}Kr atoms in EXO-200 as a function of time. Data points in blue and orange are for Phase I and Phase II, respectively. The null (no leak) hypothesis is disfavored at $\sim 3.7\sigma$ when combining the p-values from both phases. However, the leak rate is still below what is needed to explain the electron lifetime in EXO-200.

and the leak hypothesis we find that the null hypothesis is disfavored at $\sim 3.7\sigma$ when combining the p-values from both phases.

The above analysis appears to indicate that the EXO-200 data disfavor a hypothesis that no ^{85}Kr is introduced into the active liquid volume during the experiment. However, systematic variations in the detector threshold throughout Phase I can impact this conclusion and the consistency of the data with the "no-leak" hypothesis. Note that such a leak would not be explained by sources of ^{85}Kr within the detector (e.g., diffusing out of the PTFE or acrylic) since such impurities would also decay with the expected half-life during the diffusion process. The best fit values for the

leak rate appear at first glance to be too small to explain the steady-state leak rate of $4 \times 10^{-6}\,\mathrm{mbar\,L\,s^{-1}}$ inferred above. However, there are substantial assumptions required for this analysis, including the concentration of ^{85}Kr in the cleanroom air, the equilibration of gas/liquid impurities, and the purification rate, etc, which might account for the inconsistency.

4.2.1.4 Solvent Properties of Liquid Xenon

Despite xenon being a noble gas, which under usual conditions does not prefer to undergo chemical reactions, it has been shown that xenon as a liquid can act as a solvent for hydrogen and nitrogen. A study has seen a crystalline material containing XeF_2 when liquefying xenon in a container with PEK [152]. It has been previously also demonstrated that xenon will create molecular bonds with the two elements with the highest electron affinity, which are fluorine and oxygen. However, it is unclear from the available literature whether we can expect that xenon will dissolve plastics under the conditions in nEXO. Possible solvent properties of LXe [153–155] is a primary reason that any materials planned for use in nEXO should be first validated through small-scale samples tested in LXe purity monitors.

4.2.1.5 Impurities Introduced During Enrichment

During the initial fill of EXO-200 impurities consistent with centrifuge lubricants in the Xe believed to arise from the enrichment process were identified. This contamination may have arisen from Perfluorinated Polyether (PFPE) lubricants introduced into the gas during isotopic separation. Such lubricants and their products may in principle be highly electronegative, and even sub-ppt concentrations might be dominant over ∼100 ppt concentrations of O_2 in the liquid. While the SAES getters were operated at a higher than normal temperature to remove these impurities in EXO-200, it is unclear what the residual impurity level introduced by contaminants in the enriched Xenon

(^{enr}Xe) was, and whether this is a plausible source for the dominant electronegative impurities. Additional information on this contamination is provided by the RED-100 collaboration, which used the Xe tailings depleted in ^{136}Xe from the enrichment of EXO-200 and KamLAND-Zen xenon and also observed similar impurities. RED-100 claims measurement of species such as SF_6 and hydrocarbons of the form $C_mH_nR_k$ in their depleted Xe prior to purification. In particular, if SF_6 really were present, it is expected to have an electron capture cross-section that is $\sim 10^3$ times higher than O_2 [138]. To remove these impurities, RED-100 employed a dedicated pre-purification step prior to filling the detector and purification with the SAES getters. It is unclear whether similar impurities will be present in the ^{enr}Xe sourced for nEXO, but this experience indicates that a dedicated program to test and purify the Xe prior to filling the detector will be required.

4.2.2 Electronegative Impurity Control in nEXO

4.2.2.1 Conceptual Design

In the current conceptual design for nEXO plastics, such as PTFE and Acrylic that were used in EXO-200, are omitted in the TPC. However, small amounts of Kapton as insulation for cables or as part of the SiPM interposer, and epoxy for the cable feedthroughs for the charge and light modules will be used [85]. While outgassing measurements of these components are underway, estimates on the outgassing of these materials can be given based on the values for PTFE.

4.2.2.2 Outgassing from Kapton and Epoxy

nEXO plans to use of about 12 500 cm^3 of 50 µm thick Kapton as insulation for cables [85]. The diffusion constant and activation energy of Kapton and Epoxy is still unknown. To estimate their outgassing rate, we assume the same solubility of oxygen in Kapton and the Epoxy, the same diffusion constant, and the same activation energy

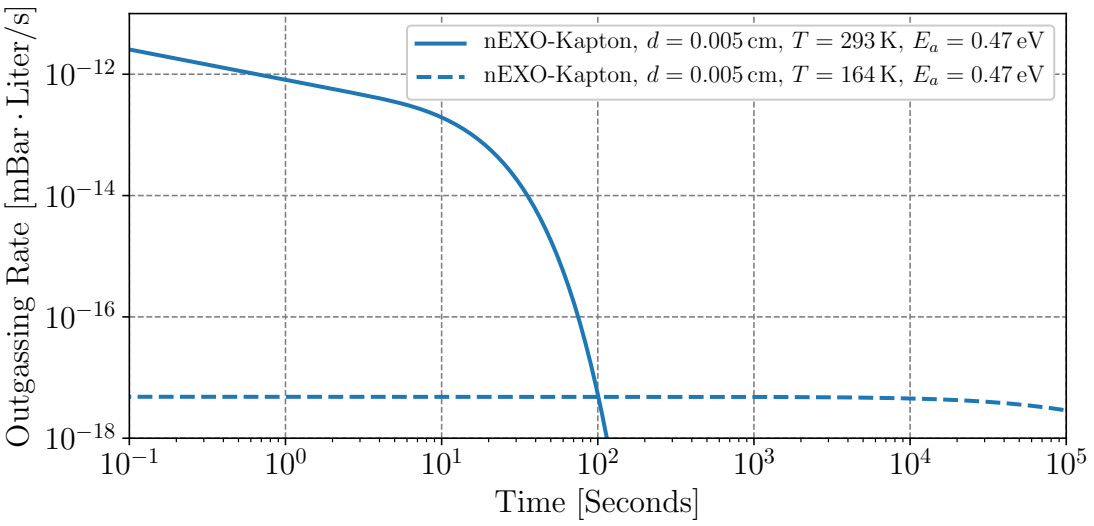

Figure 4.22: Calculated outgassing rate as a function of time for thin Kapton cables in nEXO.

as in PTFE. The result for the outgassing rate of oxygen trapped in Kapton is shown in figure 4.22. The amount of oxygen trapped in Kapton in the detector is completely negligible as it outgasses sufficiently fast and will be removed through the purifier without harming the electron lifetime of the experiment.

The amount of epoxy that will be used in nEXO is not fully determined. Current designs include 8 feedthroughs where each has a 1 cm thick epoxy plug with a surface area of 10 cm^2. The outgassing rate for these epoxy plugs is shown in Figure 4.23. Thinner pieces of epoxy are also considered to be used as part of the SiPM assembly but the outgassing rate from these pieces will be subdominant.

4.2.2.3 R&D Tasks for Liquid Xenon Purity in nEXO

The outgassing of atmospheric gases trapped in plastics such as PTFE alone is unlikely to be the main contributor to the lifetime limits seen in EXO-200 and avoiding them altogether to achieve the proposed 10 ms lifetime for nEXO will not necessarily provide the desired increase in lifetime. In fact, RED-100 and LZ have reached 7 ms–10 ms lifetimes in a dual-phase detector with large PTFE reflectors [135, 156]. This provides

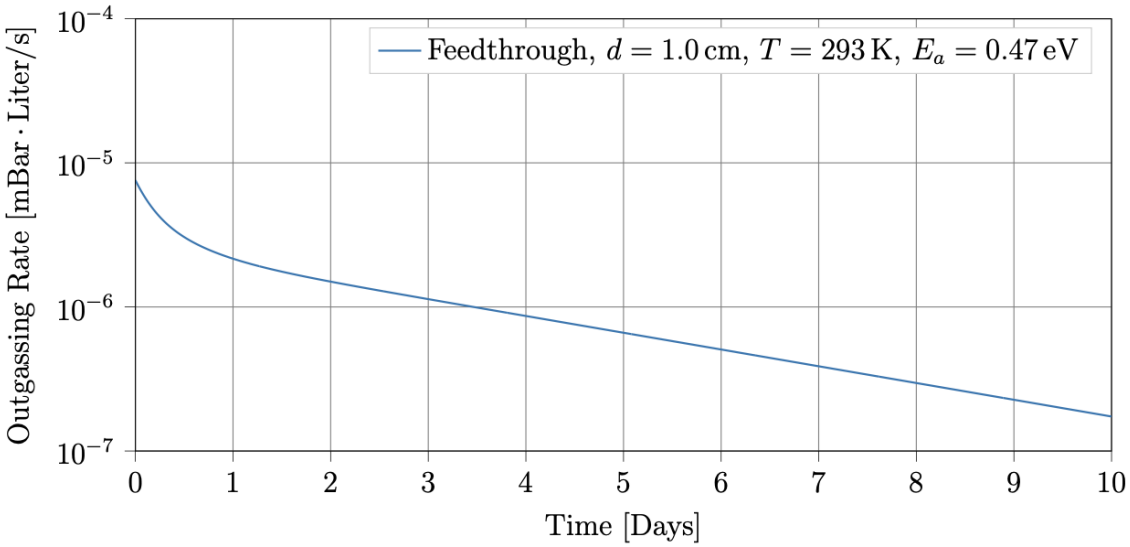

Figure 4.23: Calculated outgassing rate as a function of time of 1 cm^2 thick epoxy used for the feedthroughs in nEXO.

circumstantial evidence that cold plastics are not necessarily the primary sources of impurities. Additional possibilities include that the source of impurities arose from the EXO-200 acrylic, outgassing of the plumbing, or small undetected leaks to the atmosphere. This experience will guide the design and R&D tasks needed to ensure nEXO achieves the desired lifetimes. Some key aspects need to be well measured in a dedicated xenon purity setup to arrive at a reliable and predictive model for the LXe purity in nEXO such as:

1. The diffusion process depends on the temperature through the exponential dependence of the diffusion coefficient. Figure 4.24 shows the dependence of the diffusion coefficient on the temperature and for different activation energies. In order to reliably predict the outgassing rate of materials the diffusion constant D_0 and the activation energy E_a need to be determined for each solute and material combination in question. A recent measurement (see Section 4.2.3) of the activation energy of diffusion of oxygen from PTFE gave $E_a = 0.47\,\mathrm{eV} \pm 0.04\,\mathrm{eV}$ which is about three times as large as the (very conservative) value assumed in [121]. Given the exponential dependence on activation energy, it is

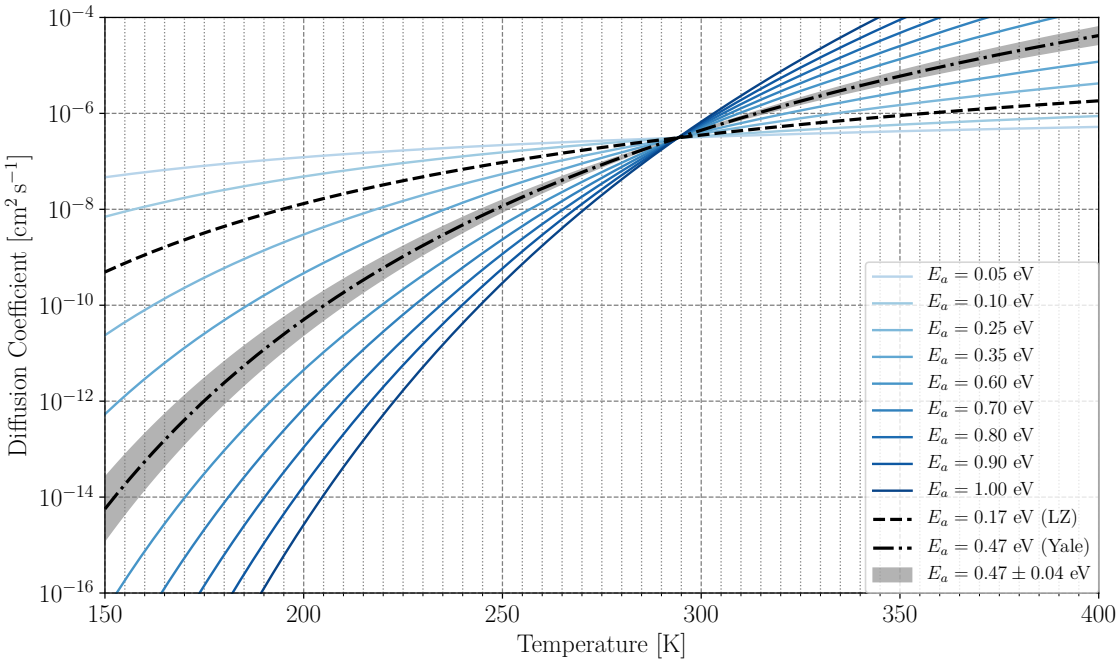

Figure 4.24: The diffusion coefficient as a function of temperature plotted for different activation energies. The dashed line shows the value from [121] and the dashed-dotted line shows the measurements done at Yale. The grey band shows the uncertainty in the measurement. Due to the exponential dependence, small changes in the activation energy for the diffusion process can lead to orders of magnitude variation in the predicted outgassing at low temperature.

important to ensure this parameter is understood for all materials to be used in nEXO at LXe temperatures.

2. Impurities can enter the detector at locations where the xenon is in the gas phase. The concentration of impurities in the gas phase then has to be translated into a corresponding impurity concentration in the liquid phase where one would see the effect on the electron lifetime. In equilibrium, this ratio is defined through Henry's coefficient. Initial measurements have found the relative concentrations in gas and liquid are expected to differ by a factor of ∼60 for oxygen impurities in the gas and liquid phases (see Section 4.2.4.4). Further work is required to understand whether this equilibrium situation holds during recirculation in large detectors, and the corresponding concentrations for other impurity species.

3. It is not understood in detail what the primary species of electronegative impurities limiting the lifetime in EXO-200 and previous detectors are. Further R&D is required to remeasure the electron capture cross-sections of various impurities that could be relevant in nEXO (e.g., O_2, H_2, CO_2, etc.) and use this information in combination with the model above to predict the electron lifetime.

4. Looking at Figure 4.16 we see a systematic offset in the average electron lifetime that is achieved between Phase I (Run 0-6600) and Phase II (Run 6800-9600) of EXO-200. Between the two phases, the cartridges for the two purifiers that were used in parallel were exchanged. The ultimate lifetime achievable might be purifier dependent as it is difficult to rule out that different cartridges provide a different maximum purity. The heated zirconium getters from SAES specify an output purity of < 1 ppb for input gases with ppm level impurities and at input flow rates of several SLPM (depending on the specific getter's specifications) [157]. Certain impurities, such as the centrifuge lubricants observed in EXO-200, are removed only at higher getter temperatures than recommended for standard operation. In these conditions, it is unclear what the absolute purity the SAES getter technology can achieve upon continued recirculation of ultra-pure ($\ll 1$ ppb) gas. However, individual systems LZ [156] and RED-100 [135] have reported electron lifetimes up to 10 ms using gas phase purification.

4.2.3 Vacuum Outgassing Setup

While the ultimate goal of this work is to correlate the amount of outgassed atmospheric gases with an effect on the electron lifetime in LXe, a significantly simpler procedure would allow us to infer that relationship from measurements of the outgassing into vacuum at around room temperature. The motivation for this setup is to measure the relevant parameters governing the diffusion process, which includes the activation

energy E_a and the diffusion constant D_0 as a function of temperature for a variety of candidate plastic materials that might be used inside the nEXO TPC. Using the Arrhenius relationship in Equation 4.18 we can predict the amount of outgassing at LXe temperatures and confirm the expected impact on the electron lifetime in LXe with a dedicated LXe purity monitor that will be discussed in Section 4.2.4. One major benefit from such a relationship would be the development of a significantly easier and faster procedure for qualifying materials in terms of their electronegative impurity output and their contribution to the overall impurity budget for nEXO.

4.2.3.1 Experimental Setup and Procedure

The experimental setup consists of a stainless steel conflat vacuum chamber with a diameter of ∼20 cm and a height of ∼12 cm. The base pressure of the chamber can reach $\sim 5 \times 10^{-8}$ mbar using an Edwards pumping station (T-station 85 [158]) combining a turbomolecular pump with a dry diaphragm pump and is monitored by an Edwards dual-range gauge [159]. Figure 4.25 shows images of the entire setup, the inside of the vacuum chamber, and the various measurement devices.

The temperature of the vacuum chamber is controlled by a Peltier thermoelectric cooler and heater [160] that is attached to the bottom of the chamber and can provide a stable temperature from 10 °C–60 °C. The temperature of the sample is measured via two K-type thermocouples attached to the top and bottom sides of the sample and read out with an Omega Temperature Data Logger (RDXL6SD-USB [161]). Lastly, the gas content of the chamber is monitored via an Residual Gas Analyzer (RGA) (SRS RGA-200 [162]), measuring the partial pressure as a function of atomic mass, and which is connected to the main chamber via a manual valve that can be closed to keep the RGA under vacuum conditions at all times and prevent any adsorption of gases on the filament during sample loading when the chamber is exposed to the atmosphere. All sensors and equipment in the setup are computer controlled and

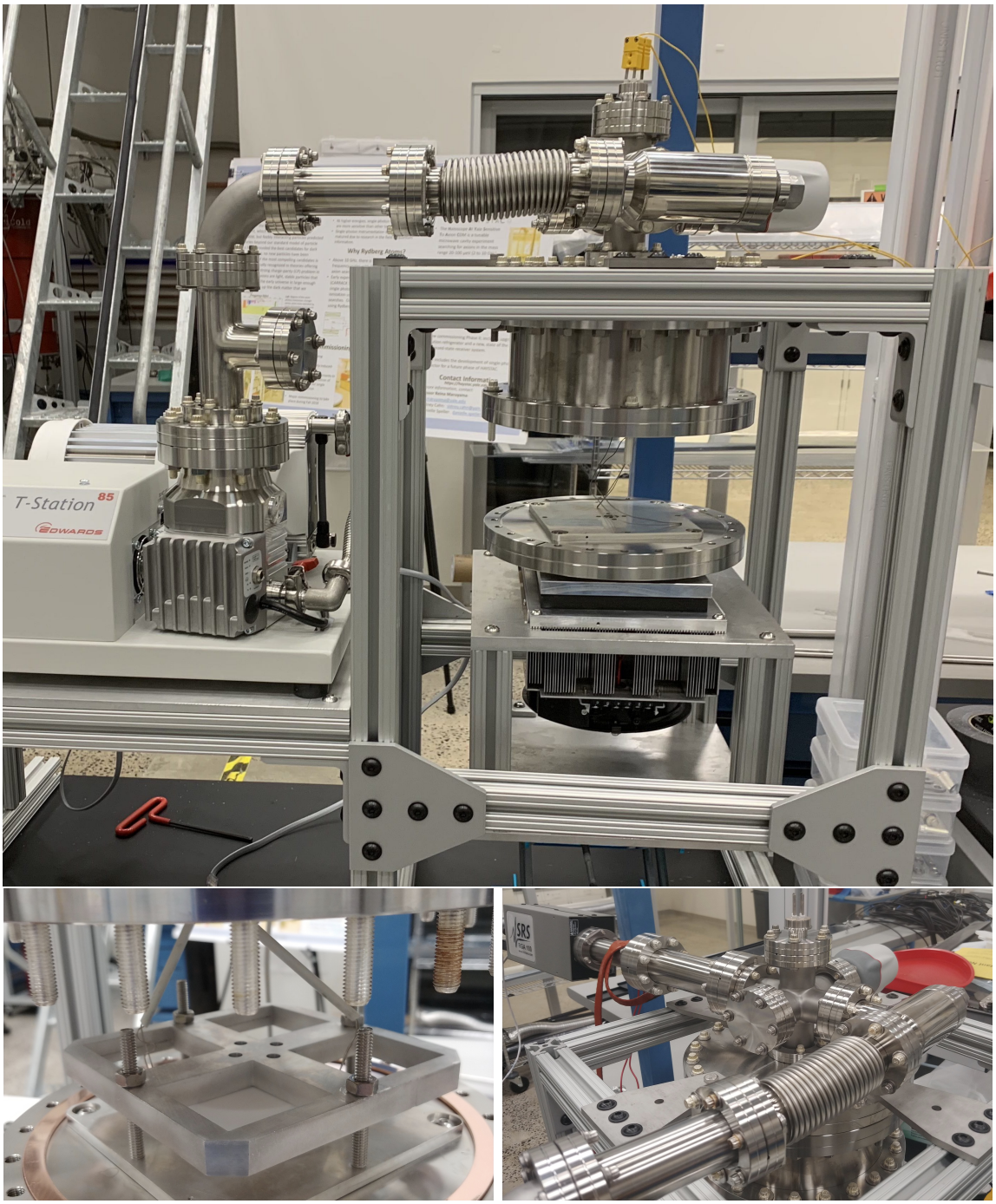

Figure 4.25: Pictures of the outgassing setup used to measure the activation energy and diffusion constant of sample materials for nEXO.

Figure 4.26: Pictures of installing a PTFE sample into the outgassing setup.

the measurement runs fully automatically once the sample has been manually loaded into the chamber, improving the throughput of this setup for measuring candidate materials.

Particular care was given to only using low outgassing materials inside the vacuum chambers such as stainless steel, aluminum, ceramic and thin (50 µm) Kapton for cable insulation. In addition, control runs are performed with no sample present to exclude that any long-term outgassing materials were added to the system and adsorbed to the vacuum chamber walls either by the sample itself (possibly due to evaporation or dissolution at elevated temperatures) or during operations on the system. It is crucial to maintain a low-outgassing background to increase the partial pressure sensitivity to especially small sample geometries and atmospheric gases undergoing diffusion on a much longer time scale.

The sample is placed in between two polished aluminum plates which are in close thermal contact with the sample and the bottom of the vacuum chamber, as can be seen in Figure 4.26. Additionally, they are connected via four additional copper straps for improved thermal conductivity to ensure that the top and bottom plates are at the same temperature and the sample is heated uniformly. A COMSOL simulation of the system indicated that the temperature gradient across the sample can be $\Delta T < 2\,^{\circ}\mathrm{C}$ and will be taken into account in the analysis of the data described in Section 4.2.3.2.

Depending on the size of the sample in the linear dimension relevant for diffusion,

i.e. thickness in the case of a slab or radius in the case of a cylinder, the chamber with the sample present is allowed to be evacuated and pumped on for around 12 h before increasing the temperature. This is to guarantee that a sufficiently low base pressure is reached and that we are approaching the regime in which diffusion is the dominant outgassing process as most of the mono-layers on the stainless steel surfaces would have desorbed (as was discussed in Section 4.2.1 and illustrated in Figure 4.13). The temperature is increased in increments of 10 °C and kept at the new temperature for another 12 h. This procedure is repeated until the sample reached a temperature of 60 °C.

The RGA takes data continuously during the entire operation and completes a full scan from $0 - 100$ amu every 30 s. Via the through-put method, the measured partial pressure from the RGA can be related to the outgassing rate of a given gas species I via

$$J_I = \frac{C_I \cdot p_I}{A} \tag{4.34}$$

where p_I is the partial pressure in the chamber, C_I is the conductance of the pumping line and so far was measured to be $C_I = 10\,\mathrm{L\,s^{-1}}$ for $I = O_2$, and A is the surface area of the sample.

4.2.3.2 Results

An example data set is shown in Figure 4.27, containing the partial pressure of various gases as a function of time. The obtained data is fitted against the model in Equation 4.16 where the diffusion constant is replaced by Equation 4.18 and both E_a and D_0 are freely floating parameters in the fit. The temperature data used in the fit is an average between the two thermocouples at the top and bottom of the sample. The analysis so far was limited to oxygen but can be easily extended to other gas species of interest such as N_2, CO_2, and H_2O.

The largest uncertainty in our measurement is the systematic error in the temper-

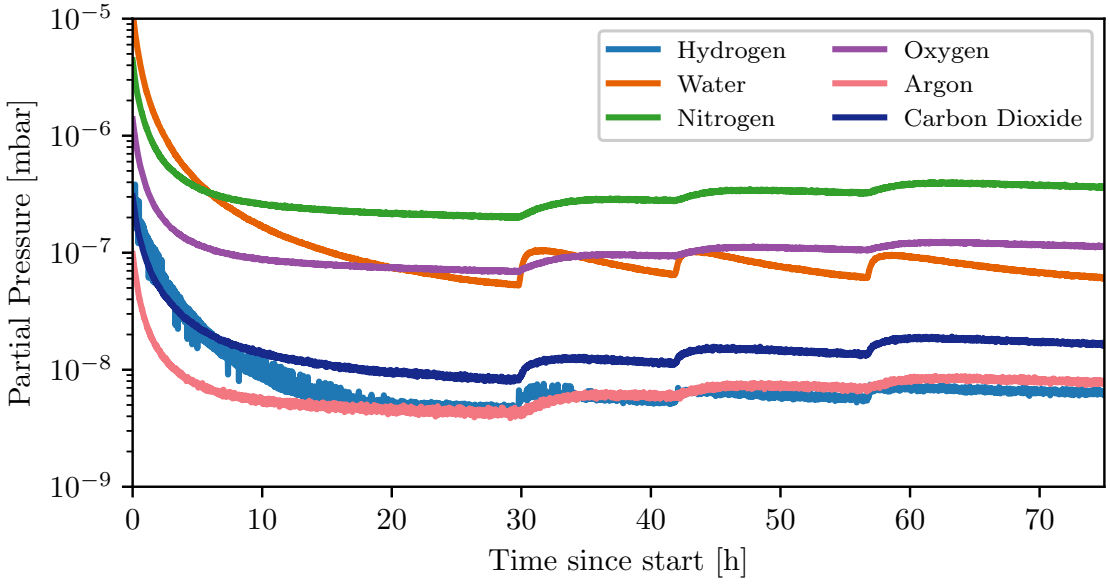

Figure 4.27: Measured partial pressure of various gases from a PTFE sample. The increase in partial pressure in ∼12 h intervals is due to an increase in the temperature according to the procedure described in the text.

ature uniformity across the sample which was propagated to E_a and D_0 by refitting the data using only the data from the thermocouple measuring the bottom or top surface of the sample. The results obtained for the outgassing parameters of O_2 in various materials are summarized in Table 4.2.

Despite numerous measurements of diffusion parameters for a variety of polymers in the literature, a full understanding of the microphysics of diffusion is not well

Material	Diffusion Constant D_0	Activation Energy E_a
PTFE #1	$(0.003^{+0.006}_{-0.002})\,\mathrm{cm^2\,s^{-1}}$	$(0.46^{+0.03}_{-0.02})\,\mathrm{cm^2\,s^{-1}}$
PTFE #2	-	$(0.5^{+0.4}_{-0.2})\,\mathrm{cm^2\,s^{-1}}$
Acrylic	$(0.00042^{+0.05}_{-0.00041})\,\mathrm{cm^2\,s^{-1}}$	$(0.34^{+0.18}_{-0.14})\,\mathrm{cm^2\,s^{-1}}$
Vespel	$(3.3^{+5}_{-3})\,\mathrm{cm^2\,s^{-1}}$	$(0.66^{+0.06}_{-0.14})\,\mathrm{cm^2\,s^{-1}}$
Epoxy	$(1.2^{+0.11}_{-0.15})\,\mathrm{cm^2\,s^{-1}}$	$(0.69^{+0.01}_{-0.03})\,\mathrm{cm^2\,s^{-1}}$

Table 4.2: Summary of measurements of the activation energy E_a and diffusion constant D_0 for the outgassing of O_2 from various materials.

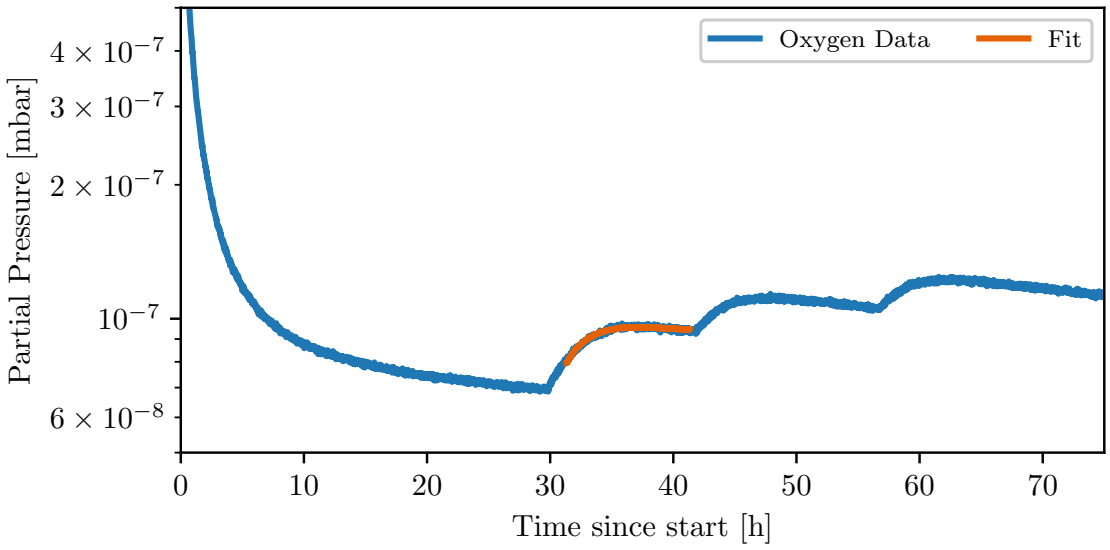

Figure 4.28: Measured partial pressure of oxygen from a PTFE sample and an example fit to the data to obtain the diffusion parameters E_a and D_0 using Equation 4.16.

established beyond recognizing empirical relationships. Based on the activated zone theory of diffusion [163] the activation energy can be understood as a composite energy $E_a = E_i + E_b$, where E_i characterizes the energy needed to overcome the intermolecular energy between polymer chains in the material of interest and for penetration into the polymer structure, and E_b is the intramolecular energy needed to bend neighboring polymer chains. These two terms are expected to depend on the gas molecule diameter σ_I with $E_{i,I} \propto \sigma_I$ and $E_{b,I} \propto \sigma_I^2$. In addition, an empirical relationship between D_0 and E_a was pointed out in a meta-study of measurements of various glassy and rubbery polymers [164] and is plotted in Figure 4.29 together with data from Table 4.2, showing good agreement.

4.2.3.3 Conclusion and Outlook

The above measurements provide a first step towards developing a data-driven purity model for LXe for nEXO. The obtained measurements of E_a and D_0 are in good agreement with literature values but procedural optimizations will help reduce the

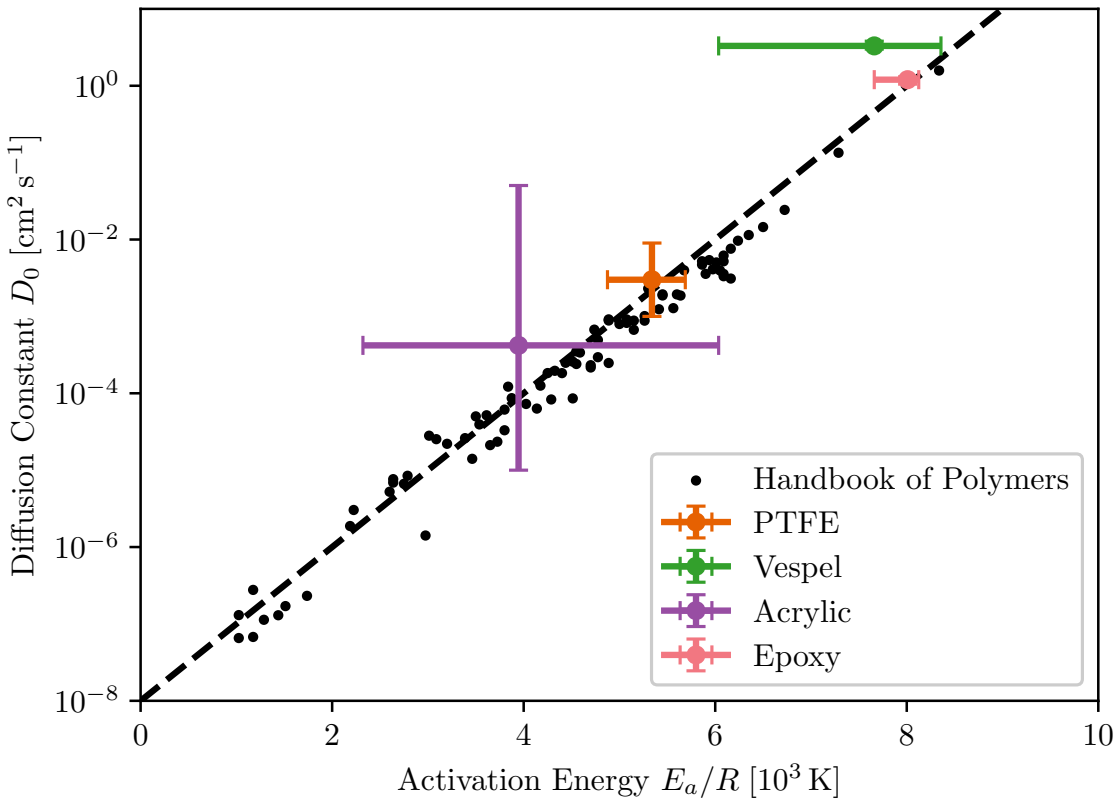

Figure 4.29: Plot of the diffusion constant D_0 vs E_a/R, where R is the ideal gas constant, for results obtained with the Yale Outgassing Setup together with a metastudy of various other polymers [164] and the best fit line.

uncertainties. With the measured data in Table 4.2 the expected outgassing rate at LXe temperature can be predicted using equations 4.18 together with equations 4.14 or 4.17. A confirmation of these predictions in a dedicated LXe setup would be a huge success as it would allow utilizing a much simpler vacuum system to estimate the impact of certain materials on the electron lifetime in LXe. The next steps include

- tightening the error bars by reducing the temperature gradient across the sample, corresponding to the largest systematic error
- varying the temperature profile to see the effect on the data and model agreement
- extracting the diffusion parameters for other gas species from the same sample
- extending the catalog of measured samples to various candidate materials that

could potentially be used in nEXO

- understanding the scaling of the outgassing from a small-scale sample in this test setup to the outgassing from the actual geometry used in nEXO
- deriving a qualification procedure for candidate materials

4.2.4 Liquid Xenon Purity Monitor

Purity monitors are widely used in noble liquid experiments to measure the electron lifetime of the experiment in situ. The core principle is the release of a known amount of charge at the cathode that is drifted under the influence of an electric field towards the anode where it is collected. The ratio of collected charge to released charge $R = Q(t)/Q_0$ can be related to the electron lifetime via

$$Q(t) = Q_0 \cdot e^{-t/\tau} \tag{4.35}$$

$$\rightarrow \tau_e = \frac{-t}{\ln R} \tag{4.36}$$

where t is the drift time, which depends on the drift length and electric field. In the limit of vanishingly small impurities roughly the same amount of charge is detected at the anode as was released at the cathode and therefore the electron lifetime approaches infinity.

While the longest possible electron lifetime is generally preferred, the measurements of critical input parameters for the purity model only rely on relative electron lifetime changes. However, the electron lifetime should nevertheless be sufficiently long to reduce systematic errors. The Yale Purity Monitor (YPM) is designed to be able to measure electron lifetimes on the order of 10 ms and to derive and validate a data-driven purity model. The relevant parameters to quantify the expected effect from a sample material on the electron lifetime in LXe are

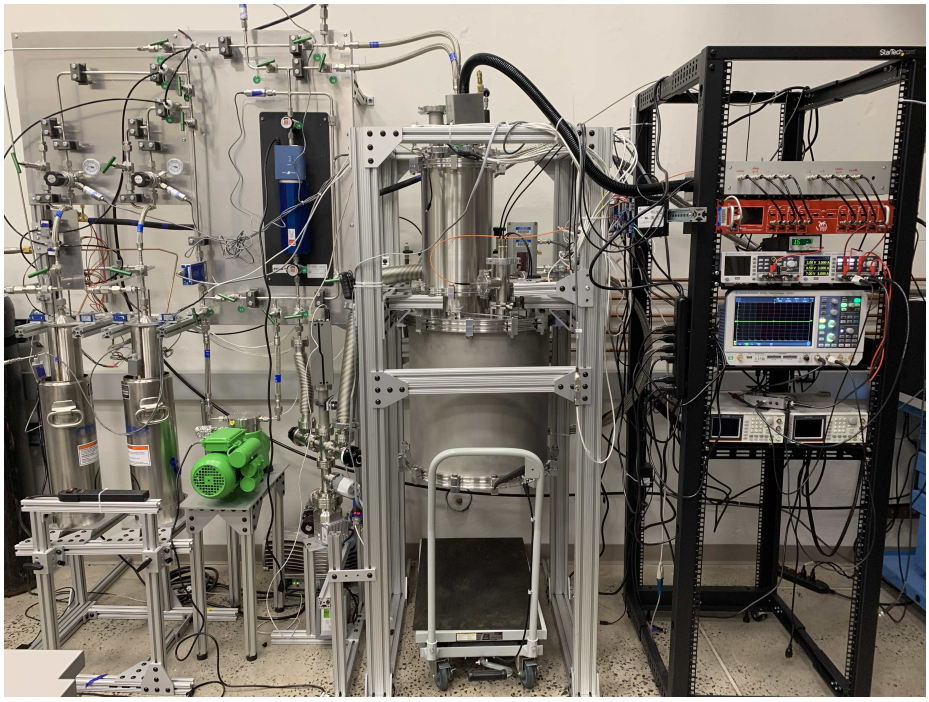

Figure 4.30: Image of the Yale Purity Monitor setup, including the gas handling system (left), the cryostat and xenon cell (center), and the DAQ system (right).

- the outgassing rate of various gas species at LXe temperatures
- the molar fraction of atoms from a given gas species in the liquid phase compared to the gas phase, typically denoted as the Henry's coefficient
- the electron attachment cross-section of various gas species at the relevant electric drift field for nEXO

This section will provide an overview of the setup design, some initial validation measurements, and the first results towards a purity model for nEXO.

4.2.4.1 Experimental Setup

The entire YPM setup is shown in Figure 4.30 and consists of several parts:

- xenon cell and field cage
- gas handling system

- cold-trap enhanced RGA system [165]
- data acquisition

Xenon Cell and Field Cage The xenon cell is made of 304 stainless steel 4 5/8 in conflat (CF) flanges with a total length of ∼20 cm and can hold up to 3 kg of LXe. It is attached to a 12 in 304 stainless steel reducer and flange which is connected to the xenon supply line and high voltage and signal feedthroughs. The inside of the xenon cell only contains ultra-high vacuum compatible materials such as low outgassing Kapton-insulated wires, ceramic, and metals (such as aluminum, stainless steel, and copper). The field cage is confined by 3 rods that are made of machinable ceramic and are 15 cm long. The anode and cathode are attached to the two opposite sides of the rods and secured with ceramic screws. The field shaping rings with a diameter of ∼35 mm are also made of stainless steel and can be inserted into slots in the ceramic rods separated by 1 cm. A total of 15 FSRs are connected via 10 MΩ–50 MΩ thick-film surface-mount resistors that are mechanically mounted to the side of the FSRs with stainless steel screws and washers. The closest FSRs to the cathode and anode can be equipped with a meshed grid to serve as a Frisch grid, shielding the two electrodes from induced current during the charge drift. The mesh has a wire thickness of 1 mm and wire pitch of 10 mm, resulting in optical transparency of >90 %. For a twice as strong electric field after the Frisch grid than before the grid, a 100 % efficient electron transmission is achieved [166]. The high voltage is provided by an eight-channel reversible high voltage power supply [167], which can provide up to ±5.5 kV per channel. The connections from the HV feedthrough to the field cage are made via custom Kapton-insulated 26 wire gauge cables with ring terminals crimped to one end and bolted onto the cathode, cathode grid, anode grid, and anode, respectively. The cathode grid is kept at ground potential, while the other three electrodes can be biased independently to provide an electric field of up to ∼400 V cm^{-1}. This is sufficiently

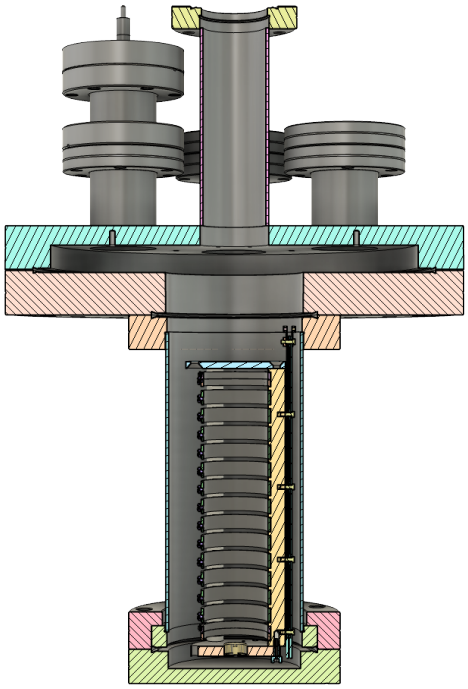

Figure 4.31: Section view of the CAD model of the xenon cell including the field cage, xenon level meter, and feedthroughs.

high to test dependencies on the electric field and to operate at the nominal drift field for nEXO of $\sim$400 V cm^{-1} [85]. The entire field cage is suspended from the top 12 in CF flange with a stainless steel post. Figure 4.31 shows a section view of the CAD model of the xenon cell and field cage inside.

The LXe level is monitored with a custom level meter which is comprised of two stainless steel parallel plates separated by 1 mm with ceramic washers and bolted into one of the ceramic rods with ceramic screws. The change in capacitance, which is readout with 0.1 pF uncertainty by a BK precision capacitance meter [168], as the LXe occupies the space between the plates is used to infer the LXe level. The combination of surface area and separation distance provides a $\sim$1 mm resolution on the LXe level.

The entire xenon cell is surrounded by an outer cryostat, maintaining an insulation vacuum at a pressure of $\sim 1 \times 10^{-2}$ mbar via a Leybold Ecodry 40 plus scroll pump [169]. The cryostat is made of 304 stainless steel Klein Flansche (KF) flanges with a total

diameter of ∼55 cm. In addition, the outer cryostat is filled with 20 layers of highly reflective vacuum super insulation foil to shield the xenon cell against thermal photons from the black body radiation of the cryostat, which is kept at room temperature. The xenon cell is suspended from the top of the outer cryostat by two 1 cm diameter rods, limiting the thermal link to the components at room temperature.

To liquefy xenon the temperature of the xenon cell needs to be maintained at ∼165 K for an operating pressure of 1 bar inside the cell. The cooling is provided via a Cryomech PT60 cryocooler [170] connected to a Cryomech CP830 compressor and can deliver up to 80 W of cooling power at 77 K. The connection from the cryocooler cold finger to the xenon cell is made with a combination of highly thermally conductive copper blocks and straps. To improve the temperature uniformity and heat conductance the barrel of the xenon cell was surrounded by two cylindrical copper pieces ("copper jacket"). An additional copper and aluminum ring were added to the 12 in to 4 5/8in reducer and the bottom flange of the xenon cell, respectively, for similar thermal reasons. To stabilize the temperature around a given setpoint a heater cartridge with 50 W of maximum heating power is attached to the copper ring, the copper jacket, and the bottom flange, respectively. The temperature is measured at 4 locations via Resistance Temperature Detectors (RTDs) including the bottom of the xenon cell, the copper jacket, the copper ring, and on the cryocooler cold finger.

The production of electrons is achieved by illuminating a gold-coated photo-cathode with VUV photons, which are produced by a xenon flash lamp [171] and guided to the xenon cell via multi-mode solarization resistant optical fibers with a core diameter of 600 µm [172]. The discharge of the xenon in the flash lamp is initiated with an external trigger pulse that is provided by an arbitrary function generator [173]

Gas Handling System A schematic of the YPM gas handling system is shown in Figure 4.32 and the major components comprise the following items:

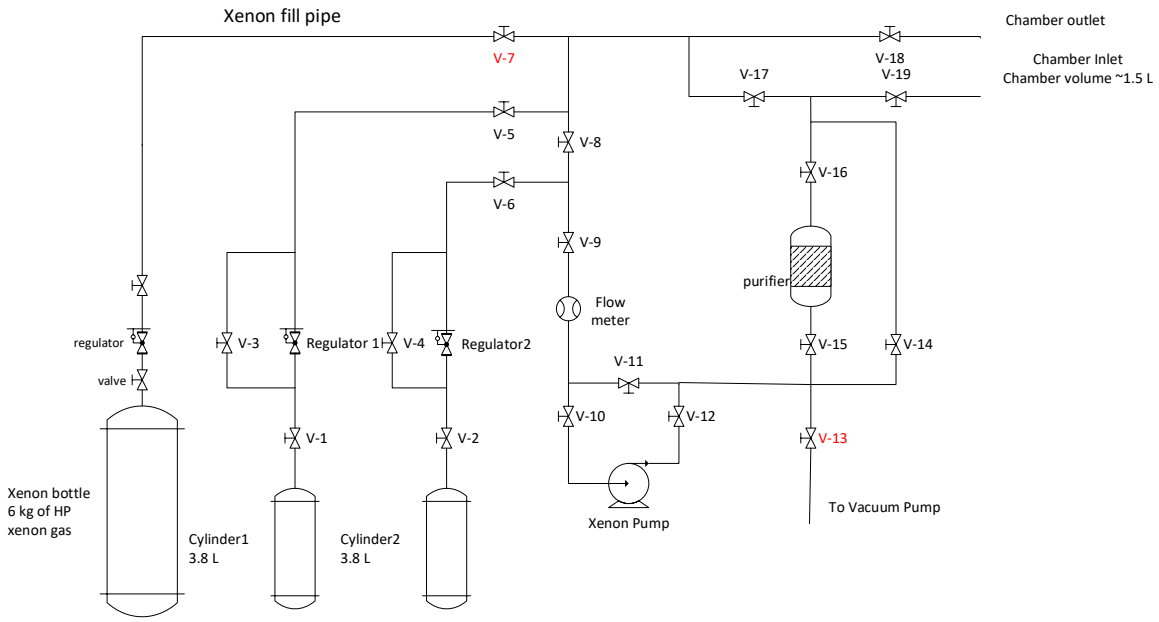

Figure 4.32: Schematic drawing of gas handling system of the YPM.

- The gaseous xenon is stored in two high-pressure 304 stainless steel cylinders with a total volume of 3.8 L and a maximum pressure rating of 124 bar [174]. The xenon storage cylinders are each connected to a manual high-pressure valve sealing it off from the rest of the gas handling system as well as to a common 1000 L nylon balloon allowing it to contain the xenon gas in case of a rupture or malfunction and to possibly retrieve the xenon back. The pressure inside each cylinder is monitored with a Setra ultra high purity pressure transducer [175] attached to the high-pressure side of a manually adjustable pressure regulator. The xenon on the low-pressure side is then injected into the rest of the gas handling system via computer-controlled pneumatic valves.

- A SAES MonoTorr with a heated zirconium getter [157] can be used to further purify the xenon gas either before the initial condensation into the xenon cell or during continuous recirculation. At a flow rate of <3 SLPM it is designed to reduce the concentration of electronegative impurities such as oxygen to $<1 \times 10^{-8}$.

- Typically, a single pass through the purifier during liquefaction is sufficient to achieve an electron lifetime of $\tau_e > 1\,\mathrm{ms}$. However, in case the purity is not sufficiently high a double diaphragm pump [176] can be used to circulate the vapor gas in the xenon cell above the liquid phase in a closed loop through the purifier.

- To properly model the effect various gas species have on the electron lifetime in LXe a calibrated leak valve was added to the system to allow for controlled injection of a known amount of impurities into the system. This leak valve was calibrated for oxygen with a leak rate of $1 \times 10^{-6}\,\mathrm{mbar\,L\,s^{-1}}$ but can be re-calibrated for other gas species.

- The entire system, including the gas handling and the xenon cell, is evacuated and pre-pumped with an Edwards nXDS6i dry scroll pump [177] and a base pressure of $1 \times 10^{-7}\,\mathrm{mbar}$ is achieved with an Edwards nEXT55 turbomolecular pump [177].

- The last part of the gas handling system is an addition that allows for high sensitivity mass spectroscopy of gas species with a cold-trap enhanced RGA system [165]. RGAs typically have a dynamic range of 5 order of magnitude below the base pressure of the system, i.e. $\sim 1 \times 10^{3}\,\mathrm{mbar}$ during xenon liquefaction, and therefore would only be sensitive to partial pressures of $\sim 1 \times 10^{-2}\,\mathrm{mbar}$ and correspondingly electron lifetimes of $\tau_e < 100\,\mu\mathrm{s}$. By sampling the xenon gas above the liquid phase through a calibrated and adjustable leak valve and freezing it to the walls of the stainless steel piping the base gas pressure reduces to the vapor pressure of solid xenon of $3 \times 10^{-5}\,\mathrm{mbar}$ at 77 K. The freezing of the xenon is achieved by submerging a U-shaped section of the piping after the adjustable leak valve in liquid nitrogen. The connection to the RGA, which is attached to the pumping section of the gas handling system, can be established

via opening manual valves. Through this procedure the RGA's partial pressure sensitivity improves significantly from $\sim 1 \times 10^{-2}$ mbar to $\sim 1 \times 10^{-10}$ mbar. This method allows measuring ultra-low concentrations of gas species whose freezing point is above that of liquid nitrogen at 77 K, such as N_2, O_2 and some mixtures of CH_4. This partial pressure sensitivity is necessary to understand the limiting factor for electron lifetimes beyond 10 ms.

Data Acquisition The Data Acquisition (DAQ) system is based on the National Instrument CompactRIO [178], which handles the recording of environmental variables such as temperatures and pressures and power delivery to the heaters. The custom-written PID control software runs on the onboard FPGA and allows the operation of the system independently of the remote computer. A LABVIEW-based software is used to interact with the system, i.e. reading data, performing calibrations, controlling the pneumatic valves, and adjusting the heater output.

The current signals from the anode and cathode are fed into a Cremat charge-sensitive pre-amplifier (CR-150-R5 CSP evaluation board [179] with a CR-110 [180]) before the charge signal can be displayed on a multi-channel scope (Rohde and Schwartz [181]) with 125 MHz sampling rate and is written to disk. An SRS low-noise voltage preamplifier [182] provides additional filtering and amplification.

4.2.4.2 High Voltage Switching

The initial design of the field cage was intended to demonstrate a novel method to drift charge over meter-long distances. The 4 central most field rings were attached to Behlke high voltage switches [183], which can switch up to 12 kV with a frequency of 50 kHz, trapping the drifting electrons in a confined drift region of 4 cm. This would enable drifting electrons over meter-long distances without the need to acquire and liquefy large amounts of xenon. However, the periodic HV switching resulted in

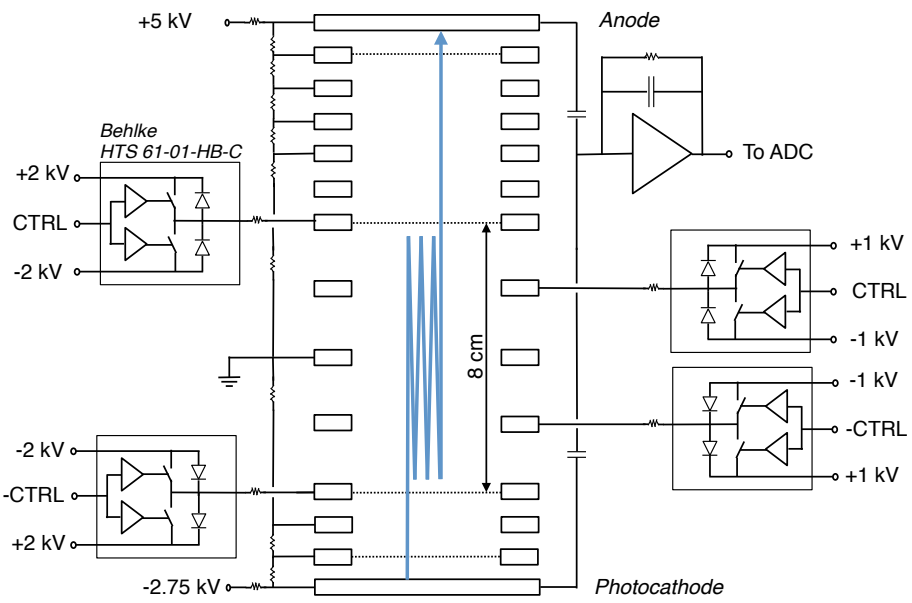

Figure 4.33: Diagram of the purity monitor circuit diagram for a switching HV setup. Frisch grids are shown as dotted lines. A simplified version of the electron path is shown in blue, traveling from the photocathode on the bottom into the HV switching region and then to the collection anode at the top.

a substantial injection of current into the pre-amplifiers that were time coincident with the expected signal. As mentioned, a long electron lifetime is desirable but not necessary to perform the measurements needed to validate our purity model. Therefore, this design was temporarily put on hold due to difficulties in obtaining a sufficiently low-noise signal and might be revisited in the future when doing precision measurements of the xenon purity.

4.2.4.3 Electron Lifetime Measurements

Similar to the outgassing rate J in a vacuum that was defined in Section 4.2.1, one can define a related quantity for LXe. The concentration N_I of the impurity I can be changed either by adding impurities to the system via an "out-diffusion" rate R_0 or removed through the purification system which will depend on the purification efficiency η and the flow rate $\mathcal{F}$. This simple model [185] can be written down as a

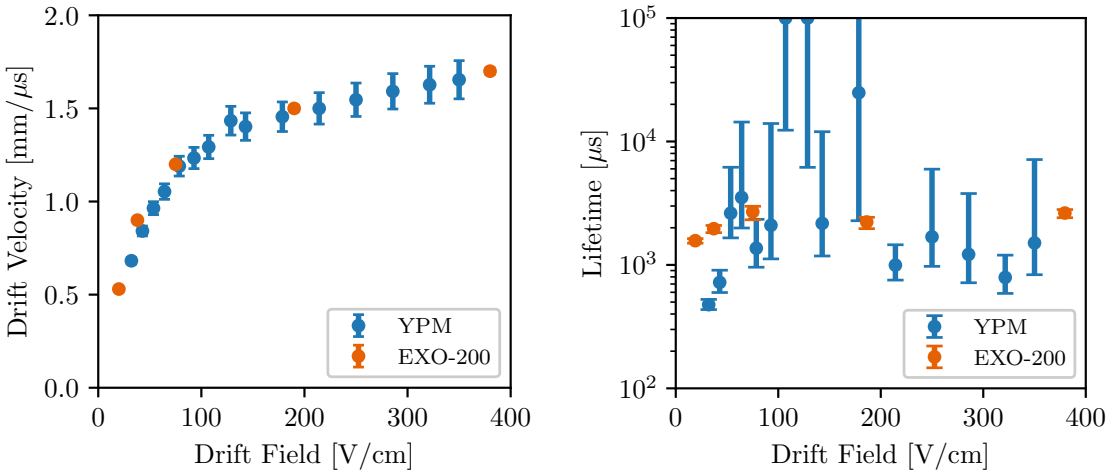

Figure 4.34: Measured drift velocity as a function of drift field in the YPM (blue). The data from EXO-200 is shown for comparison (orange) [184].

differential equation

$$\frac{M}{\rho}\frac{\mathrm{d}N_I(t)}{\mathrm{d}t} = R_0 - N_I(t)\eta\mathcal{F} \tag{4.37}$$

where M is the total mass of xenon in the system and $\rho = 5.5 \times 10^{-3}\,\mathrm{kg\,L^{-1}}$ is the xenon gas density. A solution to the above equation is

$$N_I(t) = S_{I,0}e^{-\frac{\rho\eta\mathcal{F}}{M}t} + \frac{R}{\eta\mathcal{F}}\left[1 - e^{-\frac{\rho\eta\mathcal{F}}{M}t}\right] \tag{4.38}$$

with $S_{I,0}$ the impurity concentration at $t = 0$.

Rewriting Equation 4.25 with this solution and using the electron attachment cross-section at $400\,\mathrm{V\,cm^{-1}}$ from [138] we get

$$\tau_e = \frac{0.3}{n_0 e^{-\frac{\rho\eta\mathcal{F}}{M}t} + \frac{R}{\eta\mathcal{F}}\left(1 - e^{-\frac{\rho\eta\mathcal{F}}{M}t}\right)}\,[\mathrm{ms}] \tag{4.39}$$

which can be simplified in the limit of $t \to \infty$ to

$$\tau_e(t \to \infty) = \frac{0.3 \cdot \eta \mathcal{F}}{R_0}\,[\mathrm{ms}] \tag{4.40}$$

One can use the above equation to estimate the tolerable outgassing rate into the LXe in order to maintain an electron lifetime of $\tau_e = 10\,\mathrm{ms}$ for a given purification system. Assuming a purification efficiency of $\eta = 100\,\%$, a flow rate of $\mathcal{F} = 100\,\mathrm{L\,s^{-1}}$, a total xenon mass of $M = 5000\,\mathrm{kg}$ and an initial impurity concentration of $S_{I,0} = 1\,\mathrm{ppb}$ the acceptable outgassing rate would have to be less than

$$R_{\mathrm{LXe}} \lesssim 1 \times 10^{-11}\,\mathrm{L\,s^{-1}} \tag{4.41}$$

to surpass an electron lifetime of $\tau_e = 10\,\mathrm{ms}$ after $\sim$30 d of purification. A similar performance can be achieved with a less efficient purification system at $\eta = 50\,\%$ but twice as fast flow rate of $\mathcal{F} = 200\,\mathrm{L\,s^{-1}}$.

In addition to benchmark measurements against EXO-200 data such as the drift velocity and electron lifetime as a function of electric drift field shown in Figure 4.34, a measurement of the maximal intrinsic outgassing rate of the system itself in LXe was done. Purity data was taken for $\sim$5 h and was fit against the model in Equation 4.39 without the purification term to obtain an outgassing rate of

$$R_{\mathrm{LXe}} = 7.2 \times 10^{-13}\,\mathrm{L\,s^{-1}} \tag{4.42}$$

This measurement suggests that the cleanliness of the YPM is significantly better than required to measure impurity concentration relevant for nEXO and that the system can be used to reliably qualify sample materials for nEXO.

4.2.4.4 Henry's Coefficient of Oxygen

As mentioned in Section 4.2.3.3 one of the key input parameters for a data-driven purity model is Henry's coefficient for various gas species in LXe, which is needed to translate the outgassing rate to the impurity concentration in LXe and correspondingly its effect on the electron lifetime. Henry's coefficient is defined as the ratio of the impurity concentration in the gas phase above the liquid and the impurity concentration in the LXe at thermal equilibrium.

Through the calibrated leak valve known amounts of oxygen were injected into the xenon chamber, which combined with the piping has a total volume of 2.14 L. Prior, the xenon chamber was pumped on for a couple of days until a base pressure of 1×10^{-7} mbar was reached. In order to have a high signal-to-background ratio, oxygen was added until the chamber was filled with a partial pressure of about 1×10^{-2} mbar of oxygen. The total amount of added oxygen is likely larger than expected from just the partial pressure alone since oxygen can adsorb to the stainless steel walls of the piping and xenon cell. While no data is available on the desorption rate of oxygen from stainless steel it is likely that the process will be temperature dependent and could be significantly suppressed at LXe temperature. The system was then filled with xenon gas until a total system pressure of 1 bar was reached, resulting in an impurity concentration of ~ 10 ppm. The measurement of the remaining oxygen partial pressure is performed through sampling the gas mixture via the cold-trap enhanced RGA system.

An initial RGA measurement with a purely gas phase mixture serves as a reference measurement. The liquefaction of known amounts of xenon, which is based on the measurement of the pressure drop in xenon storage cylinders, reduces the concentration of oxygen in the gas phase as some of it will dissolve into the LXe. Since the timescale for the dissolution and achieving a thermal equilibrium is not known, periodic measurements of oxygen partial pressure were taken until the oxygen partial

pressure stabilized, suggesting that a thermal equilibrium was reached. Typically, this meant waiting for ∼60 min before continuing with the liquefaction of xenon. The data for one such measurement campaign is shown in Figure 4.35. The reduction of the oxygen concentration in the gas phase, after properly accounting for fractional volumes occupied by the liquid and gas phase, can be used to calculate Henry's coefficient of oxygen in LXe. After three different measurement campaigns an average value of

$$H_{\mathrm{O_2,LXe}} = \frac{c_{\mathrm{O_2,gas}}}{c_{\mathrm{O_2,liquid}}} = 59 \pm 14 \tag{4.43}$$

is obtained, which is in agreement with other recent measurements [186]. The systematic errors in the measurement come from uncertainty in the xenon cell pressure when sampling the gas mixture with the cold-trap enhanced RGA system, where the variations arise from the PID cycle of the system trying to stabilize the temperature and result in changes in the order of 1 K. The central value suggests that the distribution of oxygen in a LXe system in thermal equilibrium can be described by ideal gas behavior, where Henry's coefficient is simply given by the ratio of the vapor pressures of oxygen and xenon at the LXe temperatures. Using available data on the parameters of the semi-empirical Antoine Equation [187, 188], describing the vapor pressure of a gas as a function of temperature we find

$$p_{\mathrm{LXe}}(T = 165\,\mathrm{K}) = 1.01\,\mathrm{bar} \tag{4.44}$$

$$p_{\mathrm{O_2}}(T = 165\,\mathrm{K}) = 65.23\,\mathrm{bar} \tag{4.45}$$

$$H = \frac{p_{\mathrm{LXe}}(T = 165\,\mathrm{K})}{p_{\mathrm{O_2}}(T = 165\,\mathrm{K})} = 64.28 \tag{4.46}$$

which is in good agreement with our measurement. Once Henry's coefficient has been determined for other impurity species, the setup can be used to inject a known amount of different gases into the system via the calibrated leak valve and correlate the

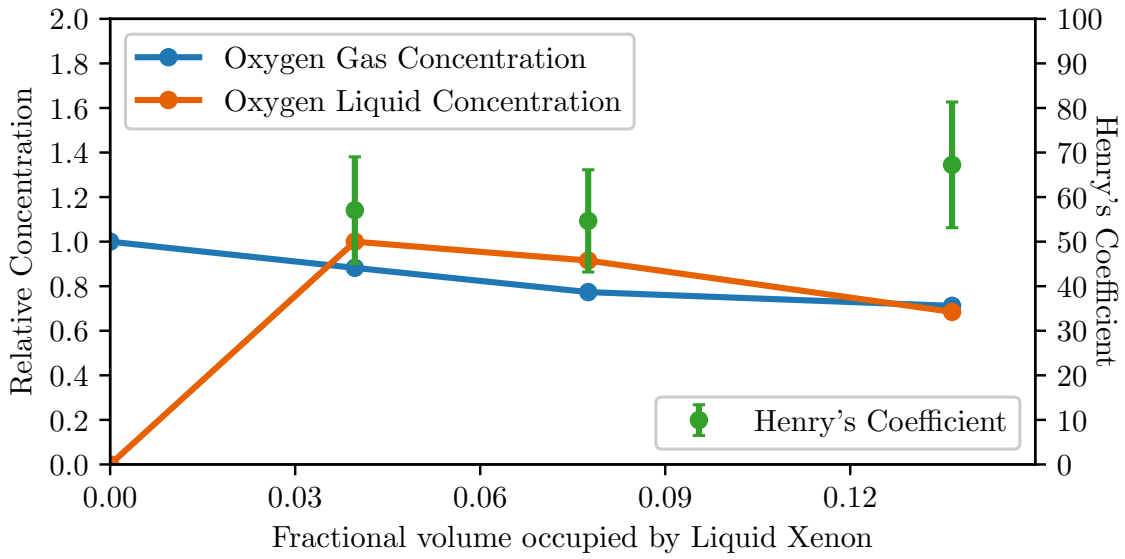

Figure 4.35: Measurement of the oxygen concentration in the xenon cell as a function of LXe level. The reduction in oxygen concentration is consistent with a Henry coefficient of ~ 60, indicating that the oxygen is dissolving into the liquid phase.

measured gas concentration with an effect on the electron lifetime in the purity monitor. This would allow a direct measurement of the electron attachment cross-section for various gas species and can be compared to literature values [138].

4.2.5 Conclusion and Outlook

The YPM is part of a two-setup system designed to develop a data-driven purity model for LXe and estimate the effect of impurity outgassing on the electron lifetime in a LXe TPC. The xenon cell was designed with intrinsically low-outgassing materials, which will provide a reliable and high sensitivity test setup to measure impurity concentrations at the level necessary for nEXO's electron lifetime goal of 10 ms. Initial measurements demonstrate a good understanding of the charge drift in LXe with good agreement with EXO-200 data and the first measurements of Henry's coefficient of oxygen in LXe were performed. The next steps for this setup include:

- expanding the catalog of Henry's coefficients for other gas species

- combining impurity concentration measurements with electron lifetime data to calculate the expected electron attachment cross-section for various gas species in LXe
- validating the Arrhenius relationship for the diffusion constant at LXe temperatures by measuring samples from the outgassing setup in the YPM
- qualifying candidate materials for nEXO

4.3 Energy Resolution

The model described in this section to estimate the energy resolution of nEXO follows the formalism developed in [80]. The optimal estimator $\langle E \rangle$ of the energy E of an event is given by a linear combination of the best estimator for the number of charge quanta $\langle n_q \rangle$ and scintillation quanta $\langle n_p \rangle$ produced

$$\langle n \rangle = \frac{\langle E \rangle}{W} \propto \cos\theta \cdot \langle n_q \rangle + \sin\theta \cdot \langle n_p \rangle \tag{4.47}$$

where $W = 11.5\,\text{eV}$ [80] is the average energy needed to create either an ionization electron or scintillation photon. This measurement of W from the EXO-200 is in good agreement with another recent measurement [189] but is in tension with the reported value of $W = 13.7\,\text{eV}$ in NEST [190]. θ is the rotation angle in the light-vs-charge parameter space to optimally take advantage of the anti-correlation between charge and light [191] and minimize the energy resolution. Each component is given by

$$\langle n_q \rangle = \frac{\langle E \rangle}{W} \cdot (1 - R) \tag{4.48}$$

$$\langle n_p \rangle = \frac{\langle E \rangle}{W} \cdot (I + R) \tag{4.49}$$

with R the fraction of recombining electron-ion pairs and I the fraction of photons produced through excitation. The energy resolution is simply given by the variance of the energy estimator $\langle n \rangle$ as

$$\frac{\sigma_n^2}{\langle n \rangle^2} = \frac{\sigma_q^2 + \sigma_p^2 + 2 \cdot \mathrm{Cov}_{q,p} + \sigma_{\mathrm{Xe}}^2}{\langle n \rangle^2} \tag{4.50}$$

where the first two terms represent the variance of the estimators for the number of quanta in the charge and light channels, respectively, and will be discussed in more detail below. The covariance term captures additional fluctuations in the number of quanta due to an imperfect recombination efficiency ϵ_r, i.e. the fraction of recombined electrons that produce a scintillation photon. The recombination efficiency is typically assumed to be perfect ($\epsilon_r = 1$) and therefore the variance σ_r^2 due to recombination fluctuations in either channel will perfectly cancel the contribution from the covariance term $\mathrm{Cov}_{q,p} = -\sigma_r^2$. A detailed measurement of the light and charge response of the EXO-200 detector put a constraint on the recombination efficiency of $\epsilon_r \in [0.97, 0.99]$ at the 68 % CL. A significant deviation from perfect recombination would need to be accounted for and could be added to Equation 4.50 via an additional term σ_r^2.

Light Readout

In nEXO, the total number of detected avalanches for an event is given by

$$n_{\mathrm{av}} = (\epsilon_p \cdot n_p + n_{\mathrm{DCR}}) \cdot (1 + \langle \Lambda \rangle) + n_{p,\mathrm{noise}} \tag{4.51}$$

where $\epsilon_p = \epsilon_{\mathrm{PTE}} \cdot \epsilon_{\mathrm{PDE}}$ is the total light collection efficiency, Λ is the number of additional correlated avalanches per parent avalanche within 1 µs, n_{DCR} is number of dark count events within the same time window and $n_{p,\mathrm{noise}}$ is the contribution from electronics noise. We can explicitly write down the variance of each term:

- The number of detected photons $n_{\mathrm{det}} = \epsilon_p n_p$ is the sum of n_p independent trials

in which each photons has a probability ϵ_p of being detected and $(1-\epsilon_p)$ of being absorbed elsewhere. Therefore, n_{det} follows a binomial distribution and its variance is given by $\sigma^2_{n_{\text{det}}} = n_p\epsilon_p(1-\epsilon_p)$. Its contribution to the variance of n_p is

$$\left(\frac{\mathrm{d}n_p}{\mathrm{d}n_{\text{det}}}\right)^2 \sigma^2_{n_{\text{det}}} = \frac{1}{\epsilon_p^2} n_p\epsilon_p(1-\epsilon_p) = \frac{n_p}{\epsilon_p}(1-\epsilon_p) \tag{4.52}$$

- The number of detected avalanches n_{av} will be greater than the sum of actually detected photons and the number of dark count events in a given time window by the number of correlated avalanches Λ. Assuming that the number of additional correlated avalanches follows a Poisson distribution with mean $\mu = (\epsilon_p \cdot n_p + n_{\text{DCR}}) \cdot \Lambda$, which for $\Lambda < 0.4$ generally is a good approximation, the variance of n_{av} is $\sigma^2_{n_{\text{av}}} = \mu = (\epsilon_p \cdot n_p + n_{\text{DCR}}) \cdot \Lambda$ and its contribution to the variance of n_p is

$$\begin{aligned}\left(\frac{\mathrm{d}n_p}{\mathrm{d}n_{\text{av}}}\right)^2 \sigma^2_{n_{\text{av}}} &= \left(\frac{1}{\epsilon_p \cdot (1+\Lambda)}\right)^2 (\epsilon_p \cdot n_p + n_{\text{DCR}}) \cdot \Lambda \\ &= \frac{n_p \cdot \Lambda}{\epsilon_p \cdot (1+\Lambda)^2} + \frac{n_{\text{DCR}} \cdot \Lambda}{\epsilon_p^2 \cdot (1+\Lambda)^2}\end{aligned} \tag{4.53}$$

- An additional term needs to be added to account for the number of additional avalanches from poor reconstruction due to noise in the light readout electronics.

$$\left(\frac{\mathrm{d}n_p}{\mathrm{d}n_{p,\text{noise}}}\right)^2 \sigma^2_{p,\text{noise}} = \frac{1}{\epsilon_p^2(1+\Lambda)^2} \sigma^2_{p,\text{noise}} \tag{4.54}$$

The likelihood of counting an additional 0.5 photo-electrons can be modeled by a complementary cumulative distribution of a normal distribution of mean 0.5 photo-electrons and width given by the electronics noise $\sigma_{p,\text{noise}}$

$$\eta^2_{noise} = \frac{N}{2}\left[1 - \text{erf}\left(\frac{0.5 \text{ SPE}}{\sqrt{2}\sigma_{p,noise}}\right)\right] \tag{4.55}$$

However, because of the very high signal-to-noise ratio and the excellent single photon resolution capabilities of SiPMs this contribution is completely negligible.

- Lastly, the accuracy to which the lightmap, described in section 4.1.5, can be calibrated, i.e. how well ϵ_p as a function of position in the detector is known, will add additional fluctuations to our estimate of n_p in the form of

$$\left(\frac{\mathrm{d}n_p}{\mathrm{d}\epsilon_p}\right)^2 \sigma^2_{\epsilon_p} = \left(\frac{n_{\mathrm{det}}}{\epsilon_p^2}\right)^2 \sigma^2_{\epsilon_p} = n_p^2 \frac{\sigma^2_{\epsilon_p}}{\epsilon_p^2} = n_p^2 \sigma^2_{lm} \tag{4.56}$$

where we call the fractional uncertainty in ϵ_p the lightmap error σ_{lm}.

Combining all this into a variance for n_p we get

$$\begin{aligned}\sigma_p^2 &= \left(\frac{\mathrm{d}n_p}{\mathrm{d}n_{\mathrm{det}}}\right)^2 \sigma^2_{n_{\mathrm{det}}} + \left(\frac{\mathrm{d}n_p}{\mathrm{d}n_{\mathrm{av}}}\right)^2 \sigma^2_{n_{\mathrm{av}}} + \left(\frac{\mathrm{d}n_p}{\mathrm{d}\epsilon_p}\right)^2 \sigma^2_{\epsilon_p} + \eta^2_{noise} + \sigma_r^2 \\ &= \frac{n_p}{\epsilon_p}\left[(1-\epsilon_p) + \frac{\Lambda}{(1+\Lambda)^2}\right] + \frac{n_{DC} + \eta^2_{noise}}{\epsilon_p^2 (1+\Lambda)^2} + n_p^2 \sigma^2_{lm} + \sigma_r^2 \end{aligned} \tag{4.57}$$

Charge Readout

The amount of collected charge is given by

$$n_e = n_q \cdot \epsilon_q + n_{\mathrm{noise}} = n_q \cdot e^{-\frac{t}{\tau_e}} + n_{q,\mathrm{noise}} \tag{4.58}$$

where $t = d/v$ is the drift time over a distance d with a drift velocity of $v = 1.73\,\mathrm{mm\,\mu s^{-1}}$ [90] and τ_e is the electron lifetime in LXe, i.e. the time after which only $1/e$ of the initially drifted secondary electrons have not yet been captured by electronegative impurities in the LXe. For the expected $\tau_e = 10\,\mathrm{ms}$ the charge collection efficiency is at least $\epsilon_q > 93\,\%$ throughout the entire detector. $n_{q,\mathrm{noise}}$ is the number of additional electrons detected due to noise in the charge readout electronics. Similar to the light readout we can breakdown the variance of each contribution as:

- n_e also follows a binomial distribution with mean $n_q \epsilon_q$ and variance $n_q \epsilon_q (1 - e_q)$

and its contribution to the variance of n_q is given by

$$\left(\frac{\mathrm{d}n_q}{\mathrm{d}n_e}\right)^2 \sigma^2_{n_e} = \frac{1}{\epsilon_q} n_q (1-\epsilon_q) \tag{4.59}$$

- The charge collection efficiency e_q or equivalently the electron lifetime τ_e are also subject to uncertainties from imperfect calibrations (similar to the lightmap error in the light readout) and hence add additional fluctuations of the form

$$\left(\frac{\mathrm{d}n_q}{\mathrm{d}\tau_e}\right)^2 \sigma^2_{\tau_e} = \left(\frac{n_e}{e^{-t/\tau_e}} \frac{-t}{\tau_e^2}\right)^2 \sigma^2_{\tau_e} = n_q^2 \left(\frac{t}{\tau_e}\right)^2 \frac{\sigma^2_{\tau_e}}{\tau_e^2} = n_q^2 \left(\frac{t}{\tau_e}\right)^2 \sigma^2_{\epsilon_q} \tag{4.60}$$

  where σ_{ϵ_q} is the fractional uncertainty in the charge collection efficiency.

- Unlike in the light readout the contribution from electronics noise dominates the fluctuations in the charge readout and can be written as

$$\left(\frac{\mathrm{d}n_q}{\mathrm{d}n_{q,\mathrm{noise}}}\right)^2 \sigma^2_{q,\mathrm{noise}} = \frac{1}{\epsilon_q^2} \sigma^2_{q,\mathrm{noise}} \tag{4.61}$$

  where the value for $\sigma^2_{q,\mathrm{noise}}$ is calculated for $0\nu\beta\beta$ events inside the FV after summing over the mean number of channels for an event with charge deposits in a given integration window. The charge noise term also includes possible correlated noise arising from instability in the cathode voltage which induces an RMS noise on the anode that would be picked up by the charge electronics. For a $100e^-$ current noise in the front-end ASIC an event-based noise of $1132e^-$ electrons is obtained for $\sigma^2_{q,\mathrm{noise}}$.

The total variance in the charge readout then reads

$$\begin{aligned}
\sigma_q^2 &= \left(\frac{\mathrm{d}n_q}{\mathrm{d}n_e}\right)^2 \sigma^2_{n_e} + \left(\frac{\mathrm{d}n_q}{\mathrm{d}\tau_e}\right)^2 \sigma^2_{\tau_e} + \left(\frac{\mathrm{d}n_q}{\mathrm{d}n_{q,\mathrm{noise}}}\right)^2 \sigma^2_{q,\mathrm{noise}} + \sigma_r^2 \\
&= \frac{n_q}{\epsilon_q}(1-\epsilon_q) + \frac{n_q^2}{\epsilon_q^2}\left(\frac{t}{\tau}\right)^2 \sigma^2_{\epsilon_q} + \frac{1}{\epsilon_q^2}\sigma^2_{q,\mathrm{noise}} + \sigma_r^2
\end{aligned} \tag{4.62}$$

Estimated Energy Resolution

Taking into account the contributions from the charge readout, light readout, and intrinsic fluctuations in the LXe to the variance of $\langle n \rangle$ the energy resolution can be estimated using:

$$\frac{\sigma_n}{\langle n \rangle} = \frac{\sqrt{\sigma_q^2 + \sigma_p^2 + 2 \cdot \mathrm{Cov}_{q,p} + \sigma_{\mathrm{Xe}}^2}}{Q + S} \tag{4.63}$$

$$= \frac{\sqrt{\sigma_q^2 + \sigma_p^2 + \langle n \rangle \epsilon_f}}{Q + S} \tag{4.64}$$

where in the second line we have made the general assumption that the anti-correlation is perfect and dropped the terms related to the recombination fluctuation. The LXe intrinsic contribution σ_{Xe}^2 arises from fluctuations in the number of quanta produced on an event-by-event basis for the same energy. It is typically parameterized as a fractional error on the total number of quanta $\langle n \rangle \epsilon_f$ where ϵ_f is the Fano factor. Even though the Fano factor has never been directly measured, calculations suggest a value of $\epsilon_f \approx 0.06$ [194]. Regardless of its true value even the most pessimistic scenario of $\epsilon_f = 1$, resulting in Poisson-like fluctuations of $\langle n \rangle$, has only a negligible impact on the energy resolution.

Using the values summarized in Table 4.3 the energy resolution of nEXO at $Q_{\beta\beta}$ is estimate to be $\sigma/Q_{\beta\beta} = 0.86\,\%$, significantly better than the required $\sigma/Q_{\beta\beta} = 1\,\%$ [85]. In addition, Figure 4.36 shows a summary plot of the dependence of the energy resolution on the various input parameters. Some parameters such as the PDE, PTE, τ_e and $\sigma_{q,\mathrm{noise}}^2$ are well motivated and rely on experimental measurements. Among these variables, the dominant terms in the light and charge channels are the light collection efficiency ϵ_p and charge readout electronics noise $\sigma_{q,\mathrm{noise}}^2$, respectively. On one side the baseline value for the former is a conservative estimate based on the worse

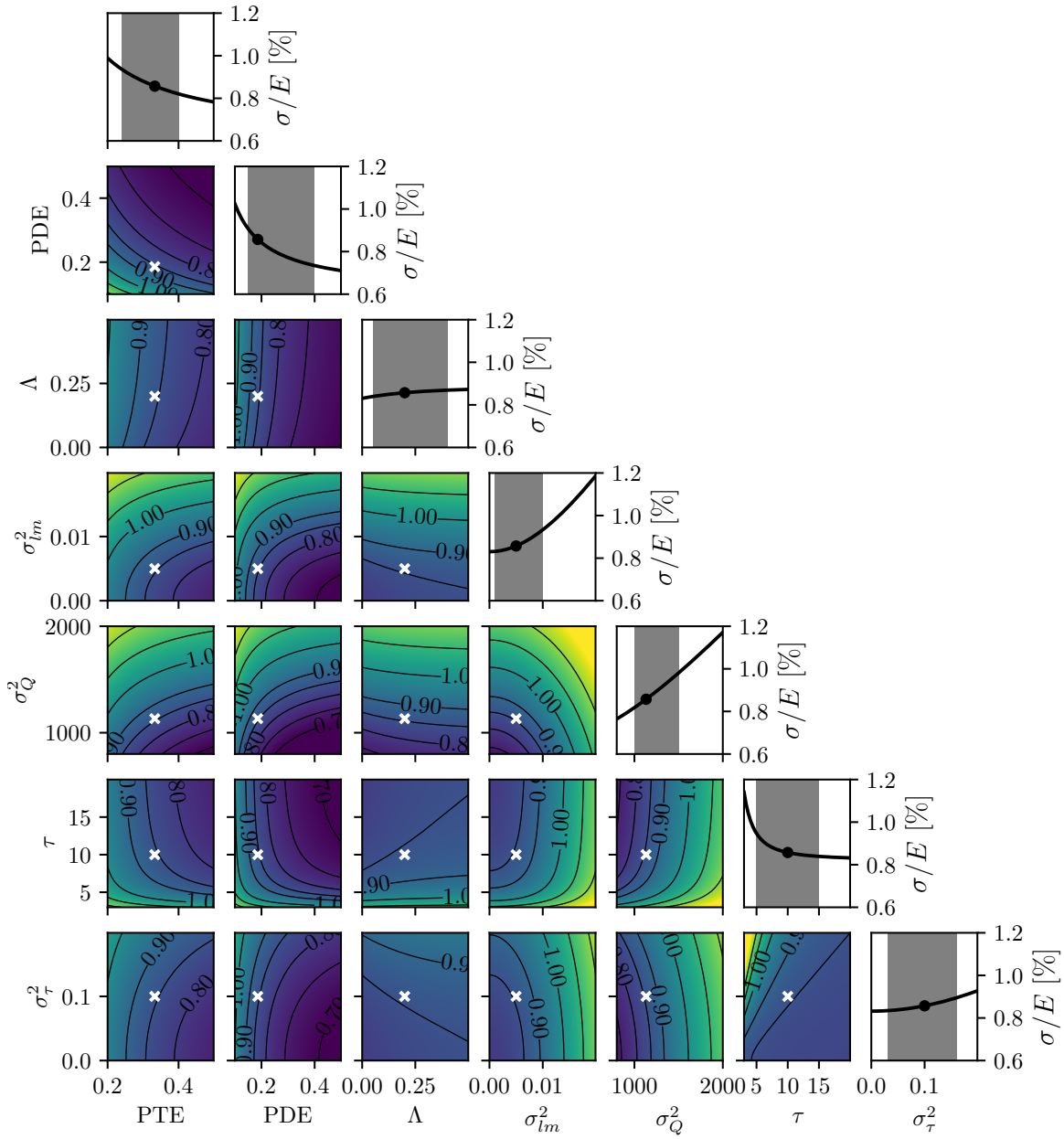

Figure 4.36: Evaluation of the predicted energy resolution as a function of all input parameters to the resolution model. The white cross in each panel indicated the value for the energy resolution for the current baseline parameters that are summarized in 4.3. The grey bands in the 1D plots show the possible range of the given parameter.

Parameter	Value	Description
Q	2.458 keV	Q-value of ^{136}Xe [192, 193]
W	11.5 eV	W-value in LXe [80]
n	213739	Number of Total Quanta; $\frac{Q}{W}$
γ_p	0.037 ph/eV	Light Yield at 400 V cm^{-1} [80]
n_p	90946	Number of Photons; $Q \cdot \gamma_p$
n_q	122793	Number of Electrons; $n - n_p$
ϵ_f	0.06	Fano Factor [194]
d	600 mm	Average Drift Length
v	1.73 mm µs^{-1}	Electron Drift Velocity at 400 V cm^{-1} [90]
σ_Q	1132 e^-	Charge Electronics Noise [33]
τ_e	10 ms	Electron Lifetime [33]
σ_{τ_e}	10 %	Systematic Error on τ_e [33]
PTE	33.3 %	Photon Transport Efficiency [33]
PDE	18.4 %	Photon Detection Efficiency [105]
ϵ_p	6.7 %	Light Collection Efficiency; PDE $\cdot$ PTE
σ_{lm}	0.5 %	Light Map Error [33]
$\langle\Lambda\rangle$	20.0 %	Mean Number of CA [33]
σ_Λ	20.0 %	Fluctuation in Number of CA [33]

Table 4.3: Summary of baseline parameters for evaluating nEXO's energy resolution using the semi-empirical resolution model.

performing VUV4 SiPMs resulting in $\epsilon_p = 6.7\,\%$ whereas the FBK devices would yield a significantly better $\epsilon_p = 9.4\,\%$, which would correspond to an improved energy resolution of $\sigma/Q_{\beta\beta} = 0.78\,\%$. On the other side the estimated value for $\sigma^2_{q,\mathrm{noise}}$ is on the more optimistic side assuming a $100e^-$ RMS current noise which, based on a simplistic analysis of the integrated noise of a $0\nu\beta\beta$ event using a optimized trapezoid filter, yields an event-based noise of $\sigma^2_{q,\mathrm{noise}} = 1132e^-$. Even though the charge readout electronics noise could be significantly worse a more sophisticated algorithm based on an optimum filter analysis [195] would allow compensating.

In other cases, such as σ^2_{lm} and σ^2_τ, measurements are not possible since it depends on the actual experiment and its performance after construction and commissioning. However, the baseline parameters for those variables were chosen based on previous experience in EXO-200 and by studying this resolution model to define specifications for the detector calibration such that their contribution to the overall energy resolution is sub-dominant. This results in a specification for the lightmap error to be $\sigma^2_{lm} < 0.5\,\%$ and the uncertainty in the electron lifetime to be $\sigma^2_\tau = 10\,\%$ at $\tau_e = 10\,\mathrm{ms}$, $\sigma^2_\tau = 6\,\%$ at $\tau_e = 7\,\mathrm{ms}$ or $\sigma^2_\tau = 3\,\%$ at $\tau_e = 5\,\mathrm{ms}$.

Despite the success of this resolution model when applied to EXO-200 data [80] it lacks additional effects present in a real experiment such as temporal variations, spatial non-uniformities, and non-gaussian shapes of the input parameters. The validation of some of the assumptions made here will need to be demonstrated in a small-scale LXe test setup, specifically designed to achieve a sub-percent energy resolution. This will allow placing well-informed constraints on the light and charge calibration systems for nEXO to ensure that the energy resolution goal of $\sigma/Q_{\beta\beta} \leq 1\,\%$ can be met. The impact of the energy resolution on the physics reach of nEXO will be discussed in Section 5.5.2.

Chapter 5

Exclusion and Discovery Sensitivity of nEXO

5.1 Monte Carlo Simulation 131

5.2 Event Reconstruction and Background Rejection 133

5.3 Background Model 142

5.4 Statistical Analysis 151

5.5 Results 163

5.6 Effective Majorana Neutrino Mass Sensitivity 180

5.7 Conclusion and Outlook 185

This chapter describes the evaluation of the exclusion and discovery sensitivity of the nEXO experiment to $0\nu\beta\beta$ in ^{136}Xe [33]. An overview of the input parameters of the simulation, reconstruction, background model, and likelihood fits is given, resulting in a robust bottom-up estimate of the physics reach of nEXO.

The content of this chapter is based on [33]. The author of this thesis contributed by developing a new light simulation framework that significantly improved the realism of the light transport and detection, implementing parts of the reconstruction algorithm, and contributing to all parts of the analysis including statistical tests to evaluate the discovery sensitivity and physics reach of nEXO.

5.1 Monte Carlo Simulation

The simulation of events, starting from the generation of the primary particles to the particle transport and their interactions in the LXe in nEXO is based on Geant4 [77]. The detector geometry was implemented using standard Geant4 shapes, leading to approximations due to the simplicity of the shapes, which are not expected to have any significant impact on the realism of the simulation. A rendering of the detector geometry in Geant4 is shown in Figure 5.1.

The relevant background events originate from radioactivate decays from the ^{238}U and ^{232}Th decay chains and from ^{40}K. However, only decays were simulated that will result in the emission of a γ with an energy of at least 800 keV and a branching ratio of $>1\,\%$. The isotopes that meet these criteria are:

- ^{238}U decay chain: ^{234}Pa and ^{214}Bi
- ^{232}Th decay chain: ^{228}Ac, ^{212}Bi and ^{208}Tl

The full background model will be discussed in more detail in Section 5.3. To optimize computation time some of the decay daughters were simulated independently and later combined, accounting for the proper branching ratios. Depending on their classification into a small, medium, or large contributor to the background budget a total of 100 yr worth of decays, at least one hit in the energy ROI or less than 20 % uncertainty in the overall rate in the energy ROI are deemed sufficient statistics, respectively.

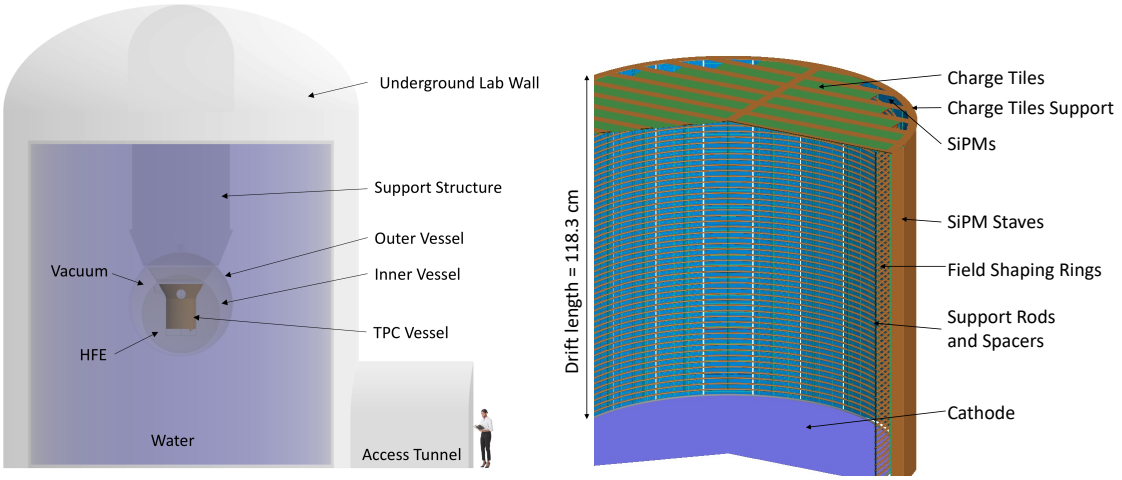

Figure 5.1: Rendering of the nEXO detector geometry in Geant4. The left side shows a section view of the large-scale components such as the water tank, inner and outer cryostat, and the TPC. The right side shows a close-up view of the TPC. Figures from [33].

The simulation of the $2\nu\beta\beta$ spectrum was split into a bulk region far away from the energy ROI below 2250 keV and a tail above 2250 keV possibly leaking into the ROI. A total of 5×10^9 events were simulated for both regions and then properly combined into a single energy spectrum of the $2\nu\beta\beta$ decay. This procedure ensures that a high statistics energy spectrum is obtained throughout the entire energy range and most importantly close to the ROI.

The production of charge and light quanta as ionizing radiation deposits energy in the LXe is simulated using the Noble Element Simulation Technique (NEST) [196]. Only the production of the quanta is handled by Geant4 and the transport is performed using standalone charge propagation and digitization simulations [89] and light propagation simulations (see Section 4.1). Version 2.0.1 of NEST [197] was modified to adjust the charge and light yields to better match the results obtained in EXO-200 [80]. The first modification regards the removal of an unphysical excess noise term that NEST added to the total number of produced quanta, which effectively inflated the Fano noise term mentioned in Section 4.3. As mentioned before, the Fano noise term is not well and an unphysical parameterization was used in NEST to match detector

effects, which may not be predictive for nEXO. Furthermore, this excess noise term is in tension with the noise model developed for and validated by EXO-200 [80] and the demonstrated energy resolution of 0.64 % by LZ [156]. In the second change, the NEST photoelectric model was replaced with the beta model for all electron recoil processes, which is in good agreement with EXO-200 data, suggesting that there are only marginal differences in the charge and light yields for βs and γs at the same energy [80]. These changes resulted in negligible differences in the charge and light quanta production in the bulk of the fiducial volume with a uniform electric field of $\sim$400 V cm^{-1}.

5.2 Event Reconstruction and Background Rejection

The event reconstruction in nEXO generally follows the successful procedure developed in EXO-200. The ability of the TPC technology to reconstruct the position of individual energy deposits in 3D and their energy enables a powerful multi-variate analysis combining the total energy, spatial distribution, and topological information.

5.2.1 Position Reconstruction

The position reconstruction of energy deposits happens independently in the x-y-plane and along the z-axis, which is defined to be parallel to the charge collection plane and the symmetry axis of the cylindrical TPC, respectively.

The z-position is determined using the waveforms of the induced current on the charge collection tiles. A simple threshold-based algorithm searches backward through the MC-truth waveforms, which have no added readout electronic noise, to determine the first sample below 95 % of the peak amplitude. The difference between the waveforms' start time and the threshold time, together with the known drift velocity,

can be used to infer the z-position.

To reconstruct the x-y-position of an energy deposit unambiguously, at least one x-strip and y-strip on the same tile have to be triggered. Corresponding x-y-strips are only combined if their z-position, based on the above method, matches. If such a match has been found the intersection of those strips will be used as the x-y-position for that energy deposit.

The radial position of the outermost deposit and the z-position of all deposits is used for defining a standoff distance, which is the distance to the closest detector surface and is used for fiducialization. Events that have a standoff distance of $>20\,\mathrm{mm}$ are rejected by the fiducial volume cut.

While the position reconstruction in LXe TPCs is generally based on the charge readout information because of the high charge collection efficiency and signal-to-noise-ratio compared to the light readout, nEXO's unique photon-detection system will have the capability to assist with the position reconstruction using the prompt scintillation signal in edge cases where charge collection is compromised or not possible.

5.2.2 Energy Reconstruction

The total energy of an event is reconstructed by performing an optimal linear combination of reconstructed ionization and scintillation energy, which will result in a significantly better energy resolution than possible with either light or charge information due to the anti-correlation in the production of light and charge quanta [191]. For simplicity, the two components are added without any weighting, which translates to a 45° rotation angle in Equation 4.47. This assumption is justified since the contribution from either light or charge channel to the overall energy resolution is comparable in nEXO. This is in contrast to EXO-200 where the noise in the light channel dominated the energy resolution and an optimal rotation angle that minimized the energy resolution had to be determined experimentally.

Ionization Energy The reconstruction of the ionization energy currently relies on MC-truth information by summing the electron lifetime corrected number of electrons from all channels that have truly collected charge (i.e. induction-only channels are excluded). The charge collection inefficiency due to a finite electron lifetime is corrected by inverting Equation 4.36 using $\tau_e = 10\,\text{ms}$ and the measured drift time on each channel. The final reconstructed charge also includes an additional Gaussian noise term with $\sigma_q^2 = 1130e^-$. This value was determined in a standalone study of waveforms from uniformly distributed $0\nu\beta\beta$ events, in which a trapezoidal filter is used to determine the number of collected charges by integrating the waveforms. The integration and rise time of the trapezoidal filter were optimized to yield the lowest possible energy resolution at $Q_{\beta\beta}$ and was found to be $\sim$40 µs. A shorter integration window results in underestimating the amount of collected charge whereas a longer integration beyond the event size will result in noise being added. In both cases, the energy resolution will become worse. The longer integration window is especially detrimental because of the significant $1/f$ component of the noise profile of charge readout ASIC mentioned in Section 3.2. The construction of an improved energy estimator is expected to significantly improve the uncertainty in the charge energy measurement. One such algorithm is based on an optimum filter [195].

Scintillation Energy In order to simulate the number of scintillation photons detected for each event, the light collection efficiency $\epsilon_p(r, z)$ was calculated as a function of the radial (r) and longitudinal (z) initial position inside the detector (see Section 4.1.5). The light collection efficiency is determined by multiplying the lightmap in Figure 4.9, containing the information about the position-dependent PTE, with the SiPM-dependent PDE. The photon transport simulation already accounts for the reflectivity of photons at the SiPM surfaces. Therefore the PDE, which is typically measured at an angle close to normal incidence, needs to be corrected for the

reflectivity in order to not double count this effect. The total light collection efficiency will be

$$\epsilon_p(r,z) = \mathrm{PTE}(r,z) \cdot \frac{\mathrm{PDE}}{1-R_0} \tag{5.1}$$

where R_0 is the reflectivity at or close to normal incidence. For this study PDE = 13.4 % [105] and R_0 = 28 % [110] for the HPK VUV4 were used as a conservative estimate since the FBK VUV-HD1 devices perform better with PDE = 21.1 % [102] and R_0 = 25 % [110].

The corresponding $\epsilon_p(r,z)$ is applied to each scintillation hit ($\epsilon_p^{\mathrm{hit}}$) in an event, and a binomial distribution with N_P trials and $\epsilon_p^{\mathrm{hit}}$ probability is used to determine the number of detected photons: $N_P^{\mathrm{hit}} \sim B(N_P,\, \epsilon_p^{\mathrm{hit}})$. The contribution from correlated avalanches is modelled by a Poisson distribution: $N_\Lambda^{\mathrm{hit}} \sim \mathrm{Pois}(\Lambda \cdot N_P^{\mathrm{hit}})$, where $\Lambda = 0.2$ is the total number of correlated avalanches per avalanche in a time window of 1 μs, conforming with recent measurements [102, 105]. The same measurements also show that the dark count rate and other electronic noise can be completely neglected. Therefore, the total number of scintillation photons triggering an avalanche in each event (N_P^{evt}) is the sum of N_P^{hit} and N_Λ^{hit} for all hits. The number of reconstructed photons ($\tilde{N}_P$) in each event is obtained by the correction $\tilde{N}_P = N_P^{\mathrm{evt}}/[\epsilon_p^{\mathrm{evt}} \cdot (1+\Lambda)]$, where $\epsilon_p^{\mathrm{evt}}$ is the energy-weighted average of all $\epsilon_p^{\mathrm{hit}}$. The position and energy information in this correction is retrieved from the scintillation hits generated by NEST. An additional systematic error due to imperfect knowledge of $\epsilon_p^{\mathrm{evt}}$ has been added and is assumed as a 0.5 % relative error. Based on our energy resolution model this is the value below which its contribution to the rotated energy resolution can be considered subdominant. Additional work to better understand position-dependent variations and the resulting requirements for the detector calibration will be part of future studies.

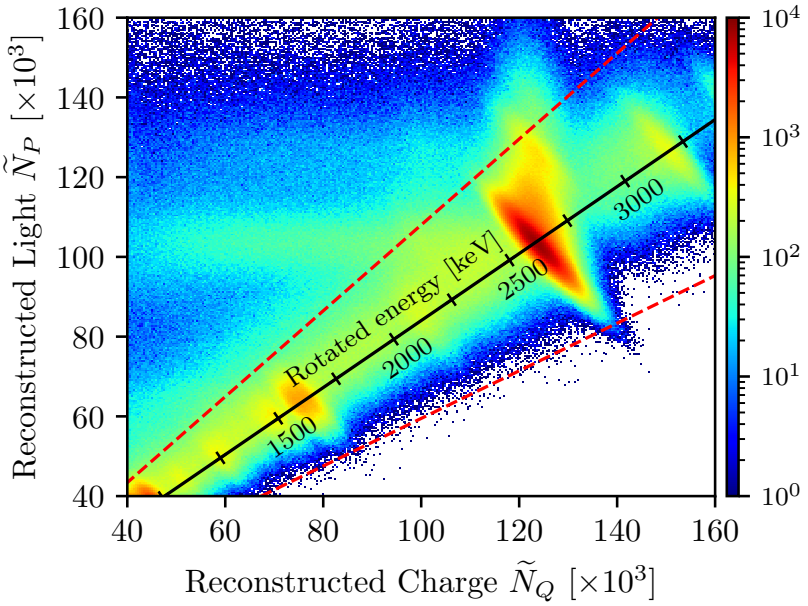

Figure 5.2: Reconstructed light and charge for simulated events from the ^{232}Th decay chain originating from the TPC vessel. These events lie within the fiducial volume. The projected of these events onto the rotated energy axis, which is shown as a black line at an angle of $-45°$, results in a significantly improved energy resolution than any individual channel would allow. The implemented cut on the charge-to-light ratio is shown as red dashed lines and rejects all events outside their boundaries. Figure from [33].

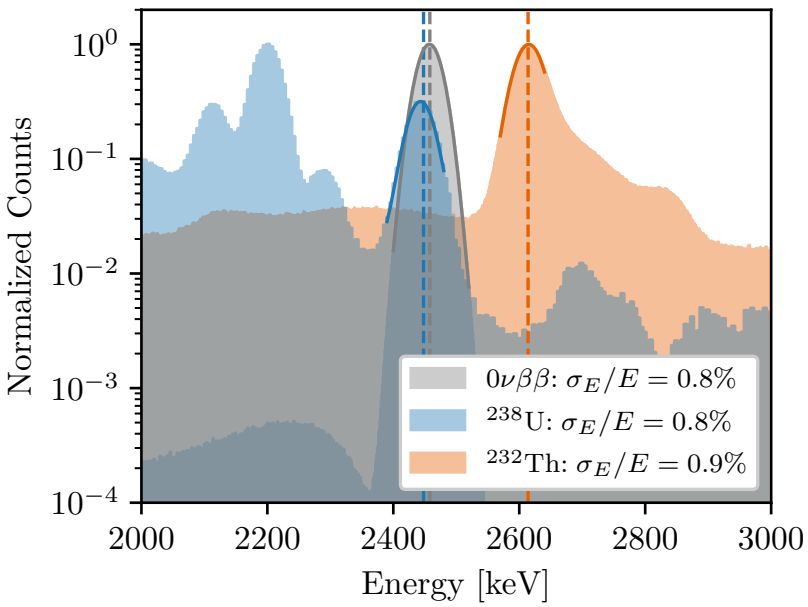

Figure 5.3: Normalized energy spectra of simulated $0\nu\beta\beta$, ^{232}Th and ^{238}U events inside the fiducial volume using the rotated energy variable. Gaussian fits to the known peaks of $0\nu\beta\beta$, ^{214}Bi and ^{208}Tl, indicated via dashed lines, yields the expected energy resolution σ_E/E. Figure from [33].

Charge-to-Light Ratio The reconstructed number of generated photons $\tilde{N}_P$ and electrons $\tilde{N}_Q$ is shown in Figure 5.2 for simulated events from the ^{232}Th decay chain originating from the TPC vessel. The simultaneous measurement of light and charge allows placing a cut on their ratio to reject background events or events with an anomalous charge-to-light ratio. This cut is optimized using full-absorption peaks from simulated ^{208}Tl and ^{40}K γ-decays retaining 99 % of events and validated against simulated $0\nu\beta\beta$ events for which a 99.7 % signal efficiency was achieved.

Energy Resolution The event energy is calculated by

$$E = (\tilde{N}_P + \tilde{N}_Q) \cdot W \tag{5.2}$$

where W is the average energy to create a single quantum of either charge or light. Figure 5.3 shows the rotated energy for simulated events from ^{232}Th and ^{238}U chain decays in the TPC vessel as well as from $0\nu\beta\beta$ decays in the LXe. The energy

resolution extracted at the peak energies are $\sigma/Q_{\beta\beta} \simeq 0.8\,\%$. These values were found to be similar for γ events with single or multiple energy deposits. These results are consistent with the model described in Ref. [85], and validated with EXO-200 data [80]. Studies of the dependence of the energy resolution on the electron lifetime show that a 10 ms, 7 ms or 5 ms lifetime calibrated to 10 %, 6 % or 3 % accuracy, respectively, would reduce the overall energy resolution by only 0.03 %, in absolute value, making its contribution subdominant. The effect of the energy resolution on the nEXO $0\nu\beta\beta$ sensitivity is discussed in Section 5.5.2.

5.2.3 DNN-Based Background Rejection

The development and adaptation of machine learning based tools to distinguish between signal and background events have grown significantly in the particle physics community over the last decade [198]. They provide a compelling and easy-to-implement alternative to more traditional analysis methods using high-level event information such as energy, spatial distribution, and topology.

Boosted Decision Trees (BDTs) are a commonly used machine learning algorithm to make use of such information to provide an improved background rejection. In EXO-200, a BDT-based analysis yielded a ∼15 % improvement in the final sensitivity compared to a more traditional single-site and multi-site separation [32, 69]. One drawback of this method is the reliance of the BDT input parameters on the robustness of the reconstruction and the underlying assumptions. Therefore, an algorithm that can extract topological information based on lower-level information such as the raw waveforms is expected to perform better. One such way would be the use of a deep neural network (DNN) based event classifier which has been successfully implemented in EXO-200 [32, 199].

Following the same general approach, a DNN discriminator was developed for nEXO [89]. The training dataset for the DNN included 1.4×10^6 $0\nu\beta\beta$ and γ events,

respectively. The events of both types were uniformly distributed in the detector and their energy was randomly drawn from a uniform distribution between 900 keV and 3600 keV. This choice of event samples ensures that the DNN prioritizes the topological differences between $0\nu\beta\beta$ and γs instead of their spectral shape in energy and position space. This method will yield an independent third dimension to the multi-variate analysis, maximizing the discrimination of backgrounds. The training data consists of two-dimensional images of the charge readout waveforms, where all channels with a true number of collected electrons were included and channels that have a combination of collection and induction signals.

The DNN discriminator, when applied to an event, will provide a DNN score from 0 to 1, where events with a DNN score of 0 or 1 are more background-like or signal-like, respectively. The left column in Figure 5.4 shows the distribution of DNN scores for $0\nu\beta\beta$ events as well as γ backgrounds from the ^{232}Th and ^{238}U decay chain originating in the TPC vessel with energies within the energy ROI around $Q_{\beta\beta}$. The distribution for γ backgrounds peaks around a DNN score of 0 which corresponds to the events undergoing Compton-scattering and being highly multi-sited. However, an additional smaller population of events closer to 1 exists, which are interactions in which the γ deposits all its energy via the photo-electric effect in a single location and is almost indistinguishable from the similarly spatially contained $0\nu\beta\beta$ events. On the contrary, the DNN score distribution of $0\nu\beta\beta$ events is centered close to a value of 1 but has a less pronounced lower tail of DNN values from $0\nu\beta\beta$ undergoing Bremsstrahlung and appearing more background-like.

To evaluate the performance of a binary classifier, such as the DNN discriminator, it is common to use the Receiver Operating Characteristic (ROC) curve, which shows the signal efficiency as a function of background misidentification for any given point along the DNN score axis. The performance of a classifier approaches the optimum as the area under the curve approaches unity. In this case, all signals are perfectly

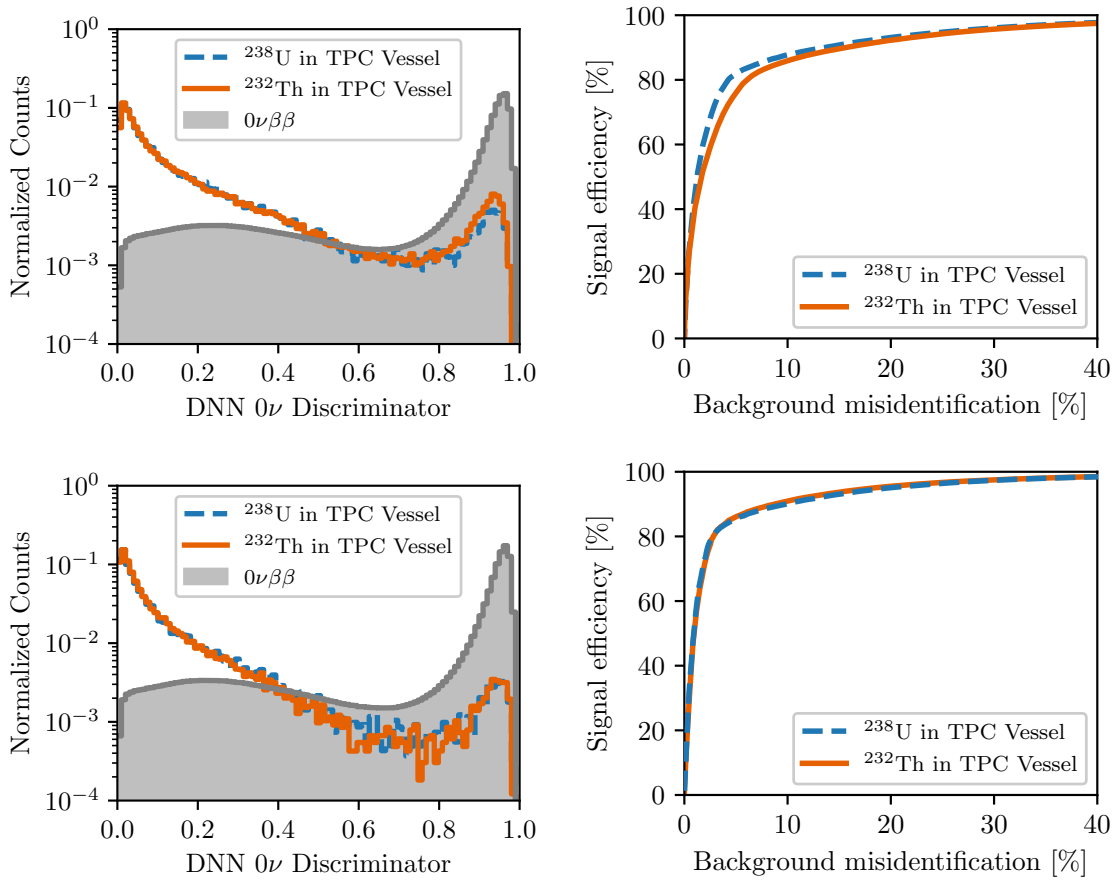

Figure 5.4: (left) Plot of the distribution of DNN scores for simulated $0\nu\beta\beta$, for ^{232}Th and ^{238}U background events originating from the TPC vessel. (right) ROC curves show the signal efficiency as a function of background misidentification, quantifying the performance of the DNN. The top row is for events within the full fiducial volume, whereas the bottom row applied a tighter fiducial volume cut using only events within the innermost 2000 kg (i.e. a standoff distance of larger than 104 mm).

separated, resulting in a 100 % rejection of backgrounds without sacrificing signal efficiency. For events within the full fiducial volume (i.e. for a standoff distance larger than 20 mm) the discrimination of ^{238}U backgrounds is more efficient than for ^{232}Th backgrounds. The main γs of concern from these two decay chains are the ^{214}Bi and ^{208}Tl with an energy of 2448 keV and 2615 keV, respectively. The energy of the ^{208}Tl γ is outside the energy ROI and is therefore unlikely to produce any signal-like backgrounds in the ROI when interacting via the photoelectric effect. However, it can undergo an initial Compton scatter in the LXe skin, depositing only a small

amount of energy before interacting within the FV and depositing the remaining energy inside the FV in a single location. For ^{214}Bi γ the opposite is true where only single photo-electric interactions will produce signal-like backgrounds due to its proximity to $Q_{\beta\beta}$ and a prior Compton-scatter would push the energy deposited outside the energy ROI. The contribution from these events comes predominantly from events close to the edge of the FV and the discrimination power for both types of γs is similar once a tighter fiducial volume cut is imposed, as can be seen in the bottom row of Figure 5.4.

Overall, the DNN discriminator allows removal of $\sim$95 % of the background events from external γs while keeping $\sim$85 % of the $0\nu\beta\beta$ signal. It should be stressed though that while these benchmarks are useful in comparing the performance of this DNN discriminator to other topological discriminators, nEXO's multi-variate analysis takes advantage of the entire DNN score distribution of signal and backgrounds and optimally weights them when performing a binned negative log-likelihood fit to MC toy data (described in more detail in Section 5.4).

5.3 Background Model

A robust estimate of the performance of nEXO, and any other experiment in the design phase, relies critically on a reliable and well-founded background model. The sensitivity of an experiment typically scales as

$$T_{1/2}^{0\nu} \propto \sqrt{t} \tag{5.3}$$

where t is the livetime of the experiment as long as it is performing a background limited search. Upcoming tonne-scale experiments are approaching the quasi-background free regime ($b \sim 1 \times 10^{-5}\,\mathrm{cts\,kg^{-1}\,yr^{-1}\,FWHM^{-1}}$) in which the reachable sensitivity will

start scaling more favorably as

$$T_{1/2}^{0\nu} \propto t \tag{5.4}$$

Achieving background levels low enough to run a quasi-background-free experiment requires stringent radioactivity control. One key aspect is extensive radio-assay measurements of all detector components to only choose the most radio-pure materials. The success of this approach has been successfully demonstrated by EXO-200, which has pioneered the construction of ultra-pure LXe-based TPCs and achieved an excellent agreement between their predicted background and the observed data to within fit uncertainties [63]. nEXO builds upon EXO-200 experience [64] and has expanded its catalogue of screened materials substantially [33, 85, 92].

Not all backgrounds are equally important for a dedicated $0\nu\beta\beta$ search with a Q-value of 2458 keV and only backgrounds that can produce an energy deposit within the energy ROI, defined as $Q_{\beta\beta} \pm \mathrm{FWHM}/2$, are of primary interest. Furthermore, as mentioned in earlier chapters γ-backgrounds with energies at the MeV-scale tend to undergo Compton-scattering and have a different topology than the spatially contained $0\nu\beta\beta$-events. The categorization into single-site or multi-site events is based on the DNN-discriminator score (described in Section 5.2.3), where events with DNN > 0.85 have a more signal-like (single-site like) topology. This categorization recovers the discrimination power of a simple classical classification based on event multiplicity as was used in [92]. To quantify the importance of each background component the fraction of total events that fulfill the following conditions is calculated:

- within the energy ROI $\longrightarrow$ $E \in [2415, 2481]$
- within the innermost 2000 kg $\longrightarrow$ $x_{\mathrm{standoff}} > 104$ mm
- has signal-like topology $\longrightarrow$ DNN > 0.85

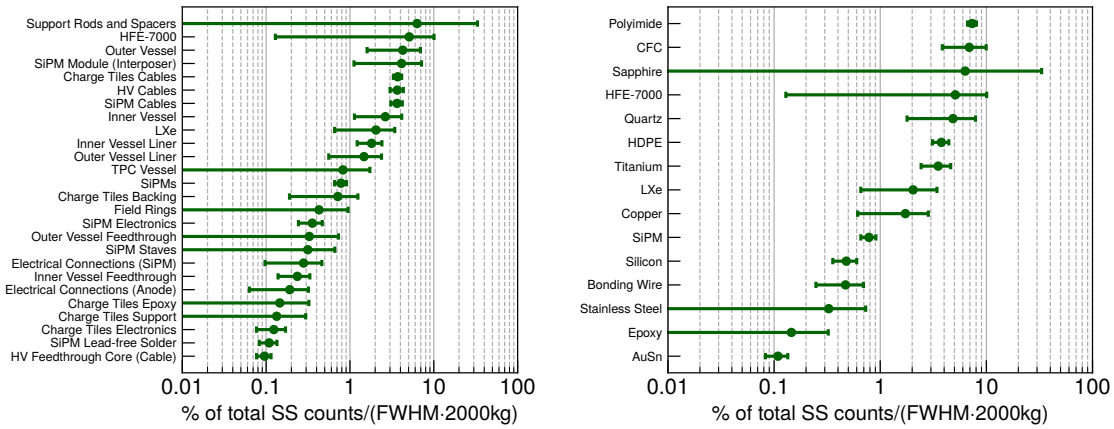

Figure 5.5: Breakdown of the percent contribution of various intrinsic backgrounds based on the component (left) or the material (right). Only events with a DNN score of > 0.85, energy within one FWHM around $Q_{\beta\beta}$, and a standoff distance larger than 104 mm are selected. Figures from [33]

This is referred to as the "hit efficiency". Choosing the innermost 2000 kg as a criterion is because this region is significantly more radio-pure because of the excellent shelf-shielding capabilities of LXe and ∼95 % of the overall half-life sensitivity comes from this region compared to the full fiducial volume. This will be discussed in more detail in Section 5.5.1. Additionally, for this study, only backgrounds were considered that would deposit at least >700 keV of energy in the TPC as events below that threshold are unlikely to have any impact on the energy ROI.

Background components in nEXO can be broadly categorized as coming from intrinsic, exposure-based, and ^{222}Rn-based radioactivity and will be discussed separately below.

5.3.1 Intrinsic Radioactivity

The radioactive backgrounds originating from the materials the detector is made of or are present in the LXe fall into this category. A summary of the individual contributions by material and components is shown in Figure 5.5.

Long lived radionuclides contained in the detector materials are a concern, especially the backgrounds from decays of daughters in the ^{238}U and ^{232}Th chains. They have a very long half-life of 4.47×10^9 yr [200] and 1.4×10^{10} yr [201], respectively, and therefore will be present throughout the livetime of any experiment. This results in a continuous production of the most prominent radioactive daughters ^{214}Bi and ^{208}Tl, respectively. Due to their significantly shorter half-life, their presence in the detector is assumed to be in secular equilibrium.

The ^{214}Bi γ-decay has an energy of 2448 keV and directly overlaps with the energy ROI. The γ released from the decay of ^{208}Tl has an energy of 2615 keV. Due to the significant Compton-scattering of γs at these energies the former can be rejected more efficiently (as shown in Figure 5.4). While the latter has its full absorption peak outside the energy ROI it can undergo Compton-scattering in which only a small part of its energy could be deposited outside the fiducial volume, pushing the full absorption peak into the ROI when depositing the remaining energy inside the fiducial volume.

^{60}Co and ^{40}K have major γ-lines at 1173 keV, 1332 keV and 1460 keV, respectively. While these energies are far outside the energy ROI and don't pose any direct concern for the $0\nu\beta\beta$ search they are important in constraining and measuring the $2\nu\beta\beta$ energy spectrum. In addition, other physics analyses such as the search for the $2\nu\beta\beta$ or $0\nu\beta\beta$ of ^{134}Xe with a $Q_{\beta\beta} = 825.8 \pm 0.9$ keV [202], Majoron-emitting modes of $2\nu\beta\beta$ in ^{136}Xe [203, 204] or other more exotic searches [205] depend on a well-constrained background model at lower energies. Despite the sum energy of both coincident ^{60}Co γs with 2505 keV being close to the energy ROI these events can be very effectively rejected because of their highly multi-sited topology since the likelihood of both γs interacting at the same spot within the fiducial volume (within the position resolution of the detector) is completely negligible.

Liquid Xenon based backgrounds arise from radionuclides other than ^{136}Xe that are present in the enriched LXe for nEXO. The enrichment process will yield 90 % $^{\text{enr}}$Xe in ^{136}Xe, where the remainder will be largely comprised of ^{134}Xe. With a Q-value below 1000 keV, this poses no background for the $0\nu\beta\beta$ search of ^{136}Xebut could be a significant background for lower energy exotic searches.

An irreducible background is the $2\nu\beta\beta$ decay of ^{136}Xe which has a half-life of $(2.165 \pm 0.061) \times 10^{21}$ yr [66]. Because of the similarities with a $0\nu\beta\beta$ event in terms of its topology and spatial distribution in the detector, the only way to reduce this background is with a good energy resolution. At the expected $\sigma/Q_{\beta\beta} = 0.8\,\%$ the expected rate of $2\nu\beta\beta$ events leaking into the energy ROI is estimated to be $\sim 2 \times 10^{-3}\,\text{cts}\,\text{FWHM}^{-1}\,\text{t}^{-1}\,\text{yr}^{-1}$ and is therefore negligible. As will be discussed in Section 6.2, a future kilo-tonne scale LXe experiment searching for $0\nu\beta\beta$ will need to further improve the energy resolution to ∼0.5 % to render the $2\nu\beta\beta$ background subdominant.

A relatively recent addition to the background model is ^{42}Ar which will be present in trace amounts in the xenon. The most prominent decay channel is the β-decay of its daughter ^{42}K with a Q-value of 3525 keV, overlapping with the energy ROI. In 0.02 % of the cases this decay will emit a 2424 keV γ. Obtaining a reliable estimate for the concentration of ^{42}Ar in $^{\text{enr}}$Xe is difficult and depends on various assumptions, such as the ratio between ^{42}Ar and the more abundant ^{40}Ar before and after enrichment. Measurements of the ^{40}Ar concentration in the $^{\text{enr}}$Xe in EXO-200 [206] are used to obtain a ^{42}K activity of $2.59 \times 10^{-9}\,\text{mBq}\,\text{kg}^{-1}$, which is negligible for nEXO even if the activity was 5 times as large [33].

5.3.1.1 Electro-formed Copper

In [92] the background model for nEXO was dominated by intrinsic radioactivity from ^{238}U and ^{232}Th in the TPC vessel, which was assumed to be made from the

most radio-pure copper that is commercially available. However, further reduction in intrinsic radioactivity can be achieved by electroplating high-purity copper in a sulfate solution onto a cylindrical mandrel cathode made of stainless steel [207]. Impurities in the copper from ^{238}U and ^{232}Th can be effectively reduced by a factor of 25 and 13, respectively, due to the difference in electrochemical potential relative to copper. The MAJORANA demonstrator has pioneered the construction of components from in-house custom electroformed copper (EFC) [208, 209]. Therefore, in the current conceptual design nEXO will use EFC for building the TPC vessel, the FSRs, and parts of the cathode. The major engineering challenges are related to realizing a large enough chemical bath to produce the large-scale copper structure for nEXO and growing the electroformed copper in a reasonable time scale (current growth times are on the order of mm per month).

5.3.2 Exposure-based Radioactivity

Additional backgrounds, besides the intrinsically present backgrounds above, can be added to the detector either during the procurement of materials, construction of parts, or general handling of any detector component before assembly. Furthermore, cosmogenic activation of detector components needs to be considered and is comprised of an initial above-ground contribution and a later steady-state activation underground.

Initial studies have estimated that the above-ground activation of copper-based cosmogenically activated isotopes can be controlled to negligible levels. This would involve limitations to the above-ground exposure and sufficiently long storage time underground for any activated isotopes to decay away to a negligible amount.

The steady-state cosmogenic activation underground is largely concerned with the production of ^{137}Xe via

$$^{136}\mathrm{Xe} + n \longrightarrow {}^{137}\mathrm{Xe}^{*} \longrightarrow {}^{137}\mathrm{Xe} + \gamma\,(4026\,\mathrm{keV}) \tag{5.5}$$

which undergoes a β-decay with a Q-value of 4173 keV and a half-life of $T^{0\nu}_{1/2} = 3.82$ min. The difficulty with this background is the β-like event signature that overlaps with the energy ROI.

The primary source for these neutrons is assumed to be the spallation of cosmogenic muons. However, a detailed study is needed to assess the contribution of radiogenically produced neutrons from the surrounding material in the underground laboratory. Since the muon rate drops significantly with increasing overburden, a deeper underground laboratory is preferred. The dependence of the ^{137}Xe rate with respect to the site of the experiment and the corresponding impact on the sensitivity will be discussed in Section 5.5.3.

As discussed in Section 3, the nEXO TPC and cryostats will be submerged in a water tank that is instrumented with PMTs and serves as a water Cherenkov detector. Interactions of muons in the water thank will produce Cherenkov light, that are detected by the PMTs, and which can be used in coincidence with the prompt γs with a total energy of 4026 keV from the de-excitation of ^{137}Xe in the TPC. It is estimated that a veto efficiency of >70 % can be achieved with this scheme and a negligible loss in livetime of <1 day per year.

5.3.3 Radon-based Radioactivity

The relevant decay in the ^{222}Rn chain is the β-decay of ^{214}Bi with a Q-value of 3272 MeV and a half-life of 19.9 min. Only such decays that happen in the TPC are of concern and trace concentrations of radon in the HFE are estimated to be negligible. The decay to the ground state of ^{214}Po has a branching ratio of 19.67 %, but in 1.58 % of the cases the decay happens to an excited state of ^{214}Po, releasing a γ with an energy of 2448 keV. This decay is quickly followed by the α-decay of ^{214}Po with a half-life of 162.3 µs. The tagging of this BiPo coincidence is ∼100 % efficient for a 1500 µs veto time and for events that happen inside the fiducial volume

since αs are unambiguously identified through their vastly different light to charge ratio compared to βs or γs. However, some fraction of the ^{222}Rn decay daughters are produced as positively charged ions [210] and are drifted towards the negatively biased cathode and FSRs. For plated out ^{222}Rn decay daughters, 50 % of the time the α from the ^{214}Po decay is emitted into the bulk and the tagging efficiency of the BiPo decay chain drops correspondingly. The details about the simulated ion fractions and tagging efficiencies for various parts of the TPC can be found in [33]. The tagging of surface-based backgrounds from the FSRs through the charge information is heavily compromised due to poor charge collection and large systematic errors in regions of highly non-uniform electric fields. The unique light detection system in nEXO with its granular pixelization, high signal-to-noise ratio, and good light collection efficiency could be used in these edge cases to tag the ^{214}Bi γ through the light response from the accompanied β with a reduced Q-value of 824 keV. Studies to investigate the effectiveness of this method and the potential rejection of surface-based radon backgrounds are ongoing.

The estimate of the ^{222}Rn background in nEXO is based on an extrapolation from EXO-200, where a steady-state population of 200 radon atoms in the TPC was observed. Furthermore, it is assumed that ^{222}Rn was largely emanating from surface areas in the xenon plumbing and recirculation line. Given the difference in the size of the purification lines in nEXO, the projected steady-state population is 600 atoms. To better understand the source of radon in EXO-200, its gas handling system has been reassembled to perform detailed radio-assay measurements.

Due to the significant reduction in intrinsic radioactivity through the use of in-house EFC, the radon background in the current conceptual design contributes $\sim$50 % of the total background budget. Therefore, an additional screening program will select all materials, that would be in contact with the xenon, based on their radon emanation rate. This also requires careful handling of detector components in radon-depleted

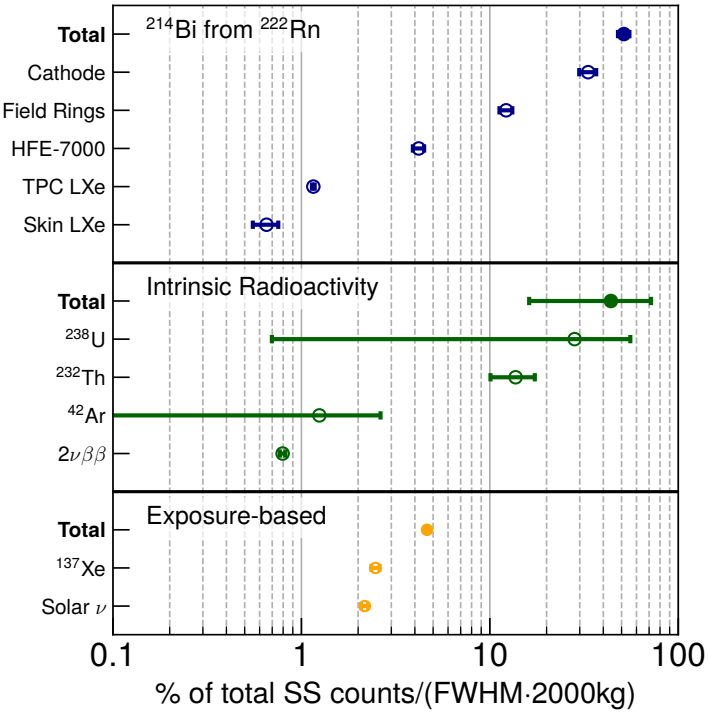

Figure 5.6: nEXO's background budget, divided into contributions from ^{222}Rn based, intrinsic and exposure-based radioactivity. The reduction of the intrinsic background contribution through the planned use of in-house EFC makes this now the second largest contribution after background from ^{222}Rn. Figure from [33].

clean rooms. The LXe TPC technology has the advantage of allowing upgrades to the recirculation and purification system to improve the radiopurity of the xenon if the radon level is higher than expected. A successfully demonstrated method for radon removal is the use of an inline distillation column [211, 212].

5.3.4 Background Budget

The overall background budget, which includes contributions from all the abovementioned sources is shown in Figure 5.6. In nEXO's current conceptual design the largest background contributor is ^{222}Rn, comprising ∼50 % of the total backgrounds. More specifically, ^{222}Rn daughters plated out on the cathode are the dominant background source with ∼30 %. The impact a potential increase due to mismodeling or reduction

due to future improvements of each category has on the sensitivity will be discussed in Section 5.5.3.

5.4 Statistical Analysis

Searches for new physics, including $0\nu\beta\beta$, rely on the proper inference of the statistical significance of a given dataset. In the case of discovery, the predictions of the Standard Model are taken as the null hypothesis H_0, including only known process, and which needs to be tested against an alternative hypothesis H_1, which proposes the existence of a new process. These hypothesis tests return a p-value ($1 - p = \mathrm{CL}$) which quantifies the significance of the observed signal and typically needs to fall below the false discovery probability of $\alpha = 3 \times 10^{-6}$ to qualify for discovery in particle physics. It is common to convert the p-value into an equivalent significance Z, which can be defined as the distance in standard deviations of a Gaussian distribution for which the cumulative probability is equal to $1 - p$

$$Z = \Phi^{-1}(1 - p) \tag{5.6}$$

where Φ is the quantile function of the standard normal distribution, i.e. the inverse of the cumulative distribution function. The above false discovery probability, therefore, is equivalent to a 5σ significance. For $0\nu\beta\beta$ searches, the discovery sensitivity is typically reported for a p-value of 0.03, which corresponds to a significance of $Z = 3\sigma$ or a confidence level of 99.7 %.

In the absence of new physics, one can instead evaluate the exclusion sensitivity, quantifying the upper limit on the number of signal counts one would get with the expected backgrounds and no true signal at the 90 % CL. In this scenario, H_0 and H_1 switch roles, where the background-only hypothesis is the alternative hypothesis that is tested against the null hypothesis which assumes the presence of a new physics

signal.

For both cases, this generally requires computationally expensive Monte Carlo calculations to obtain a statistically representative ensemble of toy datasets that can be used to estimate the expected exclusion and discovery significance. A common method in particle physics to evaluate the expected exclusion or discovery sensitivity is via a frequentist analysis using the likelihood ratio test method for building a test statistic, that can be used to run the abovementioned hypothesis tests [213, 214]

The next few sections will give an overview of the methodology used for evaluating the exclusion or discovery sensitivity of nEXO to $0\nu\beta\beta$ of ^{136}Xe.

5.4.1 Likelihood Function and Test Statistic

Ideally, one would construct an un-binned likelihood function that will preserve all the underlying details of the probability density functions (PDFs) (discussed in (see Section 5.4.4)) of the signal and background components. However, due to the high dimensionality of the PDFs (see Section 5.4.4.1), number of background components (see Section 5.4.4) and number of total events this becomes prohibitive from a computational perspective. Instead, the signal and backgrounds PDFs are multi-dimensional histograms and therefore a binned likelihood function is built from a product of Poisson probabilities

$$\mathcal{L} = \left[\prod_i \frac{n_i^{d_i} e^{-n_i}}{d_i!}\right] \times \prod_j e^{-(N_j - N_j')^2/(2\sigma_j^2)} \tag{5.7}$$

where n_i and d_i are the expected and observed numbers of events in bin i, respectively. The second product includes systematic errors in the form of Gaussian constraints incorporating information from standalone studies. In this work, a constraint on the number of ^{222}Rn atoms is considered, which is based on data from EXO-200 indicating that it can be measured to within 10 % of its estimated value [63]. Additionally, the

known rate of ^{8}B solar neutrinos [215] and uncertainty is included as another Gaussian constraint.

To limit the computational time the total number of bins needs to be limited and the choice of binning can be optimized to increase the resolution in regions with a high signal-to-background ratio (see Section 5.4.4.2). To perform a statistical analysis of a given dataset for the parameter of interest, denoted as μ, a test statistic needs to be constructed. A commonly chosen method, due to the computation expense of scanning a large parameter space, is the profile likelihood ratio test [214] and is defined as

$$\lambda(\mu) = -2 \ln \frac{\mathcal{L}(\mu_0, \hat{\boldsymbol{\theta}}_0)}{\mathcal{L}(\hat{\mu}, \hat{\boldsymbol{\theta}})} \tag{5.8}$$

where μ_0 is a specified value for μ (the number of $0\nu\beta\beta$ events) under the null hypothesis, $\hat{\boldsymbol{\theta}}_0$ are the best fit values of the nuisance parameters (i.e. values of no direct interest to the search at hand which includes parameters such as background rates, detector efficiencies, calibration parameters, etc.) that maximizes the likelihood function for $\mu = \mu_0$ and $\hat{\mu}$ and $\hat{\boldsymbol{\theta}}$ are the corresponding best fit values for the alternative hypothesis.

As mentioned before, the significance of the alternative hypothesis is tested against the null hypothesis using a p-value, which quantifies the probability of the obtained value for the test statistic being larger than expected if the null hypothesis was true. If the p-value is smaller than a predetermined α, the null hypothesis will be rejected. However, this requires knowing the underlying probability distribution of the test statistic λ under the null hypothesis. Under certain conditions, the test statistic distribution for H_0 converges towards chi-squared distribution with m degrees of freedom, χ^2_m. This is known as Wilks' theorem [216] and most likely doesn't apply in the case of nEXO due to its quasi-background-free nature where the profiled parameter

is approaching the physical bound of 0. In cases where Wilks' theorem doesn't hold, the distribution of λ needs to be calculated via computationally expensive toy MC simulations. Via the Frequentist approach, many toy datasets are generated under the hypothesis that H_0 is true and the value of the test statistic is recalculated for each toy.

The definition of the test statistic depends on whether the exclusion or discovery sensitivity is calculated and will be discussed in the following two sections.

5.4.2 Exclusion Sensitivity

To calculate the exclusion sensitivity the above test statistic can be modified to

$$\lambda(\mu) = \begin{cases} -2\ln\frac{\mathcal{L}(\mu_0,\hat{\boldsymbol{\theta}}_0)}{\mathcal{L}(\hat{\mu},\hat{\boldsymbol{\theta}})} & \hat{\mu} \geq 0 \\ -2\ln\frac{\mathcal{L}(\mu_0,\hat{\boldsymbol{\theta}}_0)}{\mathcal{L}(0,\hat{\boldsymbol{\theta}}(0))} & \hat{\mu} < 0 \end{cases} \tag{5.9}$$

where since the true value for the signal should be $\mu \geq 0$ and if $\hat{\mu} < 0$, the likelihood ratio is calculated against the case of $\mu = 0$.

The distribution of $\lambda(\mu)$ for each value of μ is determined from 5000 toy datasets and the value of $\lambda(\mu)$ for which

$$p = \int_{\lambda}^{\infty} f(\lambda|\mu)\,\mathrm{d}\lambda = 10\,\% \tag{5.10}$$

as a function of the hypothesis μ is referred to as the critical lambda curve and is shown in Figure 5.7. As expected the critical lambda curve converges towards the value from Wilks' approximation of $\lambda(\mu \to \infty) \simeq 2.71$, which can be seen in Figure 5.7 together with an example profile likelihood curve for a single toy dataset.

A polynomial of 2nd order is fit against the profile likelihood ratio data points in black and any number of signal counts beyond the intersection point between the polynomial fit and the critical lambda curve can be excluded at 90 % CL.

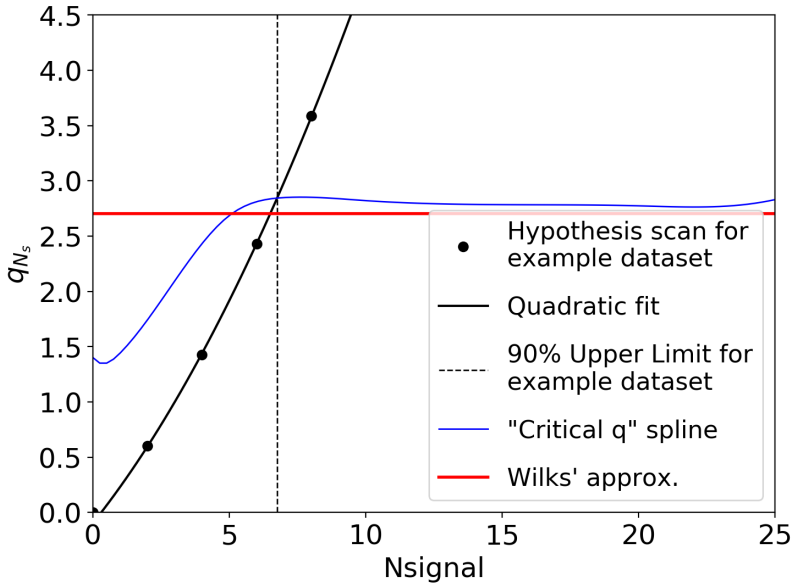

Figure 5.7: Profile likelihood ratio curve for an example toy dataset. The intersection of the profile likelihood ratio curve with the critical lambda curve (blue) is the upper limit of signal counts that can be excluded at the 90 % CL. The expected value for exclusion at 90 % CL for the test statistic in the limit where Wilks' theorem holds is given by 2.71 and is shown as a red vertical line. Figure from B. Lenardo.

The above procedure is repeated for 5000 toy datasets to obtain an ensemble of upper limits, which is shown in Figure 5.8. The median of this distribution is the quoted median exclusion sensitivity at the 90 % CL.

5.4.3 Discovery Sensitivity

The test statistic for a discovery sensitivity hypothesis test is given by

$$\lambda(0) = \begin{cases} -2\ln\frac{\mathcal{L}(0,\hat{\boldsymbol{\theta}}_0)}{\mathcal{L}(\hat{\mu},\hat{\boldsymbol{\theta}})} & \hat{\mu} > 0 \\ 0 & \hat{\mu} \leq 0 \end{cases} \tag{5.11}$$

where for $\hat{\mu} =< 0$ we set $\lambda(0) = 0$ so that unphysical negative fluctuations in the observed number of signal events are not considered as evidence against the null hypothesis H_0.

The distribution of the test statistic $f(\lambda(0)|0)$ is calculated via 10^5 toy datasets,

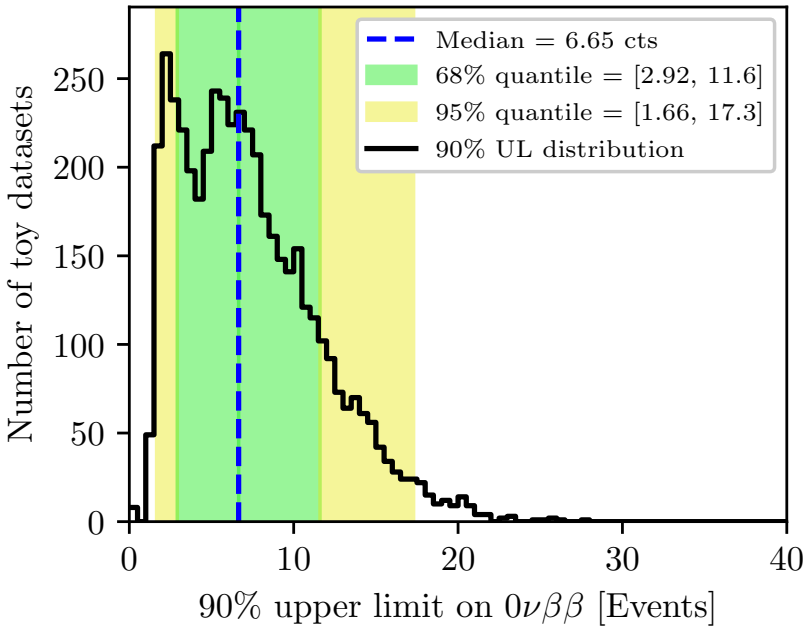

Figure 5.8: Distribution of 90 % CL upper limits on the number of $0\nu\beta\beta$ counts for 5000 toy datasets. The median corresponds to a bound on the $0\nu\beta\beta$ decay half-life of $T^{0\nu}_{1/2} > 1.35 \times 10^{28}$ years. The 68 % and 95 % percentiles around the median are shown in green and yellow, respectively. Figure from [33].

which are needed to reduce the statistical uncertainty in determining the value of $\lambda(\mu)$ at the 3σ significance. For the alternative hypothesis H_μ, we need only the median of $f(\lambda(0)|\mu)$ for which 5×10^3 toy datasets are sufficient to reduce the statistical error to $\sim$1 %

Example distributions of the test statistic (here $\Delta\text{NLL} = -\lambda/2$) for the null hypothesis $f(\lambda(0)|0)$ (in grey) and for several different alternative hypotheses $f(\lambda(0)|\mu)$ (in color) are shown in Figure 5.9. The median of each $f(\lambda(0)|\mu)$ for different alternative hypotheses is converted into a p-value via

$$p_0 = \int_{\lambda(0)_{\text{median}}}^{\infty} f(\lambda(0)|0)\,\mathrm{d}\lambda \tag{5.12}$$

where $\lambda(0)_{\text{median}}$ is the value of test statistic distribution $f(\lambda(0)|0)$ that corresponds to the median of $f(\lambda(0)|\mu)$. This p-value can then be converted into a significance via equation Equation 5.6. For $Z \geq 4$ Wilks' approximation is used because of

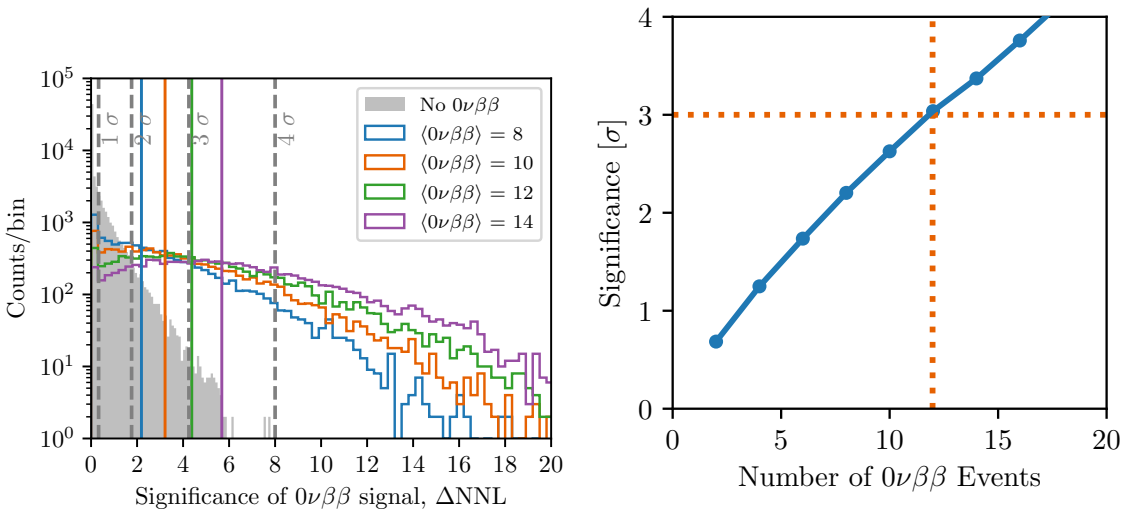

Figure 5.9: (left) Distribution of ΔNNL for the null hypothesis $f(\lambda(0)|0)$ in grey and for alternative hypotheses $f(\lambda(0)|\mu)$ in color. The p-value is gotten from counting the number toy data sets in $f(\lambda(0)|0)$ that are above the median of $f(\lambda(0)|\mu)$, shown as vertical colored lines. The grey vertical dashed lines represent the values of ΔNNL that corresponds to a significance of $1\sigma, 2\sigma, 3\sigma, 4\sigma$, respectively. (right) Shown is the significance as a function of the average number of signal events used for generating the toy data sets. The number of signal events that the median experiment in an ensemble of toy experiments would have to have to be able to exclude the background-only hypothesis and claim a discovery with a 3σ significance can be calculated via linear interpolation between the data points. This is shown via the dotted lines. This dataset corresponds to an exclusion sensitivity of $T^{0\nu}_{1/2} > 0.74 \times 10^{28}$ yr at 3σ significance. Left figure is from [33].

low statistics of toy data sets for p-values above 0.001, assuming that $f(\lambda(0)|0)$ is χ^2-distributed with one degree of freedom.

By plotting the significance of each alternative hypothesis against the number of signal events present in their toy data sets and using a linear interpolation one can calculate the exact number of signal events μ that would produce a median significance of 3σ, as shown in right plot in Figure 5.9. This value is then reported as nEXO's median discovery sensitivity at 3σ significance.

5.4.4 Fit Model

The construction of the signal and background components follow the same general methodology that was outlined in [92]. The simulated MC data, that was described in Section 5.1, is used to generate probability density functions (PDFs) for the $0\nu\beta\beta$ signal and each background component. The following selection cuts are applied to the MC data beforehand:

- only events with a total energy between 1000 keV and 3500 keV are selected
- due to non-uniformities in the electric field towards the edge of the field cage, resulting in worse charge collection and reconstruction, events whose outermost energy deposit is closer than 20 mm to any TPC component are disregarded
- as mentioned in Section 5.2 α-backgrounds can be rejected with very high efficiency by deploying a cut in the light-vs-charge space in 5.2 in addition to poorly reconstructed βs and γs with partial energy deposits in the LXe skin

These cuts and other data quality cuts have a $0\nu\beta\beta$ signal efficiency of 96 % in the Monte Carlo simulation. The normalized PDF for component i is scaled according to

$$N_i = M_i \cdot A_{s,i} \cdot T \cdot \frac{N_{1,i}}{N_{0,i}} \tag{5.13}$$

where M_i is the mass (surface area) of component i, $A_{s,i}$ its specific activity per unit mass (unit surfaces area), $N_{1,i}$ the number of events passing all the abovementioned selection cuts, $N_{0,i}$ is the number of initially simulated MC events and T the amount of time the experiment will run.

In order to optimize the computation time, PDFs from certain components were grouped based on their location within the detector and possible degeneracy with other components. The groups are

- $0\nu\beta\beta$

- $2\nu\beta\beta$
- ^{238}U from TPC vessel components
- ^{232}Th from TPC vessel components
- ^{238}U from components within the TPC vessel
- ^{232}Th from components within the TPC vessel
- ^{60}Co from TPC vessel components and components within
- ^{40}K from TPC vessel components and components within
- ^{222}Rn inside the LXe and on the cathode and FSRs
- ^{137}Xe and ^{42}Ar inside the LXe
- Elastic scattering of ^{8}B solar neutrinos with the LXe
- An additional far group comprised of ^{238}U, ^{232}Th, ^{60}Co, ^{40}K and ^{222}Rn events from components outside the TPC vessel

The expected number of counts from the full fit model containing all groups is given by

$$n_j = N_{0\nu\beta\beta} + \sum_j N_j \cdot f_{ji} \tag{5.14}$$

where $N_{0\nu\beta\beta}$ is the number of $0\nu\beta\beta$ events, N_j is the number of counts from groups j and $f_j i$ is the relative contribution from a component i to group j.

Due to the lack of existing data for nEXO the abovementioned fit model serves as a placeholder. To evaluate the exclusion and discovery sensitivities toy MC datasets can be generated from this fit model. The uncertainties in the measured radio-assay values are propagated by sampling the specific activity in Equation 5.13 from a truncated normal distribution for every toy dataset [33].

5.4.4.1 Fit Dimensions

Similar to the approach in EXO-200 [32,69], we are using multiple variables to perform a multi-dimensional likelihood fit of the model to the data. The reconstruction variables, described in Section 5.2, which include the energy, standoff distance, and DNN score of an event, are used as separate dimensions, maximizing the background discrimination capabilities.

To quantify the improvement in nEXO's physics reach by performing a multi-variate profile likelihood analysis, the discovery sensitivity was evaluated as a function of fit dimensions. The results are summarized in Table 5.1 where a total improvement of a factor of 21 is observed when using the combined information from energy, standoff, and DNN variables instead of just the energy variable. The addition of the DNN fit dimension improves the discovery sensitivity more substantially than the standoff distance, which is due to the loss in discrimination power of the standoff distance variable beyond the innermost 2000 kg. Signal-like events ($0\nu\beta\beta$ or γ-backgrounds) in this region, where we expect $\sim$95 % of our full sensitivity (see Section 5.5.1), can only be further discriminated based on their topology.

These studies can be compared to similar studies performed with EXO-200 for the last two $0\nu\beta\beta$ searches [32, 69]. To perform a more direct comparison with EXO-200, where a single variable fit (i.e. energy only) was still performed in SS and MS space simultaneously and linked via SS-fraction, we ran additional studies. As determined in Section 5.4, choosing DNN values above 0.85 results in a similar SS and MS separation as a more traditional classification algorithm, similar to the previous estimate of nEXO's sensitivity [92] or in EXO-200 before using a DNN [69]. Therefore, fits in which the fit variables only include energy and standoff have an additional DNN axis with two non-uniform bins separated at 0.85. The results of these studies are shown in Table 5.2. nEXO's larger size results in better self-shielding and therefore in a greater improvement when adding the standoff variable to the analysis compared to

Fit variables	Disc. Sens. Improv.
E	1.0
E + SD	4.7
E + DNN	12.0
E + SD + DNN	21.0

Table 5.1: Summary of the improvement in discovery sensitivity vs different sets of variables used in the likelihood fits. The 21-fold improvement over a simple 1D energy search highlights the strength of nEXO's multi-dimensional analysis approach.

EXO-200. The relative improvement when adding the DNN variable is similar between both experiments. While the smaller charge channel pitch in nEXO might lead to more topological information being available for the DNN to discriminate signals from backgrounds this can be counteracted by more diffusion due to the large size of the detector and the charge channel noise.

5.4.4.2 Binning Optimzation

The binning in each fit dimension (energy, standoff distance, and DNN value) should be chosen such that we can fully capture the information in the distributions while not making the likelihood fits computationally too expensive.

From studying the dependence of the sensitivity as a function of fiducial volume, which will be discussed in Section 5.5, we know that we gain most of our sensitivity in the innermost 2000 kg (corresponding to a standoff distance of larger than 104 mm), which is the point where the gain in sensitivity due to an increase in sensitive mass is outweighed by the increase in background counts due to external backgrounds. Our likelihood fit analysis, in stark contrast to a simple counting experiment, can take advantage of the spatial distribution of events and the topological difference between signal and background that is encoded in the DNN parameter. Figure 5.10 shows a contour plot of the distribution of $0\nu\beta\beta$ events (in blue) and background events from

Fit variables in nEXO	Disc. Sen. Improv.	Excl. Sens. Improv.
E + b-DNN(0.85)	1.0	-
E + SD +b-DNN(0.85)	1.79	-
E + SD + DNN	2.22	-
Fit variables in EXO-200	-	-
E + SS/MS	1.0	1.0
E + SD + SS/MS	1.15	1.07
E + SD + BDT + SS/MS	1.38	1.15
E + SD + DNN	-	1.3

Table 5.2: Comparison of the improvement in exclusion and discovery sensitivity between EXO-200 and nEXO for using different variables in the likelihood fits. Due to its bigger size and monolithic design, we see a larger improvement by adding the standoff distance to the energy in nEXO compared to EXO-200. The relative improvement of adding the DNN variable as an additional variable is similar for both experiments.

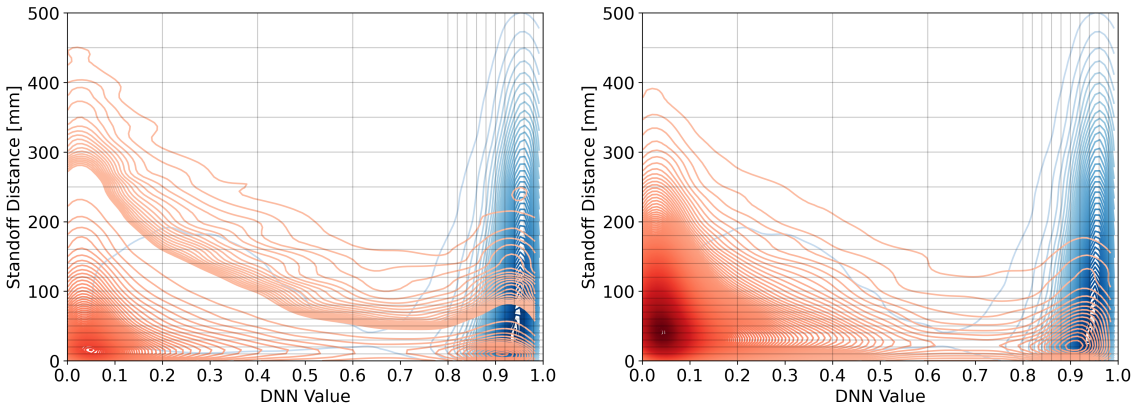

Figure 5.10: Shown are contours of the distribution of $0\nu\beta\beta$ events (in blue) and background events (in red) from ^{232}Th (left) and ^{238}U (right) in the TPC vessel in standoff distance vs DNN space. Only events with energy in the ROI and that have passed our quality cuts are shown.

^{238}U and ^{232}Th in the TPC vessel (in red) in standoff distance versus DNN space, highlighting the difference between signal and background PDFs.

These plots illustrate the advantage of nEXO's monolithic design and how the standoff distance variable can be used to define a low background region inside the detector where very few signal-like (high DNN score) γ-like events are present. For events close to the edge of the innermost 2000 kg or beyond the discrimination power of the standoff distance variable diminishes and the DNN can provide additional discrimination based on the topology. The DNN can separate signal-like γ-like events which have undergone a photo-electric effect and $0\nu\beta\beta$ events based on the size of the initial charge cloud before diffusion, i.e. a 2.5 MeV photo-electron travels further in liquid xenon than two βs with the same energy total energy. Figure 5.11 shows the efficiency, defined as the fraction of events below or above a DNN value of 0.85 for background or signal, respectively, as a function of event size. The event size was determined with a simple algorithm calculating the maximum euclidean distance between energy deposits and is based on MC truth information.

This effect manifests itself as a shift in the contour maxima between the signal and background distributions at DNN values larger than 0.85 in the plots in Figure 5.10. The chosen non-uniform binning in standoff and DNN, which was optimized to take advantage of the spatial and topological differences between γ-events and $0\nu\beta\beta$ is shown as grid lines in Figure 5.10. Indeed, an 13 % and 18 % improvement in the exclusion and discovery sensitivities were observed, respectively, compared to a coarser uniform binning with 20 mm.

5.5 Results

This section will provide an overview of the physics reach of nEXO, both in terms of the baseline design as well as by studying the dependence of the exclusion and

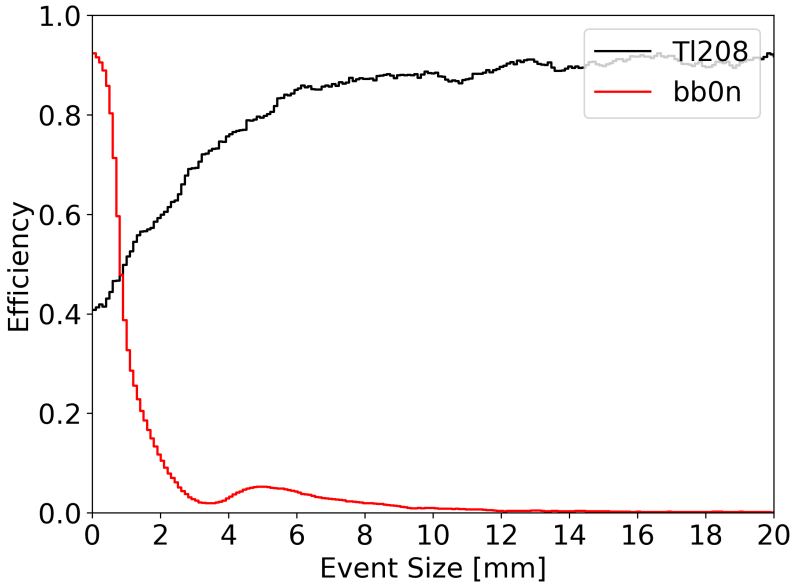

Figure 5.11: Selection efficiency, defined as the fraction of events below or above a DNN value of 0.85 for background or signal, respectively, as a function of an approximate event size metric. This demonstrates that the DNN, as expected, discriminates γ-like backgrounds against $0\nu\beta\beta$ events based on their topological differences encoded in the initial event size during the interaction with the LXe.

discovery sensitivity on various detector parameters. This includes changes in the achievable energy resolution, mismodeling of the background levels, and the case in which the only remaining irreducible background is the $2\nu\beta\beta$ spectrum.

5.5.1 Baseline Physics Reach

The goal for the upcoming tonne-scale experiments is to cover the inverted neutrino mass ordering, which requires a half-life sensitivity of $\sim 10^{28}$ yr. nEXO's updated sensitivity projections compared to what was previously reported in [92] are shown in Figure 5.12. After ten years of data taking nEXO is expected to reach a exclusion and discovery sensitivity of $T^{0\nu}_{1/2} > 1.35 \times 10^{28}$ yr at 90 % CL and $T^{0\nu}_{1/2} > 0.74 \times 10^{28}$ yr at 3σ significance, respectively. The major improvements yielding this $\sim$45 % improvement in the exclusion sensitivity are largely related to the more efficient background discrimination using a DNN (contributing $\sim$15 %) and the reduced ^{232}Th

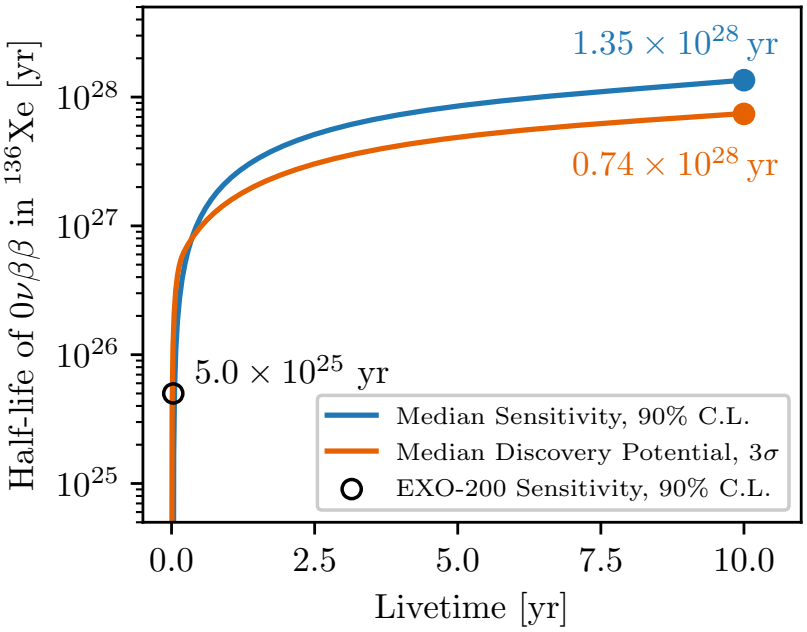

Figure 5.12: Projected median exclusion and discovery sensitivity as a function of livetime at the 90 % CL and 3σ CL, respectively. nEXO will surpass a half-life sensitivity of $>10^{27}$ yr and $>10^{28}$ yr after just ∼0.5 yr and 6 yr, respectively. During the initial few months, the experiment will be effectively running background free, resulting in fewer counts needed to make 3σ significant observation than can be excluded at 90 % CL. After the full ten years of data taking, the final projected exclusion at at 90 % CL and discovery sensitivities at 3σ CL are $T^{0\nu}_{1/2} > 1.35 \times 10^{28}$ yr and $T^{0\nu}_{1/2} > 0.74 \times 10^{28}$ yr, respectively. Figure from [33].

and ^{238}U content due to the adaptation of in-house EFC (contributing ∼30 %).

Even before the ten year mark, nEXO will reach milestones such as surpassing a half-life sensitivity of $>10^{27}$ yr and $>10^{28}$ yr at 90 % CL after just ∼0.5 yr and 6 yr, respectively. The reported exclusion sensitivity of $T^{0\nu}_{1/2} > 5 \times 10^{25}$ yr at 90 % CL from EXO-200 using the complete dataset [32] will be exceeded in less than a month of running nEXO. Moreover, in the first few months, the experiment will effectively run in a quasi-background-free mode which results in a higher discovery than exclusion sensitivity, as can also be seen in Figure 5.20.

The final projected exclusion sensitivity of nEXO improves upon previous and existing xenon-based $0\nu\beta\beta$ experiment, including EXO-200 [32] with 5×10^{25} yr and KamLAND-Zen [31] with 1.3×10^{26} yr, by two orders of magnitude. More importantly,

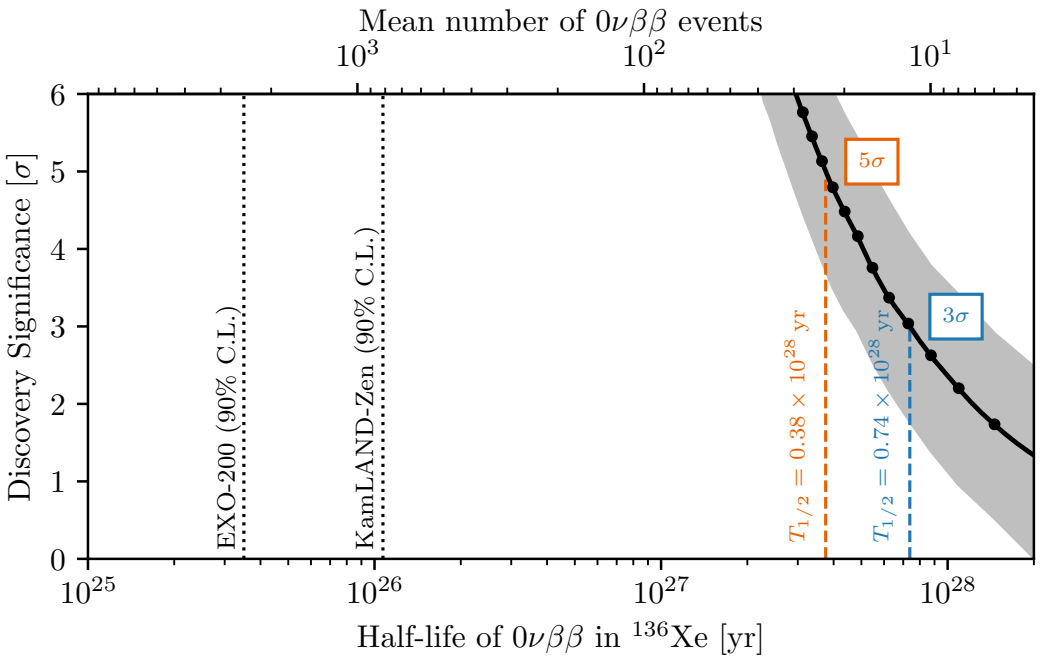

Figure 5.13: Projections of the median discovery significance for $0\nu\beta\beta$ with ten years of nEXO data. The grey band indicates the 68 % symmetric quantile around the median. As a comparison, the excluded half-lifes of other xenon-based $0\nu\beta\beta$ experiments at 90 % CL are shown as vertical dashed lines, including EXO-200 [32] and KamLAND-Zen [31]. The median significance of a discovery in nEXO exceeds 5σ for $0\nu\beta\beta$ half-lifes as long as 0.38×10^{28} yr and even for a half-life of 1×10^{28} yr a median 2.4σ significant observation can be made.

nEXO has a high discovery sensitivity, where the significance of discovery in nEXO exceeds 5σ for $0\nu\beta\beta$ half-lifes as long as 0.38×10^{28} yr, which is more than an order of magnitude beyond existing limits. Even for a half-life of 1×10^{28} yr a 2.4σ significant observation can be made. A comparison of these projections is shown in Figure 5.12.

The dependence of the achievable sensitivity as a function of fiducialization is shown in Figure 5.14, showing that by using the innermost 2000 kg of LXe we get ∼95 % of the full sensitivity for the entire fiducial mass of 3281 kg. nEXO's monolithic detector design and the excellent self-shielding capabilities of LXe are crucial for achieving these projected sensitivities. The outer LXe regions measure and constrain the external γ-background with high statistics and provide a very radio-pure inner LXe region that has a high sensitivity to $0\nu\beta\beta$.

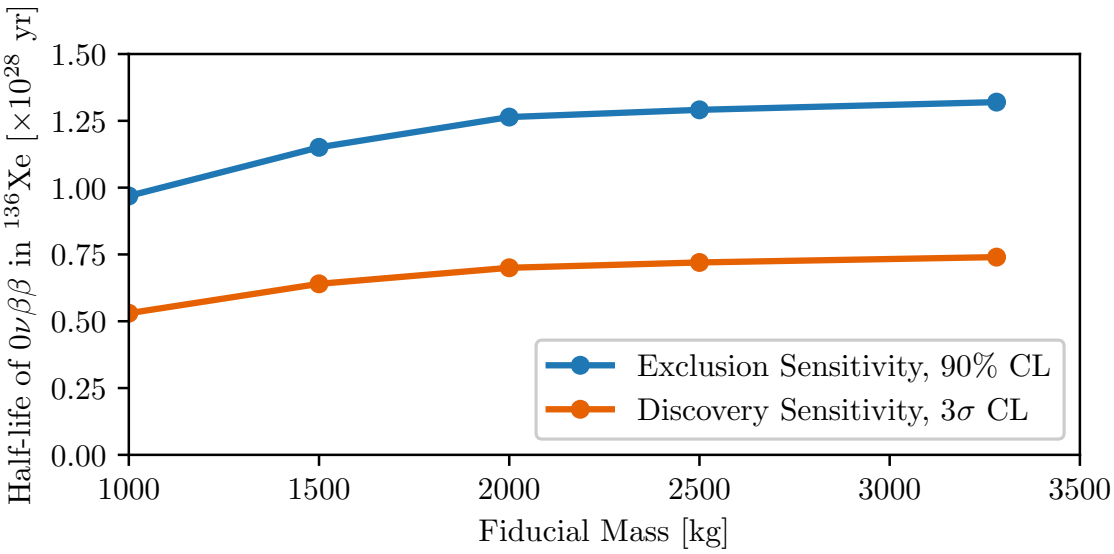

Figure 5.14: Projected median exclusion and discovery sensitivity as a function of fiducial mass at the 90 % CL and 3σ CL, respectively. Using the innermost 2000 kg of LXe already delivers ∼95 % of the full exclusion and discovery sensitivity compared to the full fiducial mass of 3281 kg relative to the full 5000 kg total LXe mass.

If $0\nu\beta\beta$ were to be observed, nEXO with its LXe TPC has the unique advantage of being able to exchange the highly $^{\text{enr}}$Xe with natural Xenon ($^{\text{nat}}$Xe) or depleted xenon to confirm the discovery independently.

5.5.2 Dependence on Energy Resolution

The estimate of the projected energy resolution in nEXO was presented in Section 4.3 and is founded on a robust semi-empirical model whose validity was tested against EXO-200 data [80]. However, certain input parameters to this model such as those related to calibrations of the detector response can't be fully validated yet. This includes uncertainties due to spatial or temporal differences between the measured and true lightmap and electron lifetime in the detector. Figure 4.36 summarizes the impact of various input parameters on the expected energy resolution in nEXO.

To quantify the impact that a worse energy resolution would have on the sensitivity, the reconstructed energy E, which is one of the dimensions of our binned 3D PDFs, is

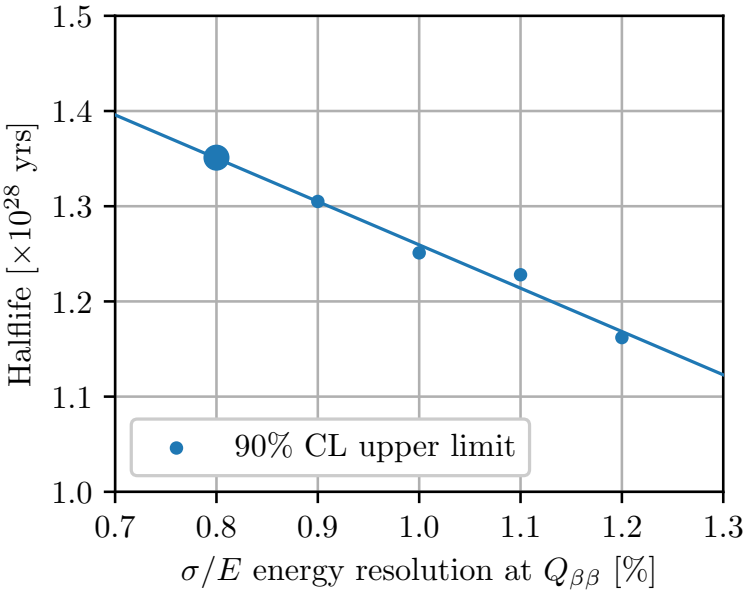

Figure 5.15: Projected half-life exclusion sensitivity as a function of the energy resolution at $Q_{\beta\beta}$ at the 90 % CL. A linear fit to the data point is also shown. The baseline value for the projected energy resolution in nEXO is $\sigma/Q_{\beta\beta} = 0.8\,\%$. Figure from [33].

smeared by drawing from a Gaussian distribution with mean E and width

$$\sigma = E \cdot \left[R^2 - (0.8\,\%)^2\right] \tag{5.15}$$

where 0.8 % is the projected baseline energy resolution at $Q_{\beta\beta}$ and R is the worsened energy resolution. The exclusion sensitivity was recalculated using the smeared PDFs and the results are shown in Figure 5.15. Even for the worst energy resolution of $\sigma/Q_{\beta\beta} = 1.2\,\%$ considered here, the exclusion sensitivity stays beyond the 1×10^{28} yr half-life goal for the upcoming tonne-scale experiments.

The worsening of the energy resolution using the above methodology treats the energy variable as independent of other detector performance parameters. Depending on the source of noise that adds to the energy estimator in Equation 4.50, other parts of the reconstruction might be affected, too. For instance, a higher charge readout noise could, in addition to a worse energy resolution, also affect the discrimination power of

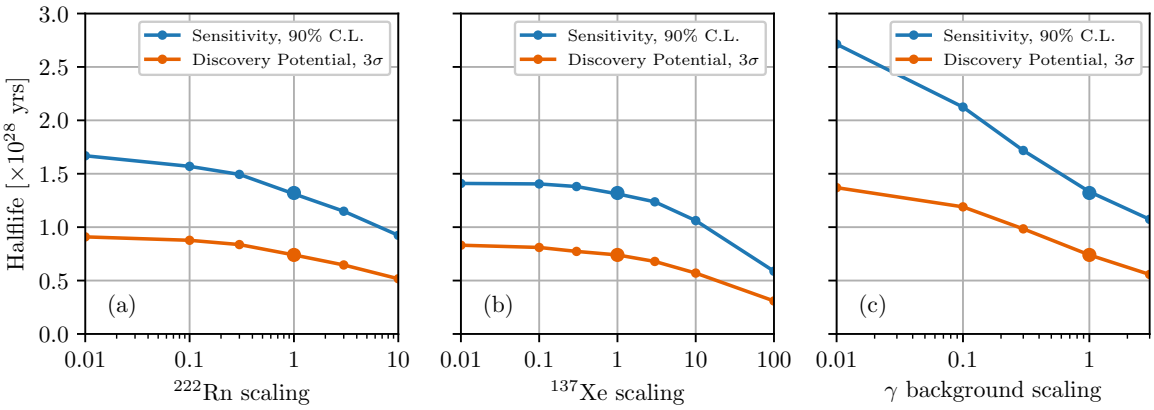

Figure 5.16: Dependence of the exclusion and discovery sensitivity on changing the background components related to ^{222}Rn, ^{137}Xe or all γ-backgrounds. This shows the impact of potential mismodeling of backgrounds or the potential gain in further reducing these backgrounds. Figure from [33].

the DNN which is trained on the charge readout waveforms. A more comprehensive study will be required, that will change parameters at the reconstruction level or possibly even at the MC simulation level to fully propagate the effect to the sensitivity of nEXO.

5.5.3 Dependence on Background Mismodeling

nEXO's background model is based on a robust bottom-up estimate and is described in detail in Section 5.3. Nevertheless, to estimate the impact of our backgrounds the exclusion and discovery sensitivity was evaluated as a function of:

- The estimate of the expected ^{222}Rn content in nEXO is based on an extrapolation from EXO-200, which relies on various assumptions about the source and scaling of the radon emanation with surface area. Because it contributes $\sim$50 % of the total background budget it is imperative to understand its production and impact on nEXO's sensitivity. The ^{222}Rn content in nEXO was scaled between 0.01 and 10 times its baseline value, where the lower bound could potentially be achieved via an online removal system using a radon distillation column [211]. The results are shown in the leftmost plot in Figure 5.16 and indicate that in

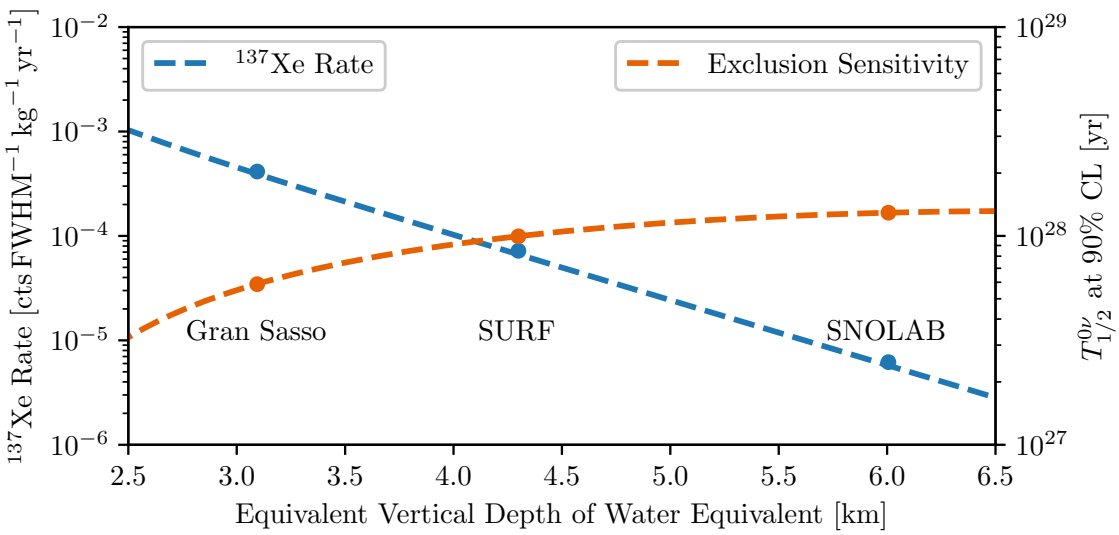

Figure 5.17: (left axis) Estimated rate of ^{137}Xe backgrounds and (right axis) projected half-life exclusion sensitivity at 90 % CL as a function of vertical depth in meters of water equivalent. The current conceptual design is assuming that nEXO will run at SNOLAB. The reduction in sensitivity at a shallower site, such as SURF or Gran Sasso, can be counteracted with a more sophisticated muon veto scheme than the current and simplistic scheme used for this analysis.

the most pessimistic case the reduction in the exclusion and discovery sensitivity is ∼31 % and ∼23 %, respectively.

- The ^{137}Xe background rate depends on the depth of the underground laboratory and is shown in Figure 5.17. The location of nEXO at a shallower experimental site is equivalent to scaling up the ^{137}Xe background for which the exclusion and discovery sensitivities were re-evaluated and are shown in the middle plot in Figure 5.17. In the current baseline design, nEXO is assumed to be located at SNOLAB which would provide an overburden of ∼6000 m of water equivalent. With the current simplistic veto scheme, discussed in Section 5.3.2, the operation of nEXO at Gran Sasso would reduce the projected exclusion sensitivity to $\sim 0.6 \times 10^{28}$ yr at the 90 % CL. In principle, nEXO could be run at another experimental site but would require a more sophisticated muon veto system to recover the loss in sensitivity.

- To illustrate the potential gain in sensitivity by continually improving the detector design and further reducing the backgrounds, a final study varied all γ-backgrounds and the dependence of the exclusion and discovery sensitivities are shown in the rightmost plot in Figure 5.17. Equivalently, one can determine the dependence of the sensitivity on the corresponding background index B, as shown in Figure 5.18, and show that nEXO's sensitivity scales more favorably with

$$T^{0\nu}_{1/2} \propto b^{-0.23} \qquad \text{(Exclusion Sensitivity, 90 \% CL)} \tag{5.16}$$

$$T^{0\nu}_{1/2} \propto b^{-0.26} \qquad \text{(Discovery Sensitivity, } 3\sigma \text{ CL)} \tag{5.17}$$

  than one would assume from the generic $T^{0\nu}_{1/2} \propto b^{-0.5}$ scaling of the sensitivity, which applies in the case of a counting experiment. However, nEXO's multivariate analysis enables a more sensitive search than the background index alone would suggest. More details about a comparison to a counting experiment are provided in Section 5.5.5.

5.5.4 $2\nu\beta\beta$-only Case

A unique possibility among candidate isotopes for $0\nu\beta\beta$, experiments deploying ^{136}Xe could, at least in principle, identify the ^{136}Ba daughter nucleus to reach a nearly background-free experiment. The only remaining background would be the irreducible $2\nu\beta\beta$ background, which will similarly produce ^{136}Ba in the final state. However, as mentioned in Section 5.3.1 the $2\nu\beta\beta$ background leakage into the energy ROI is 0.1 events during the entire data-taking period of ten years for nEXO. The calculated median exclusion sensitivity for this case is 3.6×10^{28} yr at the 90 % CL, which is a $\sim$2.6 times improvement over the baseline exclusion sensitivity. This highlights how close nEXO's conceptual design is to being background free.

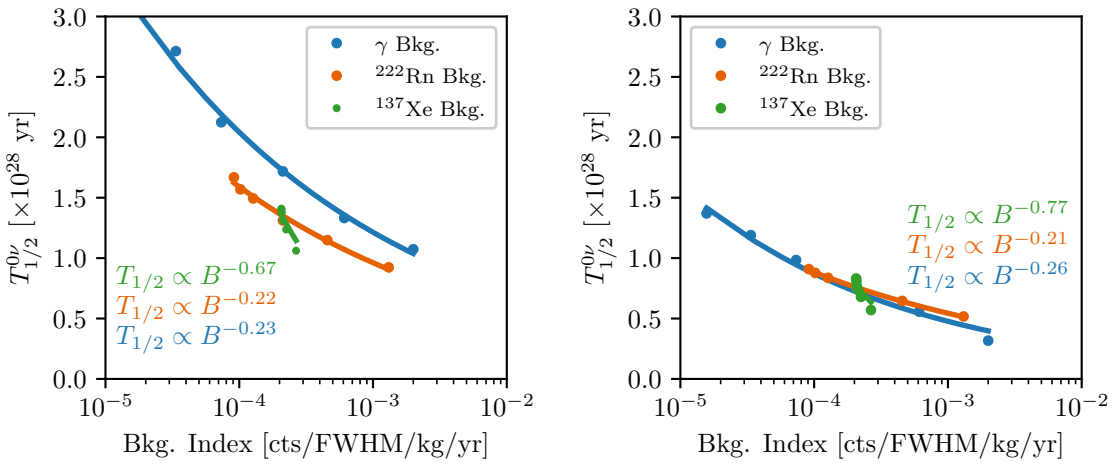

Figure 5.18: Exclusion (left) and discovery (right) sensitivity as a function of the background index for scaling the backgrounds from ^{222}Rn, ^{137}Xe and all γs. A power law fit to the projected sensitivities as a function of all γ backgrounds yields a power of -0.23 and -0.26 for the exclusion and discovery sensitivity, respectively, highlighting that nEXO's sensitivity is scaling more favorably than the typical power of -0.5 for a counting experiment.

Techniques to tag the barium are being actively developed and a major breakthrough in identifying and performing spectroscopy on a single barium atom in a solid xenon matrix has been successfully demonstrated in a small test setup [217]. The implementation into an experiment such as nEXO requires a significant amount of additional engineering and is currently not part of the conceptual design. Since the efficiency of Ba-tagging is likely to be $<100\,\%$ the obtainable result will be somewhere between the reported $2\nu\beta\beta$-only and baseline cases.

5.5.5 Counting Experiment and Background Index

In a counting experiment, the exclusion and discovery sensitivities can be calculated with significantly simpler Poisson statistics, using just the expected number of background counts b and signal counts s in the ROI that have passed all the analysis cuts. This type of analysis omits any additional shape information from the signal and background distributions, effectively collapsing the entire fit into a single bin. The

Fiducial Mass [kg]	Backgrounds b [cts]
500	0.28
1000	0.94
1500	2.04
2000	4.24
2500	8.7
3000	16.3
3281	22.5

Table 5.3: Summary of the mean number of background counts, that have energy with the FWHM around $Q_{\beta\beta}$ and a DNN score of >0.85, for different fiducial masses after 10 yr of livetime of nEXO.

MC signal efficiency for $0\nu\beta\beta$ events having total energy within the energy ROI, being at least 20 mm away from the closest detector surface and having a DNN score of larger than 0.85 is $\epsilon^{c}_{\text{sig}} = 58\,\%$. The purpose of evaluating the exclusion and discovery sensitivity for a counting experiment is twofold:

1. It highlights the power of nEXO's multi-dimensional analysis, incorporating information about the energy, spatial distribution, and topology of events, which results in a better exclusion and discovery sensitivity than an analysis based solely on the background index

2. We can calculate an "equivalent background index" that compares our multi-dimensional likelihood analysis with a simple counting experiment and provides a metric for comparison with other experiments.

There are multiple ways to evaluate the counting experiment exclusion and discovery sensitivities:

- **Likelihood ratio method** [218]:

For a Poisson counting experiment, the likelihood function can be written as

$$L(s) = \frac{(s+b)^n}{n!} e^{-(s+b)} \tag{5.18}$$

Assuming that Wilks' approximation holds the test statistic based on the likelihood ratio method converges towards a $\chi^2_{m=1}$ distribution and the significance for the discovery and exclusion sensitivities can be written as

$$\begin{aligned} Z_{\text{disc}} &= \sqrt{\lambda(0)} \\ &= \sqrt{-2 \cdot \ln\left(\frac{b^n}{n!} e^{-b}\right)} \\ &= \sqrt{-2\left[n \cdot \ln(b) - \ln(n!) - b\right]} \\ &= \sqrt{-2\left[n \cdot \ln(b) - n\ln(n) + n - b\right]} \\ &= \sqrt{2\left[n \cdot \ln\left(\frac{n}{b}\right) + b - n\right]} \end{aligned} \tag{5.19}$$

and

$$\begin{aligned} Z_{\text{excl}} &= \sqrt{\lambda(\mu)} \\ &= \sqrt{-2 \cdot \ln\left(\frac{(s+b)^n}{n!} e^{-(s+b)}\right)} \\ &= \sqrt{-2\left[n \cdot \ln(s+b) - \ln(n!) - (s+b)\right]} \\ &= \sqrt{-2\left[n \cdot \ln(s+b) - n\ln(n) + n - (s+b)\right]} \\ &= \sqrt{-2\left[n \cdot \ln\left(\frac{s+b}{n}\right) + n - (s+b)\right]} \\ &= \sqrt{2\left[(s+b) - n - n \cdot \ln\left(\frac{s+b}{n}\right)\right]} \end{aligned} \tag{5.20}$$

For the discovery sensitivity, we want to compare our alternative hypothesis H_1 which contains $s+b$ to our null hypothesis H_0 with only b. In the case of the exclusion sensitivity, this is reversed and $s+b$ is our null hypothesis H_0 while

the alternative hypothesis H_1 is given by the background-only hypothesis with only b. Instead of running an ensemble of MC simulations for various values of n, probing different alternative hypotheses, we make use of a representative "Asimov" dataset [218]. In this approximation, the ensemble of MC toy datasets for various values of n can be replaced by the median expected number of events, which is $n_{\text{disc}} = s + b$ and $n_{\text{sens}} = b$ for the discovery sensitivity and sensitivity, respectively. This simplifies the above equation to

$$Z_{\text{disc}} = \sqrt{2\left[(s+b)\cdot\ln\left(1+\frac{s}{b}\right) - s\right]} \tag{5.21}$$

$$Z_{\text{excl}} = \sqrt{2\left[s - b\cdot\ln\left(1+\frac{s}{b}\right)\right]} \tag{5.22}$$

In Figure 5.19 the expected discovery sensitivity significance is shown as a function of the mean number of signal events for different fiducial masses and livetimes. Via linear interpolation one can determine the mean number of signal counts that corresponds to a discovery or exclusion sensitivity at 3σ CL or at 90% CL, respectively.

- **Poisson likelihood**:

  This method is based on [219]. Suppose our test statistic is given by a Poisson distribution with mean $\mu = b$ or $\mu = s + b$ as our null hypothesis H_0 for the discovery and exclusion sensitivity, respectively. We then calculate the observed value of the test statistic for each H_1, i.e. the probability of observing n counts with a mean of $\mu = s + b$ or $\mu = b$, and compute the p-value under the null

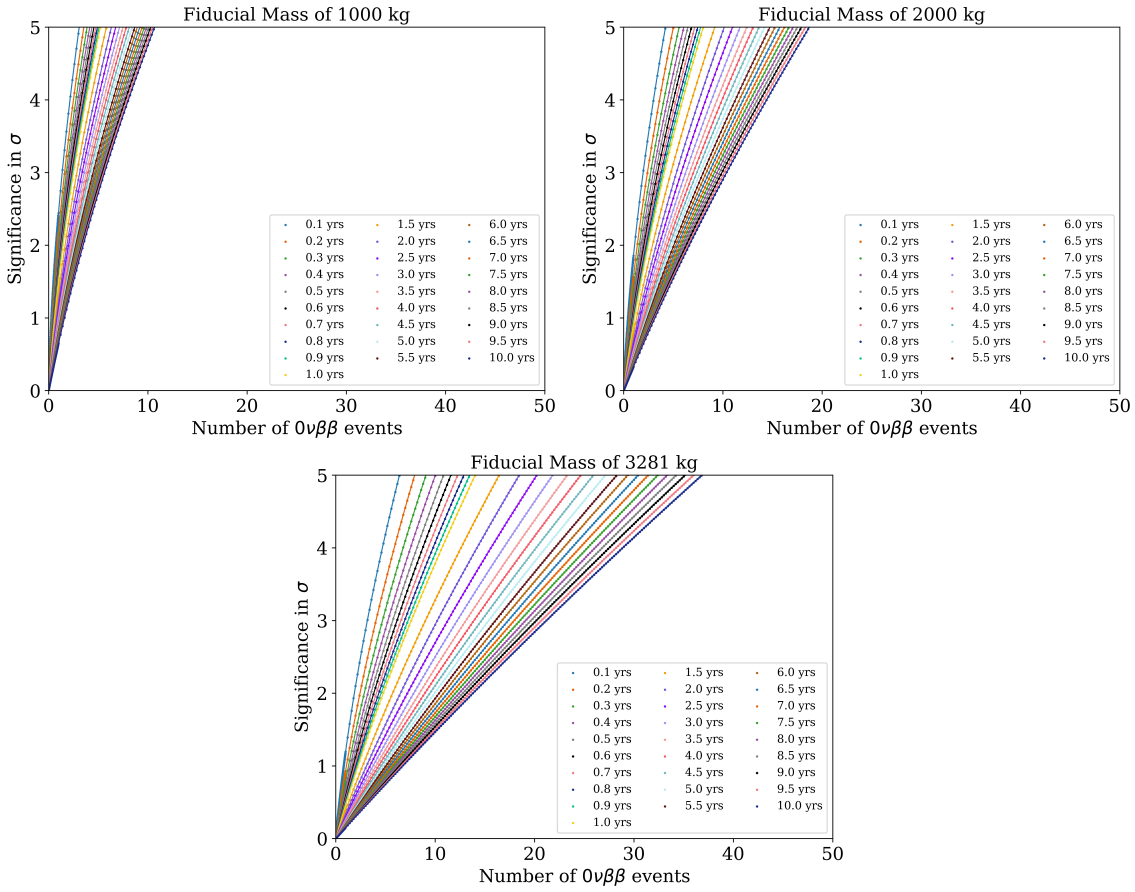

Figure 5.19: Discovery significance of a counting experiment as a function of the mean number of signal events. Each plot is for a different fiducial mass and each curve within is for a different livetime. Data points are connected via a linear interpolation curve to determine the mean number of signal events necessary for a 3σ discovery.

hypothesis:

$$\begin{aligned} p_{\text{disc}}(n,b) &= \sum_{k=n}^{\infty} P(k|b) \\ &= 1 - \frac{\int_0^b t^{n-1}e^{-t}dt}{\int_0^\infty t^{n-1}e^{-t}dt} \\ &= 1 - \frac{\Gamma(n,\ b)}{\Gamma(n)} \\ &= \frac{\gamma(n,\ b)}{\Gamma(n)} \end{aligned} \tag{5.23}$$

$$\begin{aligned} p_{\text{sens}}(n,b,s) &= \sum_{k=0}^{n} P(k|s+b) \\ &= 1 - \frac{\int_0^{s+b} t^{(n+1)-1}e^{-t}dt}{\int_0^\infty t^{(n+1)-1}e^{-t}dt} \\ &= 1 - \frac{\gamma(n+1,\ s+b)}{\Gamma(n+1)} \\ &= \frac{\Gamma(n+1,\ s+b)}{\Gamma(n+1)} \end{aligned} \tag{5.24}$$

where we have used the definition of the $\Gamma(x)$, $\gamma(x,y)$ and $\Gamma(x,y)$ which are the ordinary, lower incomplete, and upper incomplete gamma functions, respectively, to simplify the equations. Usually, one can generate many random numbers n from a Poisson distribution with mean μ, corresponding to the alternative hypothesis, and use the above equations to get a distribution of p-values. The median of that distribution can be used to determine the significance Z. This procedure can be repeated for an increasing μ until the desired confidence level is reached, which is either 3σ for discovery sensitivity or 90% for sensitivity. This method of calculating the median significance exhibits a well-known feature where for small μs the sensitivity increases with increased background due to the discrete nature of the Poisson distribution as shown in Figure 5.20. Alternatively, one can calculate the corresponding significance for each draw of n and take

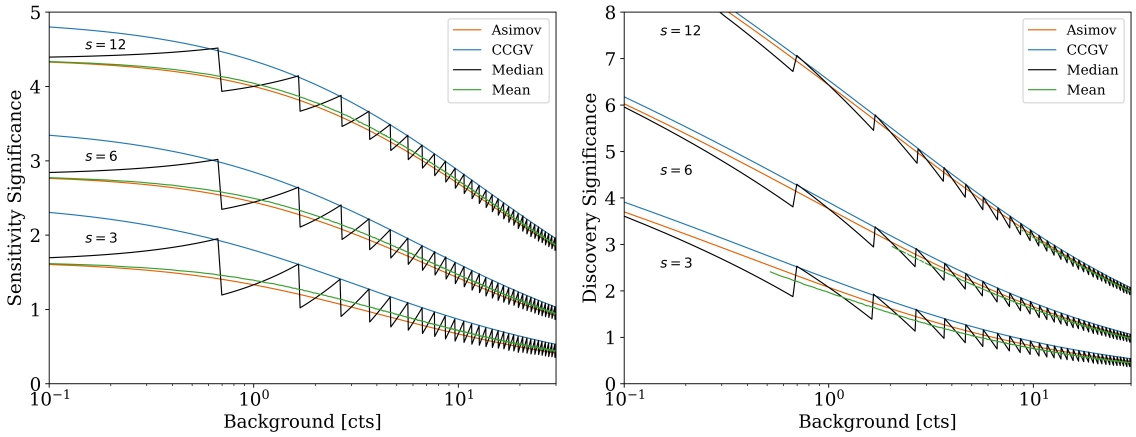

Figure 5.20: Shown is the exclusion significance (left) and discovery significance (right) as a function of mean background counts b for different values of the mean number of signal counts s. Different versions of the Poisson likelihood method are compared together with the Asimov approximation of the likelihood ratio method.

the median (or mean) of the distribution of Z's as a metric to find the μ for which the desired confidence level is reached. A third option would be to use the same Asimov approximation as in the likelihood ratio method above. This will simplify the above procedure and equations and can be rewritten as:

$$p_{\text{disc}}(n, b) = \frac{\gamma(s+b,\ b)}{\Gamma(s+b)} \tag{5.25}$$

$$p_{\text{sens}}(n, b, s) = \frac{\Gamma(b+1,\ s+b)}{\Gamma(b+1)} \tag{5.26}$$

- **Feldman & Cousins (FC) method**:

  This is the commonly used method for evaluating the sensitivity in counting experiments in particle physics and is based on [213]. However, this method is similarly subject to the discreteness of the Poisson distribution as the above Poisson likelihood method. In order to smooth out this discreteness one can use a likelihood weighted sum of 90 % CL upper limits:

$$\mu_{\text{up}} = \sum_{n_{\text{obs}}} = P(n_{\text{obs}}|b) \cdot \text{FC}(n_{\text{obs}}|b) \tag{5.27}$$

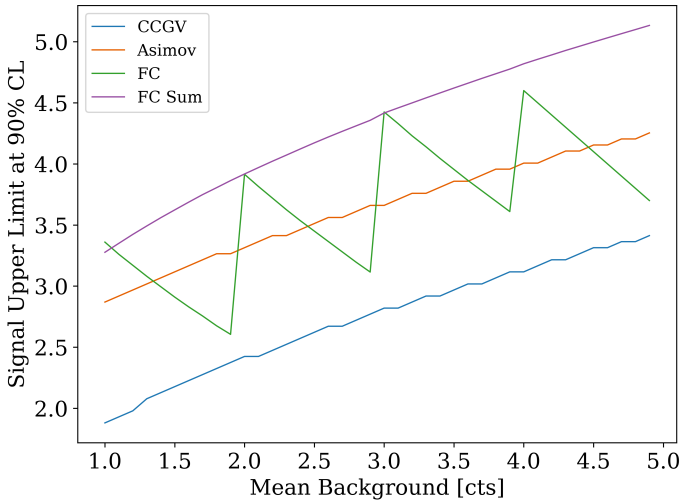

Figure 5.21: Shown is the 90 % CL upper limit of signal counts as a function of the mean number of background events. Compared are the Asimov approximation of the Poisson likelihood method (here just called Asimov) and the likelihood ratio method (here called CCGV for the initials of the authors in [218]) together with the standard FC method (here FC) and the likelihood weighted FC method (here FC Sum). All methods, besides the FC method, have a smooth transition while only the Asimov curve follows the standard FC curve most closely without over or underestimating the exclusion sensitivity.

where we have defined $\mathrm{FC}(n_{\mathrm{obs}}|b)$ as the upper limit that the FC method would return for observing n_{obs} when an average of b counts where expected.

We can use the various methods to calculate nEXO's exclusion and discovery sensitivity as a function of fiducial volume after 10 yr of livetime using the expected number of background counts b for different fiducial volumes from Table 5.3. The results are shown in Figure 5.22 where the spread among different methods is larger for the exclusion sensitivity ($\sim 20\,\%$) compared to the discovery sensitivity where all methods converge for larger average background counts. Compared to the abovementioned FC and likelihood ratio methods the integration method in combination with the Asimov approximation provides a simpler and less assumptious way, respectively, to calculate the exclusion and discovery sensitivity. Therefore, we will use results for a counting experiment obtained with this method to compare to our likelihood analysis results.

By gradually scaling the average background counts in the fiducial volume (3281 kg)

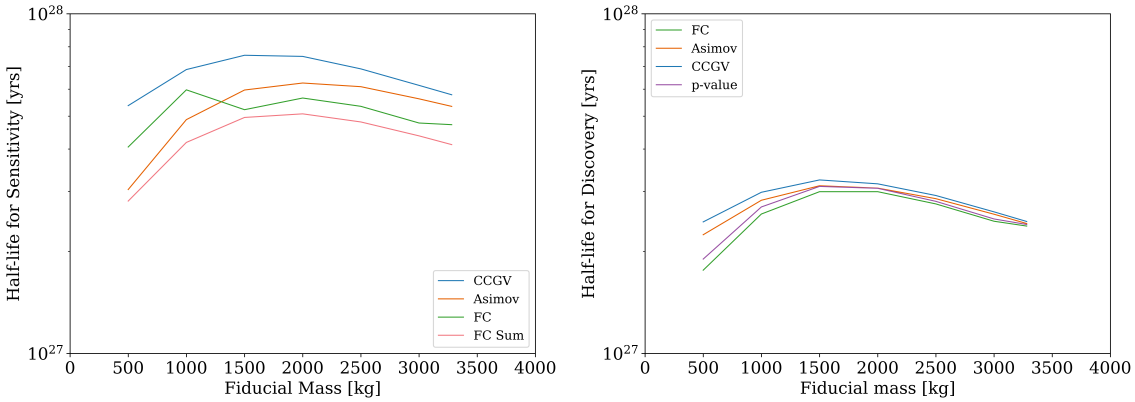

Figure 5.22: Plot of the exclusion sensitivity (left) and the discovery sensitivity (right) as a function of the fiducial mass. The background index as a function of fiducial mass is listed in Table 5.3. This indicates that if nEXO would run as a counting experiment the optimal fiducial mass for the search that maximizes the sensitivity would be between 1500 kg and 2000 kg.

we can extract the exclusion and discovery sensitivity as a function of the background index as shown in Figure 5.23. This allows us to extract an equivalent background index for which a counting experiment achieves a similar sensitivity. We have chosen sensitivity as a metric for defining the equivalent background index as it is the one more commonly used in the field. Thus, an exclusion sensitivity of 1.35×10^{28} yr at 90 % CL requires a background index of $\sim 7 \times 10^{-5}$ cts FWHM^{-1} kg^{-1} yr^{-1}.

5.6 Effective Majorana Neutrino Mass Sensitivity

In the case of a null result, the lower limit on the half-life at 90 % CL can be converted into an upper limit on the physics quantity of interest, the effective Majorana neutrino mass which is defined as

$$\langle m_{\beta\beta} \rangle^2 = \left| \sum_{i=1}^{3} U_{ei}^2 m_i \right| , \tag{5.28}$$

and can be related to the half-life of $0\nu\beta\beta$ via

$$\frac{1}{T_{1/2}^{0\nu}} = \frac{\langle m_{\beta\beta} \rangle^2}{m_e^2} \cdot G_{0\nu}(Q, Z) \cdot g_A^4 \cdot |M^{0\nu}|^2 \tag{5.29}$$

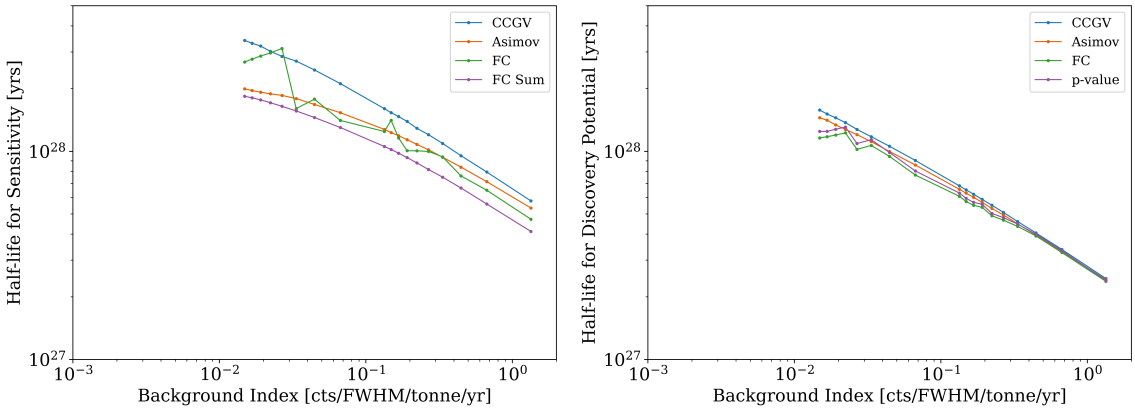

Figure 5.23: Exclusion sensitivity (left) and discovery sensitivity (right) as a function of the background index. This plot can be used to convert our likelihood analysis sensitivity into an equivalent background index.

where it is assumed that the light neutrino exchange is the dominant mechanism mediating this decay. $G_{0\nu}(Q, Z)$ is the kinematic phase space factor which depends on the atomic number Z and the Q-value and can be calculated to subdominant precision, g_A is the axial-vector coupling constant, m_i are the neutrino mass eigenstates, U_{ei} are the elements of the PMNS neutrino mixing matrix and $M^{0\nu}$ is the dimensionless nuclear matrix element (NME) governing the transition between the initial and daughter nuclei.

Figure 5.24 shows the allowed parameter space for $\langle m_{\beta\beta} \rangle$ as a function of the lightest neutrino mass for the inverted and normal neutrino mass ordering, where the bands correspond to uncertainties arising from the completely unknown Majorana phases in the PMNS matrix and the experimental uncertainties in neutrino mixing parameters at the 90 % CL [238]. The dashed lines only include the former uncertainties, whereas the solid lines include the contribution from both sources of uncertainties. nEXO's exclusion sensitivity to $\langle m_{\beta\beta} \rangle$ is shown as a vertical band where the width corresponds to the uncertainties in the NMEs. For all NMEs, except for one, nEXO will be able to exclude all available parameter space in the inverted neutrino mass hierarchy and begins to probe new parameter space in the normal neutrino mass ordering.

Method	Year	^{136}Xe	^{76}Ge	^{100}Mo	Citation
NSM	2008	1.7	2.22	-	[220]
QRPA	2010	3.35	5.52	-	[221]
EDF	2010	4.20	4.60	5.08	[222]
QRPA	2013	3.36	5.82	5.15	[223]
QRPA	2013	1.55	5.09	-	[224]
QRPA	2013	2.18	5.16	5.4	[225]
EDF	2013	4.77	5.55	6.59	[226]
QRPA	2014	2.02	4.64	5.05	[227]
IBM	2015	3.05	4.68	4.22	[228]
EDF	2015	4.32	6.13	6.58	[229]
QRPA	2015	2.91	5.26	3.90	[230]
NSM	2016	1.63	3.37	-	[231]
EDF	2017	-	2.35	-	[232]
QRPA	2018	3.53	5.95	4.8	[233]
NSM	2018	2.28	2.89	-	[234]
QRPA	2018	2.72	4.85	5.87	[235]
QRPA	2018	1.11	3.12	-	[236]
IBM	2020	3.34	6.14	4.96	[237]

Table 5.4: Summary of NME value used for calculating nEXO's sensitivity to the effective Majorana neutrino mass.

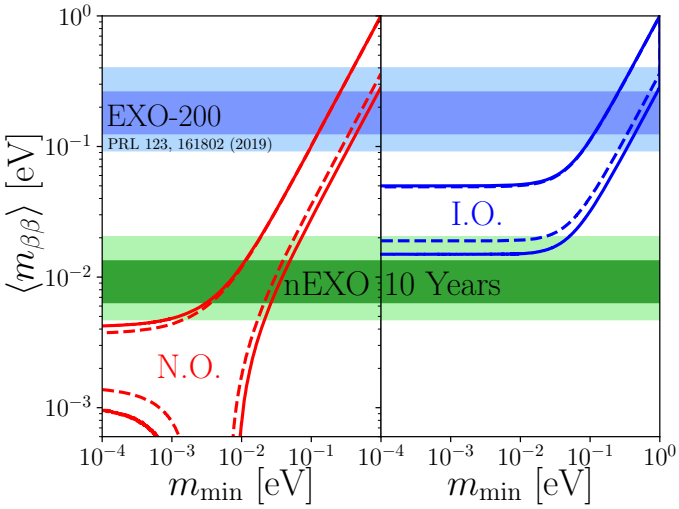

Figure 5.24: Plot of the allowed parameter space of effective Majorana neutrino mass as a function of the lightest neutrino mass eigenstate. The bands correspond to uncertainties arising from the completely unknown Majorana phases in the PMNS matrix and the experimental uncertainties in neutrino mixing parameters at the 90 % CL [238]. The dashed lines only include the former uncertainties, whereas the solid lines include the contribution from both sources of uncertainties. The exclusion sensitivity of nEXO to the effective Majorana neutrino mass at 90 % CL is shown as horizontal green bands where the width arises from the uncertainties in the NMEs. Figure from [33].

Theoretical Uncertainties NMEs are subject to large systematic uncertainties and their values can vary by up to a factor of 3 for the same isotope depending on the theoretical model that is used. Table 5.4 shows a summary of recent NME calculations using different calculation techniques for ^{76}Ge, ^{100}Mo and ^{136}Xe. The calculations of NMEs are a complex many-body problem, which involves the interaction of a large number of nucleons and their correlations, which has no analytical solutions and relies on simplifications to derive numerical solutions. Systematic errors from these assumptions are difficult to assess. The most commonly used approaches for calculating NMEs include the Nuclear Shell Model (NSM), Quasi-random Phase Approximation (QRPA), the Energy-Density Functional (EDF) and the Interacting Boson Model (IBM) [26].

Since the NMEs encode the physics that mediates the decay, its uncertainties need

Experiment	Isotope	$G_{0\nu}$ [$10^{-15}\,\mathrm{yr}^{-1}$]	Disc. Sens.	Excl. Sens.
LEGEND [239]	^{76}Ge	2.363 [25]	$1.3 \times 10^{28}\,\mathrm{yr}$	$1.6 \times 10^{28}\,\mathrm{yr}^{-1}$
CUPID [240]	^{100}Mo	15.92 [25]	$0.11 \times 10^{28}\,\mathrm{yr}$	$0.15 \times 10^{28}\,\mathrm{yr}$
nEXO [33]	^{136}Xe	14.58 [25]	$0.74 \times 10^{28}\,\mathrm{yr}$	$1.35 \times 10^{28}\,\mathrm{yr}$

Table 5.5: Comparison of upcoming tonne-scale experiments in terms of their kinematic phase space factor, median discovery, and exclusion sensitivities.

to be reduced significantly to below ∼20 % to allow possible discrimination between neutrino mass mechanisms beyond the light neutrino exchange based on the measured half-life.

Comparison among Tonne-Scale Experiments Definitive proof of the existence of $0\nu\beta\beta$ will likely require a high significance measurement in multiple isotopes and detectors. In addition to reducing the impact of systematic errors that might be uniquely related to a given detector technology, these measurements would be valuable inputs to the abovementioned NME calculation. The NMEs for different decay mediators are likely to be dependent on the nucleus in which the decay occurs.

The upcoming tonne-scale experiments (nEXO [33], LEGEND-100 [239] and CUPID [240]) are aiming to reach exclusion sensitivities on $\langle m_{\beta\beta}\rangle$ of <15 meV. Figure 5.25 plots the discovery and exclusion sensitivities to $\langle m_{\beta\beta}\rangle$ for nEXO against the other two experiment, highlighting a small preference for ^{136}Xe.

It is illustrative to decouple the NME contribution, which has large uncertainties associated with it, from the half-life and phase space factor contributions that are known to have negligible uncertainty. Figure 5.26 shows the NME values for various isotopes as a function of their phase space weighted half-life sensitivity. This dimensionless $T^{0\nu}_{1/2} \times G_{0\nu}$ variable provides a model-independent estimate of the physics reach of an experiment that to first order normalizes the isotope dependence. The uncertainties due to the NMEs are visualized as spread along the y-axis and the

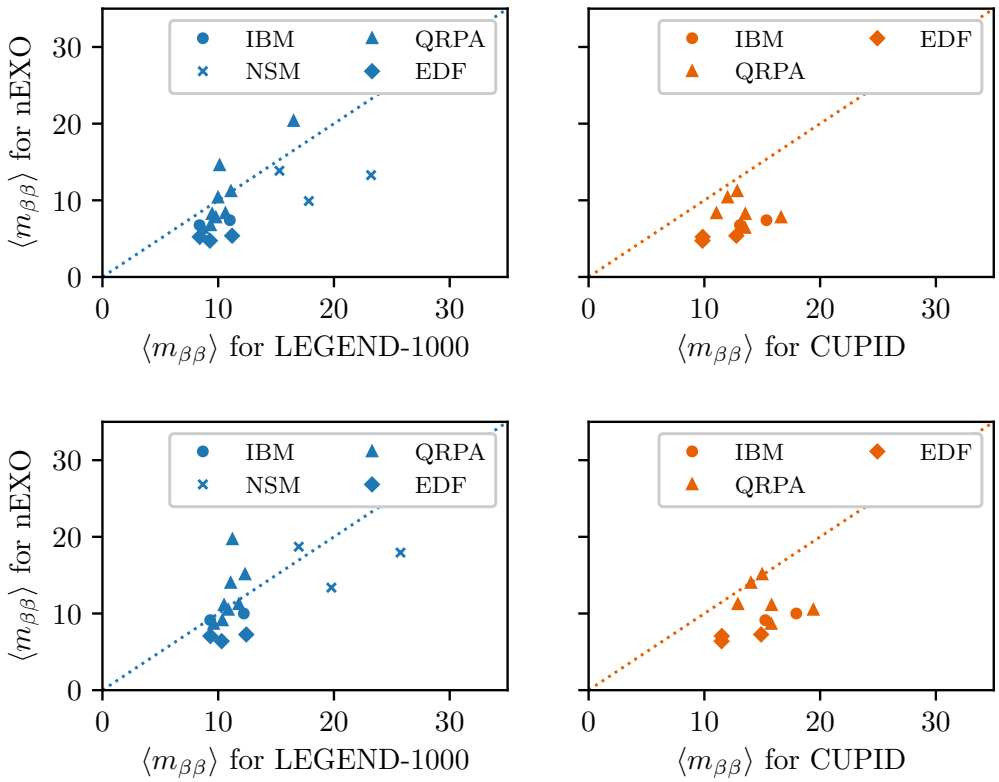

Figure 5.25: Exclusion (top) and discovery (bottom) sensitivity to $\langle m_{\beta\beta} \rangle$ for nEXO vs LEGEND-1000 (left) or CUPID (right), respectively. The sensitivities for LEGEND-1000 and CUPID are taken from [239] and [240], respectively.

corresponding sensitivity to $\langle m_{\beta\beta} \rangle$ is plotted as diagonal lines.

5.7 Conclusion and Outlook

The LXe TPC technology is a mature and highly competitive detector concept to search for $0\nu\beta\beta$. nEXO benefits from the experience gained in EXO-200, which has pioneered the ultra radio-pure LXe technology and improved upon its design with more radio-pure material selection and by deploying a novel charge and light readout system. This enables a powerful multi-variate analysis, exploiting the self-shielding capabilities of LXe by measuring backgrounds with high precision using the outer xenon and providing a near background-free inner xenon region with high sensitivity

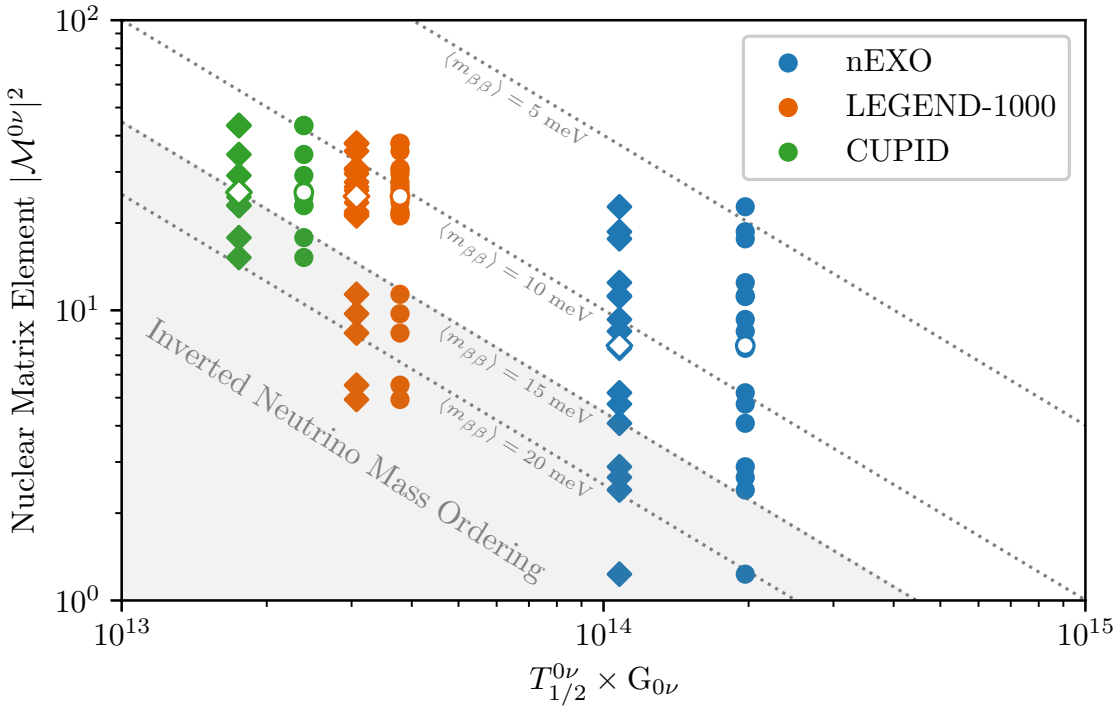

Figure 5.26: Phase space factor weighted half-life exclusion (circles) and discovery (diamonds) sensitivity versus various NMEs values for the upcoming tonne-scale $0\nu\beta\beta$ decay experiments. Compared to Figure 5.25 the exactly calculable contribution $T^{0\nu}_{1/2} \times G_{0\nu}$ are separated from the NME contribution, which is subject to large theoretical uncertainties. The hollow points are the position of the median NME for each of the three isotopes. The different values for $\langle m_{\beta\beta} \rangle$ in this plot are shown as diagonal dashed lines and values in the inverted are shown in grey. With nEXO's projected exclusion sensitivity the inverted neutrino mass ordering can be ruled out at 90 % CL except for the least favorable NME.

to $0\nu\beta\beta$.

At the same time, nEXO is still running an active R&D program to further improve upon its conceptual design to maximize its physics reach. This includes the following hardware and software-based efforts

- in-situ removal of ^{222}Rn through a distillation column
- improved direct VUV-sensitivity of SiPMs
- light-only discrimination of surface-based backgrounds

The upcoming tonne-scale experiments searching for $0\nu\beta\beta$ will all be able to reach

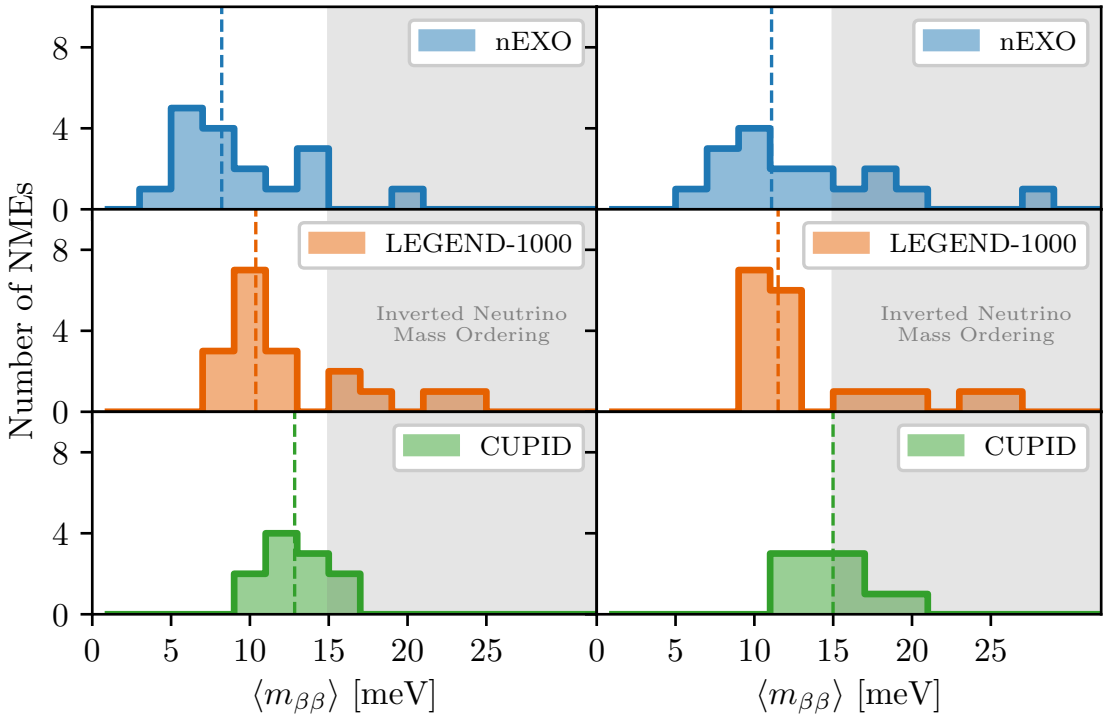

Figure 5.27: Median exclusion (left) and discovery (right) sensitivity to $\langle m_{\beta\beta} \rangle$ for nEXO (top), LEGEND (center), and CUPID (bottom), for different NMEs. The dashed vertical lines represent the median value of $\langle m_{\beta\beta} \rangle$ and the grey area represents values in the inverted neutrino mass ordering. Even though the NME calculations don't follow a statistical distribution it is illustrative to compare the number of NMEs that yield an $\langle m_{\beta\beta} \rangle$ smaller than a given benchmark value.

median exclusion sensitivities beyond the goal of 15 meV for covering the entire inverted neutrino mass ordering, as shown in Figure 5.27. With high discovery sensitivities, these experiments will probe a large fraction of available parameter space and could discover if the inverted neutrino mass ordering is realized in nature. However, in the case of a null result, the LXe technology provides a plausible way to scale to even larger detector sizes up to the kilo-tonne scale. A conceptual design for such a detector design, possibly reaching a half-life exclusion sensitivity of $\sim 1 \times 10^{30}$ yr, will be described in Chapter 6.

Chapter 6

Kilotonne Liquid Xenon Detectors for Rare Event Searches

6.1 Motivation 189

6.2 Irreducible Backgrounds 191

6.3 Detector Concept 194

6.4 Optical Simulations and Light Collection 196

6.5 Scintillation and Cherenkov Light Separation 198

6.6 Sensitivity to $0\nu\beta\beta$ 203

In the case of a null result from the upcoming tonne-scale experiments [85, 98, 240] the LXe TPC technology provides a plausible path forward for scaling to larger sizes, possibly reaching half-life sensitivities beyond $\sim 1 \times 10^{30}$ yr with a kilotonne-scale LXe detector. This chapter provides an overview of such a detector concept.

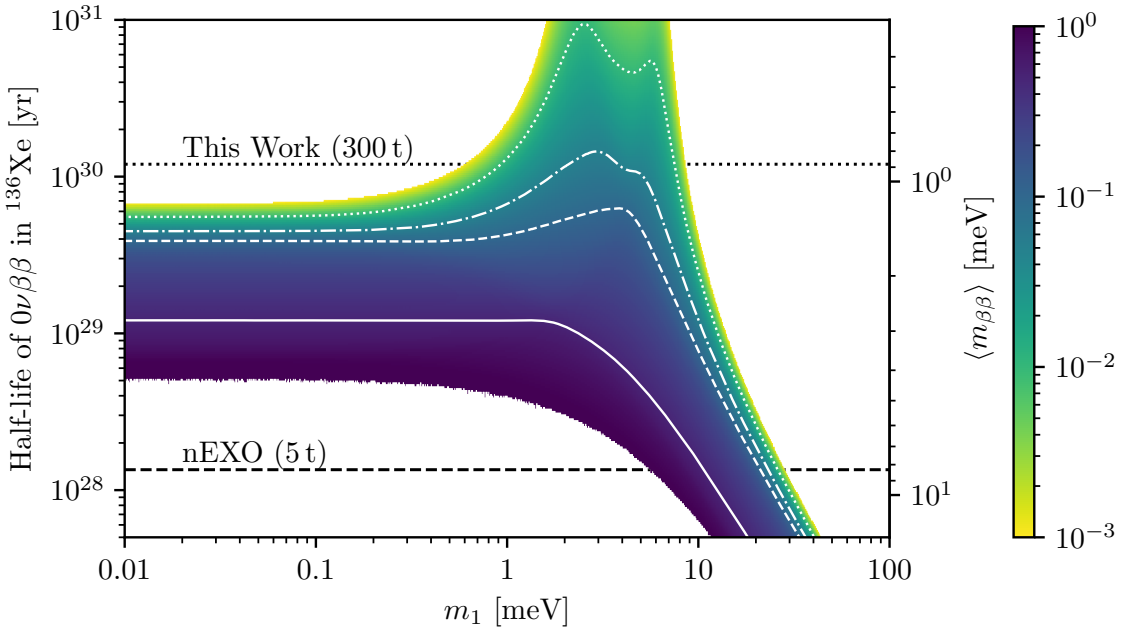

Figure 6.1: Available parameter space for the half-life (left axis) and effective Majorana mass (right axis) in the normal ordering, based on the neutrino oscillation parameters from [28,241]. The unknown Majorana phases are assumed to be uniformly distributed. The color scale indicates the likelihood of a given $\langle m_{\beta\beta}\rangle$ and m_1 pair. The regions for which 50% (solid), 90% (dashed), 95% (dash-dotted), and 99% (dotted) of the available parameter space can be excluded for a given $\langle m_{\beta\beta}\rangle$ sensitivity are given by the white contour curves. The conversion between $T^{0\nu}_{1/2}$ and $\langle m_{\beta\beta}\rangle$ assumes $|\mathcal{M}^{0\nu}| = 2.7$, which corresponds to the median value among currently published models [33]. For reference, the estimated sensitivities of the upcoming tonne-scale nEXO experiment and a proposed concept for a kilotonne-scale LXe detector are marked with a dashed and dotted line, respectively.

6.1 Motivation

Upcoming tonne-scale $0\nu\beta\beta$ experiments [85, 98, 240] are projecting to completely cover the inverted neutrino mass hierarchy reaching a sensitivity to the effective Majorana neutrino mass of $\langle m_{\beta\beta}\rangle \lesssim 15\,\text{meV}$ using a median NME of $|\mathcal{M}^{0\nu}| = 2.7$ and $g_A = 1.27$ [33]. In the case where the normal neutrino mass hierarchy is realized in nature and the lightest neutrino mass eigenstate is $m_1 < 10\,\text{meV}$, the detection of $0\nu\beta\beta$ will be out of reach. Figure 6.1 shows the available parameter space for $0\nu\beta\beta$ in the normal neutrino mass ordering, where the color scale encodes the probability

of $\langle m_{\beta\beta} \rangle$ to be smaller than a certain given mass. This calculation assumes a flat prior on the two unknown Majorana phases in the PMNS matrix and takes into account the current global best fits for the neutrino oscillation parameters [28, 241]. Outside the region of $1\,\mathrm{meV} < m_1 < 10\,\mathrm{meV}$ a future experiment with a sensitivity of $\langle m_{\beta\beta} \rangle \sim 1\,\mathrm{meV}$ would completely cover the normal ordering and would also cover 95 % of the available parameter space inside that region, where cancellations could in principle drive $\langle m_{\beta\beta} \rangle$ down well below 1 meV. However, assuming a uniform prior for the Majorana phases this scenario is very unlikely. The standard assumption for the calculations above is that the light Majorana neutrino exchange mechanism is the main mediator of $0\nu\beta\beta$.

An effective Majorana neutrino mass sensitivity of $\langle m_{\beta\beta} \rangle \sim 1\,\mathrm{meV}$ can be translated into a half-life sensitivity of $T^{0\nu}_{1/2} \sim 1 \times 10^{30}$ year. For $0\nu\beta\beta$ at this half-life the expected event rate can be written down as

$$R = 0.3\,\mathrm{yr}^{-1} \left(\frac{m_{^{136}\mathrm{Xe}}}{100\,\mathrm{t}} \right) \left(\frac{10^{30}\,\mathrm{yr}}{T^{0\nu}_{1/2}} \right) \tag{6.1}$$

where $m_{^{136}\mathrm{Xe}} = \epsilon \cdot \eta \cdot m_{\mathrm{det}}$ is the sensitive mass. ϵ denotes the $0\nu\beta\beta$ detection efficiency, η the enrichment fraction of the LXe and m_{det} the total LXe mass. In the case of perfectly background free experiment Equation 6.1 suggests that an exposure of $\sim$1 kt yr would be required at a half-life of $T^{0\nu}_{1/2} \sim 1 \times 10^{30}$ year. Realistically, a non-zero background is expected and in Section 6.6 the sensitivity of a kilotonne-scale experiment will be evaluated as a function of detector mass.

Due to the relatively high cost of xenon procurement at this scale, this kind of detector will have to be able to pursue a plethora of other physics searches beyond searching for $0\nu\beta\beta$ [83] such as

- Lepton Number Violation at the $\Lambda \sim 10^{13}$ TeV scale [30]
- WIMP searches for detailed studies of the WIMP if discovered near the "neutrino

fog" [242] or more sensitive WIMP searches reaching into the "neutrino fog"

- Alternative dark matter models [57], including particle masses heavier than 100 GeV or composite WIMPs [243] or interaction of dark matter producing MeV-scale energy deposits in a LXe detector [59–61]

- Detection of neutrinos, including coherent elastic neutrino-nucleus scattering of atmospheric neutrinos or elastic scattering of solar neutrinos [76] with $\sim$ keV or $\sim$ MeV energy deposits, respectively and possibly supernova neutrinos if a sufficiently close event were to occur [244]

The following sections will introduce the detector design guided by optimizations of the light response, discuss rejection methods for the irreducible backgrounds and provide an estimate for the ultimate sensitivity that is achievable with such an experiment. The focus here is on a liquid phases detector design, but a gas phase TPC could in principle achieve a similar sensitivity, and details can be found in [83].

6.2 Irreducible Backgrounds

The self-shielding power of LXe at the kilotonne-scale reduces the background rate from external γs from the ^{238}U and ^{232}Th decay chains quite substantially, making them a subdominant contribution. Even ^{222}Rn based backgrounds, such as the γ-decay of ^{214}Bi at 2448 keV, can be substantially reduced. Within the bulk volume, the time coincident α-decay of the ^{214}Po daughter can be tagged with $\sim$100 % efficiency. Moreover, the surface-based ^{222}Rn based backgrounds from drifting charged ion daughters, which is currently the largest background component in nEXO [33], can be removed with high efficiency with a stronger fiducialization given the size of the experiment.

However, previously negligible backgrounds in a tonne-scale experiment such as the high energy tail of the $2\nu\beta\beta$ spectrum and the elastic scattering of solar neutrinos

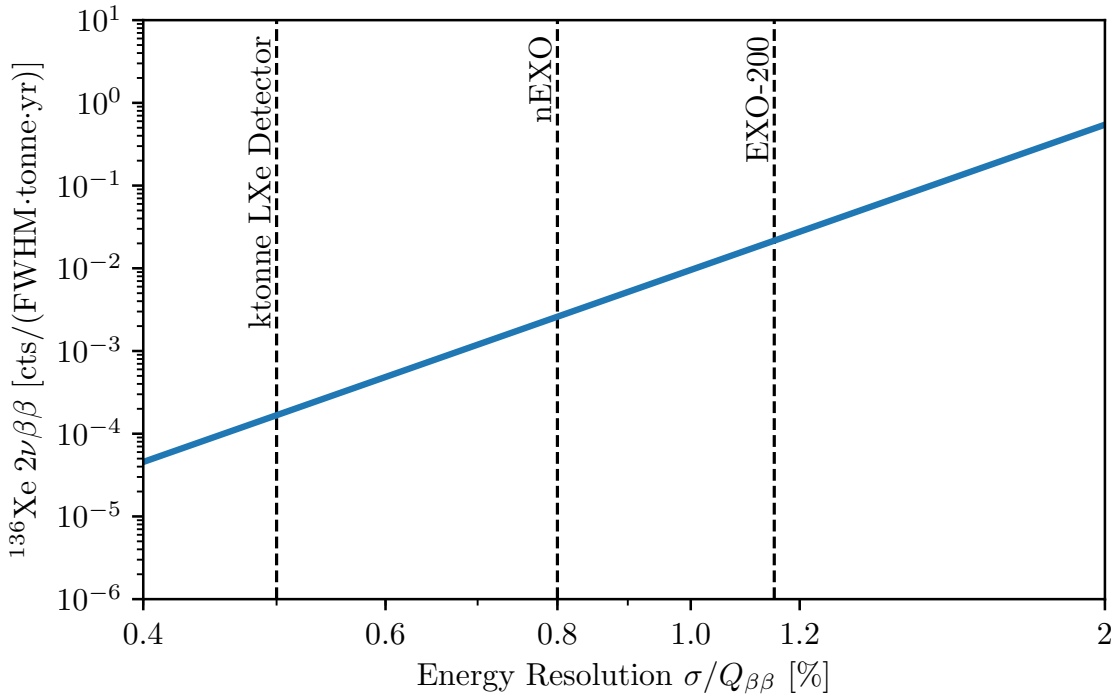

Figure 6.2: Event rate of $2\nu\beta\beta$ events inside the energy ROI defined as $Q_{\beta\beta}\pm$FWHM/2 as a function of the energy resolution of the detector. Plot is based on [92].

become major irreducible backgrounds that require an improved energy resolution and novel rejection methods, respectively.

6.2.1 $2\nu\beta\beta$

At the 10^{30} yr half-life sensitivity an experiment will observe $\sim 10^{9}$ $2\nu\beta\beta$ events for every $0\nu\beta\beta$ event since $T^{2\nu}_{1/2} = 2.11 \pm 0.04(\text{stat.}) \pm 0.21(\text{sys.}) \times 10^{21}$ yr [66]. In order to avoid a significant leakage of $2\nu\beta\beta$ events into the energy ROI, the experiment needs to have a good energy resolution. Based on Figure 6.2 an energy resolution of $\sigma/Q_{\beta\beta} \sim 0.5\,\%$ would result into a background rate of $2\nu\beta\beta$ events inside the ROI of less than $0.5\,\text{cts}\,\text{FWHM}^{-1}\,\text{yr}^{-1}$ in the case of a 3 kt detector and would make it subdominant. Based on the experience from previous LXe experiments the energy resolution is known to be dominated by uncertainties in the light detection and more specifically the light collection efficiency. Other tonne-scale LXe experiments, such as

XENONnT and LZ have already demonstrated an energy resolution of $\sigma \sim 0.81\,\%$ [245] and $\sigma \sim 0.64\,\%$ [156] at 2615 keV, respectively. In Section 6.4 the results from a dedicated light simulation of a kilotonne LXe detector are described and the requirements for the light collection efficiency to achieve this goal are derived.

6.2.2 Solar Neutrinos

With a detector of this size, the rate of solar neutrino interactions in the detector can't be ignored anymore, which is analogous to dark matter experiments approaching the "neutrino fog" [242]. Charged current interactions of neutrinos ($\nu + {}^{136}\mathrm{Xe} \rightarrow {}^{136}\mathrm{Cs}^{*} + e^{-}$) have an event rate of $10.3\,\mathrm{t}^{-1}\,\mathrm{yr}^{-1}$ [76] but can be effectively rejected based on their highly multi-sited event topology consisting of a high energy β and the de-excitation gammas from of the ^{136}Cs daughter nucleus. The major irreducible background arises from the elastic scattering of ^{8}B solar neutrinos off of xenon atoms ($\nu + {}^{136}\mathrm{Xe} \rightarrow {}^{136}\mathrm{Xe} + e^{-}$) with an estimated event rate of $\sim 4.9\,\mathrm{kt}^{-1}\,\mathrm{yr}^{-1}\,\mathrm{FWHM}^{-1}$ at an energy resolution of $\sigma/Q_{\beta\beta} = 0.5\,\%$ [83]. Traditional background rejection techniques can't distinguish between these spatially uniform β-like events with a flat energy distribution that overlaps with the signal energy ROI and $\beta\beta$-like signal events in the ROI. Possible ways to reduce this background are through

- enrichment of the xenon to increase the ratio of atoms undergoing $0\nu\beta\beta$ relative to the number of atoms providing a target for elastic scattering of solar neutrinos
- novel separation technique of β and $\beta\beta$-like events within the ROI based on the amount of emitted Cherenkov light using fast photodetectors and time-of-flight information
- directional sensitivity, correlating the emission of the β from a solar neutrino elastic scattering against the direction of the sun compared to the uniformly emitted $\beta\beta$-events

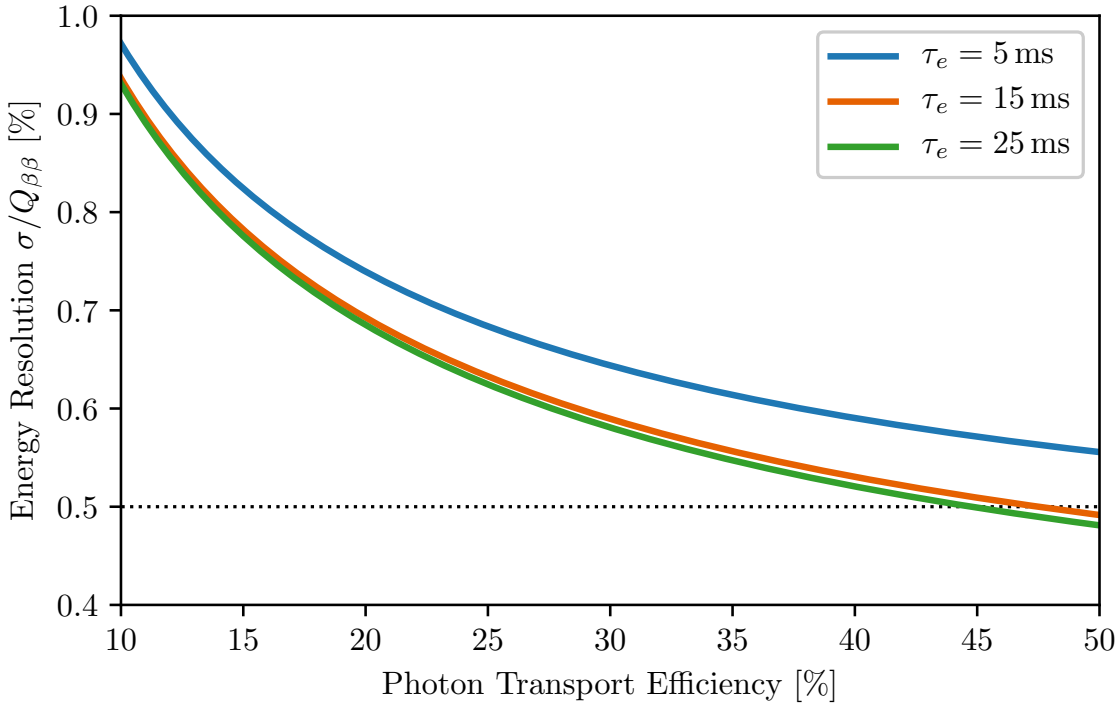

Figure 6.3: Estimated energy resolution at the $Q_{\beta\beta}$-value (based on the semi-empirical equation in Section 4.3) as a function of the PTE inside the detector for various electron lifetimes. The assumed PDE is taken from [102] and the charge readout noise is assumed to be $\sigma_{q,\text{noise}} = 600e^-$. There is only marginal improvement in the energy resolution when increasing the electron lifetime beyond 15 ms.

While in the final detector a combination of all three would be implemented and weighted against cost and engineering complexity here we focus on the separation of β and $\beta\beta$-like events via their Cherenkov light emission using fast photodetectors and the time-of-flight information of the detected photons.

6.3 Detector Concept

The concept for the detector closely follows that of existing [121,130] and upcoming [33, 85] tonne-scale LXe detectors and is generally expected to be scalable to the kilotonne-scale. The major uncertainty for such an experiment is the procurement of large quantities of the isotope of interest. In the absence of this constraint, i.e. in the case

of liquid argon detectors, experiments such as DUNE are being designed that will consist of multiple kilotonne-scale detectors with a total active mass of ∼40 kt.

The concept in the discussion here will be a single liquid-phase cylindrical TPC with equal height and diameter to optimally take advantage of the substantial self-shielding provided by a detector of this size. Using our understanding of the energy resolution in LXe detectors (see Section 4.3 or [33, 80]) we can invoke requirements on the light and charge readout in order to meet our requirement of $\sigma/Q_{\beta\beta} \leq 0.5\,\%$, mainly driven by the need suppress the leakage of the irreducible $2\nu\beta\beta$ background into the ROI.

To achieve this energy resolution the charge collection needs to be highly efficient and the charge readout needs to be sufficiently low noise. This requires a substantially better electron lifetime beyond the 5 ms required for nEXO [33] with a charge drift of just ∼1.2 m. Existing tonne-scale experiments employing a liquid phase purification scheme have demonstrated electron lifetimes beyond 20 ms [246]. At an electric drift field of $200\,\mathrm{V\,cm^{-1}}$ this would results in a charge loss of $\lesssim 10\,\%$. In a single-phase LXe TPC (similar to nEXO) the charge noise will be dominated by the noise added from the charge readout electronics, which can be made subdominant to the light noise as long as $\sigma_{q,\mathrm{noise}} \lesssim 600e^-$ (see Section 4.3).

The scintillation light will be collected by SiPMs, which provides efficient light detection with negligible electronics readout noise. Based on Section 4.3 a total light collection efficiency of $\epsilon_p = \mathrm{PDE} \cdot \mathrm{PTE} \approx 10\,\%$ is needed to achieve this goal. In Section 6.4 the results of the PTE from light simulation of a kilotonne-scale detector will be discussed.

Figure 6.3 shows the estimate of the energy resolution as a function of the PTE for several electron lifetimes. Using the PDE values from [102] and assuming a charge readout noise of $\sigma_{q,\mathrm{noise}} = 600e^-$ we can see that there is only marginal improvement in the energy resolution when increasing the electron lifetime beyond 15 ms.

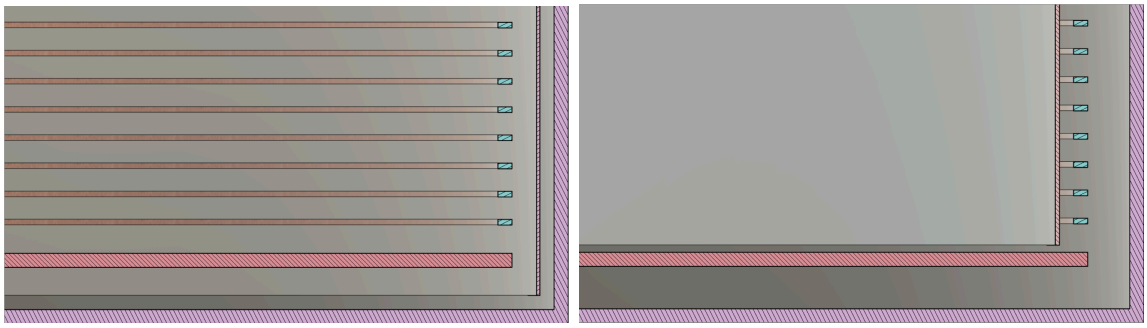

Figure 6.4: Sectional view of a conceptual design for a kilotonne-scale LXe detector, where only a simplified vessel, cathode, FSRs, PTFE reflectors, and photo-detectors are shown. Two different designs were studied: (left) open field cage design with photo-detectors positioned behind the FSRs around the barrel of the vessel and (right) closed-field cage design with the photo-detectors on the flat sides of the detector and PTFE reflectors covering the barrel inside the FSRs.

A detector of this size poses significant challenges for the procurement and enrichment of the xenon given current worldwide production and processing capabilities. However, more efficient alternatives for xenon extraction from the air are being investigated [83].

6.4 Optical Simulations and Light Collection

Typically, large liquid xenon detectors at the ∼100 kg or tonne-scale are limited in their total energy resolution by the resolution in the light channel and more specifically by the light collection efficiency. In a kilotonne LXe experiment with a height and radius of about 3.5 m the optical properties of the liquid xenon like the absorption length and the scattering length are significantly more important than for any previous or currently running large LXe detector.

The Rayleigh scattering length has been previously measured, and while no consistent value is reported the range of values is constrained to between 30 cm–50 cm at the 178 nm scintillation light wavelength (see Section 4.1.2). Therefore, the Rayleigh scattering length is significantly smaller than the linear dimensions of the TPC, resulting in diffusive propagation and significantly longer travel distances of

Parameter	Value
Vessel height	7.4 m
Vessel diameter	7.4 m
Drift length	7.32 m
Field ring inner diameter	7.3 m
Field ring width	10 mm
Field ring height	4 mm
Field ring spacing	20 mm
Number of field rings	365
PTFE reflector inner diameter	7.27 m
PTFE reflector thickness	3 mm

Table 6.1: Summary of the dimensions of detector components used for the light transport simulations of a kilotonne LXe detector.

the scintillation light. In contrast, the absorption length is difficult to measure and depends on the LXe purity. The nEXO, LZ and XENON1T experiments assume an absorption length of $\lambda_{\text{abs}} = 20\,\text{m}$ [33], $\lambda_{\text{abs}} = 30\,\text{m}$ [121] and $\lambda_{\text{abs}} = 50\,\text{m}$ [247], respectively.

To estimate the effect of both the λ_{scat} and λ_{abs} on the light collection efficiency a dedicated light transport simulation with Chroma [248] was performed. In addition, an open and closed field cage design was separately simulated and a sectional view of both designs is shown in Figure 6.4. The former has the photo-detectors behind the FSRs covering the barrel of the TPC vessel (similar to nEXO [33, 87]) whereas the latter makes use of PTFE reflectors covering the barrel in front of the FSRs and photo-detectors are placed on the flat side of the TPC (similar to EXO-200 [72] and other LXe based dark matter experiments [121, 247]). The parameters describing the detector geometry are summarized in Table 6.1. The relevant optical parameters for these simulations are largely based on [33] and are also summarized in Table 6.2.

The absorption length λ_{abs} was varied from 1 m–100 m for a Rayleigh scattering length of 30 cm or 50 cm, respectively. At each value of λ_{abs} a total of 5×10^6 photons were uniformly distributed within the field cage and the reported PTE is the average across the entire simulated volume. As can be seen in Figure 6.5 the open field cage design outperforms the closed field cage design in terms of PTE for the range of absorption lengths considered. More importantly, both designs appear to the reach a PTE larger than 35 % at around $\lambda_{\text{abs}} = 80$ m and $\lambda_{\text{scat}} = 50$ cm which is sufficient to reach the energy resolution goal of ∼0.5 % (see Figure 6.3).

While the transport of scintillation light over such distances needs to be demonstrated experimentally it seems at least plausible that a sufficiently high PTE can be achieved based on these results. This requires only marginally longer λ_{abs} than what is already assumed in tonne-scale detectors [121, 247] where the requirement on the electron lifetime is not as stringent as for a kilotonne-scale experiment. In addition, given the rate at which the SiPM technology has matured and improved over the last decade [96] an additional increase in their PDE for VUV scintillation light seems likely, resulting in less stringent requirements on the PTE to reach the same energy resolution.

6.5 Scintillation and Cherenkov Light Separation

In addition to the production of scintillation light as a charged particle traverses the LXe, charged particles can also produce Cherenkov light if their velocity exceeds the phase velocity of light in LXe. The Cherenkov light spectrum depends on the index of refraction of LXe which can be calculated using [250], which shows good agreement with measurements. For this simulation, the Cherenkov photons are assumed to be all emitted with a wavelength of 300 nm and the corresponding optical parameters at this wavelength are summarized in Table 6.2. Using the proper $^{\text{enr}}$Xe density of

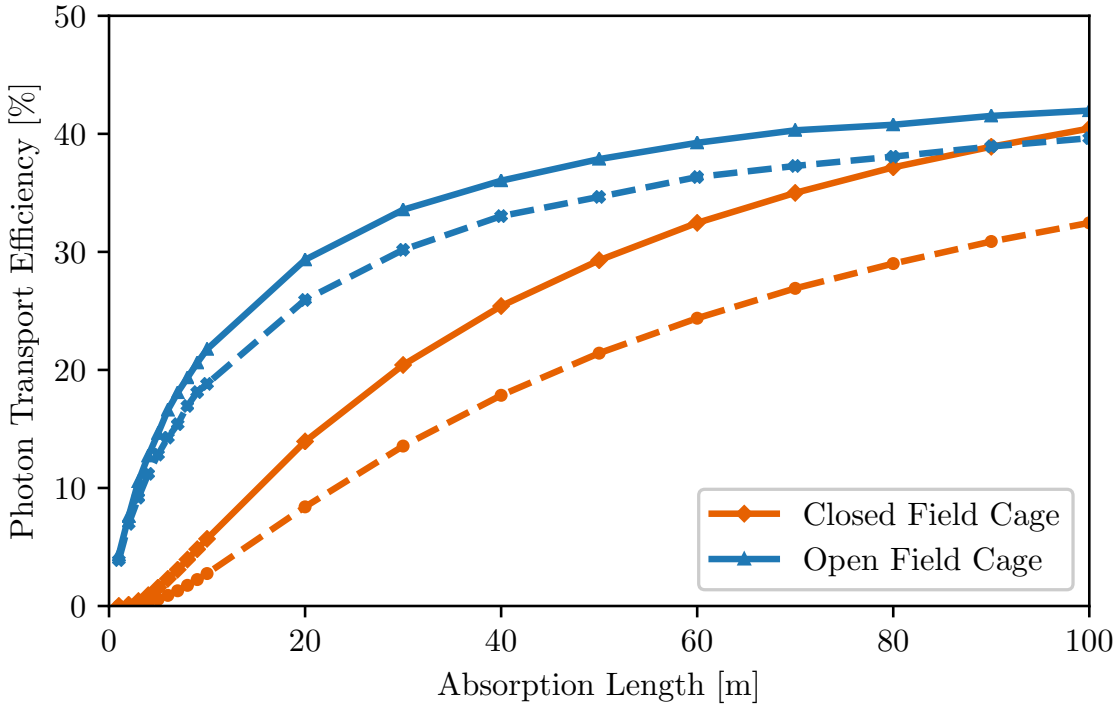

Figure 6.5: Estimated PTE from a Chroma light propagation simulation of a kilotonne LXe detector using a geometry as defined in Table 6.1 and assigned optical properties defined in Table 6.2. The dashed and solid curves are for $\lambda_{\text{scat}} = 30\,\text{cm}$ and $\lambda_{\text{scat}} = 50\,\text{cm}$, respectively.

$3.057\,\text{g}\,\text{cm}^{-3}$ [85] the index of refraction at 178 nm and 300 nm become $n = 1.69$ and $n = 1.43$, respectively. The yield of Cherenkov photons can be calculated using the continuous slowing down approximation in combination with stopping power values from [251], which was simulated with Geant4 in [249]. The distribution of light yields is assumed to be Gaussian distribution for simplicity with the mean and width approximated from [249] and is shown on the left side in Figure 6.6. As can be seen a β-event with the same energy as a $\beta\beta$-event will on average produce more Cherenkov light, where the difference is maximal if the two βs each share exactly half the total energy. The number of emitted Cherenkov photons is $\sim$100 times smaller compared to that of the scintillation light [249]. However, due to the longer wavelength of the Cherenkov photons, they travel faster through the LXe and are detected before the scintillation light. The simulated time distribution of Cherenkov and scintillation

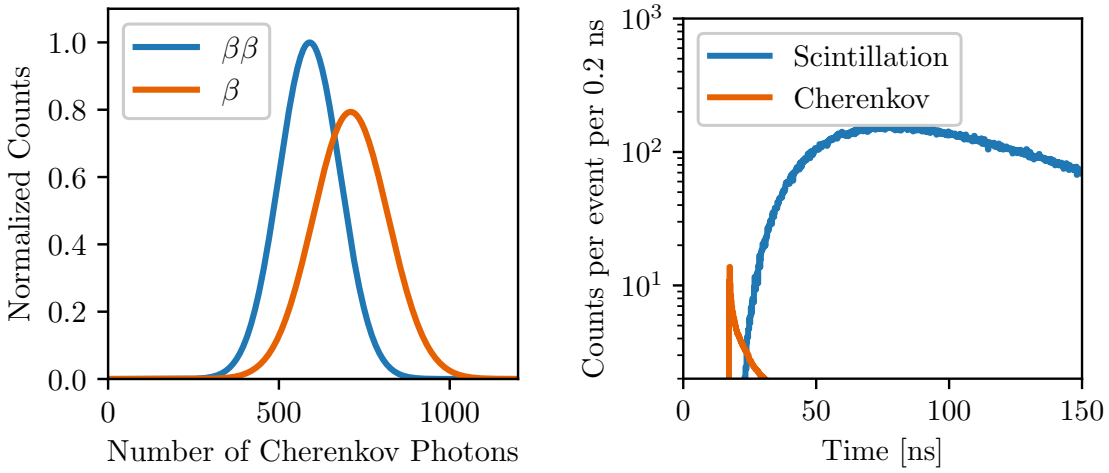

Figure 6.6: (left) Distribution of number of produced Cherenkov photons in LXe for β and $\beta\beta$ events with an energy of 2458 keV which are based on [249]. (right) Simulated arrival time of Cherenkov photons at $\lambda = 300$ nm and scintillation photons at $\lambda = 178$ nm from the center of a kilotonne LXe detector.

photons is shown in Figure 6.6, where one can see that in kilotonne-scale LXe detector 80 % of the light detected within the first 10 ns are Cherenkov photons. The earliest Cherenkov light is detected around $t_{\text{Cherenkov}} = 3.7\,\text{m}/(c/1.43) = 17.7$ ns after the event happened which is in contrast to the earliest scintillation light detected at around $t_{\text{Scintillation}} = 3.7\,\text{m}/(c/1.69) = 20.9$ ns. Therefore, an experiment with sufficiently fast light sensors with ns-scale timing resolution such as Photon-Digital-Converters (PDC) [252] is in principle capable of rejecting background events based on their Cherenkov light signature and time-of-flight information. This technique can be similarly applied to other γ-backgrounds producing a β-like event when interacting with the LXe via the photoelectric effect.

To evaluate the discrimination capability of this technique 1×10^5 toys are generated for which the following procedure is applied

1. Integrate the time distribution of scintillation and Cherenkov photons in the right plot in Figure 6.6 to get a cumulative number of detected photons as a function of time $N_p(t, \lambda)$

Parameter	Scintillation	Cherenkov
Wavelength	178nm	300nm
LXe Absorption Length	20m	50m
LXe Scattering Length	30cm	242cm
LXe Index of Refraction	1.69	1.43
Cathode	80%	90%
Field Shaping Rings	80%	90%
Anode	20%	38%
Vessel	0%	0%
Diffuse Reflectivity	0%	0%
PTFE Specular Reflectivity	0%	0%
PTFE Diffuse Reflectivity	95%	95%
SiPMs	[126]	[126]

Table 6.2: Summary of optical parameters used to simulate the light response of a kilotonne LXe detector in Chroma.

2. Draw a random number from the distribution of light yields in the left plot in Figure 6.6

3. Rescale the number of detected photons by their respective light yields $N_p(t, \lambda) \cdot \eta(\lambda)$

4. Apply the light collection efficiency, which is drawn from a Binomial distribution with survival probability $p(\lambda) = \epsilon_p(\lambda) = \mathrm{PTE}(\lambda) \cdot \mathrm{PTE}(\lambda)$

5. Generate the distribution of detected photons $N_p(t, \lambda) \cdot \eta(\lambda) \cdot \epsilon_p(\lambda)$ as a function of integration time as shown in Figure 6.7 for 1 ns, 10 ns and 20 ns

The further the two distributions are separated the more effective the discrimination based on the Cherenkov signature will be. For a time resolution of ∼10 ns, the separation appears largest and starts to reduce when integrating for longer as

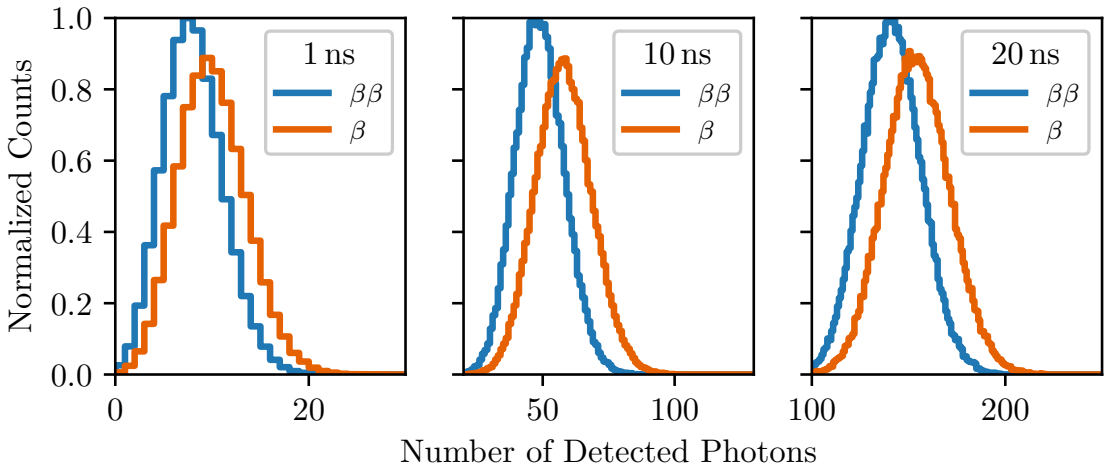

Figure 6.7: Distribution of detected photons for different integration times of 1 ns, 10 ns and 20 ns. For short integration times, not enough photons are detected to distinguish β-like from $\beta\beta$-like events. Conversely, for longer integration times more of the scintillation will be collected smearing out the Cherenkov light signature. An integration time of 10 ns provides the optimal separation.

more scintillation light will be detected, washing out the Cherenkov light signature. Integrating these two distributions for any given integration time yields the receiver operating characteristic (ROC) curves shown in Figure 6.8. At a time resolution of 10 ns this technique can reject ∼65 % of β-like solar neutrino backgrounds while keeping ∼65 % of $\beta\beta$-like signal events. These results are in good agreement with previous simplified studies of this rejection technique for a tonne-scale LXe detector [249] and will provide a boost in sensitivity for kilotonne scale experiments which will be discussed in Section 6.6.

There are some simplifications made in this analysis such as

- only simulating scintillation and Cherenkov photons at single wavelengths instead of incorporating the full emission spectrum
- ignoring the directionality of the Cherenkov light, but given the size of a kilotonne LXe detector possibly much of that directionality is washed out because of Rayleigh scattering by the time photons are detected

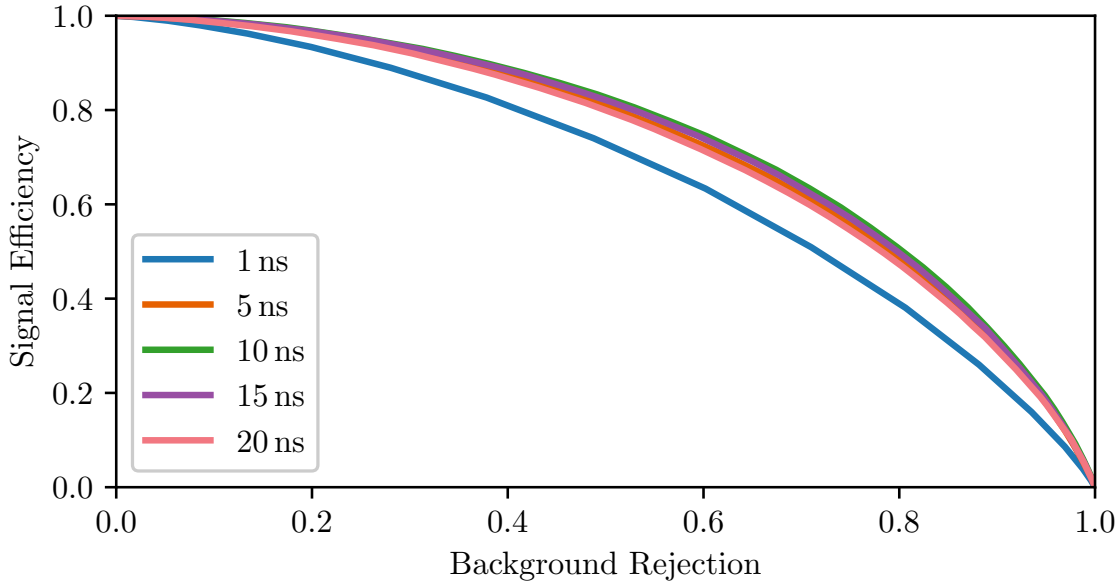

Figure 6.8: Signal efficiency as a function of background rejection when using a time-of-flight based discrimination of β-like and $\beta\beta$-like events. This study suggests that a 10 ns time resolution of the photo-detectors maximizes the rejection capabilities and results in an optimal rejection of ∼65 % of background events while keeping ∼65 % of the signal events.

- only generating events in the center of the detector, where a dedicated study is needed to take advantage of spatial variation in the discrimination of βs and $\beta\beta$s (presumably worse as you get closer to the edge since scintillation photons will become dominant)

6.6 Sensitivity to $0\nu\beta\beta$

The exclusion sensitivity for this kilotonne LXe detector was evaluated by generating toy Monte Carlo data sets from the background-only model (described in detail in [83]) for which the 90% CL upper limit on the $0\nu\beta\beta$ signal was determined from a profile likelihood of the signal PDF. The fits were performed only within the energy ROI and assuming negligible normalization errors, the background PDFs were held constant and only the signal PDF was allowed to freely float. The discovery sensitivity was

estimated using the same general approach but determining the number of $0\nu\beta\beta$ events for which the background-only hypothesis can be rejected at the 3σ CL for a median experiment in the case of a true $0\nu\beta\beta$ being present.

The exclusion and discovery sensitivity results are shown in Figure 6.9, where a $^{\text{nat}}$Xe detector concept with a total mass ranging from 1 kt–5 kt was studied separately from a $^{\text{enr}}$Xe detector (90 % in ^{136}Xe) with a mass ranging from 0.1 kt–0.5 kt. It was found that an enrichment fraction of at least 50 % is necessary to reach a half-life sensitivity of $>1 \times 10^{30}$ yr [83]. The additional boost in sensitivity from deploying a Cherenkov light-based discrimination of background events is shown as dashed lines in Figure 6.9. In the case of the $^{\text{enr}}$Xe or $^{\text{nat}}$Xe detector the increase in sensitivity is $\sim$15 % and $\sim$40 %, respectively.

The sensitivity scales with $\sim \sqrt{t}$, as expected from a background limited experiment, where the majority of the sensitivity is gained within 10 yr of data taking and only another 30 % relative gain in sensitivity when running the experiment for 20 yr.

The future of such a LXe-based program up to the kilotonne scale highly depends on novel ideas to bring down the cost of acquiring and enriching xenon. This needs to be done at a competitive price well below the current market price and might require a staged approach where an intermediate $\sim$50 t–100 t could be built to test the scalability and not disrupt global xenon supply [83].

In the case of a null result from the upcoming tonne-scale experiments a next-generation kilotonne-scale $0\nu\beta\beta$ experiment based on the LXe TPC technology appears plausible and could allow to cover up to 95 % of all of the available Majorana neutrino mass parameter space. Even beyond searching for $0\nu\beta\beta$, a LXe detector at this scale can perform a plethora of rare event searches including the WIMP dark matter searches at or far beyond the "neutrino fog", measurements of solar and possibly supernova neutrinos, and searches for other exotic new physics.

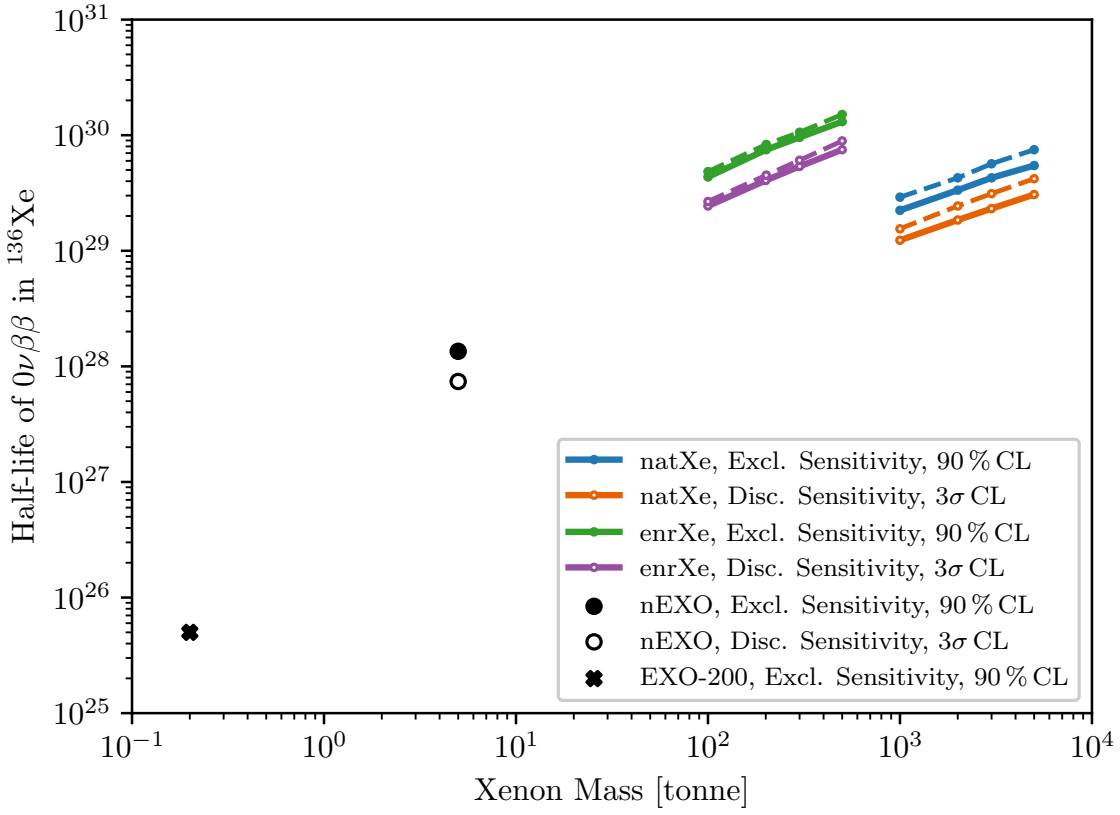

Figure 6.9: Sensitivity of LXe-based $0\nu\beta\beta$ experiments as a function of their detector mass, including the results from EXO-200 [32] and projection from nEXO [33] and this kilotonne LXe detector concept [83]. The 90 % CL exclusion sensitivity is shown with solid markers whereas the 3σ discovery sensitivity is shown with open markers. The cases with solar ν background rejection using the Cherenkov-based single β discrimination are shown as dashed lines. The half-life sensitivity goal of 1×10^{30} yr can only be reached in the case of a $\gtrsim 0.3$ kt $^{\text{enr}}$Xe detector. The $^{\text{nat}}$Xe detector with the same sensitive mass, i.e. $\gtrsim 3$ kt total mass, only reaches a 40 % lower sensitivity due to the roughly tenfold increase in the solar ν background.

Chapter 7

Conclusion

In this work, we have examined the capabilities of three generations of LXe-based TPCs, ranging from 200 kg to ∼3 kt in total detector mass in the search for rare processes. The search for rare events at the weak scale is a promising doorway for unraveling new insights into our universe. Historically, reconciling the peculiarities with the weak force has always provided a deeper understanding of the particles in the SM and their fundamental interactions.

Search for Exotic Dark Matter Interactions in LXe

The importance of understanding what makes up about 85 % of all matter in the universe cannot be overstated. Since well-motivated dark matter candidates have thus far evaded detection by terrestrial detectors, the theoretical landscape of dark matter models is expanding. It includes novel interaction mechanisms with ordinary matter, that go beyond the WIMP-paradigm of elastic scattering of heavy dark matter with masses of $\mathcal{O}(100\,\mathrm{GeV})$.

The EXO-200 detector, which was a pathfinder to establish the LXe TPC technology in the search for $0\nu\beta\beta$, is a well-understood ultra-low background experiment that took data from 2011 through 2019 and placed stringent limits on the half-life of

$0\nu\beta\beta$ in ^{136}Xe [32]. For this thesis, the same data was analyzed for the existence of charged-current absorption signatures of fermionic dark matter. This type of dark matter interaction generates a unique event topology with energies on the order of $\mathcal{O}$(MeV). The active energy search window was extended from 3 MeV to 8 MeV. To ensure that the energy response of the detector is well understood at high energy, an energy calibration with known γ-deexcitation peaks from a custom AmBe source was performed, indicating a <1 % error in the energy calibration. One caveat about the analysis is the presently limited knowledge of the nuclear states of the ^{136}Cs. The nuclear structure of ^{136}Cs is an active field of research, and a detailed understanding is of great interest for future LXe-based neutrino detectors searching for $0\nu\beta\beta$ or studying solar neutrinos from the CNO cycle in the sun. The latter could use the decay of long-lived isomeric states to perform an essentially background-free measurement of solar neutrinos. Upon new details about additional low-lying nuclear levels, this analysis could be revisited since identifying the unique signature of a de-excitation through multiple γs would further reduce backgrounds for this search and improve the sensitivity. No statistically significant deviation from the background projections were observed, resulting in a minimum lower limit on the interaction cross-section of $6 \times 10^{-51}\,\mathrm{cm}^2$ at 8.3 MeV at the 90 % CL and excluding new parameter space for this type of dark matter with $m_\chi = 2.6\,\mathrm{MeV}$–$11.6\,\mathrm{MeV}$ [65].

It should be noted that limits from rare event experiments, such as dedicated $0\nu\beta\beta$ and DM experiments, can place competitive limits compared to searches for new physics at the LHC. Furthermore, EXO-200 has demonstrated an ultra-low electron recoil background rate of $4.0 \times 10^{-4}\,\mathrm{cts\,kg^{-1}\,yr^{-1}\,keV^{-1}}$ above 4 MeV, enabling other rare event searches to be performed with the data analyzed here, but which are beyond the scope of this work. Expanding the physics reach of existing and upcoming low-background experiments is imperative since the allowed parameter space of dark matter models is still quite vast despite the enormous efforts to date.

Search for $0\nu\beta\beta$ at the Tonne Scale

Neutrinos are the most abundant massive particles in the universe and yet they remain the least understood elementary particle in the SM. A more complete picture of their properties is key to understanding some of the most profound questions in particle physics, astrophysics, and cosmology, such as an alternative mass generation mechanism besides the Higgs mechanism, the dynamics of supernova explosions, and the matter-antimatter asymmetry in the early universe. The discovery of $0\nu\beta\beta$ would provide key insights to the above questions and would reveal a new type of particle in the SM, a Majorana fermion.

The next step in the evolution of LXe TPC-based $0\nu\beta\beta$ searches is nEXO, which is built on the experience and pioneering work done in EXO-200. nEXO will utilize 5000 kg of enriched LXe and deploy novel charge and light readout systems that will enable an improved energy resolution and event discrimination compared to EXO-200.

Light Transport

In this thesis, the details of the light and charge transport in LXe were examined. For the former, a completely new GPU-based light simulation of nEXO was developed that allowed probing a large parameter space of optical parameters to understand and improve its light response. The simulation of the position-dependent light collection in the detector was one of the major improvements in the realism of the detector response of nEXO compared to previous work. Obtaining reliable data for optical properties such as the reflectivity of detector materials for VUV photons at $\sim$175 nm is difficult. To solidify our estimates of the light collection efficiency for nEXO, a detailed light simulation of the EXO-200 detector is underway, showing promising data and MC agreement. This data can be used to estimate the allowed range of optical parameters of typical materials in the VUV range in-situ and possibly constrain LXe-based properties such as the Rayleigh scattering and absorption length.

Furthermore, the light detection system in nEXO is unique among other LXe-based TPCs for rare events searches, allowing for detailed imaging of the interactions inside the detector. Combined with the newly developed GPU-accelerated light simulations, which can produce a high statistics dataset of hit patterns for various backgrounds, a Convolutional Neural Network (CNN) would improve the discrimination capabilities of the dominant background source from surface-based ^{222}Rn decay daughters. A light-based event discriminator would provide a powerful tool for background rejection in regions with compromised or no charge collection. The reduction of surface-based γ-backgrounds can provide an increase in sensitivity for nEXO to $0\nu\beta\beta$ by up to an additional $\sim$30 % based on Figure 5.16.

Charge Transport

Regarding the charge transport in LXe, a significant amount of groundwork has been laid to develop a purity model for LXe. The purity setups at Yale have carried out initial measurements of critical input parameters to understand the release of electronegative impurities into such experiments. The next steps include the measurements of various gas species besides oxygen to understand their relative impact on the electron lifetime (most discussions in the literature estimate the tolerable impurity burden of an experiment in oxygen-equivalent quantities). Ultimately, the extrapolation of measured quantities and properties from small-scale test setups needs to be extrapolated to a detector with the size of nEXO in a meaningful way. The predictive power of such a model is crucial in informing and optimizing the design of such experiments during the R&D phase. With experiments approaching electron drift lengths of $\mathcal{O}$(m), a stringent qualification procedure for chemical purity (similar to the radiopurity) needs to be established. Preliminary data from operating large LXe experiments have shown electron lifetime above 5 ms [135, 156] using conventional heated-getter purifiers are reassuring. However, a detailed understanding of spatial and temporal systematic

uncertainties on the electron lifetime is needed to implement an effective calibration procedure that will ensure that nEXO (and possibly even larger detectors) can meet its energy resolution goal.

Physics Reach

Lastly, an overview of the robust bottom-up estimate of the physics reach of the upcoming tonne-scale nEXO experiment was given. The projected half-life exclusion and discovery sensitivity are 1.35×10^{28} yr at the 90 % CL and 0.74×10^{28} yr at 3σ significance, respectively. This represents an improvement in half-life sensitivity by about two orders of magnitude compared to the current generation experiment, allowing nEXO to fully cover the inverted neutrino mass ordering. If $0\nu\beta\beta$ were to be observed the details of the decay could be studied by measuring the angular distribution of the two outgoing βs by filling nEXO with high-pressure xenon gas. This would provide valuable input for calculations of NMEs and could reveal additional new physics through the presence of other beyond the SM particles contributing to the decay rate beyond the standard exchange of light Majorana neutrinos.

Kilotonne-scale LXe Observatory for Rare Events

However, even in the case of a null result, the LXe (and GXe) TPC technology provides an attractive and plausible path for scaling the detector mass beyond the kilotonne scale. A LXe-based detector concept was introduced that would be able to reach sensitivities that could probe a larger fraction of the remaining parameter space in the normal ordering. A major challenge for a detector of this magnitude is the procurement (and enrichment, if required) of xenon, which today for the most part is a parasitic side-product of air liquefaction plants for the steel industry. Dedicated solutions for the extraction of xenon from the air are being investigated to enable a competitive price below the current market price and also procurement of the

quantities needed [83]. Traditional radioactive backgrounds are significantly reduced for a kilotonne-scale LXe detector due to its effective stopping power against external γ-radiation. However, other backgrounds that were previously negligible start to become dominant, which includes the leakage of $2\nu\beta\beta$ backgrounds into the energy ROI around $Q_{\beta\beta}$ and the scattering of ^{8}B solar neutrinos. A dedicated light simulation was performed to evaluate the requirement of the light detection system to render the contributions from these backgrounds manageable or even negligible. The impact of a novel method for background rejection based on the temporal separation of Cherenkov and scintillation photons was investigated. The projected exclusion sensitivity for a kilotonne-scale would be $\sim 1 \times 10^{30}$ yr at the 90 % CL, probing $\sim$95 % of the still allowed effective Majorana neutrino mass parameter space (when assuming that the exchange of a light Majorana neutrino majorly contributes to the decay rate).

The LXe TPC technology is a versatile and scalable detector technology that provides some of the most stringent limits on dark matter scattering cross-sections and the half-life of neutrino-less double beta decay. Due to its excellent self-shielding capabilities, intrinsic purity, and background rejection capabilities it will remain a workhorse for searches in nuclear, particle, and astroparticle physics for the foreseeable future. Significant technological achievements are being pursued to maximize the potential of this technology. This includes

- the development of 3D-integrated digital SiPMs will enable an integrated photon-counting solution with negligible readout noise and fast timing [252]
- Fast picosecond-scale photodetectors [253] for Cherenkov-scintillation light separation for improved background rejection [249, 254]
- Pixelated low-noise charge readout with integrated front-end electronics at the pixel-level [255–258]

While these developments are not yet mature enough to be implemented in nEXO, they

might heavily influence the feasibility and design of future kilotonne-scale experiments using LXe.

A discovery might be just around the corner!

Bibliography

[1] W. Pauli. Dear radioactive ladies and gentlemen. *Phys. Today*, 31N9:27, 1978.

[2] C. L. Cowan, F. Reines, F. B. Harrison, H. W. Kruse, and A. D. McGuire. Detection of the free neutrino: a confirmation. *Science*, 124(3212):103–104, July 1956.

[3] T. D. Lee and C. N. Yang. Question of parity conservation in weak interactions. *Physical Review*, 104(1):254–258, October 1956.

[4] T. D. Lee and C. N. Yang. Parity nonconservation and a two-component theory of the neutrino. *Physical Review*, 105(5):1671–1675, March 1957.

[5] C. S. Wu, E. Ambler, R. W. Hayward, D. D. Hoppes, and R. P. Hudson. Experimental Test of Parity Conservation in β Decay. *Phys. Rev.*, 105:1413–1414, 1957.

[6] Y. Fukuda et al. Evidence for oscillation of atmospheric neutrinos. *Phys. Rev. Lett.*, 81:1562–1567, 1998.

[7] K. Eguchi et al. First results from KamLAND: Evidence for reactor anti-neutrino disappearance. *Phys. Rev. Lett.*, 90:021802, 2003.

[8] Q. R. Ahmad et al. Direct evidence for neutrino flavor transformation from neutral current interactions in the Sudbury Neutrino Observatory. *Phys. Rev. Lett.*, 89:011301, 2002.

[9] B. Pontecorvo. Neutrino Experiments and the Problem of Conservation of Leptonic Charge. *Zh. Eksp. Teor. Fiz.*, 53:1717–1725, 1967.

[10] K. Abe et al. Hyper-Kamiokande Design Report. 5 2018.

[11] B. Abi et al. Deep Underground Neutrino Experiment (DUNE), Far Detector Technical Design Report, Volume II DUNE Physics. 2 2020.

[12] JUNO Collaboration. Neutrino mass ordering. https://neutrinos.fnal.gov/mysteries/mass-ordering/#moreinfo.

[13] M. Aker et al. Direct neutrino-mass measurement with sub-electronvolt sensitivity. *Nature Phys.*, 18(2):160–166, 2022.

[14] M. M. Ivanov, M. Simonović, and M. Zaldarriaga. Cosmological Parameters and Neutrino Masses from the Final Planck and Full-Shape BOSS Data. *Phys. Rev. D*, 101(8):083504, 2020.

[15] Y. Y. Y. Wong. Neutrino mass in cosmology: status and prospects. *Ann. Rev. Nucl. Part. Sci.*, 61:69–98, 2011.

[16] E. Majorana. Teoria simmetrica dell'elettrone e del positrone. *Nuovo Cim.*, 14:171–184, 1937.

[17] G. Racah. On the symmetry of particle and antiparticle. *Nuovo Cim.*, 14:322–328, 1937.

[18] W. de Boer. Grand unified theories and supersymmetry in particle physics and cosmology. *Prog. Part. Nucl. Phys.*, 33:201–302, 1994.

[19] S. Raby. Grand Unified Theories. In *2nd World Summit: Physics Beyond the Standard Model*, 8 2006.

[20] D. Croon, T. E. Gonzalo, L. Graf, N. Košnik, and G. White. GUT Physics in the era of the LHC. *Front. in Phys.*, 7:76, 2019.

[21] A. D. Sakharov. Violation of cp invariance, c asymmetry, and baryon asymmetry of the universe. *Soviet Physics Uspekhi*, 34(5):392–393, May 1991.

[22] A. Riotto and M. Trodden. Recent progress in baryogenesis. *Ann. Rev. Nucl. Part. Sci.*, 49:35–75, 1999.

[23] W. Furry. On transition probabilities in double beta-disintegration. *Phys. Rev.*, 56:1184–1193, 1939.

[24] M. Goeppert-Mayer. Double beta-disintegration. *Phys. Rev.*, 48:512–516, 1935.

[25] J. Kotila and F. Iachello. Phase space factors for double-β decay. *Phys. Rev. C*, 85:034316, 2012.

[26] J. Engel and J. Menéndez. Status and Future of Nuclear Matrix Elements for Neutrinoless Double-Beta Decay: A Review. *Rept. Prog. Phys.*, 80(4):046301, 2017.

[27] J. Schechter and J. W. F. Valle. Neutrinoless double-β decay in su(2)×u(1) theories. *Phys. Rev. D*, 25:2951–2954, Jun 1982.

[28] I. Esteban, M. C. Gonzalez-Garcia, M. Maltoni, T. Schwetz, and A. Zhou. The fate of hints: updated global analysis of three-flavor neutrino oscillations. *JHEP*, 09:178, 2020.

[29] G. Benato. Effective majorana mass and neutrinoless double beta decay. *Eur. Phys. J. C*, 75(11):563, Nov 2015.

[30] M. J. Dolinski, A. W. P. Poon, and W. Rodejohann. Neutrinoless Double-Beta Decay: Status and Prospects. *Ann. Rev. Nucl. Part. Sci.*, 69:219–251, 2019.

[31] S. Abe et al. First Search for the Majorana Nature of Neutrinos in the Inverted Mass Ordering Region with KamLAND-Zen. *2203.02139*, 3 2022.

[32] G. Anton et al. Search for Neutrinoless Double-β Decay with the Complete EXO-200 Dataset. *Phys. Rev. Lett.*, 123(16):161802, 2019.

[33] G. Adhikari et al. nEXO: neutrinoless double beta decay search beyond 10^{28} year half-life sensitivity. *J. Phys. G*, 49(1):015104, 2022.

[34] C. Skordis and T. Zlosnik. New Relativistic Theory for Modified Newtonian Dynamics. *Phys. Rev. Lett.*, 127(16):161302, 2021.

[35] S. Dodelson. The Real Problem with MOND. *Int. J. Mod. Phys. D*, 20:2749–2753, 2011.

[36] J. H. Oort. The force exerted by the stellar system in the direction perpendicular to the galactic plane and some related problems. *Bull. Astron. Inst. Netherlands*, 6:249–287, 1932.

[37] F. Zwicky. Die Rotverschiebung von extragalaktischen Nebeln. *Helv. Phys. Acta*, 6:110–127, 1933.

[38] V. C. Rubin, J. Ford, W. Kent, and N. Thonnard. Extended rotation curves of high-luminosity spiral galaxies. IV. Systematic dynamical properties, Sa through Sc. *Astrophys. J. Lett.*, 225:L107–L111, 1978.

[39] Y. Sofue, Y. Tutui, M. Honma, A. Tomita, T. Takamiya, J. Koda, and Y. Takeda. Central rotation curves of spiral galaxies. *Astrophys. J.*, 523:136, 1999.

[40] K. Freese. Review of Observational Evidence for Dark Matter in the Universe and in upcoming searches for Dark Stars. *EAS Publ. Ser.*, 36:113–126, 2009.

[41] D. Clowe, M. Bradac, A. H. Gonzalez, M. Markevitch, S. W. Randall, C. Jones, and D. Zaritsky. A direct empirical proof of the existence of dark matter. *Astrophys. J. Lett.*, 648:L109–L113, 2006.

[42] M. Roos. Dark Matter: The evidence from astronomy, astrophysics and cosmology. *arXiv*, 1 2010.

[43] E. W. Kolb and M. S. Turner. *The Early Universe*, volume 69. 1990.

[44] R. Keisler, C. L. Reichardt, K. A. Aird, B. A. Benson, L. E. Bleem, J. E. Carlstrom, C. L. Chang, H. M. Cho, T. M. Crawford, A. T. Crites, T. de Haan, M. A. Dobbs, J. Dudley, E. M. George, N. W. Halverson, G. P. Holder, W. L. Holzapfel, S. Hoover, Z. Hou, J. D. Hrubes, M. Joy, L. Knox, A. T. Lee, E. M. Leitch, M. Lueker, D. Luong-Van, J. J. McMahon, J. Mehl, S. S. Meyer, M. Millea, J. J. Mohr, T. E. Montroy, T. Natoli, S. Padin, T. Plagge, C. Pryke, J. E. Ruhl, K. K. Schaffer, L. Shaw, E. Shirokoff, H. G. Spieler, Z. Staniszewski, A. A. Stark, K. Story, A. van Engelen, K. Vanderlinde, J. D. Vieira, R. Williamson, and O. Zahn. A MEASUREMENT OF THE DAMPING TAIL OF THE COSMIC MICROWAVE BACKGROUND POWER SPECTRUM WITH THE SOUTH POLE TELESCOPE. *The Astrophysical Journal*, 743(1):28, November 2011.

[45] D. J. Fixsen. THE TEMPERATURE OF THE COSMIC MICROWAVE BACKGROUND. *The Astrophysical Journal*, 707(2):916–920, November 2009.

[46] NASA. Wmap cosmic microwave background anisotropy map. https://map.gsfc.nasa.gov/media/121238/index.html.

[47] P. A. R. Ade et al. Planck 2015 results. XX. Constraints on inflation. *Astron. Astrophys.*, 594:A20, 2016.

[48] F. Bazzocchi and M. Fabbrichesi. Little hierarchy problem for new physics just beyond the LHC. *Phys. Rev. D*, 87(3):036001, 2013.

[49] P. W. Graham, I. G. Irastorza, S. K. Lamoreaux, A. Lindner, and K. A. van Bibber. Experimental Searches for the Axion and Axion-Like Particles. *Ann. Rev. Nucl. Part. Sci.*, 65:485–514, 2015.

[50] R. D. Peccei and H. R. Quinn. CP conservation in the presence of pseudoparticles. *Phys. Rev. Lett.*, 38:1440–1443, Jun 1977.

[51] R. D. Peccei and H. R. Quinn. Constraints imposed by CP conservation in the presence of pseudoparticles. *Phys. Rev. D*, 16:1791–1797, Sep 1977.

[52] F. Wilczek. Problem of Strong P and T Invariance in the Presence of Instantons. *Phys. Rev. Lett.*, 40:279–282, 1978.

[53] S. Weinberg. A New Light Boson? *Phys. Rev. Lett.*, 40:223–226, 1978.

[54] K. Arun, S. B. Gudennavar, and C. Sivaram. Dark matter, dark energy, and alternate models: A review. *Adv. Space Res.*, 60:166–186, 2017.

[55] Y. Zhang and Y. Zhao. Unconventional dark matter models: a brief review. *Sci. Bull.*, 60(11):986–994, 2015.

[56] R. Kolb et al. Basic research needs for dark-matter small projects new initiatives: Report of the department of energy's high energy physics workshop on dark matter. Technical report, Office of Scientific and Technical Information (OSTI), 10 2018.

[57] P. A. Zyla et al. Review of Particle Physics. *PTEP*, 2020(8):083C01, 2020.

[58] R. Essig. The low-mass dark matter frontier. *Physics*, 13, December 2020.

[59] J. A. Dror, G. Elor, and R. Mcgehee. Absorption of Fermionic Dark Matter by Nuclear Targets. *JHEP*, 02:134, 2020.

[60] M. Pospelov and A. Ritz. Resonant scattering and recombination of pseudo-degenerate WIMPs. *Phys. Rev. D*, 78:055003, 2008.

[61] H. An, M. Pospelov, and J. Pradler. Direct constraints on charged excitations of dark matter. *Phys. Rev. Lett.*, 109:251302, Dec 2012.

[62] M. J. Dolinski, A. W. P. Poon, and W. Rodejohann. Neutrinoless Double-Beta Decay: Status and Prospects. *Ann. Rev. Nucl. Part. Sci.*, 69:219–251, 2019.

[63] J. B. Albert et al. Investigation of radioactivity-induced backgrounds in EXO-200. *Phys. Rev. C*, 92(1):015503, 2015.

[64] J. B. Albert et al. Cosmogenic Backgrounds to $0\nu\beta\beta$ in EXO-200. *JCAP*, 04:029, 2016.

[65] S. A. Kharusi et al. Search for MeV Electron Recoils from Dark Matter in EXO-200. *arXiv:2207.00897*, 7 2022.

[66] N. Ackerman et al. Observation of Two-Neutrino Double-Beta Decay in ^{136}Xe with EXO-200. *Phys. Rev. Lett.*, 107:212501, 2011.

[67] M. Auger et al. Search for Neutrinoless Double-Beta Decay in ^{136}Xe with EXO-200. *Phys. Rev. Lett.*, 109:032505, 2012.

[68] J. B. Albert et al. Search for Majorana neutrinos with the first two years of EXO-200 data. *Nature*, 510:229–234, 2014.

[69] J. B. Albert et al. Search for Neutrinoless Double-Beta Decay with the Upgraded EXO-200 Detector. *Phys. Rev. Lett.*, 120(7):072701, 2018.

[70] Aurubis. Aurubis, metals for progress.

[71] 3M. 3m novec 7000 engineered fluid (hfe-7000), 2022.

[72] M. Auger et al. The EXO-200 detector, part I: Detector design and construction. *JINST*, 7:P05010, 2012.

[73] N. Ackerman et al. The EXO-200 detector, part II: auxiliary systems. *JINST*, 17(02):P02015, 2022.

[74] E. A. Mccutchan. Nuclear Data Sheets for A=136. *Nucl. Data Sheets*, 152:331–667, 2018.

[75] B. Rebeiro et al. Spectroscopy of low lying states in (136)Cs. *J. Phys. Conf. Ser.*, 689(1):012026, 2016.

[76] S. Haselschwardt, B. Lenardo, P. Pirinen, and J. Suhonen. Solar neutrino detection in liquid xenon detectors via charged-current scattering to excited states. *Phys. Rev. D*, 102(7):072009, 2020.

[77] S. Agostinelli et al. GEANT4–a simulation toolkit. *Nucl. Instrum. Meth. A*, 506:250–303, 2003.

[78] J. B. Albert et al. Improved measurement of the $2\nu\beta\beta$ half-life of ^{136}Xe with the EXO-200 detector. *Phys. Rev. C*, 89(1):015502, 2014.

[79] S. Al Kharusi et al. Measurement of the Spectral Shape of the β-Decay of ^{137}Xe to the Ground State of ^{137}Cs in EXO-200 and Comparison with Theory. *Phys. Rev. Lett.*, 124(23):232502, 2020.

[80] G. Anton et al. Measurement of the scintillation and ionization response of liquid xenon at MeV energies in the EXO-200 experiment. *Phys. Rev. C*, 101(6):065501, 2020.

[81] A. Belyaev, E. Bertuzzo, C. Caniu Barros, O. Eboli, G. Grilli Di Cortona, F. Iocco, and A. Pukhov. Interplay of the LHC and non-LHC Dark Matter

searches in the Effective Field Theory approach. *Phys. Rev. D*, 99(1):015006, 2019.

[82] A. E. Bayer and U. Seljak. The look-elsewhere effect from a unified Bayesian and frequentist perspective. *JCAP*, 10:009, 2020.

[83] A. Avasthi et al. Kiloton-scale xenon detectors for neutrinoless double beta decay and other new physics searches. *Phys. Rev. D*, 104(11):112007, 2021.

[84] J. Aalbers et al. DARWIN: towards the ultimate dark matter detector. *JCAP*, 11:017, 2016.

[85] S. A. Kharusi et al. nEXO Pre-Conceptual Design Report. *arXiv*, 5 2018.

[86] S. Kravitz, G. D. Orebi Gann, R. J. Smith, L. Hagaman, E. P. Bernard, D. N. McKinsey, L. Rudd, L. Tvrznikova, and M. Sakai. Measurements of Angle-Resolved Reflectivity of PTFE in Liquid Xenon with IBEX. *Eur. Phys. J. C*, 80(3):262, 2020.

[87] T. Stiegler et al. Event reconstruction in a liquid xenon Time Projection Chamber with an optically-open field cage. *Nucl. Instrum. Meth. A*, 1000:165239, 2021.

[88] M. Jewell et al. Characterization of an Ionization Readout Tile for nEXO. *JINST*, 13(01):P01006, 2018.

[89] Z. Li et al. Simulation of charge readout with segmented tiles in nEXO. *JINST*, 14(09):P09020, 2019.

[90] J. B. Albert et al. Measurement of the Drift Velocity and Transverse Diffusion of Electrons in Liquid Xenon with the EXO-200 Detector. *Phys. Rev. C*, 95(2):025502, 2017.

[91] O. Njoya et al. Measurements of electron transport in liquid and gas Xenon using a laser-driven photocathode. *Nucl. Instrum. Meth. A*, 972:163965, 2020.

[92] J. B. Albert et al. Sensitivity and Discovery Potential of nEXO to Neutrinoless Double Beta Decay. *Phys. Rev. C*, 97(6):065503, 2018.

[93] E. Aprile et al. Lowering the radioactivity of the photomultiplier tubes for the XENON1T dark matter experiment. *Eur. Phys. J. C*, 75(11):546, 2015.

[94] D. S. Leonard et al. Systematic study of trace radioactive impurities in candidate construction materials for EXO-200. *Nucl. Instrum. Meth. A*, 591:490–509, 2008.

[95] E. Garutti. Silicon Photomultipliers for High Energy Physics Detectors. *JINST*, 6:C10003, 2011.

[96] F. Simon. Silicon photomultipliers in particle and nuclear physics. *Nucl. Instrum. Meth. A*, 926:85–100, 2019.

[97] C. E. Aalseth et al. DarkSide-20k: A 20 tonne two-phase LAr TPC for direct dark matter detection at LNGS. *Eur. Phys. J. Plus*, 133:131, 2018.

[98] N. Abgrall et al. The Large Enriched Germanium Experiment for Neutrinoless $\beta\beta$ Decay: LEGEND-1000 Preconceptual Design Report. *arXiv*, 7 2021.

[99] A. M. Baldini et al. The design of the MEG II experiment. *Eur. Phys. J. C*, 78(5):380, 2018.

[100] D. Renker. Geiger-mode avalanche photodiodes, history, properties and problems. *Nucl. Instrum. Meth. A*, 567:48–56, 2006.

[101] D. Renker and E. Lorenz. Advances in solid state photon detectors. *Journal of Instrumentation*, 4(04):P04004–P04004, April 2009.

[102] A. Jamil et al. VUV-sensitive Silicon Photomultipliers for Xenon Scintillation Light Detection in nEXO. *IEEE Trans. Nucl. Sci.*, 65(11):2823–2833, 2018.

[103] F. Acerbi and S. Gundacker. Understanding and simulating SiPMs. *Nuclear Instruments and Methods in Physics Research Section A: Accelerators, Spectrometers, Detectors and Associated Equipment*, 926:16–35, May 2019.

[104] I. Ostrovskiy et al. Characterization of Silicon Photomultipliers for nEXO. *IEEE Trans. Nucl. Sci.*, 62(4):1825–1836, 2015.

[105] G. Gallina et al. Characterization of the Hamamatsu VUV4 MPPCs for nEXO. *Nucl. Instrum. Meth. A*, 940:371–379, 2019.

[106] Fondazione bruno kessler. https://www.fbk.eu.

[107] Hamamatsu photonics k.k. https://www.hamamatsu.com.

[108] P. Nakarmi et al. Reflectivity and PDE of VUV4 Hamamatsu SiPMs in Liquid Xenon. *JINST*, 15(01):P01019, 2020.

[109] M. Wagenpfeil et al. Reflectivity of VUV-sensitive silicon photomultipliers in liquid Xenon. *JINST*, 16(08):P08002, 2021.

[110] P. Lv et al. Reflectance of Silicon Photomultipliers at Vacuum Ultraviolet Wavelengths. *IEEE Trans. Nucl. Sci.*, 67(12):2501–2510, 2020.

[111] G. Anton et al. Search for Neutrinoless Double-β Decay with the Complete EXO-200 Dataset. *Phys. Rev. Lett.*, 123(16):161802, 2019.

[112] S. Seibert and A. Latorre. Fast Optical Monte Carlo Simulation With Surface-Based Geometries Using Chroma, 2011.

[113] J. A. Benjamin, Land, S. Naugle, and J. R. Klein. Chroma photon ray tracer for large-scale detectors, 2020.

[114] nEXO Collaboration. Chroma Simulation. https://github.com/nEXO-collaboration/chroma, 2022.

[115] L. Althueser et al. GPU-based optical simulation of the DARWIN detector. *arXiv*, 3 2022.

[116] M. Askins et al. THEIA: an advanced optical neutrino detector. *Eur. Phys. J. C*, 80(5):416, 2020.

[117] T. Kaptanoglu, M. Luo, B. Land, A. Bacon, and J. Klein. Spectral Photon Sorting For Large-Scale Cherenkov and Scintillation Detectors. *Phys. Rev. D*, 101(7):072002, 2020.

[118] J. Dalmasson, G. Gratta, A. Jamil, S. Kravitz, M. Malek, K. Wells, J. Bentley, S. Steven, and J. Su. Distributed Imaging for Liquid Scintillation Detectors. *Phys. Rev. D*, 97(5):052006, 2018.

[119] K. Fujii, Y. Endo, Y. Torigoe, S. Nakamura, T. Haruyama, K. Kasami, S. Mihara, K. Saito, S. Sasaki, and H. Tawara. High-accuracy measurement of the emission spectrum of liquid xenon in the vacuum ultraviolet region. *Nuclear Instruments and Methods in Physics Research Section A: Accelerators, Spectrometers, Detectors and Associated Equipment*, 795:293–297, September 2015.

[120] E. Hogenbirk, J. Aalbers, P. A. Breur, M. P. Decowski, K. van Teutem, and A. P. Colijn. Precision measurements of the scintillation pulse shape for low-energy recoils in liquid xenon. *JINST*, 13(05):P05016, 2018.

[121] B. J. Mount et al. LUX-ZEPLIN (LZ) Technical Design Report. *arXiv*, 3 2017.

[122] E. Aprile et al. Projected WIMP sensitivity of the XENONnT dark matter experiment. *JCAP*, 11:031, 2020.

[123] A. Baldini et al. Absorption of scintillation light in a 100 l liquid xenon gamma ray detector and expected detector performance. *Nucl. Instrum. Meth. A*, 545:753–764, 2005.

[124] E. Grace and J. A. Nikkel. Index of refraction, Rayleigh scattering length, and Sellmeier coefficients in solid and liquid argon and xenon. *Nucl. Instrum. Meth. A*, 867:204–208, 2017.

[125] G. M. Seidel, R. E. Lanou, and W. Yao. Rayleigh scattering in rare gas liquids. *Nucl. Instrum. Meth. A*, 489:189–194, 2002.

[126] P. Nakarmi et al. Reflectivity and PDE of VUV4 Hamamatsu SiPMs in Liquid Xenon. *JINST*, 15(01):P01019, 2020.

[127] L. Barkov, A. Grebenuk, N. Ryskulov, P. Stepanov, and S. Zverev. Measurement of the refractive index of liquid xenon for intrinsic scintillation light. *Nuclear Instruments and Methods in Physics Research Section A: Accelerators, Spectrometers, Detectors and Associated Equipment*, 379(3):482–483, September 1996.

[128] V. N. Solovov, V. Chepel, M. I. Lopes, and A. Hitachi. Measurement of the refractive index and attenuation length of liquid xenon for its scintillation light. *Nucl. Instrum. Meth. A*, 516:462–474, 2004.

[129] R. Kitamura, L. Pilon, and M. Jonasz. Optical constants of silica glass from extreme ultraviolet to far infrared at near room temperature. *Applied Optics*, 46(33):8118, November 2007.

[130] E. Aprile et al. Projected WIMP sensitivity of the XENONnT dark matter experiment. *JCAP*, 11:031, 2020.

[131] E. Aprile et al. The XENON100 Dark Matter Experiment. *Astropart. Phys.*, 35:573–590, 2012.

[132] E. Aprile. The XENON1T Dark Matter Search Experiment. *Springer Proc. Phys.*, 148:93–96, 2013.

[133] D. S. Akerib et al. The Large Underground Xenon (LUX) Experiment. *Nucl. Instrum. Meth. A*, 704:111–126, 2013.

[134] D. S. Akerib et al. LUX-ZEPLIN (LZ) Conceptual Design Report. *arXiv*, 9 2015.

[135] D. Y. Akimov et al. First ground-level laboratory test of the two-phase xenon emission detector RED-100. *JINST*, 15(02):P02020, 2020.

[136] X. Cao et al. PandaX: A Liquid Xenon Dark Matter Experiment at CJPL. *Sci. China Phys. Mech. Astron.*, 57:1476–1494, 2014.

[137] H. Zhang et al. Dark matter direct search sensitivity of the PandaX-4T experiment. *Sci. China Phys. Mech. Astron.*, 62(3):31011, 2019.

[138] G. Bakale, U. Sowada, and W. F. Schmidt. Effect of an electric field on electron attachment to sulfur hexafluoride, nitrous oxide, and molecular oxygen in liquid argon and xenon. *The Journal of Physical Chemistry*, 80(23):2556–2559, November 1976.

[139] J. F. O'Hanlon. *A User's Guide to Vacuum Technology*. Wiley, June 2003.

[140] C. A. Coulson. The mathematics of diffusion. *The Mathematical Gazette*, 42(340):165–165, May 1958.

[141] H. F. Dylla, J. Lab, and N. News. The Problem of Water in Vacuum Systems.

[142] M. Moraw and H. Prasoł. Gas desorption from a stainless-steel surface in ultrahigh vacuum devices. *Vacuum*, 71(4):471–479, July 2003.

[143] M. Moraw. Analysis of outgassing characteristics of metals. *Vacuum*, 36(7-9):523–525, July 1986.

[144] D. Edwards. An upper bound to the outgassing rate of metal surfaces. *Journal of Vacuum Science and Technology*, 14(4):1030–1032, July 1977.

[145] Leak tightness of vcr fittings. https://www.swagelok.com/downloads/webcatalogs/en/MS-01-24.pdf. Accessed: 2019-11-17.

[146] S. G. Bratsch and J. Lagowski. Predicted stabilities of monatomic anions in water and liquid ammonia at 298.15 k. *Polyhedron*, 5(11):1763–1770, 1986.

[147] W. Chaibi, R. J. Peláez, C. Blondel, C. Drag, and C. Delsart. Effect of a magnetic field in photodetachment microscopy. *The European Physical Journal D*, 58(1):29–37, April 2010.

[148] P. Collon, W. Kutschera, and Z.-T. Lu. TRACING NOBLE GAS RADIONUCLIDES IN THE ENVIRONMENT. *Annual Review of Nuclear and Particle Science*, 54(1):39–67, December 2004.

[149] N. Aoki and Y. Makide. The concentration of krypton in the atmosphere—its revision after half a century—. *Chemistry Letters*, 34(10):1396–1397, October 2005.

[150] J. SCHRÖDER, K. O. MÜNNICH, and D. H. EHHALT. Physical sciences: Krypton-85 in the troposphere. *Nature*, 233(5322):614–615, October 1971.

[151] J. W. Tepel. Nuclear data sheets for A = 85. *Nucl. Data Sheets*, 30:501–571, 1980. [Erratum: Nucl.Data Sheets 32, 681–681 (1981)].

[152] K. Radan and B. Žemva. Solvent capabilities of liquid and supercritical xenon, 2012.

[153] P. M. Rentzepis and D. C. Douglass. Xenon as a solvent. *Nature*, 293(5828):165–166, September 1981.

[154] R. D. Smith, S. L. Frye, C. R. Yonker, and R. W. Gale. Solvent properties of supercritical xenon and sulfur hexafluoride. *The Journal of Physical Chemistry*, 91(11):3059–3062, May 1987.

[155] V. J. Krukonis, M. A. McHugh, and A. J. Seckner. Xenon as a supercritical solvent. *The Journal of Physical Chemistry*, 88(13):2687–2689, June 1984.

[156] G. Pereira. Energy resolution of the LZ detector for High-Energy Electronic Recoils. https://indico.in2p3.fr/event/20879/contributions/109640/.

[157] SAES. Heated getter gas purifiers, 2022.

[158] Edwards. T-station 85 pumping stations, 2022.

[159] Edwards. Edwards WRG Cold Cathode Pirani. https://www.edwardsvacuum.com/content/dam/brands/edwards-vacuum/edwards-website-assets/scientific-vacuum/documents/datasheets/Edwards-WRG-Wide-Range-Gauge-3601-0236-01.pdf, 2022.

[160] I. TE Technology. Cp-200ht peltier-thermoelectric cold-plate cooler, 2022.

[161] Omega. Six channel handheld rechargeable temperature data logger. https://www.omega.com/en-us/temperature-measurement/temperature-and-humidity-data-loggers/rdxl6sd-usb-series/p/RDXL6SD-USB.

[162] S. R. Systems. Residual gas analyzer. https://www.thinksrs.com/products/rga.html.

[163] M. H. Klopffer and B. Flaconneche. Transport properdines of gases in polymers: Bibliographic review. *Oil and Gas Science and Technology*, 56(3):223–244, May 2001.

[164] D. V. Krevelen and K. T. Nijenhuis. Properties determining mass transfer in polymeric systems. In *Properties of Polymers*, pages 655–702. Elsevier, 2009.

[165] D. Leonard, A. Dobi, L. K. C. Hall, T. Langford, S. Slutsky, and Y.-R. Yen. A simple high-sensitivity technique for purity analysis of xenon gas. *Nuclear Instruments and Methods in Physics Research Section A: Accelerators, Spectrometers, Detectors and Associated Equipment*, 621(1-3):678–684, September 2010.

[166] R. Bevilacqua, A. Göök, F.-J. Hambsch, N. Jovančević, and M. Vidali. A procedure for the characterization of electron transmission through frisch grids. *Nuclear Instruments and Methods in Physics Research Section A: Accelerators, Spectrometers, Detectors and Associated Equipment*, 770:64–67, January 2015.

[167] CAEN. High voltage power supply, 2022.

[168] B. Precision. Dual display handheld capacitance meter, 2022.

[169] Leybold. Ecodry 40 plus vacuum pump, 2022.

[170] Cryomech. Pt60 cryocooler, 2022.

[171] Hamamatsu. 5w xenon flash lamp modules, 2022.

[172] Thorlabs. Ultra-high-vacuum, high-temperature multimode fiber optic patch cables, 2022.

[173] G. Instek. Dual-channel arbitrary function generator, 2022.

[174] Swagelok. Stainless steel double ended dot-compliant sample cylinder, 2022.

[175] Setra. Ultra high purity pressure transducer, 2022.

[176] KNF. Process vacuum pumps and compressors, 2022.

[177] Edwards. Dry scroll pump, 2022.

[178] N. Instruments. Compactrio systems, 2022.

[179] Cremat. Cr-150-r5 csp evaluation board, 2022.

[180] Cremat. Cr-110-r2.1 charge sensitive preamplifier, 2022.

[181] Rohde and Schwartz. R&s rtb2000 oscilloscope, 2022.

[182] S. R. Systems. Low-noise voltage preamplifier, 2022.

[183] Behlke. Fast high voltage solid-state switches, 2022.

[184] J. B. Albert et al. Measurement of the Drift Velocity and Transverse Diffusion of Electrons in Liquid Xenon with the EXO-200 Detector. *Phys. Rev. C*, 95(2):025502, 2017.

[185] K. Ni. An Empirical Purification Model for the Electronegative Contaminant Control of nEXO. Internal nEXO Note.

[186] J. Howlett. Results from the Xeclipse Liquid Purification Test System For XENONnT. https://indico.physics.ucsd.edu/event/1/contributions/83/.

[187] G. T. Brower and G. Thodos. Vapor pressures of liquid oxygen between the triple point and critical point. *Journal of Chemical and Engineering Data*, 13(2):262–264, April 1968.

[188] A. Michels and T. Wassenaar. Vapour pressure of liquid xenon. *Physica*, 16(3):253–256, March 1950.

[189] L. Baudis, P. Sanchez-Lucas, and K. Thieme. A measurement of the mean electronic excitation energy of liquid xenon. *Eur. Phys. J. C*, 81(12):1060, 2021.

[190] M. Szydagis, N. Barry, K. Kazkaz, J. Mock, D. Stolp, M. Sweany, M. Tripathi, S. Uvarov, N. Walsh, and M. Woods. NEST: A Comprehensive Model for Scintillation Yield in Liquid Xenon. *JINST*, 6:P10002, 2011.

[191] E. Conti et al. Correlated fluctuations between luminescence and ionization in liquid xenon. *Phys. Rev. B*, 68:054201, 2003.

[192] M. Redshaw, E. Wingfield, J. McDaniel, and E. G. Myers. Mass and double-beta-decay q value of ^{136}Xe. *Phys. Rev. Lett.*, 98:053003, Feb 2007.

[193] P. M. McCowan and R. C. Barber. q value for the double-β decay of ^{136}Xe. *Phys. Rev. C*, 82:024603, Aug 2010.

[194] E. Aprile and T. Doke. Liquid Xenon Detectors for Particle Physics and Astrophysics. *Rev. Mod. Phys.*, 82:2053–2097, 2010.

[195] S. R. Golwala. *Exclusion limits on the WIMP nucleon elastic scattering cross-section from the Cryogenic Dark Matter Search*. PhD thesis, UC, Berkeley, 2000.

[196] M. Szydagis, N. Barry, K. Kazkaz, J. Mock, D. Stolp, M. Sweany, M. Tripathi, S. Uvarov, N. Walsh, and M. Woods. NEST: a comprehensive model for scintillation yield in liquid xenon. *Journal of Instrumentation*, 6(10):P10002–P10002, October 2011.

[197] M. Szydagis, J. Balajthy, J. Brodsky, J. Cutter, J. Huang, E. Kozlova, B. Lenardo, A. Manalaysay, D. McKinsey, M. Mooney, J. Mueller, K. Ni, G. Rischbieter, M. Tripathi, C. Tunnell, V. Velan, and Z. Zhao. Nestcollaboration/nest: New, flexible lxe nr yields and resolution model + g4 improvements + linear noise + much more, 2019.

[198] M. D. Schwartz. Modern Machine Learning and Particle Physics. *arXiv*, 3 2021.

[199] S. Delaquis et al. Deep Neural Networks for Energy and Position Reconstruction in EXO-200. *JINST*, 13(08):P08023, 2018.

[200] E. Browne and J. K. Tuli. Nuclear Data Sheets for A = 238. *Nucl. Data Sheets*, 127:191–332, 2015.

[201] E. Browne. Nuclear Data Sheets for A = 232*. *Nucl. Data Sheets*, 107:2579–2648, 2006.

[202] J. B. Albert et al. Searches for double beta decay of ^{134}Xe with EXO-200. *Phys. Rev. D*, 96(9):092001, 2017.

[203] J. B. Albert et al. Search for Majoron-emitting modes of double-beta decay of ^{136}Xe with EXO-200. *Phys. Rev. D*, 90(9):092004, 2014.

[204] S. A. Kharusi et al. Search for Majoron-emitting modes of Xe136 double beta decay with the complete EXO-200 dataset. *Phys. Rev. D*, 104(11):112002, 2021.

[205] J. B. Albert et al. First Search for Lorentz and CPT Violation in Double Beta Decay with EXO-200. *Phys. Rev. D*, 93(7):072001, 2016.

[206] A. Dobi et al. Xenon purity analysis for EXO-200 via mass spectrometry. *Nucl. Instrum. Meth. A*, 675:40–46, 2012.

[207] E. Hoppe, A. Seifert, C. Aalseth, P. Bachelor, A. Day, D. Edwards, T. Hossbach, K. Litke, J. McIntyre, H. Miley, S. Schulte, J. Smart, and G. Warren. Cleaning and passivation of copper surfaces to remove surface radioactivity and prevent oxide formation. *Nuclear Instruments and Methods in Physics Research Section A: Accelerators, Spectrometers, Detectors and Associated Equipment*, 579(1):486–489, August 2007.

[208] E. W. Hoppe, C. E. Aalseth, O. T. Farmer, T. W. Hossbach, M. Liezers, H. S. Miley, N. R. Overman, and J. H. Reeves. Reduction of radioactive backgrounds

in electroformed copper for ultra-sensitive radiation detectors. *Nucl. Instrum. Meth. A*, 764:116–121, 2014.

[209] N. Abgrall et al. The Majorana Demonstrator radioassay program. *Nucl. Instrum. Meth. A*, 828:22–36, 2016.

[210] J. B. Albert et al. Measurements of the ion fraction and mobility of α- and β-decay products in liquid xenon using the EXO-200 detector. *Phys. Rev. C*, 92(4):045504, 2015.

[211] E. Aprile et al. Online^{222} Rn removal by cryogenic distillation in the XENON100 experiment. *Eur. Phys. J. C*, 77(6):358, 2017.

[212] X. Cui et al. Design and commissioning of the PandaX-4T cryogenic distillation system for krypton and radon removal. *JINST*, 16(07):P07046, 2021.

[213] G. J. Feldman and R. D. Cousins. A Unified approach to the classical statistical analysis of small signals. *Phys. Rev. D*, 57:3873–3889, 1998.

[214] W. A. Rolke, A. M. Lopez, and J. Conrad. Limits and confidence intervals in the presence of nuisance parameters. *Nucl. Instrum. Meth. A*, 551:493–503, 2005.

[215] K. Abe et al. Solar Neutrino Measurements in Super-Kamiokande-IV. *Phys. Rev. D*, 94(5):052010, 2016.

[216] S. S. Wilks. The large-sample distribution of the likelihood ratio for testing composite hypotheses. *The Annals of Mathematical Statistics*, 9(1):60–62, March 1938.

[217] C. Chambers et al. Imaging individual barium atoms in solid xenon for barium tagging in nEXO. *Nature*, 569(7755):203–207, 2019.

[218] G. Cowan, K. Cranmer, E. Gross, and O. Vitells. Asymptotic formulae for likelihood-based tests of new physics. *Eur. Phys. J. C*, 71:1554, 2011. [Erratum: Eur.Phys.J.C 73, 2501 (2013)].

[219] P. N. Bhattiprolu, S. P. Martin, and J. D. Wells. Criteria for projected discovery and exclusion sensitivities of counting experiments. *Eur. Phys. J. C*, 81(2):123, 2021.

[220] E. Caurier et al. The Influence of pairing on the nuclear matrix elements of the neutrinoless beta beta decays. *Phys. Rev. Lett.*, 100:052503, 2008.

[221] J. Suhonen and O. Civitarese. Effects of orbital occupancies and spin-orbit partners on 0 nu beta beta-decay rates. *Nucl. Phys. A*, 847:207–232, 2010.

[222] T. R. Rodriguez and G. Martinez-Pinedo. Neutrinoless double beta decay studied with configuration mixing methods. *Prog. Part. Nucl. Phys.*, 66:436–440, 2011.

[223] A. Meroni, S. T. Petcov, and F. Simkovic. Multiple CP non-conserving mechanisms of $(\beta\beta)_{0\nu}$-decay and nuclei with largely different nuclear matrix elements. *JHEP*, 02:025, 2013.

[224] M. T. Mustonen and J. Engel. Large-scale calculations of the double-β decay of ^{76}Ge,^{130}Te,^{136}Xe, and ^{150}Nd in the deformed self-consistent Skyrme quasiparticle random-phase approximation. *Phys. Rev. C*, 87(6):064302, 2013.

[225] F. Šimkovic et al. $0\nu\beta\beta$ and $2\nu\beta\beta$ nuclear matrix elements, quasiparticle random-phase approximation, and isospin symmetry restoration. *Phys. Rev. C*, 87(4):045501, 2013.

[226] N. L. Vaquero, T. R. Rodríguez, and J. L. Egido. Shape and pairing fluctuations effects on neutrinoless double beta decay nuclear matrix elements. *Phys. Rev. Lett.*, 111(14):142501, 2013.

[227] J. Engel, F. Simkovic, and P. Vogel. Chiral Two-Body Currents and Neutrinoless Double-Beta Decay in the QRPA. *Phys. Rev. C*, 89(6):064308, 2014.

[228] J. Barea, J. Kotila, and F. Iachello. $0\nu\beta\beta$ and $2\nu\beta\beta$ nuclear matrix elements in the interacting boson model with isospin restoration. *Phys. Rev. C*, 91(3):034304, 2015.

[229] J. M. Yao et al. Systematic study of nuclear matrix elements in neutrinoless double-β decay with a beyond-mean-field covariant density functional theory. *Phys. Rev. C*, 91(2):024316, 2015.

[230] J. Hyvärinen and J. Suhonen. Nuclear matrix elements for $0\nu\beta\beta$ decays with light or heavy Majorana-neutrino exchange. *Phys. Rev. C*, 91(2):024613, 2015.

[231] M. Horoi and A. Neacsu. Shell model predictions for ^{124}Sn double-β decay. *Phys. Rev. C*, 93(2):024308, 2016.

[232] C. F. Jiao, J. Engel, and J. D. Holt. Neutrinoless double-β decay matrix elements in large shell-model spaces with the generator-coordinate method. *Phys. Rev. C*, 96:054310, Nov 2017.

[233] L. Jokiniemi, H. Ejiri, D. Frekers, and J. Suhonen. Neutrinoless $\beta\beta$ nuclear matrix elements using isovector spin-dipole $J^\pi = 2^-$ data. *Phys. Rev. C*, 98(2):024608, 2018.

[234] J. Menéndez. Towards Reliable Nuclear Matrix Elements for Neutrinoless $\beta\beta$ Decay. *JPS Conf. Proc.*, 23:012036, 2018.

[235] F. Šimkovic, R. Dvornický, D. c. v. Štefánik, and A. Faessler. Improved description of the $2\nu\beta\beta$-decay and a possibility to determine the effective axial-vector coupling constant. *Phys. Rev. C*, 97:034315, Mar 2018.

[236] D.-L. Fang, A. Faessler, and F. Simkovic. $0\nu\beta\beta$-decay nuclear matrix element for light and heavy neutrino mass mechanisms from deformed quasiparticle random-phase approximation calculations for ^{76}Ge, ^{82}Se, ^{130}Te, ^{136}Xe , and ^{150}Nd with isospin restoration. *Phys. Rev. C*, 97(4):045503, 2018.

[237] F. F. Deppisch et al. Analysis of light neutrino exchange and short-range mechanisms in $0\nu\beta\beta$ decay. *Phys. Rev. D*, 102(9):095016, 2020.

[238] I. Esteban, M. C. Gonzalez-Garcia, M. Maltoni, T. Schwetz, and A. Zhou. The fate of hints: updated global analysis of three-flavor neutrino oscillations. *JHEP*, 09:178, 2020.

[239] N. Abgrall et al. The Large Enriched Germanium Experiment for Neutrinoless $\beta\beta$ Decay: LEGEND-1000 Preconceptual Design Report. *arXiv*, 7 2021.

[240] W. R. Armstrong et al. CUPID pre-CDR. *arXiv*, 7 2019.

[241] Nu-FIT 5.0, 2020. www.nu-fit.org.

[242] J. Aalbers et al. DARWIN: towards the ultimate dark matter detector. *JCAP*, 11:017, 2016.

[243] K. Griest and M. Kamionkowski. Unitarity limits on the mass and radius of dark-matter particles. *Phys. Rev. Lett.*, 64:615–618, Feb 1990.

[244] K. Scholberg. Supernova Neutrino Detection. *Ann. Rev. Nucl. Part. Sci.*, 62:81–103, 2012.

[245] E. Aprile et al. Energy resolution and linearity of XENON1T in the MeV energy range. *Eur. Phys. J. C*, 80(8):785, 2020.

[246] J. Ye. The Electronic Recoil Excess in XENON1T and the Prospect to Decipher it with XENONnT (TAUP 2021). https://indico.ific.uv.es/event/6178/contributions/15875/.

[247] E. Aprile et al. Physics reach of the XENON1T dark matter experiment. *JCAP*, 04:027, 2016.

[248] Fast optical monte carlo simulation with surface-based geometries. https://github.com/BenLand100/chroma.

[249] J. P. Brodsky, S. Sangiorgio, M. Heffner, and T. Stiegler. Background Discrimination for Neutrinoless Double Beta Decay in Liquid Xenon Using Cherenkov Light. *Nucl. Instrum. Meth. A*, 922:76–83, 2019.

[250] A. Hitachi, V. Chepel, M. I. Lopes, and V. N. Solovov. New approach to the calculation of the refractive index of liquid and solid xenon. *The Journal of Chemical Physics*, 123(23):234508, December 2005.

[251] S. Seltzer. Stopping-powers and range tables for electrons, protons, and helium ions, nist standard reference database 124, 1993.

[252] J.-F. Pratte, F. Nolet, S. Parent, F. Vachon, N. Roy, T. Rossignol, K. Deslandes, H. Dautet, R. Fontaine, and S. A. Charlebois. 3D Photon-To-Digital Converter for Radiation Instrumentation: Motivation and Future Works. *Sensors*, 21(2):598, 2021.

[253] A. V. Lyashenko et al. Performance of Large Area Picosecond Photo-Detectors (LAPPD^{TM}). *Nucl. Instrum. Meth. A*, 958:162834, 2020.

[254] T. Kaptanoglu, E. J. Callaghan, M. Yeh, and G. D. O. Gann. Cherenkov and scintillation separation in water-based liquid scintillator using an LAPPD^{TM}. *Eur. Phys. J. C*, 82(2):169, 2022.

[255] M. An et al. A Low-Noise CMOS Pixel Direct Charge Sensor, Topmetal-II-. *Nucl. Instrum. Meth. A*, 810:144–150, 2016.

[256] M. Lupberger, Y. Bilevych, H. Blank, D. Danilov, K. Desch, A. Hamann, J. Kaminski, W. Ockenfels, J. Tomtschak, and S. Zigann-Wack. Toward the pixel-TPC: Construction and operation of a large area GridPix detector. *IEEE Transactions on Nuclear Science*, 64(5):1159–1167, May 2017.

[257] J. Asaadi et al. First Demonstration of a Pixelated Charge Readout for Single-Phase Liquid Argon Time Projection Chambers. *Instruments*, 4(1):9, 2020.

[258] U. Einhaus and J. Kaminski. ROPPERI - A TPC readout with GEMs, pads and Timepix. In *International Workshop on Future Linear Colliders*, 3 2017.